Doctoral theses at NTNU, 2016:226

Stian Baardsgaard Hanssen

Response of Laterally Loaded Monopiles

Doctoral thesis

Stian Baardsgaard Hanssen

ISBN 978-82-326-1790-6 (printed ver.)
ISBN 978-82-326-1791-3 (electronic ver.)
ISSN 1503-8181

NTNU
Norwegian University of
Science and Technology

NTNU
Norwegian University of
Science and Technology
Thesis for the Degree of
Philosophiae Doctor
Faculty of Engineering Science and Technology
Department of Civil and Transport Engineering

Doctoral theses at NTNU, 2016:226

NTNU
Norwegian University of
Science and Technology

Stian Baardsgaard Hanssen

Response of Laterally Loaded Monopiles

Thesis for the Degree of Philosophiae Doctor

Trondheim, September 2016

Norwegian University of Science and Technology
Faculty of Engineering Science and Technology
Department of Civil and Transport Engineering

NTNU
Norwegian University of
Science and Technology

NTNU
Norwegian University of Science and Technology

Thesis for the Degree of Philosophiae Doctor

Faculty of Engineering Science and Technology
Department of Civil and Transport Engineering

ISBN 978-82-326-1790-6 (printed ver.)
ISBN 978-82-326-1791-3 (electronic ver.)
ISSN 1503-8181

Doctoral theses at NTNU, 2016:226

Printed by NTNU Grafisk senter

Preface

This dissertation is submitted in partial fulfillment of the requirements for the degree of *philosophiae doctor* (PhD) at the Norwegian University of Science and Technology (NTNU). The study is made possible by the financial support from the Faculty of Engineering Science and Technology at NTNU. The work is presented as a monograph.

Abstract

The monopile is a common foundation option for offshore wind turbines, and the foundation stiffness to horizontal loading is an important input to their structural design. The design of laterally loaded piles is often performed with simplified beam models, where a simplified soil representation typically is included as nonlinear, uncoupled, distributed springs. In the design of offshore wind turbine support structures, simplified calculation methods are of great value, due to the many load cases that need to be simulated (several thousands). Measurements on operating offshore wind turbines show that the lateral foundation stiffness for monopiles tend to be significantly stiffer than predictions with the current recommendations for nonlinear spring stiffness as simplified soil representation.

The present PhD-work focuses on understanding and describing the mechanisms controlling the soil-structure interaction stiffness. The work comprises analytical, numerical and experimental techniques, resulting in a proposed framework for determination of soil spring stiffness for laterally loaded piles. This framework includes both rotational and lateral soil springs. Analytical solutions for initial stiffness and ultimate capacity are collected from the literature, and compared to the results from a 3D-FE study. The initial stiffness and ultimate resistance of the proposed soil springs are determined partly from the analytical solutions and partly from the results of the FE-study. The proposed soil springs are tested for pile-tests reported in the literature, and a series of model tests presented in this thesis. The proposed framework shows promising results; however, it tends to predict a too stiff response compared to physical measurements, and further work is needed.

The model tests are impact vibration tests on a 1:20 scale of a simplified offshore wind turbine geometry, and are performed and reported as a part of the work. The presented tests are conducted in order to investigate the possible influence of small strain soil stiffness to the pile eigenfrequency. A thorough presentation of the setup, instrumentation, testing and results is provided. The possible influence of small strain soil stiffness is evaluated in terms of a back analysis of the performed model test. From the back analyses, the representative soil stiffness is concluded to be softer than the soil stiffness for shear-wave propagation, and stiffer than the soil stiffness measured in the oedometer test. It is concluded that the strain-dependency of the soil stiffness is important, and that the stiffness degradation from the small strain range to engineering strains must be captured in order to reproduce the physical measurements in simulations.

A procedure is presented for extracting results from a 3D-FE analysis as lateral and rotational springs. It is shown that these springs can imitate the 3D-support well, with less than 1.5 % deviation in pile head displacements for 3D- and 1D-FEM for the load cases studied. Under the assumption that a 3D-FE analysis is able to give a fair representation of the laterally loaded pile problem, this procedure is recommended for use in design.

Acknowledgments

I wish to express my gratitude to Professor Gudmund Eiksund at the Department of Civil and Transport Engineering, Norwegian University of Science and Technology (NTNU) for his guidance during this work. His ability to put focus on the details is truly impressing, and is highly appreciated. Professor Steinar Nordal and Assistant Professor Arnfinn Emdal at the above department are gratefully acknowledged for valuable feedback in reviewing the manuscript for this thesis.

The experimental part of this PhD would not have been possible without the skills and expertise of the technicians involved. I am deeply grateful to Einar Husby and Gunnar Winther who build the underpressure system, and gave it a robustness far beyond what was provided in my simple sketches. My special thanks go to Jan Jønland for his detailed memory of everything that has been done in the foundation lab over the last 30 years, and to Per Østensen for his knowledge in the world of instrumentation and data acquisition. The precision and ingenuity in the work from workshop engineers Tage Westrum and Frank Stæhli is truly appreciated. Thanks to all of you for your positive attitude and ability to tackle unforeseen events, and to lending me a hand whenever needed.

During this work, I had the pleasure of a stay at the Statoil ASA research centre in Bergen. I wish to thank the Statoil offshore wind research group for their accommodating attitude, and in particular to Ole Havmøller and Arne Rekdal for all help and access to the full-scale measurements, and to Wei He for her help in organizing the stay. I gratefully appreciate the interaction and time shared with past and present PhD candidates, and in particular my office-mate and friend Ivan Depina. Special thanks go to Ivana Anusic, Ashenafi Yifru and Joar Tistel who have provided me valuable calculation time on their computers, and to Xenia Domes, Tonje Eide Helle and Priscilla Paniagua for their leading positions in the OAC, SEC and CLC.

My gratitude is also directed to my employer Multiconsult ASA for granting me a leave to do this PhD, for providing me office space whenever needed and for their support throughout all three years. Finally, I wish to thank my beloved Mette. I am deeply grateful for her long-standing support, her many encouragements and her patience for me and my work.

Contents

Appendices

Nomenclature

Latin symbols

A	cross-section area
A	empirical correction coefficient for the ultimate capacity of API p-y curves in sand
A	coefficient for empirical determination of $G_{s,max}$
A_1	coefficient dependent on the relative density of sand
B	foundation width
C_u	coefficient of uniformity
D	pile diameter
D	damping
Dr	relative density
D_{ref}	reference pile diameter (1 m)
E	Young's modulus
E_p	Young's modulus of pile
E_{pr}	Young's modulus of soil found from the pressureometer
E_s	Young's modulus of soil
$E_{s,0}$	Young's modulus of soil, surface value
$E_{s,50}^{ref}$	reference Young's modulus for loading (soil)
$E_{s,ur}^{ref}$	reference Young's modulus for unloading-reloading (soil)
F_h	horizontal force
$F_{h,top}$	horizontal force at pile top
F_{rz}	force in z-direction
$F_{rz,i}$	incremental force in z-direction
G	shear modulus
G_p	pile shear modulus
G_s	soil shear modulus
$G_{s,max}$	soil shear modulus at very small strains
$G_{s,max}^{ref}$	reference shear modulus at very small strains
H	height
I_p	2nd area moment of pile
I_ρ	Elastic influence factor
J	empirical coefficient
L	pile length
K_H	horizontal stiffness
K_a	Rankine active earth pressure coefficient
K_r	flexibility factor from Paulos (1971)
K_p	Rankine passive earth pressure coefficient
K_0	earth pressure coefficient at rest
K_0	modified Bessel function of the second kind
K_1	modified Bessel function of the second kind
M	moment load
M	bending moment
M_s	soil constraint modulus

M_t	bending moment at pile top
M_{top}	bending moment at pile top
M_{ult}	ultimate moment resistance
N	axial force
N_c	bearing capacity factor for the cohesive part of the soil resistance
N_{p0}	function appearing in the bearing capacity formulation from Yu et al. (2015)
N_q	bearing capacity factor for the frictional part of the soil resistance
N1	constant
N2	constant
R	radius
R^2	coefficient of determination (statistics)
S	rotation of pile cross-section
V	shear force
V	vertical load
V_v	vertical shear force
Z	thickness of soil layer

a	curve fitting parameter for the Hardin-Drnevich equation
a	acceleration
a_0*	complex dimensionless frequency
a_1	coefficient for empirical determination of $G_{s,max}$
b	curve fitting parameter for the Hardin-Drnevich equation
c	cohesion
c'_{ref}	cohesion
c_u	undrained shear strength
c_0	undrained shear strength at ground surface
d_s	damping parameter
d_{10}	grain diameter at 10% passing
d_{50}	mean grain size
d_{60}	grain diameter at 60% passing
e	void ratio
f	frequency
f_n	undamped eigenfrequency
$f_{n,d}$	damped eigenfrequency
g	constant
h	height
k	spring stiffness
k	constant
k_{Gibson}	rate of stiffness increase with depth
k_{bottom}	spring stiffness for lateral spring at pile toe
k_{top}	spring stiffness for lateral spring at pile top
k_0	earth pressure coefficient at rest
k_1	stiffness coefficient for the API p-y curves for sand (denoted k in the API-guidelines)
k_θ	spring stiffness for rotational spring
m	stress exponent

m	modulus number
m^*	Janbu' modulus number, rewritten for describing Young's modulus
n	scaling factor for stiffness
n	porosity
n_{max}	maximum porosity
n_{min}	minimum porosity
n^*	exponent for determination of $G_{s,max}$ based on empirical correlations
p	soil reaction
p_{atm}	atmospheric pressure (~100 kPa)
p_i	incremental soil reaction
p_{ref}	atmospheric pressure (100 kPa)
p_u	ultimate soil reaction
$p_{u,deep}$	ultimate soil reaction at depths unaffected by the soil surface
$p_{u,shallow}$	ultimate soil reaction at depths affected by the soil surface
p_0	initial vertical stress
q	load
q_f	failure load
r	radius
s_0	shear stress with Meyerhof notation
t	wall thickness
t	time
u	displacement
v_s	shear wave velocity
w	weight
x	distance in x-direction
x_i	incremental distance in x-direction
y	pile deflection
y	displacement
y_c	Matlock's reference displacement
y_{ref}	reference displacement
z	depth below ground surface
z_{eqv}	equivalent depth below ground surface
z_i	incremental distance in z-direction

Greek Symbols

Δ	displacement
α	a function of void ratio (approximately $\varphi/2$)
α	coefficient for Rayleigh damping
α	pile/soil interface roughness
β	coefficient for Rayleigh damping
β	angle dependent on the foundation embedment depth in Meyerhof's bearing capacity theory
β_r	function of the soil friction angle (Reese notation)
γ	shear strain
γ	unit weight of soil
γ_{avg}	average shear strain
γ_p	beam shear strain

γ_r	reference shear strain
γ_s	soil shear strain
γ_s	specific density
$\gamma_{0.7}$	threshold shear strain for shear modulus degradation curve
γ'	effective unit weight of soil
δ	parameter/function when expressing p-y stiffness as a function of soil stiffness
ε	axial strain
ε_{50}	strain at 50 % of ultimate capacity from UU-triaxial tests
θ	angle dependent on embedment depth of Meyerhof foundation
θ	rotation angle
θ_r	reference angle of rotation
κ	curvature
κ_T	Timoshenko shear coefficient
λ	rate of increase with depth for undrained shear strength
μ	Poisson's ratio
μ_p	Poisson's ratio, pile
$\mu'_{s,ur}$	soil Poisson's ratio for unloading reloading
ξ	function defined by Murff and Hamilton (1993)
ξ	damping
ρ	density
σ	stress
σ_x	stress in x-direction
σ_z	stress in z-direction
σ_r	stress in radial direction
$\sigma_{r,i}$	stress in radial direction over a length increment of the pile
σ_z	stress in z-direction
σ'	effective stress
σ'_m	mean effective stress
σ'_{peak}	peak stress
σ'_r	limiting horizontal stress
σ'_v	effective vertical stress
σ'_1	largest effective, principle stress
σ'_3	smallest effective, principle stress
τ	shear stress
τ_c	critical shear stress
τ_h	shear stress on a horizontal plane
τ_{max}	maximum shear stress (alternatively τ_c)
τ_v	vertical component of shear stress
τ_{rz}	shear stress on a plane normal to the radial direction (along the pile length axis)
$\tau_{r\psi}$	shear stress on a plane normal to the radial direction and normal to the pile length axis
$\tau_{r\psi,i}$	shear stress on a plane normal to the radial direction and normal to the pile length axis, acting over a length increment i along the pile axis
φ	soil friction angle
ϕ	angle of phase lag

ψ	soil dilation angle
ψ	angle to load direction
ω	angular frequency
ω_d	damped angular eigenfrequency
ω_n	undamped angular eigenfrequency

Abbreviations

1D	one-dimensional
1DOF	one degree of freedom
2D	two-dimensional
3D	three-dimensional
API	American Petroleum Institute
CPT	cone penetration test
CPTU	cone penetration test with pore pressure measurements
DAQ	data acquisition system
DNV	Det Norske Veritas
EWEA	European Wind Energy Association
FE	finite elements
FEM	finite element method
FLS	fatigue limit state
HSS	Hardening Soil Small model
NTNU	Norwegian University of Science and Technology
OCR	over consolidation ratio
POP	previous overburden pressures
SASW	spectral analysis of surface waves
SLS	serviceability limit state
ULS	ultimate limit state
WAK	wave activated stiffness test

1 Introduction

1.1 Motivation

Offshore wind turbines provide an increasing portion of the worldwide energy generation capacity, with numerous wind farm developments expected in the future. The offshore wind turbines combine an environmental friendly energy source with security of energy supply and a solution to avoiding the public's reluctance to have wind farms onshore.

The preferred foundation option for these tall structures are large diameter monopiles, due to their ease of construction in shallow to medium water depths. Being situated offshore in a rough physical environment, one of the greatest concerns with the design of monopiles is their long-term behavior under very large numbers of cycles of lateral and moment loads. Structural design of the wind turbine support structures needs to accommodate and verify the long-term performance. At present, the structural design involves a large number of load-cases to be checked, and simulations of high computational cost. For the structural design, simplified soil representation is preferred in order to limit the computational effort.

At present, the simplified soil representation for monopile design is incorporated by means of nonlinear springs, defined through semi-empirical expressions that correlate the spring stiffness with soil parameters. Measurements of full-scale, operating offshore wind turbines show a mismatch between the designed and the measured horizontal stiffness for the monopile foundation option. This mismatch is attributed to the semi-empirical expressions for soil springs given by the leading design guidelines.

1.2 Scope and Objectives

The overall aim when it comes to design of laterally loaded piles is a reliable, widely accepted and computationally efficient design approach. The design approach should incorporate and reflect the soil response and the mechanisms that act during loading. The scope of this study is however limited to static soil response for piles modeled as a beam on a Winkler foundation, in the context of monopiles used as foundations for offshore wind turbines. To fulfill this scope, the following objectives are set out:

- Examine the hypothesis of an unknown scaling effect related to lateral stiffness of large diameter piles
- Contribute to the knowledge and understanding of soil response to lateral pile movement
- Examine the hypothesis of significant contributions from small strain soil stiffness to the lateral foundation stiffness
- Examine the validity of the p-y approach for piles with low slenderness ratio.

1.3 Thesis Outline

This thesis comprises a literature review, analytical, numerical and experimental work. To address the key research questions defined by the objectives above, the thesis is organized as follows:

- Chapter 2 – *Background and motivation*
  The background for the performed PhD study is presented.
- Chapter 3 – *Theoretical Basis for p-y Curves*
  This chapter compares analytical and empirical solutions for the initial stiffness and the ultimate resistance of p-y curves found from literature.
- Chapter 4 – *Vertical Shear Contributions to Rotational Resistance for Short and Non-Slender Piles*
  This chapter compares analytical and empirical solutions for the initial stiffness and the ultimate resistance of rotational springs found from literature. The development of an analytical solution for ultimate resistance of rotational springs is also presented.
- Chapter 5 – *Numerical Investigation of Soil Reaction Springs*
  A procedure for extracting soil springs from 3D-FEM is presented. This procedure is applied in a parametric study, and the results are compared with the solutions from literature, presented in Chapter 3 and Chapter 4.
- Chapter 6 – *New Framework for Soil Reaction Springs*
  This chapter presents formulations for lateral and rotational springs, based on the numerical work in Chapter 5 and solutions from the literature presented in Chapter 3 and Chapter 4.
- Chapter 7 – *Impact Vibration Test of Monopile Foundation Model in Dry Sand*
  Set up, testing and results from a 1:20 scale model of an offshore wind turbine foundation is presented.
- Chapter 8 – *Back Analysis of the Impact Vibration Test*
  The impact vibration test from Chapter 7 is back analyzed with 3D- and 1D-FEM. Different approaches to soil stiffness are compared. The soil springs from Chapter 6 are used as soil representation in the 1D-FEM.
- Chapter 9 – *Summary, Conclusions and Recommendations*
  Summarizes and presents the main findings of this study.

1.4 Notes on Contributions to the Publication Included as a Part of this Thesis

One publication is included in this thesis (Chapter 7):

Hanssen, S.B., Eiksund, G., & Nordal, S., (2015) Impact Vibration Test of Monopile Foundation Model in Dry Sand, in *International Journal of Physical Modelling in Geotechnics*, DOI: 10.1680/ijpmg.15.00010

The idea for the test was provided by S. Nordal. Planning, test setup, instrumentation and testing was performed by S.B. Hanssen, with valuable assistance from P. Østensen, G. Winther, E. Husby, J. Jønland, F. Stæhli, T. Westrum, A.L. Yifru and J. Hetland. S.B. Hanssen analyzed the results and wrote the paper. G. Eiksund, S. Nordal, T.E. Helle and two unknown peer reviewers are acknowledged for valuable feedback in reviewing the manuscript.

2 Background and Motivation

2.1 Offshore Wind Turbines

The world energy demand appears to be constantly increasing, and one of the means to meet this demand is electric power from offshore wind turbines. The total capacity from offshore wind turbines in Europe alone is targeted to increase from 8 GW (end of 2014) to 150 GW by 2030 (EWEA, 2009, EWEA, 2015). To reach these targets, both the number of offshore wind turbines and the size of each wind turbine are expected to increase in the near future. At present (2015), 2 MW and 3.6 MW are typical turbine capacities for offshore wind turbines. The average size of the installed turbines are however increasing every year, and prototypes as large as 8 MW exist (Vestas, 2014). Several foundation options are available for wind turbines offshore; however, this thesis is concerned with the monopile option and other foundation options are outside the scope of this thesis.

Considering the history of offshore structures, offshore wind turbines are relatively new structures. The combination of foundation dimensions, design requirements and load combinations encountered by offshore wind turbines are challenging the existing experience gained from the offshore oil and gas-industry. In short, this is due to:

a) Pile dimensions outside previous experience. Piles for offshore structures like jacket platforms are typically 40-100 m long and 1.2–2.8 m in diameter. Multiple piles are often used per structure, causing interaction effects. By contrast, monopiles for offshore wind structures are single piles, typically 20-40 m long and 4-7 m in diameter.
b) A system eigenfrequency often close to the excitation frequencies from both environmental- and rotor loads. This requires high accuracy in prediction of the dynamic response. Knowledge of the soil response to loading is important to be able to predict the overall system stiffness. Where geotechnical design of offshore oil and gas structures is mainly concerned with cyclic and static ultimate capacity, the dynamic foundation stiffness during fatigue and serviceability limit state is as equally important for offshore wind turbines.
c) Strict deformation criteria. Accumulated rotation at mud-line is typically restricted to 0.5° rotation over the lifetime of the foundation (20-50 years).

2.1.1 Structural dimensions

Figure 2-1 shows typical dimensions for a 3.6 MW wind turbine, e.g. as installed on the wind farm at Sheringham Shoal (Scira, 2015). The rotor diameter is typically close to 100 m, and the turbine tower height close to 80 m. Water depths are typically in the range of 5-30 m, and the monopile embedment depth is typically of 20-40 m. Pile diameters for existing installations are typically within the range of 4-6 m. So far, the

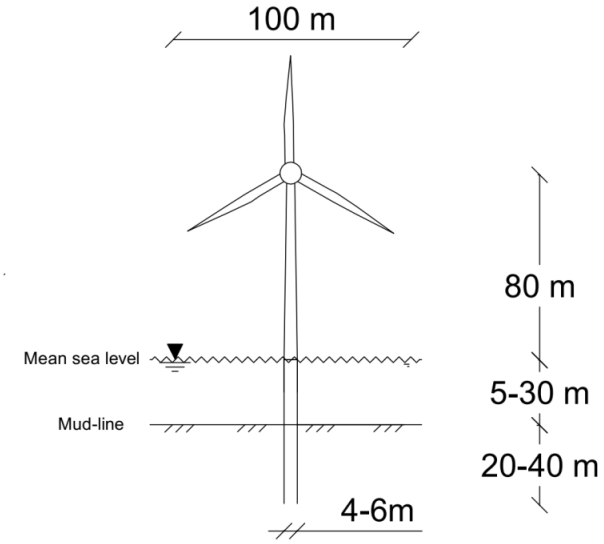

Figure 2-1. Typical loads and dimensions for a 3.6 MW offshore wind turbine. After Doherty and Gavin (2012), Scira (2015) and Lombardi et al. (2013)

trend has been increasing pile diameters with increasing turbine sizes, and piles of diameter up to 8 m have been installed. The monopile wall thickness is often varied along the pile length, but can roughly be taken as 1 % of the pile diameter.

2.1.2 Load Conditions

The main principles for loads exciting monopile supported offshore wind turbines are applicable independently of turbine location and geometry. The vertical load is due to self-weight of the structure, while the main contributions to the horizontal excitations are, according to Lombardi et al. (2013):

(a) wind and waves. Wind is commonly thought of as a random process with low-frequency content. Dominant wave frequencies might be site specific, e.g. in the North Sea, the typical predominant wave frequencies are in the range of 0.04-0.2 Hz (NORSOK, 2007).

(b) rotor loading due to possible unbalanced forces. The rotational frequency of the rotor is commonly referred to as 1P and appears as a band in Figure 2-2. The 1P frequency band in Figure 2-2 corresponds to a 3.6 MW variable-speed wind turbine with operational range between 5 and 13 rpm (0.08-0.22 Hz), as presented by Lombardi et al. (2013).

(c) Reduced drag force on the tower when the rotor blades are passing. The blade passing frequency is a multiple of the rotor frequency, and commonly referred to as 3P or 2P for a three bladed or two-bladed turbine, respectively.

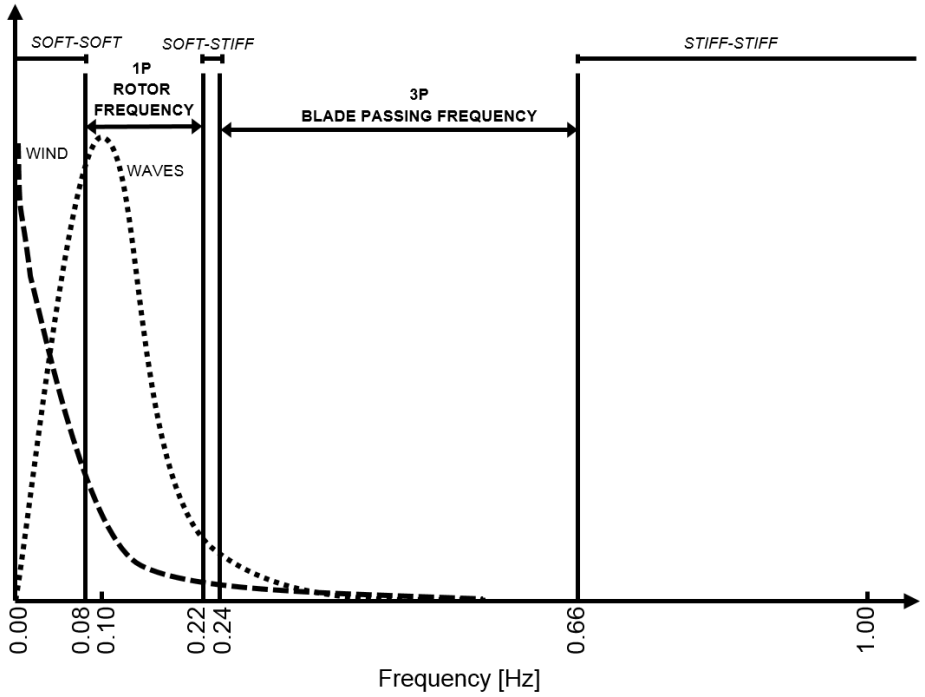

Figure 2-2. Simplified power spectral density plot of the forcing frequencies applied to a typical three-bladed 3.6 MW offshore wind turbine. After Lombardi et al. (2013)

Figure 2-2 shows the above listed horizontal excitation sources in a power spectral density plot. In order to reduce dynamic amplification of the excitation forces, the system eigenfrequency must be targeted outside the frequency content of the excitation sources. In Figure 2-2, this leaves three frequency-bands as an option for the eigenfrequency to be targeted. These three frequency-bands are denoted: *Soft-Soft*, *Soft-Stiff* and *Stiff-Stiff*. The name of these three frequency bands refers to the rotor frequency (1P) and the blade passing frequency (3P). The *Soft-Soft* frequency band is the frequency content below both the 1P and the 3P frequency. The *Soft-Stiff* frequency band is limited upwards by the 3P-frequnecy and downwards by the 1P frequency. Finally, the Stiff-Stiff frequency band contains all frequencies higher than both the 1P and the 3P frequencies. The most common design-approach for offshore wind turbines on monopile foundations already installed is reported to be the Soft-Stiff design approach (eigenfrequency targeted inside the Soft-Stiff frequency band) (Kühn, 1997, LeBlanc, 2009, Lombardi et al., 2013).

2.2 Soil and its Deformation Properties

Soil stiffness is known to be nonlinear, and the deformation behavior is known to depend on several different factors. This section does not aim to give a complete

overview of soil deformation behavior, but rather a short summary of properties believed to be relevant in the context of laterally loaded piles. For complementary readings, reference is made to textbooks such as Janbu (1970); Bowles (1968); Das and Sobhan (2013) and others. The main factors influencing the nonlinear load-deformation characteristic of soil are:

- soil grain size distribution and mineral composition
- confining stress level
- geological history
- presence of water/pore pressures
- soil strain level
- stress anisotropy
- loading rate
- load history

Knowledge of all the above points is important when considering soil deformation behavior. For laterally loaded piles, special emphasis is given to the strain level of the soil surrounding the pile. Soil stiffness is strain-dependent, and the stiffness is decreasing with increasing strain. Figure 2-3 shows the soil shear modulus G_s in a semi-logarithmic plot versus the shear strain γ. In the semi-logarithmic plot drawn after Atkinson and Sallfors (1991), Mair (1993) and Benz (2007), the stiffness reduction curve exhibits a characteristic S-shape.

With reference to the terms very small strains, small strains and larger strains defined in Figure 2-3, the soil surrounding laterally loaded piles will typically experience larger strains close to the soil surface and small- to very small strains at greater depths. The

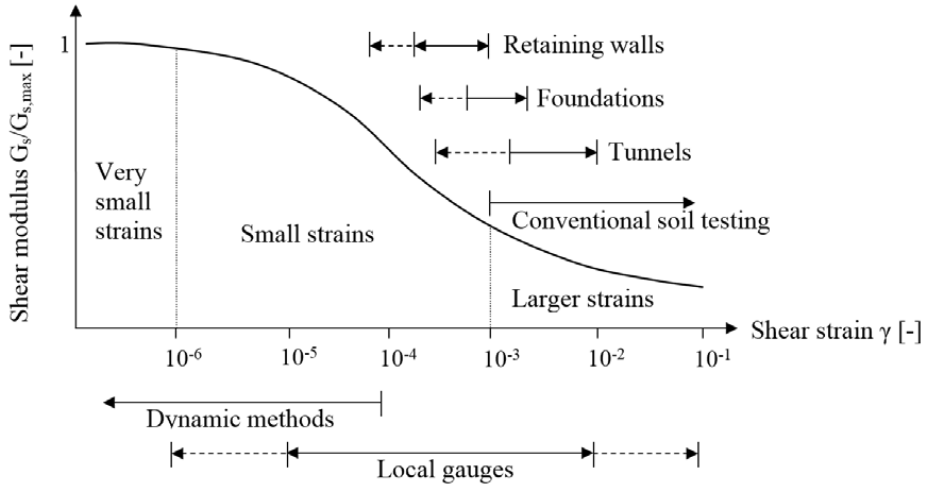

Figure 2-3. Stiffness degradation with increasing shear strain. After Atkinson and Sallfors (1991), Mair (1993) and Benz (2007).

soil strain will also decrease with radial distance from the pile, leaving only the soil close to the pile and close to the soil surface with larger strains. For monopiles supporting offshore wind turbines, the soil response at low- to moderate load levels is just as important as the soil response to larger loads (ref. Paragraph 2.1.2), making it important to be able to describe the soil response over a wide range of soil strain levels. To be able to describe the soil response, knowledge of the soil deformation behavior over the same, wide range of soil strain levels is required.

2.3 The Winkler Foundation Approach

The beam on a Winkler foundation is a simplification of the three dimensional problem of a beam with external resistance against deflection from the surrounding soil. The concept of the Winkler foundation was first formulated by Winkler (1867) and is illustrated in Figure 2-4a). The basic assumption is that a beam resting on an elastic foundation experiences a distributed resistance from the foundation, where the local foundation resistance is proportional to the local foundation displacement. In structural terms, this proportionality is represented by springs. The assumption of proportionality to the local displacement implies that the springs are uncoupled. In other words: the deformation in one spring is independent of any deformation in the neighboring springs. When the Winkler foundation is applied to laterally loaded piles, the pile is idealized as a 1-dimensional beam and the elastic foundation is the soil surrounding the pile. This is shown in Figure 2-4b).

Differential equations relevant for the case of laterally loaded piles were stated by Timoshenko (1940), and also by other writers (Reese and Van Impe, 2001). Hetenyi (1946) presented solutions to the fourth-order differential equation governing the beam

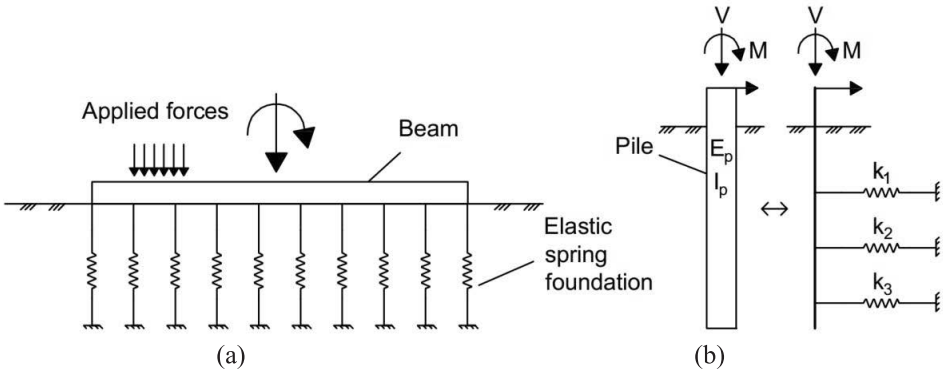

Figure 2-4. (a) Beam on elastic foundation, (b) Pile idealized as a beam on Winkler foundation

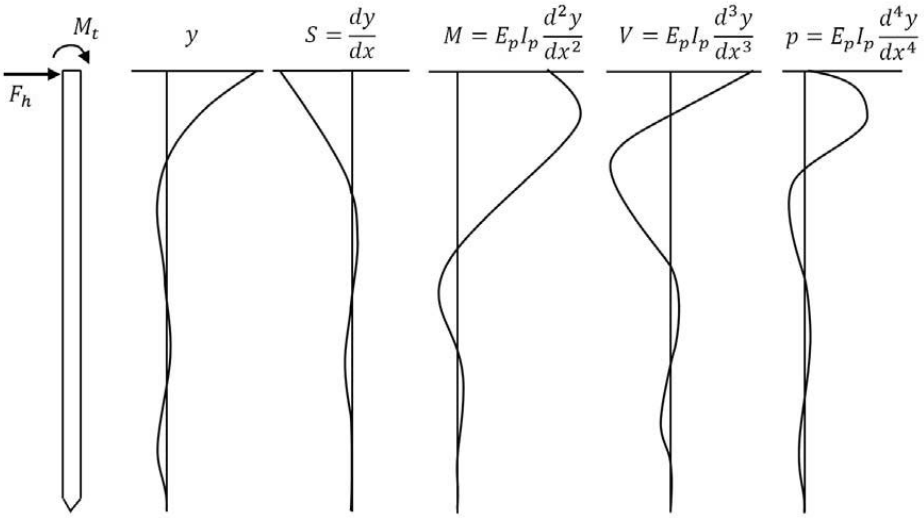

Figure 2-5. Derivatives of the 4th order beam equation. After Reese and Van Impe (2001).

resting on a foundation with linear response. Nonlinear foundation response was included by Palmer and Thompson (1948), who presented a numerical solution to the differential equation. The numerical solution made it possible to solve the differential equation with nonlinear soil by iterative procedures (finite difference methods) on a computer.

Figure 2-5 describes the relationship between the deformation (y), rotation (S), bending moment (M), shear force (V) and load (p) that follows from the 4th order beam equation. The term E_pI_p denotes the bending stiffness of the pile. Deduction of the beam equation is presented in Appendix A.

Due to its inability to take the continuity of the soil into account, the Winkler foundation is often considered a crude approximation to the true mechanical behavior of the soil material. The assumption that there is no interaction between adjacent springs results in overlooking internal shear effects in the soil volume. Internal shear effects in the soil might be different for different beam cross sections and different deformation modes of the beam. The benefit of the Winkler foundation is however its computational efficiency. Structural design of offshore wind turbines require checking a large number of load cases (Muskulus and Schafhirt (2014) estimated a few thousand). An efficient calculation method is therefore strongly preferred.

2.4 Empirical Determination of Soil Spring Stiffness

The main challenge with the Winkler foundation is to determine a spring stiffness that corresponds to the soil-structure interaction in question. Soil itself is known to have

nonlinear deformation characteristics, and as stated in Section 2.2, the soil stiffness is dependent on several site specific factors. In addition to the soil stiffness, the soil-pile interaction stiffness also depends on size, shape and the deformation mode of the contact area between the pile and soil.

The first approach to handle all the nonlinear characteristics of the pile-soil interaction stiffness was made by McClelland and Focht (1956). They reported a full-scale lateral pile load test where the soil reaction curves (spring stiffness) were back calculated from measurements of pile bending moment, pile head load and pile head deflection. The soil reaction curves computed by McClelland and Focht were found to be reminiscent of the stress-strain curves (q-ε) seen from laboratory triaxial tests. A linear relationship between the laboratory stress-strain curves and the local load-displacement curves for the pile was therefore assumed.

The method used by McClelland and Focht is based on the relationship between the beam deflection and the corresponding distributed load, as it is described by the Euler-Bernoulli beam equation. By knowing one of the quantities deformation (y), rotation (S), bending moment (M), shear force (V) or load (p) described in Figure 2-5, the remaining quantities can be found by derivation and/or integration. If a pile is instrumented with strain gauges, pile bending moments can be derived from the strain gauge measurements. The pile deflection (y) and the soil reaction (p) are then obtained by double integration and double differentiation of the bending moment profile. For the double integration from bending moments to displacements, a proper set of boundary conditions is required. This can be determined from measurements of rotations and displacements at the pile head.

The pioneering approach for determining soil resistance against lateral load reported by McClelland and Focht (1956) has later been repeated by a large number of researchers, and today, 60 years later, research papers employing the same test setup are still being published. Two of the publications that have gained most attention over the years are Matlock (1970) who presented correlations for design of laterally loaded piles in clay, and Reese et al. (1974) who presented correlations for design of laterally loaded piles in sand. The soil reaction curves presented in the two above-mentioned publications were adopted by design guidelines from the American Petroleum Institute (API, 2011) and Det Norske Veritas (DNV, 1992). The Winkler beam approach with soil reaction curves as described by Matlock (1970) and Reese et al. (1974) has been the industry standard for the design of laterally loaded piles for several decades, and has a long and proven track-record for both onshore and offshore piles.

2.5 Soil Spring Stiffness for Large Diameter Monopiles

The soil spring relations described by Matlock (1970) and Reese et al. (1974) were originally developed for the design of piles supporting jacket structures in the Gulf of Mexico. The stiffness of the nonlinear soil springs was calibrated from full-scale field tests, while the ultimate resistance of the springs was developed from analytical solutions. The main focus for performance of piles supporting jacket structures is on the pile bending moment capacity, with less focus on accurate prediction of the pile lateral displacement. In the case of large diameter monopiles supporting offshore wind turbines, the need for accurate stiffness and deformation predictions is as equally important (ref. Paragraph 2.1.2).

With respect to deformation shapes, a large diameter monopile will often experience a more rigid behavior under lateral loading compared to typical jacket piles. This difference is directly related to the difference in slenderness between the two. A long and slender pile like those typically used to support jacket structures will deform in a shape reminiscent of a damped wave when loaded laterally at the pile head. A comparatively short, large diameter pile will typically deform more like a cantilever beam, or rotate like a rigid structure. The two different deformation modes are shown in Figure 2-6, with the deformation of a slender pile in (a) and the deformation of an almost rigid pile in (b).

Measurements of eigenfrequency and the bending moment response on operating, full-scale offshore wind turbines have shown that the soil spring stiffness described by API and DNV design guidelines underpredicts the real soil stiffness. Kallehave et al. (2012) carried out measurements on three wind turbines at the Walney offshore wind farm, and found that the eigenfrequency was 5-7 % higher than predicted in design when soil

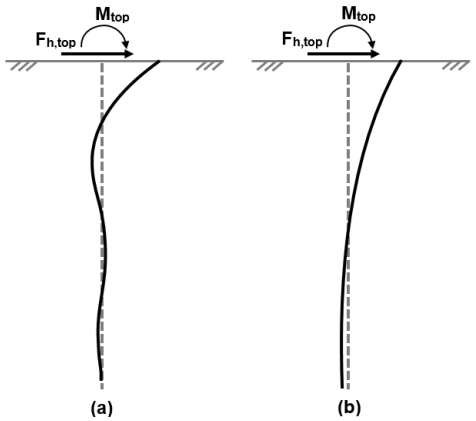

Figure 2-6. (a) Typical deformation shape for slender pile (b) Typical deformation shape for large diameter monopiles

springs from API/DNV were used. Hald et al. (2009) measured pile bending moments for a monopile supporting a wind turbine at Horns Rev offshore wind farm. The measured bending moments were found to be 30-50 % smaller than the predictions using soil springs from API/DNV.

Deflections and bending moments are known not to be very sensitive to changes in the soil stiffness (Matlock and Reese, 1960). The results from Hald et al. (2009) and Kallehave et al. (2012) find a significant deviation between predicted and observed response for both bending moments and deflections. These deviations indicate thereby that the soil stiffness provided by the design guidelines diverge significantly from the actual soil response to large diameter monopiles supporting offshore wind turbines. This deviation is in contrast to the long and proven track record the same soil springs have obtained for piles supporting jacket structures.

An apparently good performance for jacket piles, compared to an apparently poor performance for large diameter monopiles is obviously conflicting. Kallehave et al. (2012) suggested that there is an unknown scaling effect in the soil springs when the diameter is increased, while Byrne et al. (2015) suggested that the empirical calibration of the API/DNV springs is not valid for the geometry of more rigid behaving, large diameter monopiles.

To further complicate the picture, a number of authors have claimed that the soil springs defined in the design guidelines actually give a too stiff lateral response for the larger diameter monopile foundations, especially at greater depths when compared to 3D-Finite Element Modeling (3D-FEM) (Wiemann et al., 2004, Lesny and Wiemann, 2006, Achmus and Abdel-Rahman, 2012, Sørensen et al., 2010, Augustesen et al., 2010, Roesen et al., 2010).

2.6 Chapter Summary

Design of monopile foundations for offshore wind turbines requires high accuracy in the prediction of the soil-pile interaction stiffness. A Winkler foundation approach is often preferred in design of monpile foundations, mainly due to its computational efficiency. The pile is then represented by a beam, and the soil by uncoupled, nonlinear springs. When a Winkler foundation approach is used, the main challenge is to assign a spring stiffness that captures the soil response with sufficient accuracy.

Offshore wind turbines are relatively new structures, and the required pile dimensions to support these structures are partly outside previous experience. Measurements on operating offshore wind turbines suggests that the soil spring-stiffness is under-predicted in today's design guidelines, and there exists several different theories for this apparent under-prediction.

Chapter References

Achmus, M & Abdel-Rahman, K (2012) Design of Piles for Offshore Wind Energy Foundations with Respect to Horizontal Loading. In *International Offshore and Polar Engineering Conference*. pp. 143-150.

Api, API (2011) API-RP-2GEO: Geotechnical and Foundation Design Considerations. Washington, USA, API Publishing Services.

Atkinson, JH & Sallfors, G (1991) Experimental determination of stress-strain-time characteristic in laboratory and in situ tests. In *X ECSMFE*. A.A. Balkema, Firenze, vol. III, pp. 915-956.

Augustesen, A, Sørensen, SPH, Ibsen, LB, Møller, M & Brødbæk, KT (2010) Comparison of calculation approaches for monopiles for offshore wind turbines. In *Numerical Methods in Geotechnical Engineering*. CRC Press, pp. 901-906.

Benz, T (2007) Small-Strain Stiffness of Soils and its Numerical Consequences. In *Fakultät für Bau– und Umweltingenieurwissenschaften*. Universität Stuttgart, Stuttgart, vol. PhD, 150 p.

Bowles, JE (1968) *Foundation Analysis and Design.* McGraw Hill.

Byrne, BW, Mcadam, R, Burd, HJ, Houlsby, GT, Martin, CM, Zdravkovic, L, Taborda, DMG, Potts, DM, Jardine, RJ, Sideri, M, Schroeder, FC, Gavin, K, Doherty, J, Igoe, D, Muir-Wood, A, Kallehave, D & Gretlund, JS (2015) New design methods for large diameter piles under lateral loading for offshore wind applications. In *Frontiers in Offshore Geotechnics III*. CRC Press, pp. 705-710.

Das, B & Sobhan, K (2013) *Principles of Geotechnical Engineering 8th ed.*, Cengage Learning.

Dnv (1992) DNV-CN-30.4: Classification Note No. 30.4, Det Norske Veritas.

Doherty, P & Gavin, K (2012) Laterally loaded monopile design for offshore wind farms. In *Proceedings of the ICE - Energy*. vol. 165, pp. 7-17.

Ewea (2009) *Pure Power - Wind energy targets for 2020 and 2030*. Brussels, Belgium.

Ewea (2015) *The European offshore wind industry - key trends and statistics 2014*. Association, E. W. E., Brussels, Belgium.

Hald, T, Mørch, C, Jensen, L, Bakmar, CL & Ahle, K (2009) Revisiting monopile design using p-y curves –Results from full scale measurements on Horns Rev. In *European Offshore Wind Conference & Exhibition 2009*. Curran Associates, Inc, Stockholm, Sweden, vol. 3, pp. 1926-1935.

Hetenyi, M (1946) *Beams on Elastic Foundation.* MI, University of Michigan Press, Ann Arbor.

Janbu, N (1970) *Grunnlag i geoteknikk.* Trondheim, Norway, Tapir.

Kallehave, D, Leblanc, C & Liingaard, MA (2012) Modification of the API P-y Formulation of Initial Stiffness of Sand In *Proceedings of Offshore Site Investigation and Geotechnics: Integrated Technologies - Present and Future*. Society for Underwater Technology, pp. 465-472.

Kühn, M (1997) Soft or stiff - A fundamental question for designers of offshore wind energy converters. In *European Wind Energy Conference (EWEC'97)*. Slane County Meath, Dublin, Ireland.

Leblanc, C (2009) Design of offshore wind turbine support structures. In *Department of Civil Engineering*. Aalborg University, Denmark, Aalborg, Denmark, vol. PhD, 210 p.

Lesny, K & Wiemann, J (2006) Finite-Element-Modelling of Large Diameter Monopiles for Offshore Wind Energy Converters. In *GeoCongress 2006*. pp. 1-6.

Lombardi, D, Bhattacharya, S & Muir Wood, D (2013) Dynamic soil–structure interaction of monopile supported wind turbines in cohesive soil. *Soil Dynamics and Earthquake Engineering* **49(0)**:165-180.

Mair, RJ (1993) Unwin Memorial Lecture 1992- Developments in Geotechnical Engineering Research: Application to Tunnels and Deep Excavations. Delivered at the ICE on 17 March 1992. In *Proceedings of the ICE - Civil Engineering*. vol. 97, pp. 27-41.

Matlock, H (1970) Correlation for Design of Laterally Loaded Piles in Soft Clay. In *Offshore Technology Conference*. Houston Texas, pp. 577-607.

Matlock, H & Reese, LC (1960) Generalized Solutions for Laterally Loaded Piles. *ASCE Journal of the Soil Mechanics and Foundations Division* **86(5)**:63-91.

Mcclelland, B & Focht, JA (1956) Soil Modulus for Laterally Loaded Piles. *ASCE Journal of the Soil Mechanics and Foundations Division* **82(4)**:22.

Muskulus, M & Schafhirt, S (2014) Design optimization of wind turbine support structures-a review. *Journal of Ocean and Wind Energy* **1(1)**:12-22.

Norsok (2007)N -003 Actions and action effects. Lysaker, Norway.

Palmer, LA & Thompson, JB (1948) The Earth Pressure and Deflection Along the Embedded Lengths of Piles Subjected to Lateral Thrust In *Proceedings of 2nd International Conference on Soil Mechanics and Foundation Engineering* vol. V, pp. 156-161.

Reese, L, Cox, W & Koop, F (1974) Analysis of Laterally Loaded Piles in Sand. In *Offshore Technology Conference*. Houston, pp. 473–483.

Reese, LC & Van Impe, WF (2001) *Single piles and pile groups under lateral loading.* Rotterdam, A.A. Balkema.

Roesen, HR, Thomassen, K, Sørensen, SPH & Ibsen, LB (2010) *Evaluation of Small-Scale Laterally Loaded Non-Slender Monopiles in Sand*. University, A., Aalborg, Report 91, 24 p.

Scira (2015) *Sheringham Shoal - Facts and Figures*, See http://scira.co.uk/about/content.php?ln=Facts%20and%20figures2015).

Sørensen, SPH, Ibsen, L & Augustesen, A (2010) Effects of diameter on initial stiffness of p-y curves for large-diameter piles in sand. In *Numerical Methods in Geotechnical Engineering*. CRC Press, pp. 907-912.

Timoshenko, SP (1940) *Strength of materials, part II, advanced theory and prooblems.* New York, Van Nostrand.

Vestas (2014) *Vestas Annual report 2013*.

Wiemann, J, Lesny, K & Richwien, W (2004) Evaluation of Pile Diameter Effects on Soil-Pile Stiffness In *Proceedings of DEWEK 2004: 7. Deutsche Windenergie-Konferenz,* .

Winkler, E (1867) *Die Lehre von der Elastizitaet und Festigkeit.* Prag, Verlag von H. Dominicus.

3 Theoretical Basis for p-y Curves

Soil springs for laterally loaded piles are often referred to as p-y curves. “p” denotes the lateral resistance from the soil along the pile length, while “y” denotes the lateral pile displacement along the pile length. In the beam on Winkler foundation approach, the soil resistance is idealized as springs. This chapter describes the different components of soil resistance relevant for open ended circular piles.

3.1 Soil Reaction Forces to Laterally Loaded Rigid Piles

The load application point for offshore wind turbines is typically 30-100 m above seabed level. This load can be represented by a horizontal- and moment load at the seabed. A pile sufficiently stiff in bending compared to the stiffness of the surrounding soil, will respond to this load by a rotational movement. The point of rotation will be below the seabed. The soil provides resistance against the rotation, this resistance acts in the opposite direction of the pile movement, as described in Figure 3-1.

A rotational movement of the pile mobilizes soil resistance both normal and parallel to the pile axial direction. Let us assume small rotations, so that the axial and radial

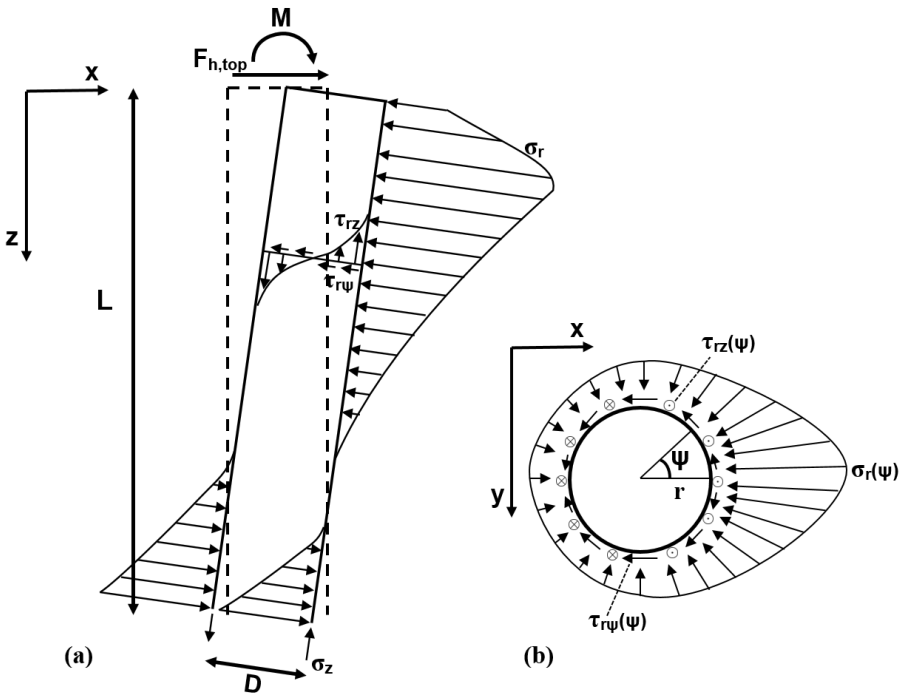

Figure 3-1. Components of soil reaction to pile movement. (a) Plane section (b) Cross section

directions of the pile coincide with the vertical and horizontal directions. The resistance in the vertical direction (τ_{rz}) in Figure 3-1 is then from vertical shear tractions at the circumference of the pile. Soil resistance in the horizontal direction is caused by stresses acting normal to the pile (σ_r) and the horizontal shear tractions acting at the pile circumference ($\tau_{r\psi}$). At the bottom of the open ended pile, stresses are acting opposite to the direction of movement, both inside and outside the pile. The vertical soil reactions at the pile tip (σ_z) to the rotational movement acts on the pile annular area. The pile annulus area is small compared to the side area, and the resulting rotational resistance is small and therefore neglected.

3.2 Horizontal and Moment Equilibrium of a Rigid Pile

The forces acting in the horizontal direction are the horizontal loads at the pile head, and the horizontal components of soil reaction. Figure 3-2 presents the forces acting on an element of the pile. The horizontal reaction σ_r and the horizontal shear traction ($\tau_{r\psi}$) are integrated over the pile circumference and represented by the incremental horizontal reaction p_i (units of kN/m). At static equilibrium, the sum of all horizontal reactions from the soil is equal to the applied horizontal load $F_{h,top}$.

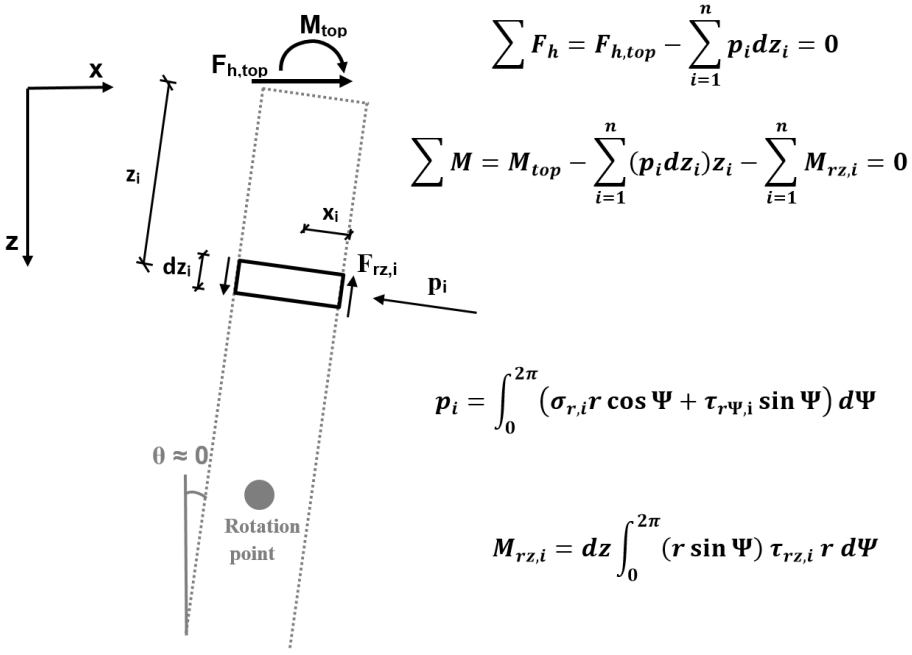

Figure 3-2. Horizontal and moment equilibrium of a rotating pile. Moment equilibrium around pile top. Symbol definitions also given in Figure 3-1.

The rotational point of the pile in Figure 3-2 is assumed to be at the centerline of the pile and closer to the pile toe than to the pile head (Foglia et al., 2012). We keep our assumption of small rotations made previously, so that the axial- and radial directions of the pile coincide with the vertical and horizontal directions. The horizontal forces acting at- and close to the pile head have significant influence to the moment equilibrium of the pile, due to the distance to the pile rotational point (large moment arm). As such, the horizontal soil reactions become less influential to the moment equilibrium the closer they act to the rotational point. The moment arm for the vertical forces acting at the pile surface is limited by the pile radius ($x_i \leq r$). The moment arm for vertical shear is independent of location with respect to distance in the pile axial direction. For piles with large L/D ratios, the moment contribution from vertical shear is often small compared to the contribution from horizontal soil reactions. The vertical contribution is therefore mainly of interest for piles with low L/D ratios. A quantification of the vertical shear contribution for different L/D ratios is presented in Chapter 6.

3.3 Soil Reaction Forces to a Laterally Loaded Long and Slender Pile

Based on the previous section, we assume that vertical shear can be neglected for both moment- and horizontal equilibrium of a long and slender pile. Equilibrium is then controlled by the horizontal soil reactions alone. A typical pattern of soil reaction forces for a long and slender pile subjected to horizontal- and moment loading at pile head are sketched in Figure 3-3. Pile deflections are decreasing with depth, showing a deflection shape reminiscent of a damped wave motion.

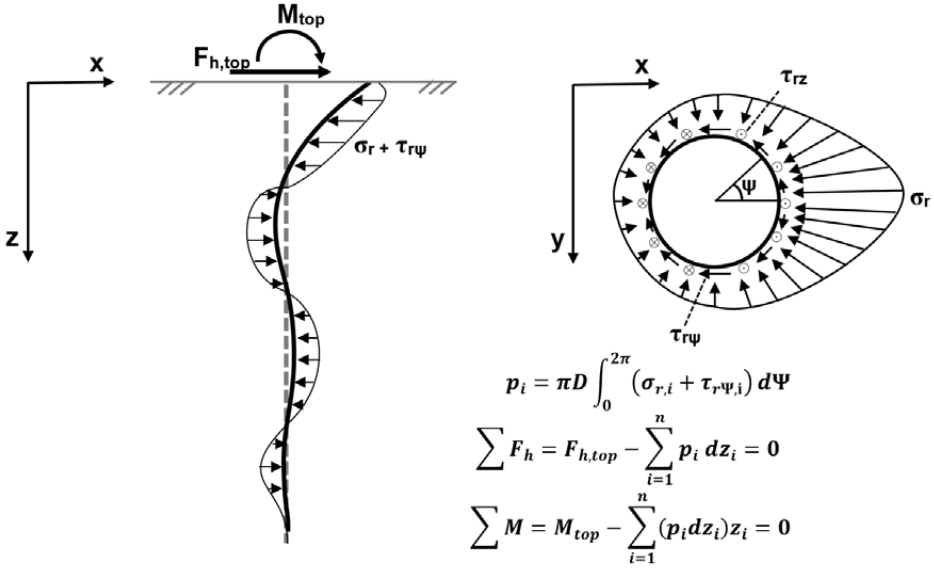

Figure 3-3. Deformation pattern and soil reactions for a long and slender pile.

3.4 Soil Nonlinearity and Simplification

A brief summary of nonlinear deformation characteristics of soil was given in Chapter 2. When soil response is described mathematically, various simplifications and idealizations are often introduced. Figure 3-4 shows the stress-strain curve from a drained triaxial test on saturated Hokksund Sand, along with a simple, linear-elastic, perfectly plastic idealization. The idealization is not capable of capturing the exact behavior of the soil; however it matches the coarse features reasonably well.

There are several ways of describing soil behavior mathematically, with different simplifications for different problems and different approaches. If the purpose was to describe the exact shape of the curve in Figure 3-4, it would be necessary to fit a more advanced mathematical expression than the bi-linear curve to model the soil behavior. This can be done rather easily with modern computers. The more advanced expressions might however complicate the engineering calculus when soil is included in engineering calculations. The goal of every simplification is to make the calculus as simple as possible, and at the same time minimize the loss of accuracy and relevant information, compared to reality.

In the following, soil is approximated as a continuum. A linear-elastic, perfectly plastic description of the soil load-deformation behavior is used to model the soil response to pile sections moved laterally. The pile section under consideration is assumed to be at a depth far below the soil surface, excluding surface effects and allowing for horizontal plane strain considerations. The linear-elastic, perfectly plastic approximation is chosen because of its mathematical simplicity, and because it provides results that are rather intuitive compared to more advanced approximations.

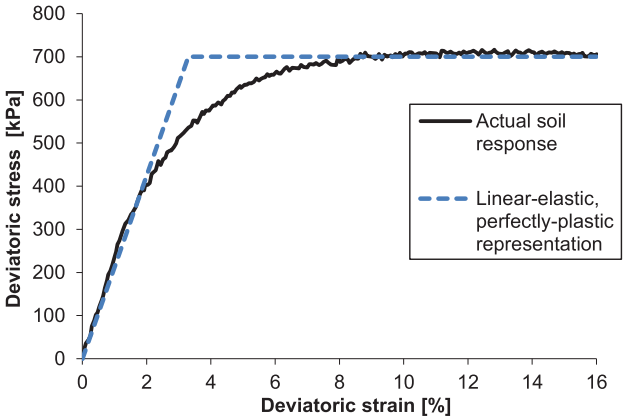

Figure 3-4. Example stress-strain curves from drained triaxial test of saturated Hokksund Sand together with simplified representation. After Tadesse (2000)

A detailed presentation of initial stiffness and ultimate lateral resistance to a pile section is given in sections 3.5 and 3.6. To illustrate some important aspects of the transition from initial stiffness to ultimate resistance, Figure 3-5 to Figure 3-9 are made with a 2D-FE code.

Figure 3-5 shows the distribution of deviatoric stresses induced by a circular, rigid disc that is moved sideways in an elastic, isotropic medium. The disc is restrained from movement out of the plane (plane strain). Figure 3-6 shows the same disc, but now in an elasto-plastic media loaded to ultimate resistance. The term ultimate resistance implies that the soil is brought to failure (perfectly plastic behavior) on the critical shear planes. At failure, the response of the entire soil volume is controlled by the soil behavior at the critical shear planes[1]. The soil outside the critical shear planes is in Figure 3-6 seen to still be in the elastic state. The difference in response for the linear-elastic state and the perfectly plastic state in terms of incremental shear strains is shown in Figure 3-7.
Studying the distribution of stresses and strains in Figure 3-5 to Figure 3-7, the following observations are made:

1) For the linear elastic material state, the distribution of deviatoric stresses and the distribution of shear strains is of similar shape (linear relation).
2) Both the distribution of deviatoric stress and shear strain change when the material goes from purely elastic state to partly elastic, partly plastic state.
3) In the elastic state, the stress distribution is not uniform over the area that turns out to be the critical shear planes at ultimate resistance. This implies that the material points at the critical shear planes reach their ultimate strength at different times. This is illustrated in Figure 3-8.

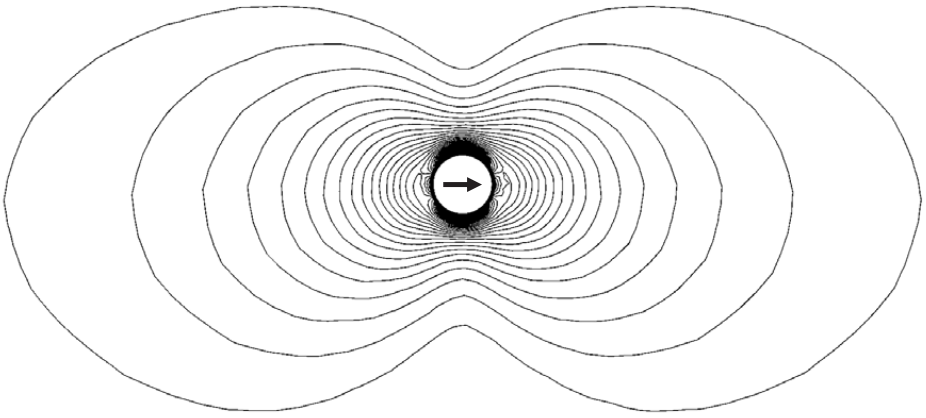

Figure 3-5. Pattern for deviatoric stress contours for linear elasticity.

[1] The location of critical shear planes depends on the failure criterion. In Figure 3-6 to Figure 3-9, a Tresca failure criterion is used for the soil.

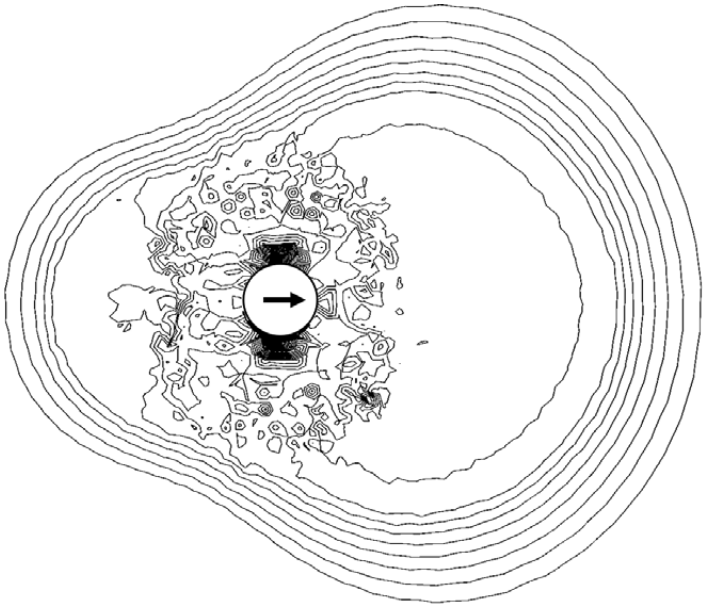

Figure 3-6. Pattern for stress contours for deviatoric stress at ultimate resistance (Tresca failure criterion and soil/pile roughness α = 1).

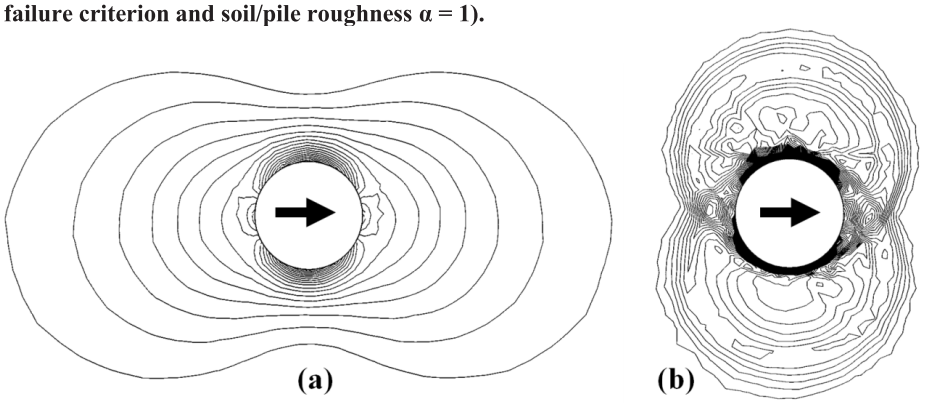

Figure 3-7. Pattern for incremental shear strains (a) linear elastic behavior (b) perfectly plastic behavior (Tresca failure criterion and soil/pile roughness α = 1)

Observation number three is important to be able to describe the shape of the resulting load-displacement curve (p-y curve) for the disc embedded in a linear-elastic, perfectly plastic medium (Figure 3-9). Instead of the sharp-angled shift from linear-elastic to perfectly plastic, seen for a single material point in Figure 3-4 and/or Figure 3-8, the overall load-displacement response of the disc has a curved transition from elastic to plastic response. This curved transition is due to the fact that the individual material points on the critical shear planes are yielding independently and at different times. As such, the load-displacement curve is not a direct multiplicative of the stress-strain curve for an individual material point, although it is reminiscent in shape.

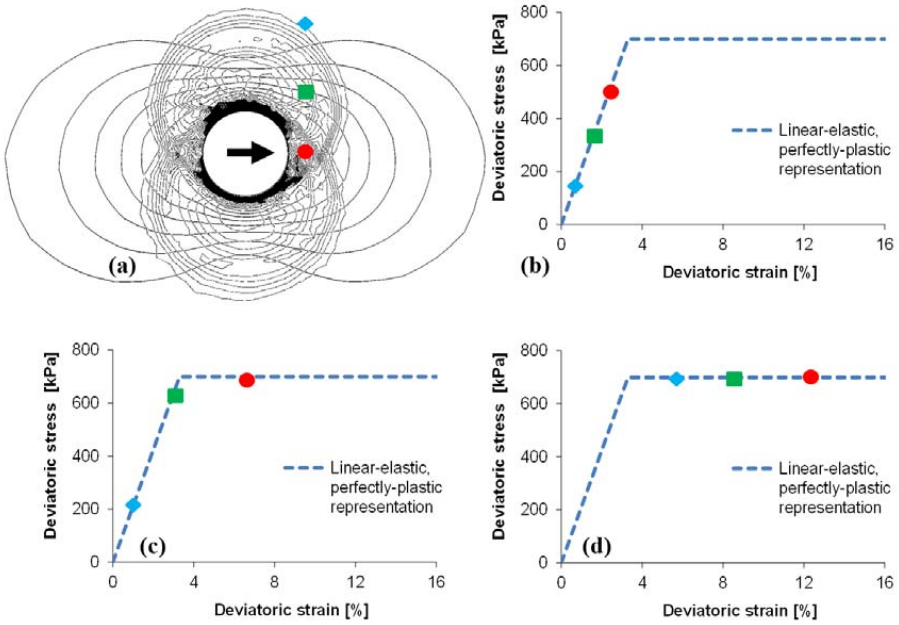

Figure 3-8. (a) Deviatoric strain field at plastic material state overlaid the deviatoric strain field at elastic material state. (b) Different material points at elastic state. (c) Different material points changing from elastic to plastic material state at different times. (d) Different material points after reaching plastic material state.

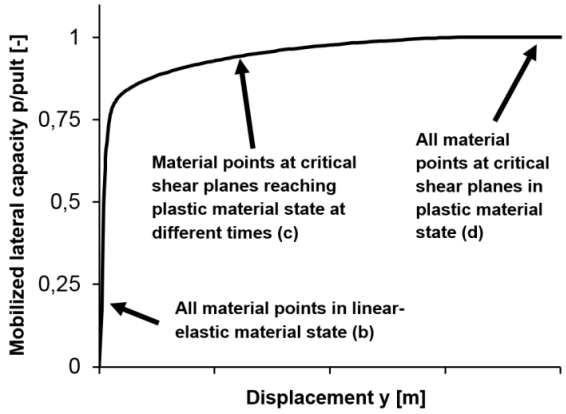

Figure 3-9. Example p-y curve for the rigid disc in linear-elastic, perfectly plastic material from Figure 3-5 to Figure 3-7. Letters b) c) and d) refer to the different states in Figure 3-8.

3.5 Initial Stiffness

Let us keep the assumption from the previous section, namely that:

1) soil can be idealized as a linear-elastic, perfectly plastic material
2) we are considering a pile section at a depth sufficiently far from the soil surface, so that plane strain conditions can be assumed.

Before any individual material point starts to yield, the linear-elastic, perfectly plastic material behaves like a linear-elastic material. As such, the initial stiffness of the load-displacement curve in Figure 3-9 can be determined by the theory of elasticity. The problem of a rigid disc moving laterally in an elastic, isotropic soil has been considered by Baguelin et al. (1977), who presented the solution in Eq.(3.1) with the corresponding Figure 3-10.

$$y = \frac{p}{8\pi E}\frac{1+\mu}{1-\mu}\left[(3-4\mu)\ \ln\left(\frac{R}{r}\right)^2 - \frac{R^2-r^2}{R^2+r^2} - \frac{(4\mu-1)}{(3-4\mu)}\frac{R^2-r^2}{R^2+r^2}\right] \qquad \textbf{(3.1)}$$

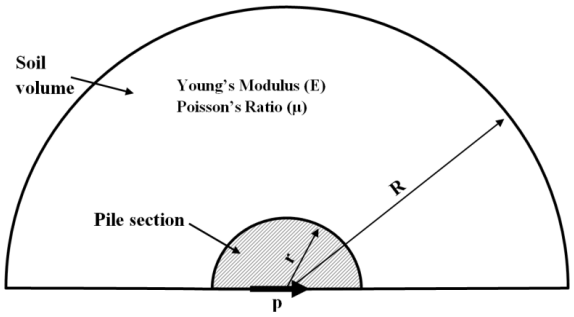

Figure 3-10. Rigid disc in elastic, homogeneous and isotropic soil. After Baguelin et al. (1977).

The displacement y in the solution from Baguelin et al. (1977) is dependent on the distance to the boundary R, and tends towards infinity as R tends towards infinity. A careful consideration of the boundary is therefore required, as will be discussed later. Other writers have used the theory of elasticity and idealized the deep pile section as a rectangular surface load on/in an elastic half-space. Settlements of a rectangular shaped loaded area on an elastic half space have a finite solution. However, if the length of the loaded area tends toward infinity (strip load), the settlement will also be infinite. The displacement of a rectangular area on/in an elastic half-space is given by Eq.(3.2) (Poulos and Davis, 1974).

$$y = q \times B \times I_\rho \times \frac{1-\mu^2}{E_s} \tag{3.2}$$

where

y = settlement
q = distributed foundation load (units of pressure)
I_ρ = influence value depending upon shape, rigidity and embedment of the foundation
μ = Poisson's ratio of the solid
B = foundation width
E_s = Young's modulus of the solid

By rearranging Eq.(3.2), Eq. (3.3a) is obtained. The product of the foundation pressure q and the foundation width B is of unit Force/Length and is representing the force per unit length (p) on the foundation. Collecting the dimensionless quantities in Eq.(3.2) into one parameter $\delta = \frac{1}{I_\rho(1-\mu^2)}$, the force-displacement relation takes the form of Eq.(3.3b).

$$\frac{qB}{y} = \frac{E_s}{I_\rho\left(1-\mu^2\right)} \tag{3.3a}$$

$$\frac{p}{y} = \delta E_s \tag{3.3b}$$

Assuming that the pile section can be idealized as a rectangular area, the initial stiffness of the curve shown in Figure 3-9 can therefore be described as a product of Young's modulus of the soil, multiplied by a factor dependent upon the Poisson's ratio of the soil and the shape and rigidity of the foundation. Expressing the initial stiffness for the p-y curve on the form of Eq.(3.3b), it is possible to compare the solutions for the surface loaded rectangle to solutions from other approximations, such as cylindrical cavity expansion, point load on beam on elastic half-space and the boundary element method.

A comparison of different values of δ found in the literature is given in Table 3-1. It should be noted that although rather different approximations are used for the various approaches, the numerical value of δ falls into the range $\delta \approx 1$ - 2 in most cases. The widest range of values is obtained for the expression from Baguelin et al. (1977) in Eq.(3.1), where the δ-value is dependent on Poisson's ratio and the distance to the boundary. δ-values based on Baguelin et al. is shown against normalized distance to boundary in Figure 3-11.

Table 3-1. Comparison of values and expressions for δ from literature

δ	Writers	Topic
$\delta = 0.74$	Terzaghi (1955)	Static loading of flexible piles
$\delta = \frac{0.65}{1-\mu^2}\sqrt[12]{\frac{E_s D^4}{E_p I_p}}$	Vesic (1961)	Point load on beam resting on elastic subgrade
$\delta = \frac{1.3}{1-\mu^2}\sqrt[12]{\frac{E_s D^4}{E_p I_p}}$	Bowles (1968)	Point load on beam inside elastic subgrade
$\delta = 0.4$	Matlock (1970)	Static loading of flexible piles in clay
$\delta = \frac{1-\mu}{1+\mu}\frac{8\pi}{[.....]}$	Baguelin et al. (1977)	Rigid disc in elastic soil. See Eq.(3.1) for full equation.
$\delta \approx 0.8 - 1.7$	Novak et al. (1978)	Rigid disc in viscoelastic soil (real part of the stiffness)
$\delta = 1.0 - 1.2$	Roesset and Angelides (1979) (Referred from Kagawa and Kraft, 1980)	Dynamic loading of flexible piles
$\delta \approx 1.2 - 1.8$	Kagawa and Kraft (1980)	Dynamic loading of flexible piles
$\delta \approx 0.9 - 3.0$	Gazetas and Dobry (1984)	Dynamic loading of flexible piles
$\delta = \frac{4}{2(1+\mu)}$	Yu and Houlsby (1991)	Cylindrical cavity expansion theory
$\delta = \frac{1.0}{1-\mu^2}\sqrt[12]{\frac{E_s D^4}{E_p I_p}}$	Ashford and Juirnarongrit (2003)	Dynamic loading of flexible piles
$\delta \approx 1.2 - 1.75$	Gerolymos and Gazetas (2006)	Static and dynamic loading of rigid caissons (in combination with moment-springs)

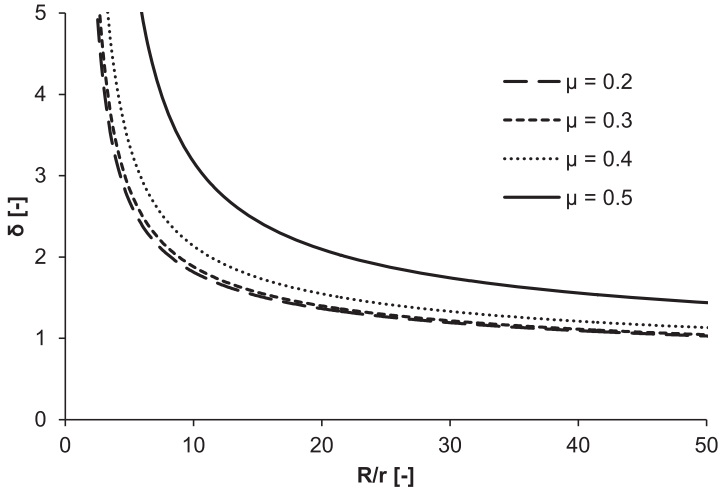

Figure 3-11. δ -values based on Eq.(3.1) from Baguelin et al. (1977)

Vesic (1961) extended Biot's (1937) solution for a point load acting on an infinite beam on an elastic subgrade to account for loading by a couple (moment) and to allow for beams of finite length. The approach by Biot (1937) and Vesic (1961) was to equate the expressions for bending moments for a beam on the elastic half-space, with the expressions for bending moments of a beam on an elastic Winkler foundation.

The solutions from Vesic (1961), Bowles (1968) and Ashford and Juirnarongrit (2003) are all on the same form (ref. Table 3-1), with factors 0.65, 1.3 and 1.0 respectively as the difference between the three expressions. Bowles (1968) argued that for a pile with soil contact around the entire circumference, the spring constant from Vesic's surface beam should be doubled. Ashford and Juirnarongrit (2003) on the other hand, stated that the back side of the pile would not contribute with any resistance. They stated that the only extra resistance experienced by a pile would be from side shear, and concluded that an average of Bowles' and Vesic's solutions was most likely.

Kagawa and Kraft (1980) equated the work done by soil reactions along the pile on a Winkler foundation model and an axis symmetric FE-model for describing δ. Roesset and Angelides (1979) constructed load-displacement relationships along the pile based on a 3D-FE formulation for the same purpose. The FEM was also use by Gazetas and Dobry (1984) to calibrate soil springs. Novak et al. (1978) derived frequency dependent springs and dashpots from analytical solutions for the plane strain case of a rigid disc in visco-elastic material. Matlock (1970) used a rectangular shaped surface load on an elastic half-space as his starting point, for which supplementary information is given in Appendix B. Gerolymos and Gazetas (2006) developed a multispring model for dynamically loaded rigid caissons in the context of bridge foundations. They used

boundary element formulations and elasto-dynamic FE-methods to derive the different spring-stiffnesses.

Based on all the different assumptions adopted for the δ-values given in Table 3-1, it is remarkable how most of the numerical values of the function δ fall into the rather narrow numerical range of $\delta \approx 1 - 2$. Further, it is noted that there appears to be a consensus in the quoted literature that the initial stiffness of the p-y curve can be expressed in the form of Eq.(3.3b), i.e. $k = \delta E_s$.

For pile sections close to the soil surface, the second assumption at the start of this section (plane strain conditions) is no longer valid. The initial stiffness of the upper part of the soil profile has caught little attention in the literature, and when mentioned (e.g. Matlock (1970), Reese et al. (1974), Reese et al. (1975)) it is commonly assumed to be equal to the stiffness for deeper pile sections.

3.6 Ultimate Resistance

As for the initial stiffness, we keep the assumption from earlier that soil can be idealized as a linear-elastic, perfectly plastic material. The previous assumption of plane strain conditions is only valid for pile sections at depths sufficiently far from the ground surface. Close to the ground surface, movement in all three dimensions must be considered.

The ultimate resistance is herein defined as when the soil is brought to plastic state along the entire critical shear surface, as illustrated in Figure 3-7b. For ultimate resistance, a conceptual difference exists between granular soils (sand, gravel etc.) and cohesive soils (clay), due to different failure criteria. Granular soils are commonly idealized with a stress-dependent strength from the Mohr-Coulomb failure criterion. Cohesive soils on the other hand, are commonly idealized with a stress-independent failure strength, known as the Tresca criterion. The conceptual difference for a material point is shown in Figure 3-12. Due to the difference in failure criteria, the ultimate strength will be treated differently for clay and sand in the following.

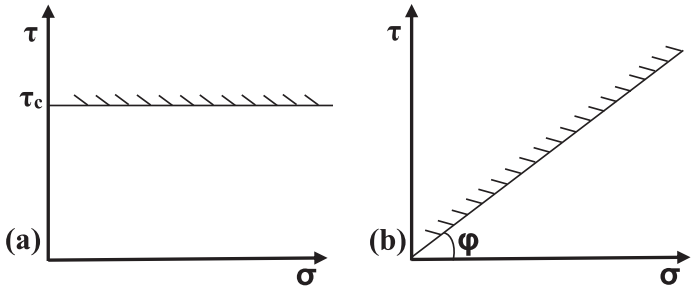

Figure 3-12. (a) Tresca and (b) Mohr-Coulomb failure criteria in τ-σ space.

3.6.1 Ultimate Resistance for Deep Pile Sections in Clay

The ultimate resistance to a deep pile section in clay has been solved analytically by Randolph and Houlsby (1984) and Martin and Randolph (2006). For practical purposes, the two solutions are identical and can be expressed as in Eq.(3.4):

$$\frac{p_u}{c_u D} = N_c = 9 + 3\alpha \tag{3.4}$$

where

p_u = ultimate lateral resistance
c_u = undrained shear strength
α = friction ratio (pile-soil interface roughness)
D = pile diameter
N_c = bearing capacity factor

The failure geometry from Randolph and Houlsby (1984) and Martin and Randolph (2006) is consistent with the geometry shown in Figure 3-7b.

3.6.2 Ultimate Resistance for Deep Pile Sections in Sand

For the ultimate resistance to a deep pile section in sand, Reese et al. (1974), Brinch-Hansen (1961) and Meyerhof (1995) have all proposed analytical solutions, based on different assumptions. Brinch-Hansen (1961) and Meyerhof (1995) both idealized the pile as a line load, and expressed the ultimate resistance in the form of Eq.(3.5).

$$p_u = \left(\gamma' z N_q + c N_c\right) D \tag{3.5}$$

where

p_u = ultimate lateral resistance
N_q = bearing capacity factor for the frictional part of the resistance
N_c = bearing capacity factor for resistance related to cohesion
c = cohesion
γ' = effective unit weight of sand
z = depth below ground surface
D = pile diameter

The bearing capacity factors N_q and N_c are both based on the soils internal angle of friction and embedment depth, and are given by Meyerhof (1951) as:

$$N_q = e^{2\theta \tan\varphi} \tan^2\left(\frac{\pi}{4} + \frac{\varphi}{2}\right) \quad \textbf{(3.6a)}$$

$$N_c = \frac{(N_q - 1)}{\tan\varphi} \quad \textbf{(3.6b)}$$

The parameter θ is a function of the foundation embedment depth, represented by the angle β in Figure 3-13. For the special case of a smooth (α = 0) strip load, θ is given as θ = π/2 + β with reference made to Meyerhof (1951) for details. At ground surface a smooth strip load has β = 0 and θ = π/2. A smooth, embedded line load at large depth (no influence of the surface) has β = π/2 and θ = π.

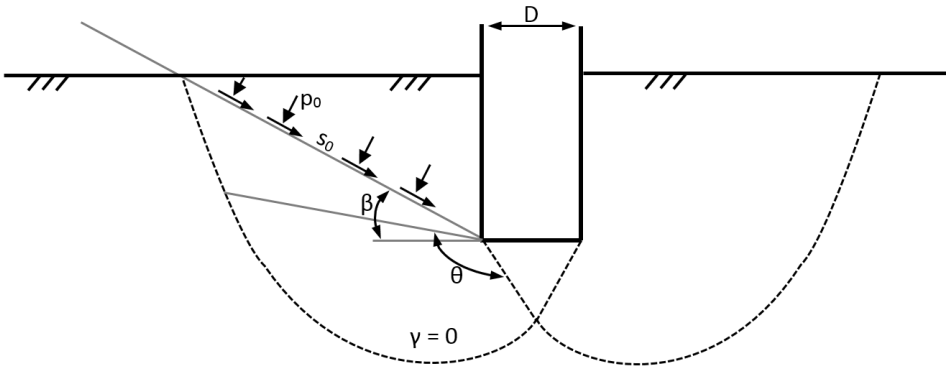

Figure 3-13. Failure geometry for Meyerhof bearing capacity. After Meyerhof (1951).

Reese et al. (1974) assumed a simplified geometry consisting of rigid blocks failing in shear, and moving around the pile as shown in Figure 3-14. The ultimate resistance for a deep pile section as determined by Reese et al. (1974) is given in Eq.(3.7).

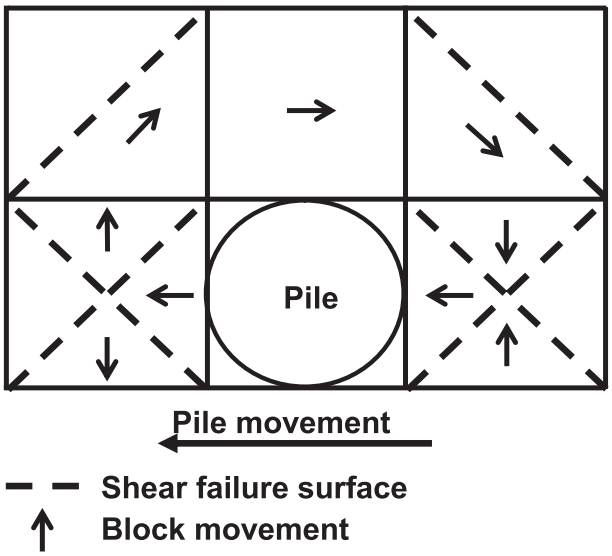

Figure 3-14. Simplified geometry assumed by Reese et al. (1974). Figure after Reese et al. (1974) and Sørensen et al. (2012)

$$p_u = D\,\gamma' z\left(K_a\,(\tan^8\beta_r - 1) + K_0 \tan\varphi \tan^4\beta_r\right) \qquad \textbf{(3.7)}$$

where

p_u = ultimate lateral resistance from the sand
K_a = Rankine coefficient for active soil pressure
K_0 = coefficient of soil pressure at rest
γ' = effective unit weight of sand
z = depth below ground surface
φ = soil internal friction angle
β_r = $45° + \varphi/2$

Reese et al. (1974) did not consider any contribution from cohesion. A comparison of the Reese et al. bearing capacity factor (expression inside the brackets in Eq.(3.7)) and the frictional part of the bearing capacity factor from Meyerhof (1951) (N_q) is given in Figure 3-15. The simplified bearing capacity factor from Reese et al. (1974) is seen to correspond well with the Meyerhof bearing capacity for an angle $\beta = 15°$.

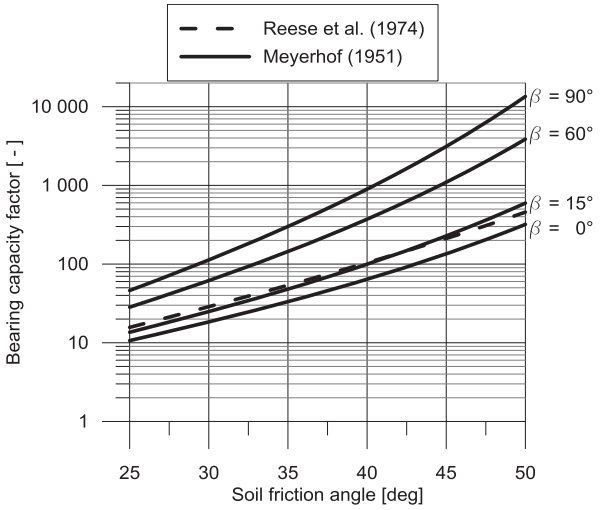

Figure 3-15. Comparison of bearing capacity factors for cohesionless sand.

3.6.3 Ultimate Resistance for Shallow Pile Sections

In contrast to soil at greater depths, soil closer to the ground surface is assumed to move in all three dimensions. Motion in three dimensions implies that the plane strain assumption is no longer valid. Reese (1957) advocated that close to the soil surface, the soil in front of a pile will move in a wedge-like form, up and away from the pile. Reese (1957) considered a wedge geometry for clay, as shown in Figure 3-16a). For sand, Reese et al. (1974) considered a wedge opening as a fan in front of the pile, shown in Figure 3-16b). An assumption of a wedge-shaped failure surface has also been explored by Norris (1986) and Ashour et al. (1998), who calculated the soil response to pile movement from a passive wedge in front of a pile. The wedge failure mechanism from Norris (1986) and Ashour et al. (1998) can be considered a refined version of the Reese et al. (1974) geometry, and is termed *the Strain wedge method*. In this method, the entire soil response is controlled by the passive wedge in front of the pile, and the wedge is considered increasing in all three dimensions with increasing pile deformation. The Strain wedge method assumes the same wedge geometry for both sand and clay. The assumption of a wedge-like or conical zone in front of the pile limiting the soil resistance is further supported by experimental work from Morita et al. (2007), Hajialilue-Bonab et al. (2011), Cuéllar (2011) and others.

The transition between the ultimate resistance for shallow pile sections and deep pile sections is commonly taken as:

$$p_u = \min\left(p_{u,shallow},\ p_{u,deep}\right) \tag{3.8}$$

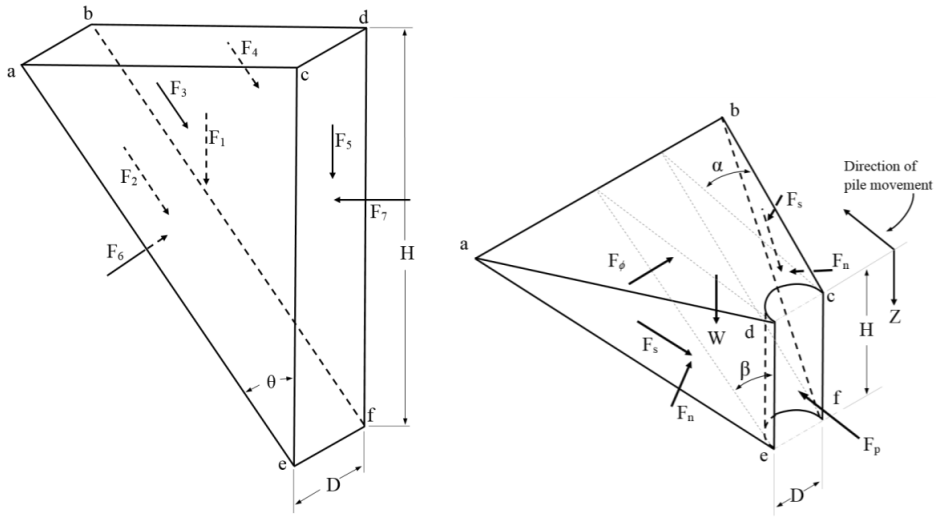

Figure 3-16. (a)Wedge-shaped failure mechanism for clay, considered by Reese (1957) (b) Wedge-shaped failure mechanism for sand considered by Reese et al. (1974)

3.6.4 Ultimate Resistance for Shallow Pile Sections in Clay

Similar to the ultimate resistance for deep pile sections in clay, the ultimate resistance for shallow pile sections can be written in the form of Eq.(3.9), with N_c being the bearing capacity factor. Reese (1957) considered horizontal and vertical equilibrium of the wedge geometry in Figure 3-16a), and gave the bearing capacity factor per unit length of the pile as Eq.(3.10). Reese (1957) made assumptions of:

- square shaped pile
- zero horizontal shear at the sides of the pile
- no vertical shear at the front and back sides of the pile
- uniform soil strength over the depth of the wedge
- fully developed undrained shear strength along the planar surfaces of the wedge

Matlock (1970) considered the same geometry as Reese (1957), however, he allowed for partly mobilization of horizontal shear at the sides of the pile. Matlock (1970) further compared the theoretical capacity with full-scale pile loading tests and found that the last term in Eq.(3.10) had to be altered by an empirical constant (J) to fit the test results. Matlock (1970) found that the wedge capacity was better described by Eq.(3.11). The detailed derivation of Eq.(3.10) and Eq.(3.11) is given in Appendix B. For the same wedge geometry, Randolph and Houlsby (1984) found that a circular pile would give an ultimate resistance per unit length of pile as expressed by Eq.(3.12).

$$\frac{p_u}{cD} = N_c \tag{3.9}$$

Reese (1957): $$N_c = 2 + \frac{\gamma' z}{c} + 2\sqrt{2}\frac{z}{D} \tag{3.10}$$

Matlock (1970): $$N_c = 3 + \frac{\gamma' z}{c} + \frac{Jz}{D} \tag{3.11}$$

Randolph and Houlsby (1984): $$N_c = 2 + \frac{\alpha\pi}{2} - \frac{\pi}{8}\frac{\gamma' D}{c} + \frac{\gamma' z}{c} + 2\sqrt{2}\frac{z}{D} \tag{3.12}$$

where

p_u = ultimate lateral resistance
c_u = undrained shear strength
γ' = effective unit weight of soil
z = depth below ground surface
α = pile-soil interface roughness
D = pile diameter
J = empirical parameter (J = 0.5 for Gulf of Mexico clays)

Murff and Hamilton (1993) considered a three dimensional conical failure mechanism and derived an upper bound solution for it from plasticity theory. Their method required several numerical integrations, in addition to nonlinear optimization techniques. Murff and Hamilton (1993) applied their approach in a parametric study and fitted an empirical equation to the corresponding results, to ease the use of their solution in practice. This empirical equation is given in Eq.(3.13). An important assumption in Murff and Hamilton (1993) is that the undrained shear strength is assumed to vary linearly with depth in the form of $c = c_0 + \lambda z$, where c_0 is the undrained shear strength at ground surface, z is the depth and λ is the rate of increase with depth for the undrained shear strength of the clay.

$$N_c = \left(N1 - N2\exp(-\frac{\xi z}{D}) \right) + \frac{\gamma' z}{cD} \tag{3.13}$$

$$\xi = \min\left(0.25 + 0.05\frac{c_0}{\lambda D}, \quad 0.55 \right) \tag{3.14}$$

where

N_1 = limiting bearing capacity factor at large depth from Eq.(3.4)
N_2 = constant value of ≈ 5 (Randolph, 2013)

Yu et al. (2015) performed a similar study to the one by Murff and Hamilton (1993) for what they claim to be a “more reasonable failure mechanism”. The same methodology is used with an upper bound solution from plasticity theory, but with a curved failure

surface obtained by rotating the Newton interpolation polynomial around the pile. An empirical equation was fitted to their results, giving the bearing capacity factor N_c as:

$$N_c = N_1 - (1-\alpha) - (N_1 - N_2)\left[1 - \left(\frac{z}{14.5D}\right)^{0.6}\right]^{1.35} + \frac{\gamma' z}{c_u} \qquad \textbf{(3.15)}$$

where:

N_1 = 11.94
N_2 = 3.22
α = pile-soil interface roughness
D = pile diameter

3.6.5 Ultimate Resistance for Shallow Pile Sections in Sand

The methods for ultimate resistance to deep pile sections in sand from Brinch-Hansen (1961) and Meyerhof (1995) do not consider the difference in failure geometry for deep and shallow pile sections. They suggest using the same set-up for both deep and shallow pile sections. Brinch-Hansen (1961) and Meyerhof (1995) take near-surface effects into account within the bearing capacity factors N_q and N_c, however no specific consideration of wedge geometries is presented. Reese et al. (1974) did consider the wedge shown in Figure 3-16b), and from horizontal and vertical equilibrium considerations, the ultimate resistance per unit length of pile was described as:

$$p_u = A\gamma' z\left[\frac{K_0 z \tan\varphi \sin\beta}{\tan(\beta-\varphi)\cos\alpha} + \frac{\tan\beta}{\tan(\beta-\varphi)}(D + z\tan\beta\tan\alpha) + K_0 z \tan\beta\,(\tan\varphi\sin\beta - \tan\alpha) - K_a D\right] \qquad \textbf{(3.16)}$$

where

A = empirical correction factor (A = 3 - 0.8 z/D)
K_a = Rankine coefficient for minimum active soil pressure
K_0 = coefficient of soil pressure at rest
z = depth below ground surface
D = pile diameter
γ' = submerged unit weight of soil
ϕ = soil internal friction angle
α = a function of void ratio, approximately $\phi/2$
β = $45° + \varphi/2$

The empirical correction factor A was assigned after comparing the analytical solution to a full-scale pile test. Broms (1964) and Fleming et al. (1992) suggested semi-empirical approaches relating the ultimate resistance for a pile section to the Rankine passive soil pressure. Based on a database of field tests, Broms (1964) gave the ultimate resistance for piles in cohesionless soils as three times the passive earth pressure

developing in front of the pile, expressed in Eq.(3.17). Fleming et al. (1992) quoted Barton (1982), who correlated the ultimate lateral resistance with the square of the Rankine coefficient for passive earth pressure, as shown in Eq.(3.18).

$$p_u = 3K_p D\,\gamma' z \quad \textbf{(3.17)}$$

$$p_u = K_p^2 D\,\gamma' z \quad \textbf{(3.18)}$$

where

p_u = ultimate lateral resistance from the sand
K_p = Rankine coefficient for passive soil pressure
γ' = effective unit weight of sand
z = depth below ground surface

The semi-empirical methods by Broms (1964) and Fleming et al. (1992) do not distinguish between shallow or deep failure modes. The lateral soil response to long and slender piles is normally controlled by the upper part of the soil. The methods from Broms (1964) and Fleming et al. (1992) are based on test results from field- and scale-testing, and these results are therefore likely to be influenced by the ultimate resistance in near-surface soil.

3.7 Transition from Initial Stiffness to Ultimate Resistance

In Figure 3-8 and Figure 3-9, it was shown how different material points on the critical shear planes change from elastic to plastic material state for different load levels. This resulted in a curved transition from an entirely elastic response to a perfectly plastic response from the soil. This transition has been modeled differently by various writers; however they are similar in the way that they all are limited upwards by ultimate resistance, and have an initial part determined from a stiffness consideration. Examples of different approaches found in the literature are:

- *Matlock (1970)* constructed a curve consisting of two line segments. The first segment has a parabolic shape and the second segment is a horizontal line at the ultimate resistance. Stiffness of the parabolic curve was tuned in by a reference displacement at 50 % of the ultimate resistance.
- *Reese et al. (1974)* constructed a curve consisting of three line segments. The first line segment being linear, with inclination defined as the initial stiffness. The third segment is a horizontal line at the ultimate resistance, and the second segment a parabola connecting the first and the third line segments.
- *O'Neill and Murchison (1983)* constructed a curve defined by the tanh-function. In the context of p-y response, the tanh-function has the convenient feature that tanh(x) = x for small values of x, and tanh(x) = 1 for large values of x. The tanh-function in relation to p-y response is investigated in detail in Appendix B. However, it can be noted that using a single function is mathematically more

convenient than constructing curves consisting of different line segments and joining them together.

- *Guo (2012)*, and also others, have constructed bi-linear, linear-elastic, perfectly plastic p-y curves. The curved transition in this type of curves is then neglected. The linear elastic part is defined by the initial stiffness and the perfectly plastic part by the ultimate resistance.

3.8 Chapter Summary

In this chapter, equilibrium of a laterally loaded, long and slender pile has been considered together with load-displacement relationships in an elasto-plastic framework. Different solutions from the literature have been presented, and it is shown that the soil reaction to pile movement can be expressed as a function of the Young's modulus of the soil if the soil is considered elastic, and as a function of the soil strength, if the soil is considered perfectly plastic. It is further seen that the soil reaction curve will have a curved transition from elastic to plastic behavior, even for a linear-elastic perfectly plastic material.

For the long and slender pile, vertical shear stresses at the pile circumference have been neglected for the lateral behavior. The vertical shear contributions to the moment equilibrium of the pile is however dependent on the pile L/D ratio, and can be expected to be more important for the moment equilibrium of shorter, more rigid, large diameter piles. This is treated in the next chapter.

Chapter References

Ashford, S & Juirnarongrit, T (2003) Evaluation of Pile Diameter Effect on Initial Modulus of Subgrade Reaction. *Journal of Geotechnical and Geoenvironmental Engineering* **129(3)**:234-242.

Ashour, M, Norris, GM & Pilling, P (1998) Lateral Loading of a Pile in Layered Soil Using the Strain Wedge Model. *Journal of Geotechnical and Geoenvironmental Engineering* **124(4)**:303-315.

Baguelin, F, Frank, R & Saïd, YH (1977) Theoretical study of lateral reaction mechanism of piles. *Geotechnique* **27**:405-434.

Barton, YO (1982) Laterally Loaded Model Piles in Sand: Centrifuge Tests and Finite Element Analyses. University of Cambridge, vol. Ph.D.

Biot, MA (1937) Bending of an Infinite Beam on an Elastic Foundation. *ASME Journal of Applied Mechanics* **59**:A1-A7.

Bowles, JE (1968) *Foundation Analysis and Design.* McGraw Hill.

Brinch-Hansen, J (1961) The Ultimate Resistance of Rigid Piles Against Transversal Forces. *DGI Bulletin* **12**:5-9.

Broms, BB (1964) Lateral Resistance of Piles in Cohesionless Soils. *ASCE Journal of the Soil Mechanics and Foundations Division* **90(SM 3)**:123-156.

Cuéllar, P (2011) Pile foundations for offshore wind turbines: Numerical and experimental investigations on the behaviour under short-term and long-term cyclic loading. Technische Universität Berlin, vol. Ph.D.

Fleming, K, Weltman, A, Randolph, M & Elson, K (1992) *Piling Engineering, Second Edition.* Taylor & Francis.

Foglia, A, Ibsen, LB & Andersen, LV (2012) An Innovative Physical Model for Testing Bucket Foundations. In *NGM 2012*. Danish Geotechnical Society, Copenhagen, Denmark, vol. 1, pp. 323-330.

Gazetas, G & Dobry, R (1984) Horizontal Response of Piles in Layered Soils. *Journal of Geotechnical Engineering* **110(1)**:20-40.

Gerolymos, N & Gazetas, G (2006) Winkler model for lateral response of rigid caisson foundations in linear soil. *Soil Dynamics and Earthquake Engineering* **26(5)**:347-361.

Guo, W (2012) Simple Model for Nonlinear Response of 52 Laterally Loaded Piles. *Journal of Geotechnical and Geoenvironmental Engineering* **139(2)**:234-252.

Hajialilue-Bonab, M, Azarnya-Shahgoli, H & Sojoudi, Y (2011) Soil deformation pattern around laterally loaded piles. In *International Journal of Physical Modelling in Geotechnics*. vol. 11, pp. 116-125.

Kagawa, T & Kraft, LM (1980) Seismic p-y responses of flexible piles. *ASCE Journal of the Geotechnical Engineering Division* **106(GT8)**:899-918.

Martin, CM & Randolph, MF (2006) Upper-bound analysis of lateral pile capacity in cohesive soil. *Geotechnique* **56(2)**:141-145.

Matlock, H (1970) Correlation for Design of Laterally Loaded Piles in Soft Clay. In *Offshore Technology Conference*. Houston Texas, pp. 577-607.

Meyerhof, GG (1951) The Ultimate Bearing Capacity of Foundations. *Geotechnique* **2(December)**:301-322.

Meyerhof, GG (1995) Behaviour of pile foundations under special loading conditions: 1994 R.M. Hardy keynote address. *Canadian Geotechnical Journal* **32(2)**:204-222.

Morita, K, Otani, J, Mukunoki, T, Hironaka, J & Pham, KD (2007) Evaluation of vertical and lateral bearing capacity mechanisms of pile foundations using X-ray CT. In *Advances in Deep Foundations*. Taylor & Francis, pp. 217-223.

Murff, J & Hamilton, J (1993) P-Ultimate for Undrained Analysis of Laterally Loaded Piles. *Journal of Geotechnical Engineering* **119(1)**:91-107.

Norris, GM (1986) Theoretically based BEF laterally loaded pile analysis. In *3rd International Conference on Numerical Methods in Offshore Piling*. Technip (ed), pp. 361-386.

Novak, M, Nogami, T & Aboul-Ella, F (1978) Dynamic Soil Reactions for Plane Strain Case. *ASCE Journal of the Engineering Mechanics Division* **104(4)**:953-959.

O'neill, MW & Murchison, JM (1983) *Evaluation of p-y Relationships in Sands*. Houston, Texas, USA, Report Research Report No. GT-DF02-83.

Poulos, HG & Davis, EH (1974) *Elastic solutions for soil and rock mechanics.* New York, Wiley.

Randolph, MF (2013) Analytical contributions to offshore geotechnical engineering. In *Proceedings of the 18th International Conference on Soil Mechanics and Geotechnical Engineering - 2nd McClelland Lecture*. Paris, France.

Randolph, MF & Houlsby, G (1984) Limiting pressure on a circular pile loaded laterally in cohesive soil. *Geotechnique* **34(4)**:613-623.

Reese, L, Cox, W & Koop, F (1974) Analysis of Laterally Loaded Piles in Sand. In *Offshore Technology Conference*. Houston, pp. 473–483.

Reese, L, Cox, W & Koop, F (1975) Field Testing and Analysis of Laterally Loaded Piles in Stiff Clay. In *Offshore Technology Conference*. Houston, Texas, pp. 672.

Reese, LC (1957) Discussion of "Soil Modulus of Laterally Loaded Piles" by Bramlette McClelland and John A. Focht. *Journal of the Soil Mechanics and Foundations Division* **83(2)**:1228-21 -1228-34.

Roesset, JM & Angelides, D (1979) Dynamic stiffness of piles. In *Numerical Methods in Offshore Piling*. Institution of Civil Engineers, London, pp. 57-63.

Sørensen, SPH, Brødbæk, KT, Møller, M & Augustesen, AH (2012) *Review of laterally loaded monopiles employed as the foundation for offshore wind turbines*. Aalborg, 54 p.

Tadesse, S (2000) Behaviour of saturated sand under different triaxial loading and liquefaction. In *Department of Civil and Transport Engineering*. Norwegian University of Science and Technology, Trondheim, vol. PhD, 144 p.

Terzaghi, K (1955) Evaluation of Coefficients of Subgrade Reaction. *Geotechnique* **5(4)**:297-326.

Vesic, AB (1961) Bending of Beams Resting on Isotropic Elastic Solid. *ASCE Journal of Engineering Mechanics* **87(2)**:35-54.

Yu, HS & Houlsby, GT (1991) Finite cavity expansion in dilatant soils: loading analysis. In *Geotechnique*. vol. 41, pp. 173-183.

Yu, J, Huang, M & Zhang, C (2015) Three-dimensional upper bound analysis for ultimate bearing capacity of a laterally loaded rigid pile in undrained clay. *Canadian Geotechnical Journal*.

4 Vertical Shear Contributions to Rotational Resistance for Short and Non-Slender Piles

In the previous chapter, lateral resistance from vertical shear tractions at the pile surface was assumed negligible for piles with large length to diameter ratios (L/D-ratios). However, when this ratio is decreased, the contribution from vertical shear is of increasing importance to the moment-equilibrium of the pile.

Monopiles for offshore wind turbines have L/D-ratios that are typically in the range of 4-6, with trends going towards even lower L/D-ratios. As will be discussed later, future forecasted L/D-ratios will have significant influence from the vertical shear forces acting on the pile in the overall load-deformation response.

The vertical shear forces acting at the pile surface are mobilized with the rotation of the pile segment, as shown in Figure 4-1. The back side of the pile segment moves upwards relative to the soil, and the front side of the pile segment moves downwards relative to the soil. The relative movement between pile and soil mobilizes a pair of forces, creating a rotational resistance for the pile segment.

For a 1-dimensional beam on a Winkler foundation, it is convenient to implement this pair of vertical forces directly as a moment resistance. Moment resistance mobilized with rotation can then be incorporated as a rotational spring. The moment resistance is found by integrating vertical shear over the pile section surface, and multiplying with the distance to the point of rotation. In the following, this rotational spring will be referred to as M-θ curves.

$$M = dz \int_0^{2\pi} (r \sin \Psi)\, \tau_{rz} r \, d\Psi$$

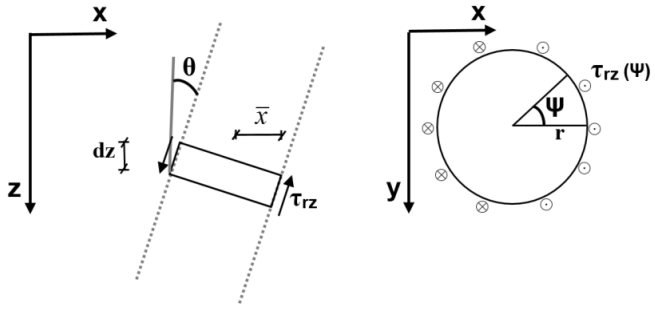

Figure 4-1. Rotational resistance to a pile segment from vertical shear tractions at the pile surface.

4.1 M-θ curves

The moment resistance is dependent on the strength and stiffness properties of the soil and the geometrical properties of the pile. As such, the M-θ curves are conceptually similar to the p-y curves, and in the following will be described in terms of initial stiffness, ultimate resistance and the transition between initial stiffness and ultimate resistance. The contribution from vertical shear through distributed moment springs has previously been included with success for both drilled piers (Davidson, 1982a, 1982b) and rigid caisson foundations (Gerolymos and Gazetas, 2006a, 2006b, 2006c). Distributed moment springs are also recently outlined to be of importance for monopile foundations for offshore wind turbines by Byrne et al. (2015).

In the following, the same assumption regarding soil behavior as in Chapter 3 will be used, namely that soil can be idealized as a linear-elastic, perfectly plastic material.

4.2 Initial Stiffness

Before any individual material points start to yield, the linear-elastic, perfectly plastic material behaves like a linear-elastic material. It follows from the assumption of a linear-elastic, perfectly plastic material that the initial stiffness of the moment-rotation curve is governed by the theory of elasticity. No exact analytical solution is found in the literature for the case of static loading; however, three different solutions are found and presented.

Novak et al. (1978) derived frequency dependent rocking-springs and dashpots from analytical solutions for the plane strain case of a rigid disc in visco-elastic material. The rotational stiffness from Novak et al. (1978) is given by:

$$k_\theta = \pi G_s r^2 (1 + \mathrm{i}\, d_s) \left[a_0^* \frac{K_0(a_0^*)}{K_1(a_0^*)} + 1 \right] \qquad \textbf{(4.1)}$$

where

k_θ	=	spring stiffness of rotational spring
G_s	=	soil shear stiffness
r	=	pile radius
d_s	=	damping parameter
a_0^*	=	complex dimensionless frequency
K_0, K_1	=	modified Bessel functions of the second kind

Davidson (1982a, 1982b) considered drilled pier foundations for electrical transmission line structures, and provided rotational springs as a part of a multispring model. The rotational spring stiffness was calibrated by linear elastic 3D FEM and field tests and given as:

$$k_\theta = 0.55 E_{pr} D^2 \tag{4.2}$$

where

E_{pr} = soil deformation modulus from the pressuremeter test
D = pile diameter

Gerolymos and Gazetas (2006c) considered rigid caisson foundations for bridges and gave distributed rotational springs as a part of a multispring model. They used boundary element formulations and elasto-dynamic FE- methods to derive the spring stiffness, and fitted the empirical expression given in Eq.(4.3) to their results.

$$k_\theta = 0.85 \left(\frac{L}{D} \right)^{-1.71} E_s L^2 \tag{4.3}$$

where

L = embedment depth
D = pile diameter
E_s = Young's modulus of the soil

The three above expressions for initial stiffness are rather different; however, they all incorporate both pile and soil properties. Considering the real part of the expression from Novak et al. (1978), the soil shear stiffness (G_s) and the pile diameter (2r) squared are of influence, and similar to the semi-empirical expression from Davidson (1982a). The semi-empirical expression from Davidson (1982a) includes the Young's modulus of the soil (E_s) and the pile diameter (D) squared. Gerolymos and Gazetas (2006c) fitted a curve dependent on the L/D ratio of the pile, the Young's modulus of the soil (E_s) and the pile length (L) squared.

4.3 Ultimate Resistance

A solution for ultimate, distributed rotational resistance of pier foundations is proposed by Davidson (1982a, 1982b). In the solution from Davidson, it is assumed that contact between pile and soil is not maintained on the back side of the pile.

The ultimate rotational resistance from the front side of the pile is given by Davidson (1982b) as:

$$M_{ult} = \alpha \frac{D^2}{2} \left(\frac{\pi}{4} c + \frac{2}{3} \sigma_r' \tan \varphi \right) \tag{4.4}$$

where

D = pile diameter
α = pile-soil interface roughness
c = soil cohesion
σ_r' = effective stress acting normal to the pile-soil interface
φ = soil friction angle

The effective stress normal to pile-soil interface (σ'_r) is in Davidson (1982b) coupled with the mobilized lateral soil resistance, and given as:

$$\sigma'_r = \frac{p - \frac{\alpha D c \pi}{4}}{\frac{\pi D}{4} + \frac{\alpha D}{3}\tan\varphi} \qquad \textbf{(4.5a)}$$

where

D = pile diameter
α = pile-soil interface roughness
c = soil cohesion
p = lateral pressure mobilized for lateral pile movement (p from p-y)
φ = soil friction angle

For zero lateral pile movement, the mobilized lateral soil resistance will be zero. This gives a lower limit to the radial effective stress less than zero. If installation effects are neglected, the lower limit to the radial effective stress can be taken as the in situ horizontal stress:

$$\sigma'_r = \max\left(k_0 \cdot \sigma'_v \quad , \quad \frac{p - \frac{\alpha D c \pi}{4}}{D\left(\frac{\pi}{4} + \frac{\alpha}{3}\tan\varphi\right)} \right) \qquad \textbf{(4.5b)}$$

4.3.1 Ultimate Resistance in Cohesive Soils

For a purely cohesive soil (φ = 0), the ultimate shear resistance is defined as:

$$\tau = c_u \qquad \textbf{(4.6)}$$

where c_u is the undrained shear strength. Davidson (1982b) assumed that contact between the pile and soil is not maintained on the back side of the pile. In an undrained situation, clay can take tensile forces. If symmetry is assumed for the front and back sides of the pile, ultimate moment resistance is found by multiplying Eq.(4.4) by 2. For a purely cohesive soil (φ = 0) contribution from both sides of the pile then becomes:

$$M_{ult} = \frac{\pi}{4}\alpha\, c_u D^2 \qquad \textbf{(4.7)}$$

where

D = pile diameter
α = pile-soil interface roughness
c_u = undrained shear strength

It should be noted that for a purely cohesive soil, the assumptions made above remove the coupling between ultimate rotational resistance and the mobilized lateral resistance.

4.3.2 Ultimate Resistance in Granular Soils

From Mohr-Coulomb theory, the shear capacity for granular materials is defined as:

$$\tau = c + \sigma' \tan\varphi \tag{4.8}$$

where c is cohesion, φ is the soil friction angle and σ' is effective stress. For the special case of a purely frictional material (c = 0) Eq.(4.4) becomes:

$$M_{ult} = \alpha\, \sigma'_r \tan\varphi \frac{D^2}{3} \tag{4.9}$$

where

D = pile diameter
α = pile-soil interface roughness
σ'_r = effective stress acting normal to the pile-soil interface (radial direction)
φ = soil friction angle

The effective stress normal to pile-soil interface (σ'_r) defined in Eq.(4.5b) is reduced to:

$$\sigma'_r = \max\left(k_0 \cdot \sigma'_v \quad , \quad \frac{p}{D\left(\frac{\pi}{4} + \frac{\alpha}{3}\tan\varphi\right)} \right) \tag{4.10}$$

where

D = pile diameter
α = pile-soil interface roughness
p = lateral pressure mobilized for lateral pile movement (p from p-y)
φ = soil friction angle

When the ultimate capacity described above is used in commercial software, the coupling between ultimate rotational resistance and mobilized lateral resistance requires that the iterative solution procedure is able to account for the coupling. Not all commercial software will allow the user to interfere with the code to make the necessary changes. In that case, a simplified uncoupled capacity for granular soil can be used. Considering that the pile-soil interface roughness can vary from 0 to 1, and that the soil friction angle for purely cohesive soil typically is found in the range of $\varphi \approx 35\text{-}45°$, the effective stress expressed by Eq.(4.10) can be assumed to be within the range of $\sigma'_r \approx 0.9p/D$ to $\sigma'_r \approx 1.25p/D$. A value of $\sigma'_r \approx p/D$ is assumed to be representative. If the mobilized lateral resistance p is replaced by the ultimate lateral resistance p_{ult}, the

rotational resistance is no longer coupled to the mobilized resistance. Eq.(4.10) can then be approximated as $\sigma'_r \approx p_{ult}/D$, which gives:

$$\sigma'_r \approx \max\left(k_0 \cdot \sigma'_v \quad , \quad \frac{p_{ult}}{D} \right) \tag{4.11}$$

4.4 Transition from Initial Stiffness to Ultimate Resistance

Similar to the p-y curves, the rotational springs need to combine the initial stiffness and the ultimate resistance by a continuous curve. Davidson (1982a) and Gerolymos and Gazetas (2006c) both approximated the rotational spring with bilinear curves, idealizing the pile-soil interaction as linear-elastic, perfectly plastic. In both cases the linear elastic response is determined by the initial stiffness, and the perfectly plastic response from the ultimate resistance. As for the p-y curves, the pile-soil response is governed by the soil deformation response. A real soil with nonlinear load-deformation response will give a nonlinear spring curve, meaning that the bilinear approach must be understood as an approximation to the real behavior.

4.5 Chapter Summary

In this chapter, a rotational restraint is presented based on the vertical shear contributions on the pile surface. Solutions for initial stiffness and ultimate capacity from the literature are presented. For applying the rotational restraint as a nonlinear spring, the initial stiffness and the ultimate resistance must be combined, in similar fashion as described for the p-y curves in Chapter 3.

Chapter References

Byrne, BW, Mcadam, R, Burd, HJ, Houlsby, GT, Martin, CM, Zdravkovic, L, Taborda, DMG, Potts, DM, Jardine, RJ, Sideri, M, Schroeder, FC, Gavin, K, Doherty, J, Igoe, D, Muir-Wood, A, Kallehave, D & Gretlund, JS (2015) New design methods for large diameter piles under lateral loading for offshore wind applications. In *Frontiers in Offshore Geotechnics III*. CRC Press, pp. 705-710.

Davidson, HL (1982a) *Laterally loaded drilled pier research. Vol 1: Design Methodology*. Pennsylvania: Gai Consultants Inc., Report EPRI-EL-2197.

Davidson, HL (1982b) *Laterally loaded drilled pier research. Vol.2: Research Documentation*. Pennsylvania: Gai Consultants Inc., Report EPRI-EL-2197.

Gerolymos, N & Gazetas, G (2006a) Development of Winkler model for static and dynamic response of caisson foundations with soil and interface nonlinearities. *Soil Dynamics and Earthquake Engineering* **26(5)**:363-376.

Gerolymos, N & Gazetas, G (2006b) Static and dynamic response of massive caisson foundations with soil and interface nonlinearities—validation and results. *Soil Dynamics and Earthquake Engineering* **26(5)**:377-394.

Gerolymos, N & Gazetas, G (2006c) Winkler model for lateral response of rigid caisson foundations in linear soil. *Soil Dynamics and Earthquake Engineering* **26(5)**:347-361.

Novak, M, Nogami, T & Aboul-Ella, F (1978) Dynamic Soil Reactions for Plane Strain Case. *ASCE Journal of the Engineering Mechanics Division* **104(4)**:953-959.

5 Numerical Investigation of Soil Reaction Springs

Chapters 3 and 4 describes different solutions from the literature for initial stiffness and ultimate resistance of translational and rotational springs. In this chapter, the expressions described in Chapters 3 and 4 are compared to results from a parametric study performed as 3D-FE modeling of the problem.

5.1 Extraction of Soil Reaction Curves from Finite Element Modeling

The derivation of p-y curves from strain gauge measurements on laterally loaded piles was described in Chapter 2. We recall that numerical integration and derivation of bending strains in the pile might introduce errors, and that only equivalent lateral forces acting on the pile can be determined. The main reason for using strain gauge readings to compute p-y curves is that reliable, direct physical measurements of deformation and soil resistance on a physical pile are problematic, due to the fact that the pile is embedded in the ground and therefore hardly accessible. The Finite Element Method (FEM) has the advantage that forces, displacements and stresses are computed for every element of the pile, and the load-displacement relationships can be extracted directly from the stresses and displacements acting on the soil-pile interface.

Extracting the soil-reaction springs from stresses acting on the pile-soil interface has two main advantages over measuring bending strains in the pile itself:

1) Errors introduced by several steps of numerical integration and derivation of the bending strains are avoided.
2) Soil reactions can be divided into lateral resistance and rotational resistance. Soil reactions derived from bending strains in the pile give an equivalent lateral resistance, incorporating the effect of both lateral and rotational resistance.

5.1.1 Extraction of Soil Reaction Springs from FEM in the Literature

Extraction of soil response from 3D-FE simulations is convenient for incorporating the 3-dimensional soil response into software which only accounts for soil response through 1-dimensional springs. Springs are computationally efficient compared to continuum models, and can be found as soil representation in a large variety of software, from simple beam-programs to advanced multi-purpose 3D-FE programs.

Fan and Long (2005) described a method for extracting p-y curves from full 3D-FE simulations where the soil reactions were taken from soil elements close to the pile, and integrated around the pile circumference to get the representative soil response. Pile displacements were taken from the pile itself. This method was also used by Kim and Jeong (2011), who compared p-y curves from 3D FEM with results from field load tests. McGann et al. (2011, 2012) investigated the effect of pile kinematics and layer

strengths to p-y curves by 3D-FEM, and extracted p-y curves from designated interface elements located at the pile-soil interface. Hanssen et al. (2013) extracted soil springs from 2D-FEM simulations to use for soil support in 3D-FEM buckling simulations of suction caissons during installation. Ibsen et al. (2013) compared the method from Fan and Long (2005) with extracting soil reactions from designated interface elements located at the pile-soil interface. They concluded that extracting stresses at the interface gave better results than extracting stresses close to the interface. The interface method described in Ibsen et al. (2013) has also been used by Østergaard et al. (2015). Byrne et al. (2015) extracted both p-y curves and M-θ curves from interface elements at the pile-soil interface from 3D-FEM simulations to create a multispring model. In addition, they extracted load-displacement curves from soil-soil interfaces at the pile toe, to construct springs to account for end-effects at the pile toe.

5.2 3D-FE Model

The numerical investigation of soil reaction curves is performed with the FE code Plaxis3D. Plaxis3D uses 10-node tetrahedral elements to model soil volumes, and 6-node triangular elements for plates (pile) and interfaces. The geometry from the base case model of the parameter study is shown in Figure 5-1. The influence of the geometry of both structure and soil volume are investigated; hence, the geometry will vary among the different simulations. The geometry shown in Figure 5-1 represents the base case geometry.

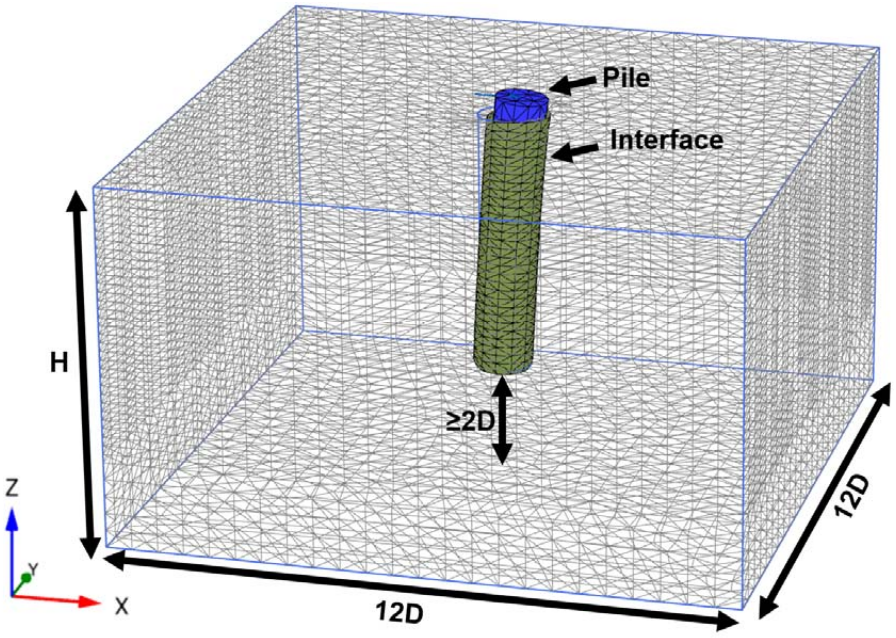

Figure 5-1. Geometry of base case model for the parameter study

The pile is modeled as an open ended steel pile, with a 1 m stick-up above the soil. The pile is loaded laterally by a point load assigned to the pile top. The top lid of the pile is given a very high stiffness (rigid for all practical purposes) in order to distribute the point load to the pile without influence of local effects at the load attachment point. The base case model is defined as a pile with 6 m diameter and 30 m embedment depth, giving an L/D ratio of 5. The physical dimensions of the base case model are summarized in Table 5-1.

As with the considerations of p-y and M-θ curves in Chapters 3 and 4, the initial stiffness and the ultimate resistance are considered separately. For the evaluation of initial stiffness, a linear elastic soil model is used. The ultimate resistance is evaluated with a linear-elastic, perfectly plastic soil model with a Tresca failure criterion for undrained soil response (clay). A Mohr-Coulomb failure criteria is used for drained soil response (sand). The element model used for stiffness evaluations consisted of 140 105 elements, while the element model used for evaluation of ultimate resistance consisted of 321 093 elements.

Special attention has been given to the distance from the pile center to the model boundaries, both for the evaluation of ultimate resistance and for the evaluation of the

Table 5-1. Base case model phyiscal dimensions, coordinate system shown in Figure 5-1

Dimension	Unit	Value
Pile Diameter	[m]	6
Pile Wall Thickness	[m]	0.06
Embedded Pile Length	[m]	30
Pile Stick Up	[m]	1
Soil Volume, X-direction	[m]	72
Soil Volume, Y-direction	[m]	72
Soil Volume, Z-direction	[m]	42

Table 5-2. Material properties, base case simulation

Dimension	Symbol	Unit	Lin-El	Lin-El, P-P
Young's modulus, steel	E_p	[kPa]	210E6	210E6
Poisson's ratio, steel	μ_p	[-]	0.3	0.3
Young's modulus, soil	E_s	[kPa]	30 000	30 000
Poisson's ratio, soil	μ	[-]	0.3	0.3
Effective unit weight, soil	γ'	[kN/m^3]	10	10
Undrained shear strength, soil	c_u	[kPa]	-	30
Friction angle (drained soil)	φ	[°]	-	35
Cohesion (drained soil)	c	[kPa]	-	0.1

initial stiffness. For the ultimate resistance, the boundary must be at a distance sufficiently far away from the pile. The geometry of the critical shear planes should not interfere with the model boundaries.

In Chapter 3, the elastic solution from Baguelin et al. (1977) was shown to approach infinite displacements when the distance from the pile center to the model boundary approached infinity. Baguelin et al. (1977) considered a rigid disc in an elastic, isotropic media, a geometry identical to the 2D-idealization of a laterally loaded pile section. When a linear elastic or a linear-elastic, perfectly plastic soil model is used, the distance to the boundary of the model will influence the calculated displacements (Benz, 2007).

For stiffness considerations of laterally loaded piles, different opinions about where to put the model boundary can be found in the literature. Skempton (1951) argued that for the similar problem regarding the settlement of strip foundations, the majority of strain would be found in a distance no more than 4 diameters below the strip load, and that 4D therefore is an appropriate distance to the boundary. Terzaghi (1955) had a similar opinion, and stated that displacements beyond a distance of about 3 diameters away from the pile would have only negligible influence to the local bending moments in the pile. Hence, he concluded that a distance to the boundary of 3D was sufficient. More recent work shows a larger scatter in both recommendations and the use of distance to the boundary. Brown and Shie (1991) and McGann et al. (2011) suggested both a boundary at 10D from pile center, based on numerical simulations of group effects in pile groups. Sørensen et al. (2009) and Augustesen et al. (2010) used a value of 20D, Achmus et al. (2007) a distance of 6D, and Ibsen et al. (2013) a distance of 7.3D. Suryasentana and Lehane (2014) kept the model boundaries constant and varied the pile diameter, resulting in a distance from pile center to boundary varying from 20D to 200D.

For the present study, a value of 6D from the pile center to the model boundary is chosen. If a distance from the pile center to the boundary of 6D is inserted in the 2D-solution from Baguelin et al. (1977), the resulting stiffness will approximate $4G_s$ for a Poisson's ratio of $\mu = 0.2 - 0.3$. G_s is the shear modulus of the soil, and relates to the Young's modulus E_s by:

$$G_s = \frac{E_s}{2(1+\mu)} \tag{5-1}$$

A stiffness of ~$4G_s$ corresponds to the horizontal stiffness per unit length of a cylinder embedded in an elastic half-space (cf. Figure 5-2). Eq.(5-2a) gives the stiffness for the entire cylinder (Gazetas, 1983).When the depth of the soil layer (Z) approaches infinity Eq.(5-2a) reduces to Eq.(5-2b). The stiffness per unit length of pile can be found by

$$K_H = \frac{4GD}{2-\mu}\left(1+\frac{1}{4}\frac{D}{Z}\right)\left(1+\frac{4}{3}\frac{L}{D}\right)\left(1+\frac{5}{4}\frac{L}{Z}\right) \quad \textbf{(5-2a)}$$

$$K_H = \frac{4GD}{2-\mu}\left(1+\frac{4}{3}\frac{L}{D}\right) \quad \textbf{(5-2b)}$$

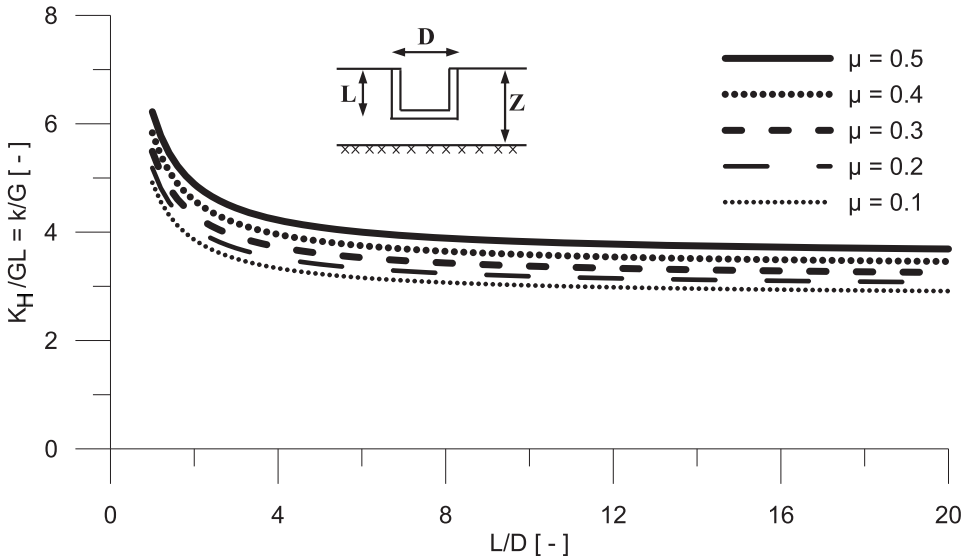

Figure 5-2. Horizontal stiffness per unit length, cylinder embedded in elastic half space.

dividing the total horizontal stiffness by the pile length. This is plotted for different Poisson's ratios of the half-space in Figure 5-2.

A stiffness of $4G_s$ also corresponds to the stiffness for cylindrical cavity expansion (Yu and Houlsby, 1991). Cylindrical cavity expansion is often used as an analogue to the laterally loaded pile, and can be considered an upper limit to the p-y stiffness (Randolph, 2013).

In the consecutive sections, the stiffness of the extracted p-y curves will be compared to the 2D-solution from Baguelin et al. (1977). To be consistent with the solutions presented in Chapter 3, the soil stiffness is expressed through the Young's modulus of the soil. It is recognized that the stiffness of the extracted p-y curves is likely to be affected by the distance to the boundary, however the comparison with the 2D-solution makes it possible to quantify 3-dimensional effects from the 3D-continuum.

5.3 Methodology for Extraction of p-y Curves

The extraction of p-y curves from the FE code Plaxis 3D requires integration of stresses along the pile-soil interface. A brief description of the developed methodology is presented below, along with examples of curves extracted from the base case. A detailed description of the methodology and mathematics involved can be found in Appendix C.

When p-y curves are extracted, displacements (y) along the pile are given directly as an output from the FE code. The line load (p) is found from integration of horizontal stresses at the interface between pile and soil. For the distributed M-θ curves, rotations are found from the difference in displacement between neighboring nodes along the depth of the pile. The moment response is found from integration of vertical shear at the pile soil surface, and multiplied with the distance to the neutral axis. For both curve sets, the load at the pile top is increased stepwise, with each step defining a point on the p-y and M-θ curves. The procedure for obtaining the different components can be described as:

y-values:

1) Direct output of horizontal pile displacements in the loading direction from plate elements

p-values:

1) Output of normal stresses and horizontal shear stresses from interface elements, both inside and outside the pile.
2) Numerical integration of components in the load direction to find resulting force in each element.
3) Numerical integration of resulting forces in each element around the pile and over a specified depth (p-y spacing) along the pile.
4) Summarize p-values from the inside and outside interface.

For extraction of p-values, points 2 and 3 are performed separately for the interface elements at the outside and at the inside of the pile, before they are summarized at each depth. To ensure that no errors are present in the procedure, the p-values are integrated over the pile length in order to check the horizontal equilibrium of the pile. For all of the calculations performed, the horizontal equilibrium is met with a tolerance in the order of the numerical tolerance in the FE code (1%) or less.

θ-values:

1) Output of horizontal and vertical pile displacements from plate elements. The horizontal displacement is taken as the component of the horizontal displacement in the load direction.

2) The displacements are assessed incrementally along the pile, and the difference in displacement between two neighboring depths (top and bottom of plate element) is used to calculate the angle with the vertical plane. The angle with the vertical plane is taken as the rotation of the element.

M-values:

1) Output of vertical shear stresses from the interface elements both inside and outside the pile.
2) Numerical integration of the vertical shear over each element to find the resulting vertical force in each element.
3) The vertical force in each element is multiplied with the distance of each element to the neutral axis.
4) Numerical integration of moment contributions from each element around the pile and over a specified depth (spring spacing) along the pile.

An example of extracted p-y curves from the base case calculation is shown in Figure 5-3. One curve is given for every meter, with the pile loaded to 50 MN in four steps for the linear elastic soil, and to 33 MN in seven steps for the linear-elastic, perfectly plastic soil. The curves giving the largest deflection are recognized as the upper portion of the rotating pile, while the curves in the third quadrant of the graph are below the rotation point of the pile. M-θ curves extracted from the same base case are shown in Figure 5-4.

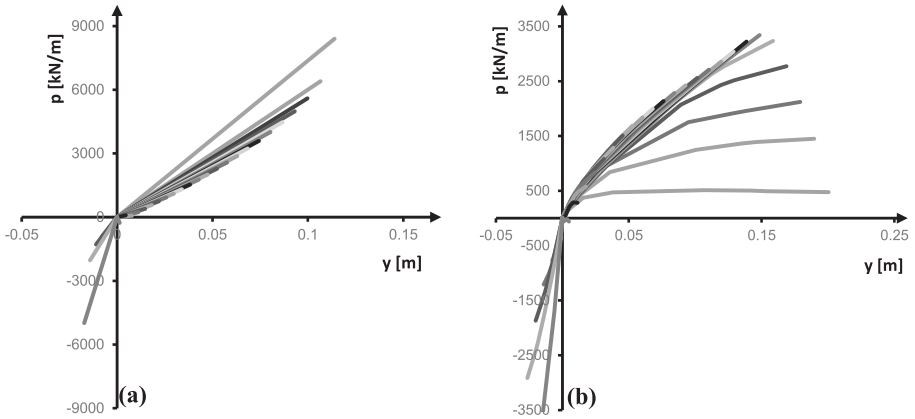

Figure 5-3. Extracted p-y curves from base-case. (a) Linear-elastic soil (b) Linear-elastic, perfectly plastic soil with the Mohr-Coulomb failure criterion.

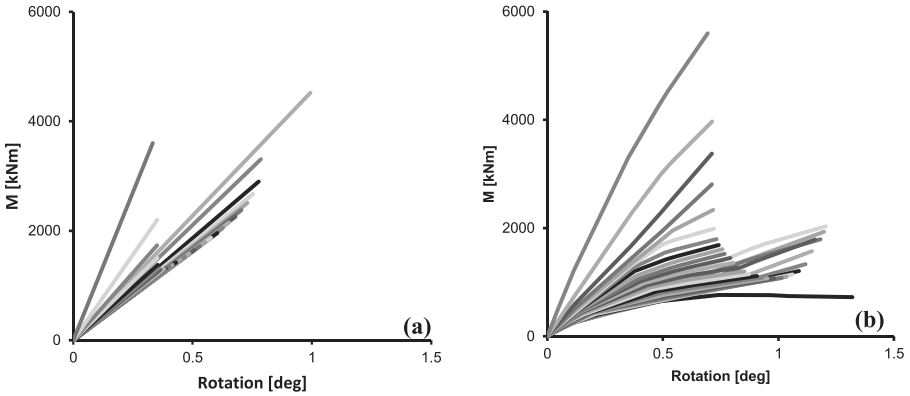

Figure 5-4. Extracted M-θ curves from base-case. (a) Linear-elastic soil (b) Linear-elastic, perfectly plastic soil with the Mohr-Coulomb failure criterion.

5.4 Initial Stiffness of p-y Curves

In Chapter 3, it was shown that the initial stiffness of p-y curves can be written on the form of Eq.(5-3):

$$\frac{p}{y} = \delta E_s \tag{5-3}$$

E_s is the Young's modulus of the soil, while δ is a dimensionless constant (or a function) relating the Young's modulus to the p-y stiffness. For the various δ-values and expressions listed in Chapter 3, different assumptions are made with respect to boundary conditions, foundation shape and end-effects.

The numerical investigation of initial stiffness is performed in order to quantify a constant or a function δ for the case of a cylindrical monopile with dimensions in the range applicable to foundations for offshore wind turbines. By expressing the stiffness of the extracted p-y curves as k = p/y, it follows from Eq.(5-3) that the numerical values of δ can be obtained by Eq.(5-4):

$$\delta = \frac{p/y}{E_s} = \frac{k}{E_s} \tag{5-4}$$

A material with the Mohr-Coulomb failure criterion and little to no cohesion will experience material yielding at very low load levels for low effective stress levels. The initial stiffness sought herein is the stiffness before any material point in the soil starts

to yield. To ensure that material yielding close to the soil surface does not influence the initial stiffens of the extracted curves, a linear-elastic soil model is considered appropriate when the initial stiffness of the curve is considered.

5.4.1 Young's Modulus of the Soil

Eq.(5-3) relates the p-y stiffness directly to the elastic stiffness of the soil. As a verification of Eq.(5-3), p-y curves are extracted from five different cases, where only the Young's modulus of the soil is varied. Geometry and soil are otherwise as described for the base case simulation with linear elastic soil in Table 5-1 and Table 5-2. Results are shown in Figure 5-5, where variations in δ are present near the center of rotation, otherwise the curves are congruent. From Figure 5-5, the p-y stiffness is seen to be a function of the soil stiffness E_s. With exception of the soil near the rotation point, Eq.(5-3) is concluded to be valid for soil with a homogeneous stiffness profile.

The analytical solution from Baguelin et al. (1977) is plotted in the same chart in order to compare the stiffness of the extracted curves with the stiffness from 2D theory. The 2D analytical solution does not account for 3D continuum effects at the pile ends or at the rotational point. For an L/D ratio of 5, these effects appear to be visible over the entire pile depth. A consequence for finite geometries is therefore that δ must be a function of distance to the edges and the point of rotation.

At and close to the rotational point there is a possibility of having force without displacement and/or displacement without force. As such, the stiffness definition k = p/y has no meaning at and close to the rotational point.

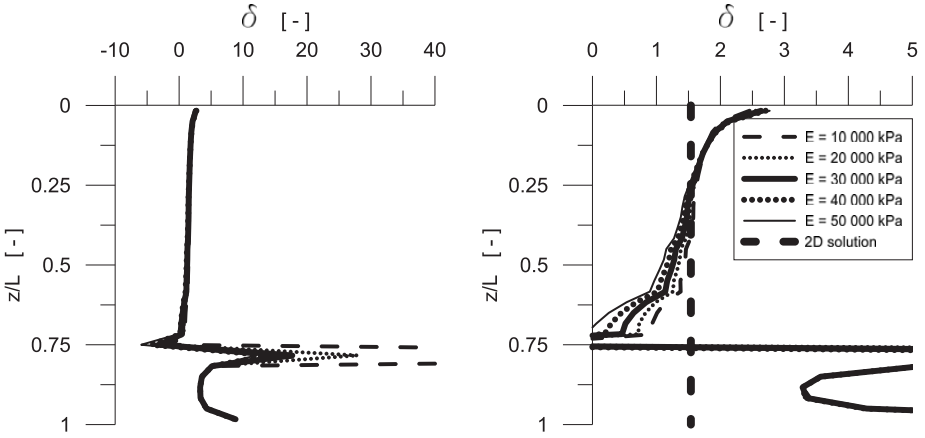

Figure 5-5. Comparison of δ for variations in Young's modulus of homogeneous soil. The same chart is shown in both plots, with different axis limits on the x-axis.

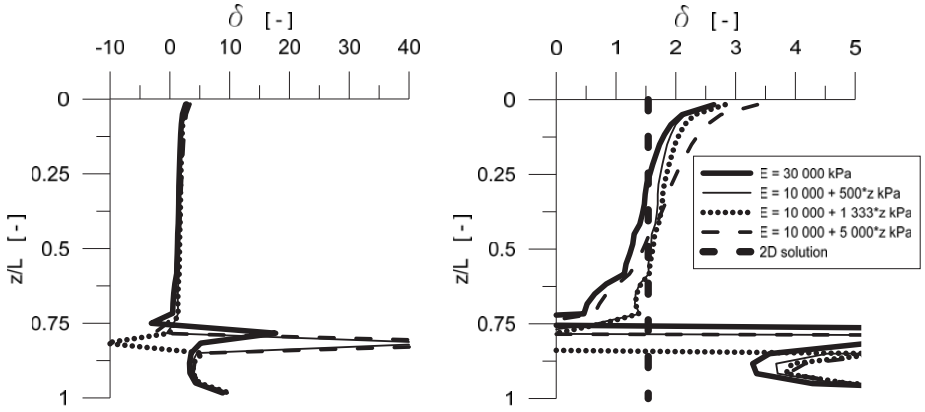

Figure 5-6. Comparison of δ -values for Gibson soil

Homogeneous stiffness profiles are typically associated with over-consolidated clays, while sands and normally consolidated clays are typically associated with stiffness that is increasing with depth. A linear increase in soil stiffness with depth is often referred to as Gibson soil (Gibson, 1967) and can be written in the form:

$$E_s = E_{s,0} + k_{Gibson} \times z \qquad \textbf{(5-5)}$$

$E_{s,0}$ is then the soil stiffness at ground surface level, k_{Gibson} is the rate of increase in soil stiffness with depth and z is the depth below ground surface. Figure 5-6 compare δ-values from four simulations where the stiffness profiles have different k_{Gibson}. The p-y stiffness at each depth is normalized with the Young's modulus of the soil at the same depth. Increasing soil stiffness with depth gives larger normalized p-y stiffness than the constant soil stiffness profile. The rate of increase is seen to influence the normalized p-y stiffness, with increasing normalized p-y stiffness for increasing $k_{Gibson.}$

While Gibson soil might be a good approximation for normally consolidated clays, the increase of stiffness with depth in sands is often approximated by square root functions. In Figure 5-7, the increase in stiffness with depth is modeled as a Janbu stiffness increase for sand (Janbu, 1963), defined as:

$$E_s = m^* p_a \left(\frac{\sigma'_v}{p_a} \right)^{0.5} \qquad \textbf{(5-6)}$$

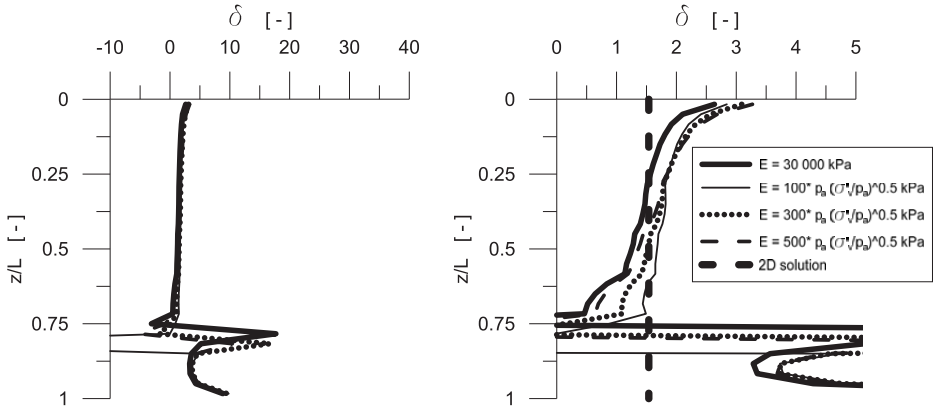

Figure 5-7. Comparison of δ-values for Janbu soil. p_a is the atmospheric pressure (100 kPa) and σ'_v the effective vertical stress.

where m^*[1] is a stiffness constant dependent on the soil type, p_a is atmospheric pressure of 100 kPa and σ'_v is the effective vertical stress. The nonlinear increase in soil stiffness with depth is seen to give an effect similar to the effect of linear increase: increasing normalized p-y stiffness for increasing rate of soil stiffness with depth. Eq.(5-3) can therefore only be considered as a crude approximation for stiffness profiles increasing with depth.

In addition to increasing soil stiffness with depth, the presence of different soil layers is often encountered for real soils. The effect of layering is investigated by comparing normalized p-y stiffness from the case of a stiff layer overlaying a soft layer and a soft layer overlaying a stiff layer, to the case of a homogeneous soil profile. The comparison is shown in Figure 5-8. Both the soft-stiff and the stiff-soft layering reveals a distinct effect of the layer boundary to the normalized stiffness. The soft-over-stiff combination gives an increase in normalized stiffness close to the layer boundary, while the stiff-over-soft combination gives a reduction in normalized stiffness close to the layer boundary. This is believed to be caused by internal shear effects in the soil (also referred to as continuum effects). The δ-values in Figure 5-8 are greatly affected by the layer boundary, as such, Eq.(5-3) is in the best case a crude approximation for layered soil profiles.

[1] Janbu (1963) defined the stiffness of sand through the constraint modulus M. To calculate the coefficient m*, the relation between Young's modulus and the constraint modulus from the theory of elasticity is used: $m^* = m(1+\mu)(1-2\mu)/(1-\mu)$

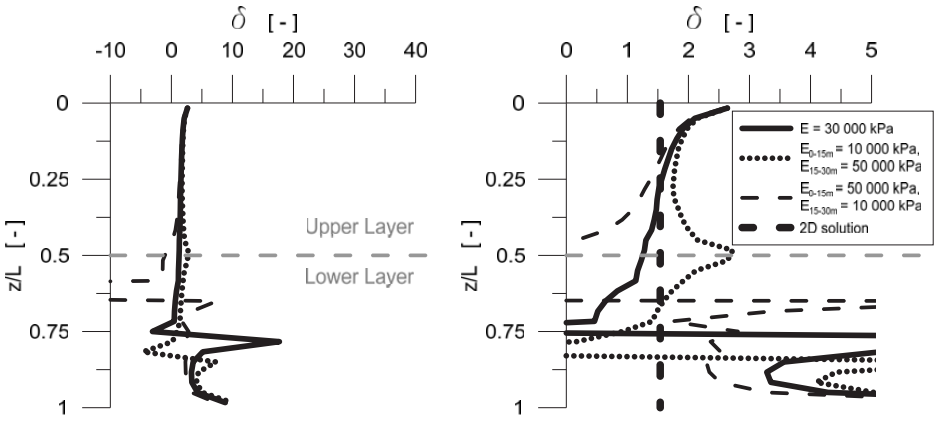

Figure 5-8. Comparison of δ-values for layered soil. Soft layer over stiff layer and stiff layer over soft layer. Homogeneous stiffness profile as reference.

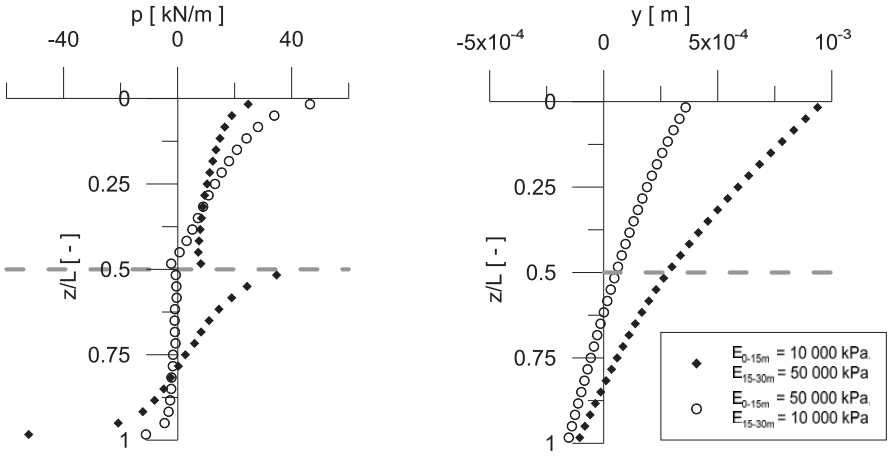

Figure 5-9. Comparison of extracted p- and y-values from soft-stiff and stiff-soft soil profiles. Horizontal load of 200 kN applied 1 m above ground surface.

In Figure 5-9, a comparison of the line load p against the displacement y along the pile length is shown for the two layered profiles from Figure 5-8. When comparing p- and y-profiles in Figure 5-9, it is seen that the reason for a negative normalized spring stiffness in Figure 5-8 relates to the depth of zero soil reaction. The depth of zero soil reaction is not corresponding to the depth of zero pile displacement. Such an effect is directly contradicting Winkler's hypothesis; however, close to the rotational point, the influence on the overall moment equilibrium of a pile is limited. For the stiff-over-soft case, negative p-y stiffness is observed for more than 10 % of the pile length. This implies that continuum effects that cause negative spring stiffness are not always limited to be close to the point of pile rotation, and might be of influence for certain

profiles of soil layering. The beam on Winkler foundation approach is not suited for structural/geotechnical design in these cases.

From the above studies of Figure 5-5 to Figure 5-9, it is concluded that Eq.(5-3) is reasonably accurate only for homogeneous soils. For non-homogeneous soils, influence from both rate of increase in soil stiffness with depth and soil layering is seen on the normalized p-y stiffness. This influence is believed to relate to 3D-continuum effects in the soil, not captured by the underlying 2D-theory for Eq.(5-3).

5.4.2 Parameters of Interest for δ

The fundamental assumption of Eq.(5-3) is that the p-y stiffness is a function of the Young's modulus of the soil. The parameter/function δ is however assumed to depend also on other parameters by different writers. Again, reference is made to Chapter 3, where δ is given as a function of one or several of the parameters: pile bending stiffness, pile diameter, Poisson's ratio of the soil and the pile L/D ratio. As discussed in the previous section, Eq.(5-3) is found inaccurate for non-homogeneous soil stiffness profiles. To be able to compare the influence of different parameters on the constant/function δ, a parameter study is performed where the Young's modulus of the soil is kept constant with depth. An overview of the parameters that are varied is shown in Table 5-3. The parameters are varied one by one, meaning that each cell (except for the BaseCase in bold) in Table 5-3 represents one variation.

Table 5-3. Parameter variations. Each cell defining one load case, giving a total of 24 load cases.

Parameter	Unit			BaseCase		
E_s	[kN/m^2]	10 000	20 000	**30 000**	40 000	50 000
μ	[-]	0.2	0.25	**0.3**	0.4	0.49
E_pI_p	[kNm^2]	4.94e7	2.47e8	**1.04e9**	3.95e9	7.90e9
D	[m]	2 3	4 5	**6**	7 8	9
L	[m]	10	20	**30**	35	40

In addition to the parameters discussed above, McGann et al. (2011) found the effects of pile-kinematics to the p-y stiffness from a numerical study. Ashour et al. (1998) and Ashour and Norris (2000) postulated the p-y stiffness to be dependent on pile head fixity, which again is believed to be directly related to the difference in pile kinematics. The pile kinematic effect is considered to be a continuum effect, and by definition not captured by 2D-theory. For the pile dimensions currently in use as monopile foundations in the context of offshore wind turbines, a rather rigid behavior is expected with limited variation in kinematic effects. However, it is seen in this study that when the pile bending stiffness is lowered and the pile acts like a slender pile, the presence of several deflection points influences the resulting soil resistance.

5.4.3 Soil Poisson's Ratio

The effect of the soil Poisson's ratio (μ) on the normalized p-y stiffness δ is given in Figure 5-10. The δ-curves are close to being congruent, showing limited effect of the Poisson's ratio on the normalized p-y stiffness, except for close to the point of rotation.

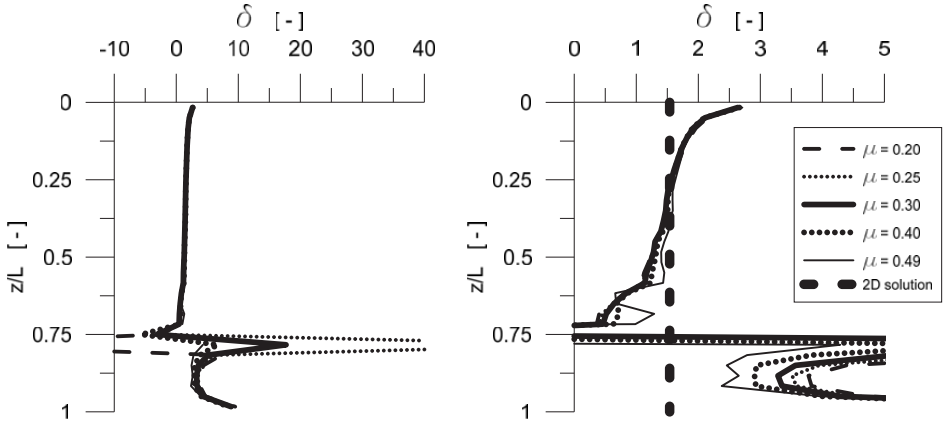

Figure 5-10. Comparison of δ-values for varying soil Poisson's ratio. 2D-solution from Baguelin et al. (1977) shown for μ = 0.3

5.4.4 Pile Bending Stiffness

The effect of the pile bending stiffness (E_pI_p) on the normalized p-y stiffness δ is shown in Figure 5-11. The pile bending stiffness is varied by changing the Young's modulus of the pile, while the pile geometry is kept constant. From Figure 5-11 it is seen that the pile bending stiffness has a noticeable effect on the normalized p-y stiffness δ, with increasing variation in δ for decreasing pile bending stiffness. Higher pile bending stiffness is also seen to give a normalized p-y stiffness closer to the stiffness from the 2D-solution by Baguelin et al. (1977). An effect of pile bending stiffness contradicts the 2D-theory discussed in Chapter 3, where pile bending stiffness is not included. As such, it is reasonable to believe that the influence from pile bending stiffness is related to 3D effects in the soil continuum.

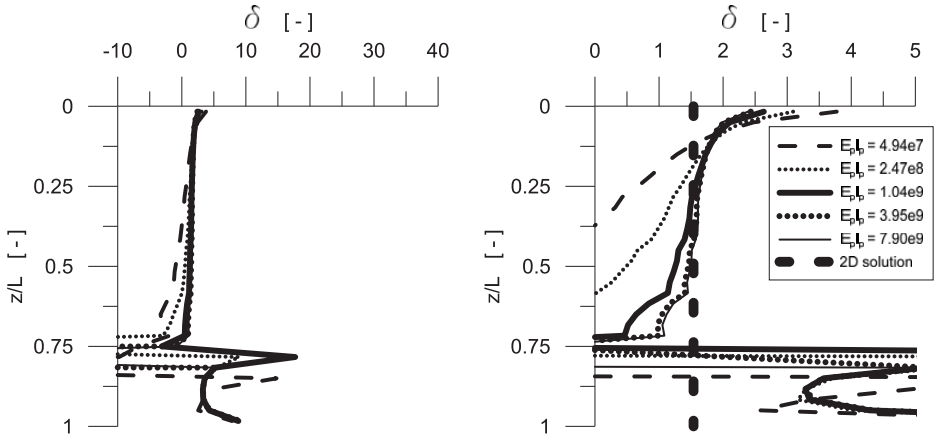

Figure 5-11. Comparison of δ-values for varying pile bending stiffness.

In the analytical solution for an elastic single-pile embedded in an elastic half-space by Poulos (1971), the displacements at the pile top includes a pile flexibility factor. The pile flexibility is defined as the pile bending stiffness divided by Young's modulus of the soil and the pile length to the power of four ($K_r=E_pI_p/(E_sL^4)$). The pile flexibility factor is a measure on the pile bending stiffness relative to the soil stiffness, implicitly saying something about the deformation shape of the pile. Let us assume that the observed change in p-y stiffness for changing pile bending stiffness is due to the relative stiffness described by Poulos (1971). Then, it is not the pile bending stiffness itself that influences the p-y stiffness, but the pile deformation shape. Different deformation shapes will distribute stresses differently in the 3-dimensional soil mass, making the p-y stiffness implicitly dependent on the pile bending stiffness. Hence, it is concluded that the normalized p-y stiffness is a function of the pile deformation shape. The deformation profiles corresponding to the normalized stiffness in Figure 5-11 are shown in Figure 5-12.

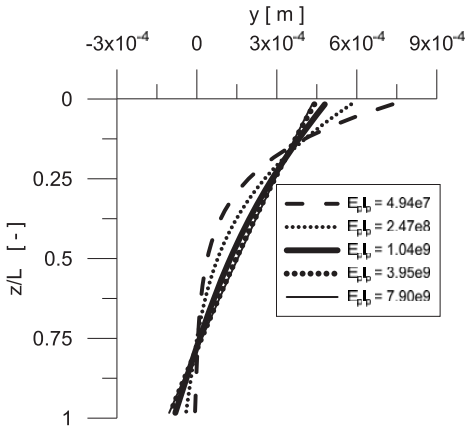

Figure 5-12. Deformation shapes for varying pile bending stiffness. Horizontal load of 200 kN applied one meter above ground surface.

5.4.5 Pile Diameter

The effect of the pile diameter on the normalized p-y stiffness δ is shown in Figure 5-13. The pile bending stiffness (E_pI_p) is kept constant for all variations of the pile diameter in order to rule out the effects of pile bending shape. The pile length is kept constant (30 m), introducing different L/D ratios. In Figure 5-13, differences in normalized stiffness are recognized close to the soil surface, close to the pile rotation point and close to the pile toe. At depths where the pile toe, pile top or rotation point are not nearby, no effects of pile diameter is observed.

In Figure 5-14, the pile depth is normalized on the pile diameter. The normalized soil stiffness close to the soil surface appears to be influenced of an end effect, dependent on the pile diameter. This end effect is visible down to approximately 1 pile diameter (1D) below the soil surface.

A similar approach is followed in Figure 5-15, where the normalized p-y stiffness is aligned at the pile toe for the different L/D ratios. The normalized stiffness appears to be influenced by an end-effect dependent on the pile diameter to approximately 1 pile diameter (1D) above the pile toe.

Both the end effect at the top and at the toe of the pile result in an increased normalized stiffness compared to the prediction from the 2D-solution.

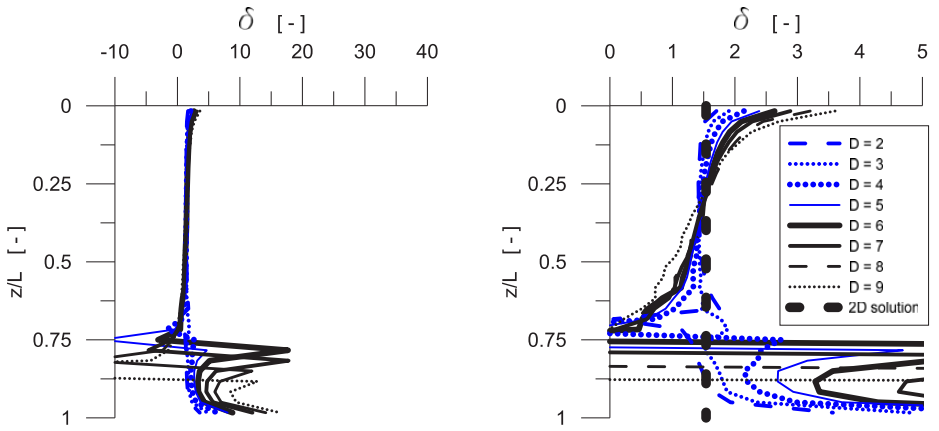

Figure 5-13. Comparison of δ-values for varying pile diameters. Pile bending stiffness kept constant.

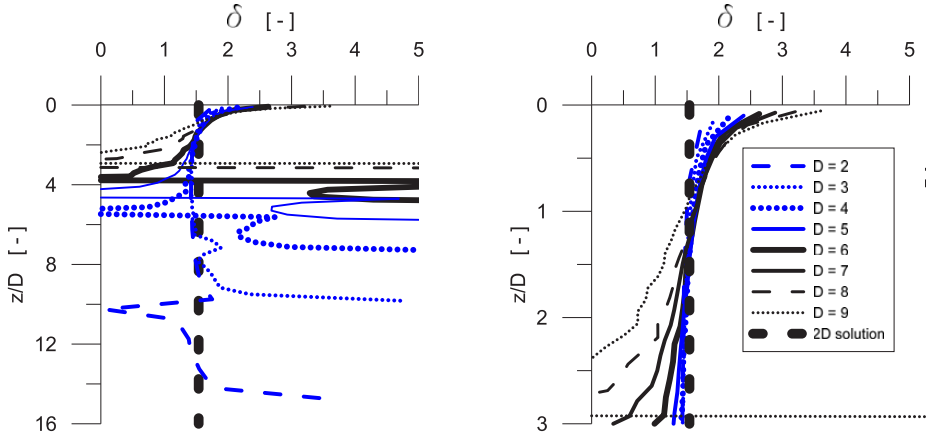

Figure 5-14. Comparison of δ-values for varying pile diameters. Depth normalized on pile diameter. The pile bending stiffness kept constant. The normalized p-y stiffness is seen to be influenced by end effects down to approximately 1 pile diameter below soil surface.

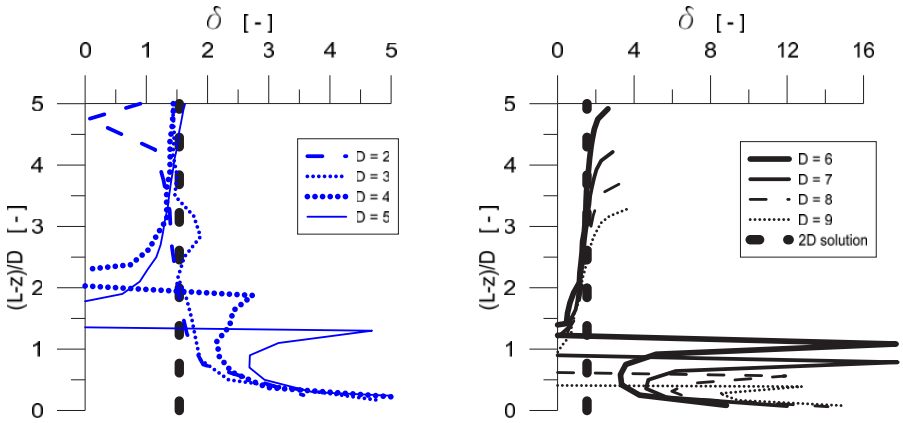

Figure 5-15. Comparison of δ-values for varying pile diameters. Stiffness profiles aligned at pile toe and pile depth is normalized on pile diameter. The pile bending stiffness is kept constant. The normalized p-y stiffness is seen to be influenced by end effects approximately up to 1 pile diameter above pile toe.

5.4.6 Pile Length

The effect of the ratio between the pile length and pile diameter on the normalized p-y stiffness δ is illustrated in Figure 5-16. The piles with the lowest L/D ratios show the effect of pile length on the normalized stiffness. In the previous section, end effects were described to appear approximately one diameter above the pile toe and one diameter below the pile top. Therefore, piles with low L/D ratios have a proportionally larger influence from the pile ends. The 10 m long pile has an L/D ratio of 1.67, meaning that end effects are affecting the entire pile. The rotation point for the 10 m pile is below the pile toe, and negative stiffness is mobilized close to the pile toe. It should be noted that an L/D of 1.67 is outside the geometrical range of what normally is denoted a "pile". With the exception of the 10 m pile, no effects of pile length are seen at the normalized p-y stiffness for the top end. A minor effect, believed to be negligible, is observed for the normalized stiffness at the pile toe.

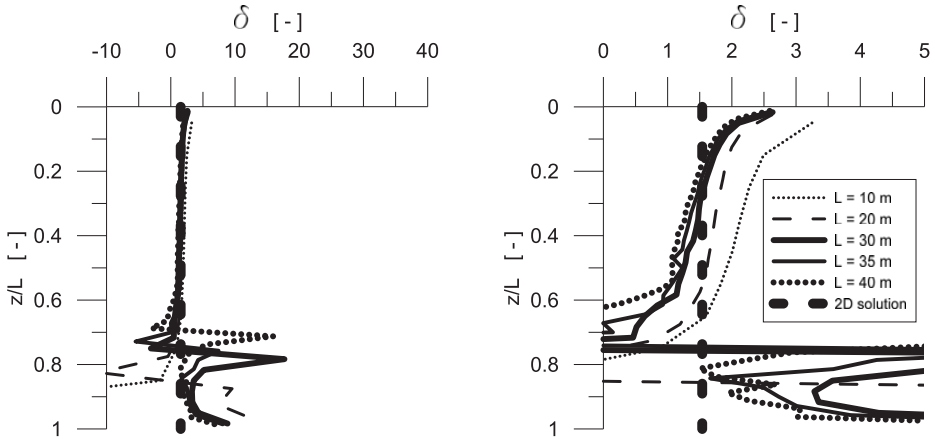

Figure 5-16. Comparison of δ-values for varying pile lengths. Pile diameter kept constant at D = 6 m.

5.4.7 End Effects at Pile Top

All plots of normalized p-y stiffness presented in Section 5.4 show increased stiffness at the pile top compared to further down the pile. The horizontal stiffness at the pile top is also higher than the plane strain solution for a rigid disc moved laterally in an elastic medium from Baguelin et al. (1977). The stiffness reduces gradually to the plane strain solution at a depth approximately one pile diameter below the pile top, as shown in Figure 5-14.

At first sight, increased horizontal stiffness at the pile top might seem counter-intuitive. If, however, the soil is simplified as a stack of rigid blocks, the increased p-y stiffness can be explained by shear forces between the blocks. This is sketched in Figure 5-17. A block at arbitrary depth will experience shear from the difference in displacement to the neighboring blocks. The neighboring block above will have a larger displacement than the block in question, and contribute with a shear force in the displacement direction. The block below the block in question will have less displacement and contribute with a shear force opposite of the displacement direction. For the block at the top end of the pile, no shear force in load direction from above blocks is present. The upper block will therefore provide more resistance to pile movement than the blocks below it.

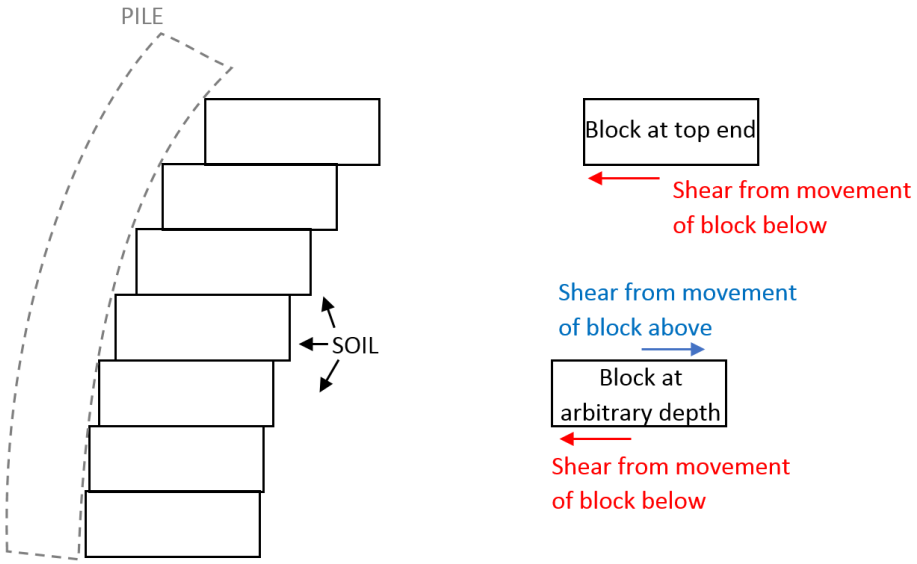

Figure 5-17. Soil simplified as a stack of rigid, homogeneous blocks with internal shear forces between.

The hypothesis that the increased stiffness at the pile top can be explained by internal shear effects in the soil is further supported by the observations in Figure 5-6 and Figure 5-7. The top end stiffness is seen there to be dependent on the rate of increase in stiffness with depth. In Figure 5-11, a dependency of the top end stiffness to the difference in pile deformation mode is visible, also supporting the hypothesis. Figure 5-13 shows a distinct dependency on pile diameter, with an increased normalized stiffness at the pile top with increasing pile diameter.

Figure 5-18 shows the stiffness at the pile top from Figure 5-13 plotted against the pile diameter. The relationship between the normalized pile stiffness and the pile diameter can be approximated by Eq.(5-7).

$$\frac{k_{top}}{E_s} = \frac{2}{(1+\mu)} + 0.065\left(\frac{D}{D_{ref}}\right)^{1.56} \qquad \textbf{(5-7)}$$

where

k = lateral spring stiffness
E_s = soil Young's modulus
D = pile diameter
D_{ref} = 1 m

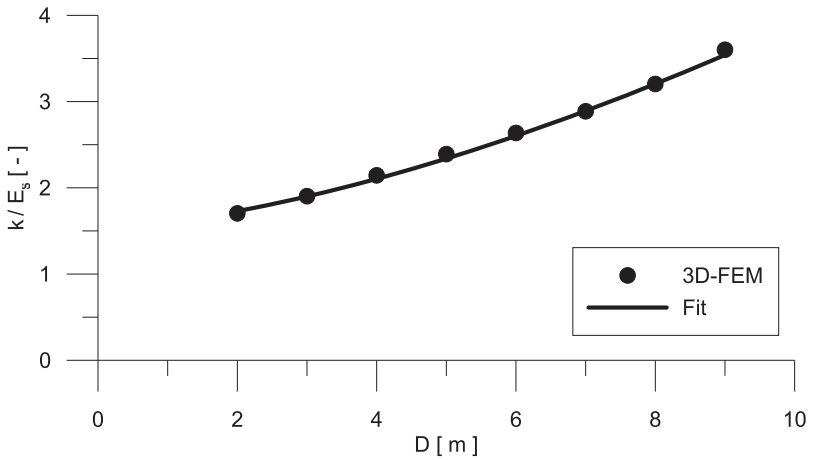

Figure 5-18. Normalized stiffness at the pile top from Figure 5-13. Fitted line given by Eq. (5-7). R^2-value from nonlinear least square fitting is $R^2 = 0.9981$.

5.4.8 p-y Curve at Pile Toe

All plots of normalized p-y stiffness presented in Section 5.4 demonstrate increased stiffness at the pile toe compared to the normalized stiffness elsewhere along the pile. The horizontal stiffness at the pile toe is also higher than the plane strain solution. The stiffness increases gradually from the plane strain solution at a depth approximately one pile diameter above the pile toe, to its maximal value at the pile toe. This is shown in Figure 5-15.

The increase in normalized stiffness at the pile from Figure 5-13 and Figure 5-16 is seen to be dependent on both the pile diameter and the pile length. The stiffness is increasing with increasing pile diameter and decreasing with increasing pile length. When the normalized stiffness at the pile toe is plotted against the pile L/D ratio in Figure 5-19, a distinct trend of increasing normalized stiffness with decreasing L/D ratio is visible. The relation between the bottom spring stiffness and the pile L/D ratio can be approximated by Eq.(5-8).

$$\frac{k_{bottom}}{E_s} = \frac{2}{(1+\mu)} + 80\left(\frac{L}{D}\right)^{-1.4} \qquad \textbf{(5-8)}$$

where

k = lateral spring stiffness
E_s = soil Young's modulus
D = pile diameter
L = pile length

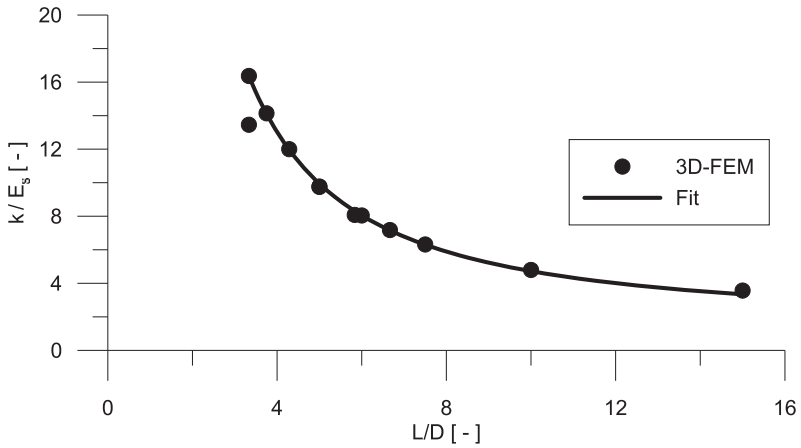

Figure 5-19. Normalized p-y stiffness at the pile toe from Figure 5-13 and Figure 5-16. Fitted line given by Eq.(5-8). R^2-value from nonlinear least square fitting is $R^2 = 0.9728$.

5.4.9 Initial Stiffness of p-y Curves – Summary

For homogeneous stiffness profiles Eq.(5-3) is found relevant, i.e. the p-y stiffness is directly related to the soil stiffness by a factor δ. Where end-effects or effects of the rotational point are not present, the stiffness is found to compare well with the 2D-solution for a rigid disc moved laterally. End effects from the pile top and pile toe are seen to influence the p-y stiffness to approximately 1 diameter below the pile top and 1 diameter above the pile toe. Effects of the rotation point are seen at a distance of approximately 0.5D at each side of the rotation point.

For non-homogeneous soil profiles, the effects of layering and rate of change in soil stiffness with depth are seen to influence the normalized p-y stiffness. Consequently, Eq.(5-3) is only approximately correct if the soil profile is non-homogeneous. The degree of approximation varies with the degree of non-homogeneity, and variation in normalized stiffness of up to 100 % are observed in the presented work.

When end-effects are disregarded, the normalized, initial p-y stiffness is seen to be independent of pile diameter. The normalized stiffness is however seen to be dependent on pile length and pile deformation shape.

The 2D-solution is not found capable to capture the exact stiffness response from the 3D model. However, if the effects from pile ends and the pile rotation point are disregarded, the 2D solution is seen to predict the stiffness with an error less than 20 % compared to the 3D-simulations.

5.5 Ultimate Resistance of p-y Curves

In Chapter 3, different analytical and empirical solutions for ultimate resistance of p-y curves were listed and discussed. In the numerical study presented, ultimate resistance is defined as when the p-y curve has a tangential stiffness of zero ($dp/dy \approx 0$), ref. Figure 5-20.

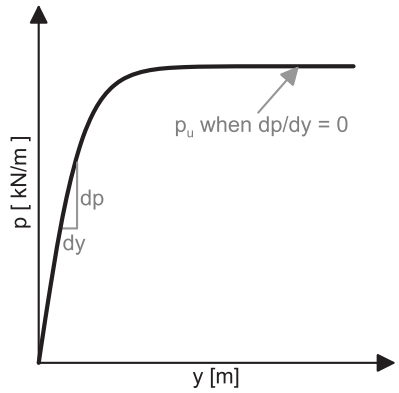

Figure 5-20. Definition of ultimate resistance (p_u).

5.5.1 Undrained Ultimate Resistance

A single-pile loaded at or above ground surface will deform with one or more points giving zero displacements along the pile depth. As seen from the numerical investigation of initial stiffness, typical dimensions for offshore wind foundations tend to give a rotational behavior of the entire pile, with only one point of zero displacement. A rotational behavior gives limited lateral displacements at and near the rotational point; meaning that a top-loaded pile never will mobilize ultimate lateral resistance over the entire pile length simultaneously. To be able to evaluate the ultimate lateral resistance at any depth, simulations are run where the entire pile is moved laterally in the soil. To ensure translational movement of the entire pile, a uniform prescribed displacement is given at pile center over the pile depth, and the pile is modeled with volume elements of very high stiffness. The use of a stiff volume pile for translational movement is to avoid local distortions of the pile structure from the prescribed displacements.

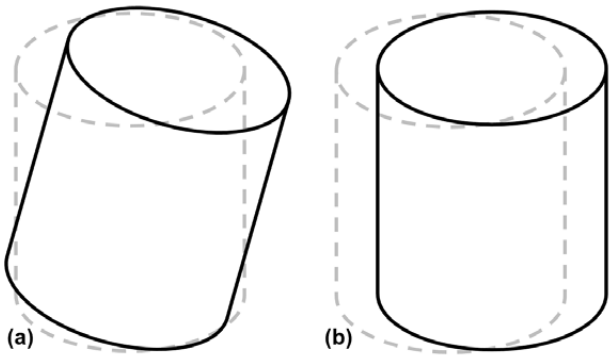

Figure 5-21. (a) Rotational movement for top-loaded pile. (b) Translational movement of pile.

A limitation with the FE code used in the analyses is that it does not create perfectly circular structural elements, but approximate curved lines as piecewise linear lines. For the special case of a laterally loaded cylinder, the kinematic admissible failure surface is the surface that goes through the nearest stress points in the soil elements adjacent to the pile (Plaxis BV, 2011). Hence, the pile-soil interface roughness in the performed study is always equal to 1, and the effective pile diameter is slightly larger than the structural diameter. The practical implication is that the ultimate resistance will be slightly overestimated.

A parametric study is performed for both the rotational and the translational pile movement. The bearing capacity factor is compared for three different pile diameters, three cases of uniform soil strength, three cases of increasing soil strength with depth and two cases of soil layering, as listed in Table 5-4.

Table 5-4. Parameter variations. Each cell defining one load case, giving a total of 10 load cases.

Parameter	Unit		BaseCase		
E_s	[kN/m^2]		**30 000**		
μ	[-]		**0.495**		
E_pI_p (rotational movement)	[kNm^2]		**1.04e9**		
D	[m]	3	**6**	9	
L	[m]		**30**		
c_u, constant	[kPa]	10	**30**	50	
c_u, lin. incr.	[kPa]	10+1.3z		10+3z	10+5z
c_u, two layer system	[kPa]	50/10		10/50	

The undrained ultimate shear strength is modeled with a Tresca failure criterion, where the governing soil parameter is the undrained shear strength c_u. The pile-soil interface roughness α is taken as 1. In Chapter 3, it was shown that the ultimate resistance of a p-y curve in clay can be written in the form:

$$p_u = N_c c_u D \tag{5-9}$$

where

p_u = ultimate resistance of p-y curve
N_c = dimensionless, undrained bearing capacity factor
c_u = undrained shear strength
D = pile diameter

When p-y curves are extracted from 3D-FE simulations, the ultimate resistance, the undrained shear strength and the pile diameter are known quantities. The bearing capacity factor is found by normalizing the ultimate resistance on the pile diameter and the undrained shear strength. An FE-simulation will converge towards the correct solution from above with increasing mesh refinement for an ultimate capacity calculation. The total overshoot in the results for the calculations here will be governed by the size of the effective pile diameter and fineness of the mesh, and is evaluated by comparison with the 2D solution from Randolph and Houlsby (1984).

Deep Pile Sections

The 2D-solution from Randolph and Houlsby (1984) is considered correct for all practical purposes. For a soil-pile interface roughness of $\alpha = 1$, the solution from Randolph and Houlsby (1984) gives an N_c-value of 11.94 for the plane strain case. For the ultimate resistance of p-y curves in clay, focus has been on the ultimate resistance close to the pile ends.

Pile Sections near the Soil Surface

For the near-surface failure mode, several solutions were presented in Chapter 3. The two solutions seen to perform best in this study are the one from Murff and Hamilton (1993) and the one from Yu et al. (2015). Both of them adopt the solution from Randolph and Houlsby (1984) at greater depths. The solutions are plotted against the N_c-values found from the 3D-FE simulations, together with the solution from Matlock (1970). In contrast to the first two solutions, the solution from Matlock (1970) is limited upwards by a value of $N_c = 9$ at greater depths (plane strain conditions). The solution from Matlock (1970) is however the solution adopted by design guidelines, and is used as a reference value. The three different solutions are all based on different failure geometries, and repeated in Eq.(5-10) for convenience.

Matlock (1970):

$$N_c = 3 + \frac{\gamma' z}{c} + \frac{Jz}{D} \qquad \textbf{(5-10a)}$$

Murff and Hamilton (1993):

$$N_c = \left(N1 - N2 \exp(-\frac{\xi z}{D}) \right) + \frac{\gamma' z}{cD} \qquad \textbf{(5-10b)}$$

Yu et al. (2015)

$$N_c = N_1 - (1-\alpha) - (N_1 - N_2)\left[1 - \left(\frac{z}{14.5D} \right)^{0.6} \right]^{1.35} + \frac{\gamma' z}{c_u} \qquad \textbf{(5-10c)}$$

Undrained Shear Strength

Eight simulations with different undrained shear strength are performed. Figure 5-22 shows the calculated N_c-value for three different homogeneous shear strength profiles, compared to the failure criteria given in Eq.(5-10). For homogeneous shear strength, the rotational pile movement is seen to mobilize more soil resistance close to the soil surface compared to the translational movement. The solution from Murff and Hamilton (1993) is seen to predict the capacity closest to the simulation results, while the solution from Yu et al. (2015) predicted less resistance.

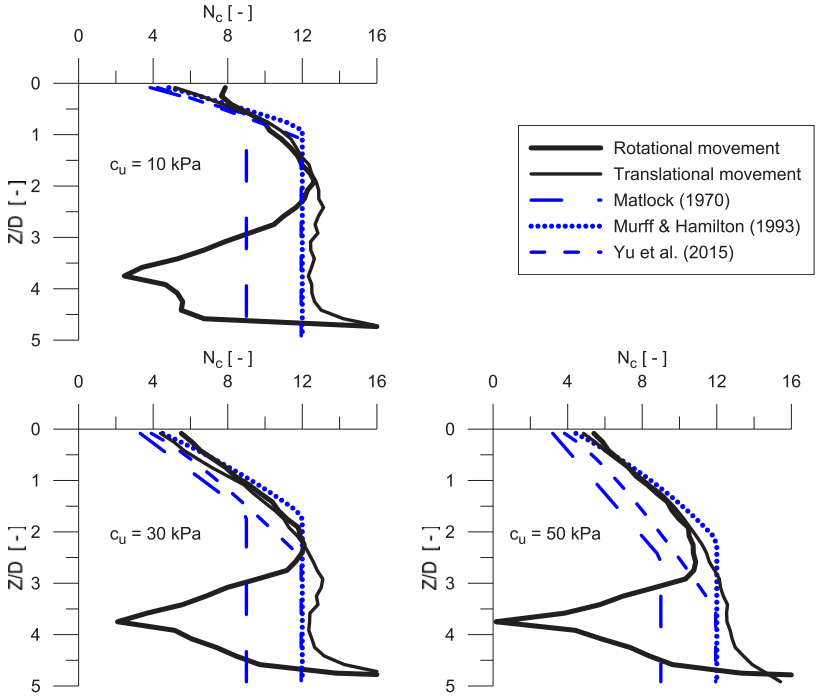

Figure 5-22. Comparison of bearing capacity factor N_c for homogeneous shear strength profiles.

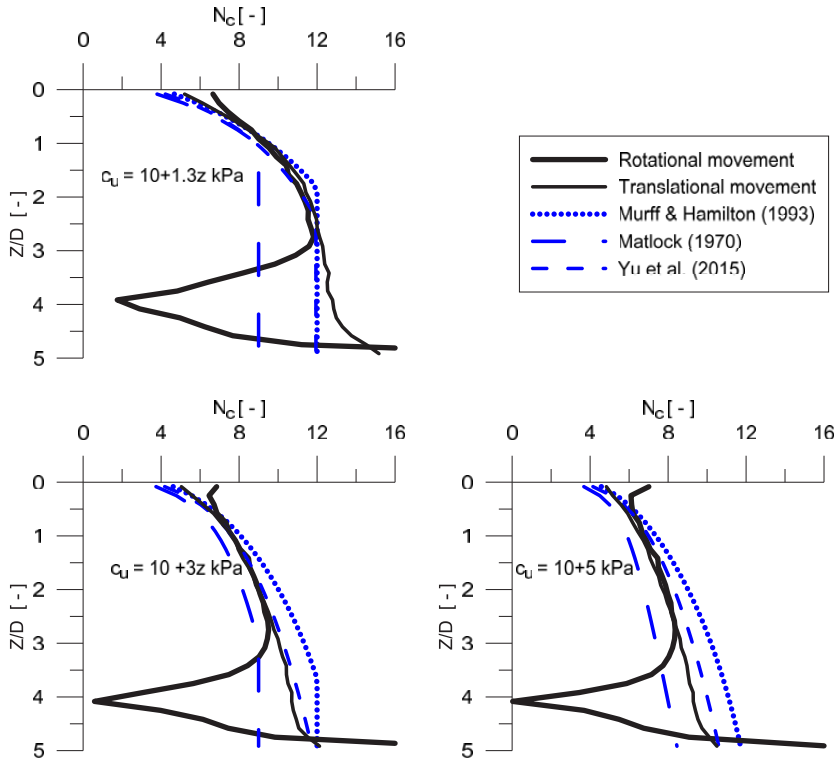

Figure 5-23. Comparison of bearing capacity factor N_c for linearly increasing shear strength profiles.

Figure 5-23 shows the calculated N_c-factor for three different profiles of linearly increasing shear strength. When the shear strength is increased linearly with depth, the solution from Yu et al. (2015) is considered to provide the best fit. The solution from Murff and Hamilton (1993) predicts an ultimate resistance higher than the one found from the 3D-FE simulations.

The N_c-value calculated from simulations involving soil layering is shown in Figure 5-24. Continuum effects from internal shear in the soil are believed to reduce the soil resistance from the stronger layer and increase the resistance from the weaker layer. The soil layering is seen to affect the bearing capacity factor at a distance of approximately one pile diameter (1D) above the layer boundary, and 1D below the layer boundary.

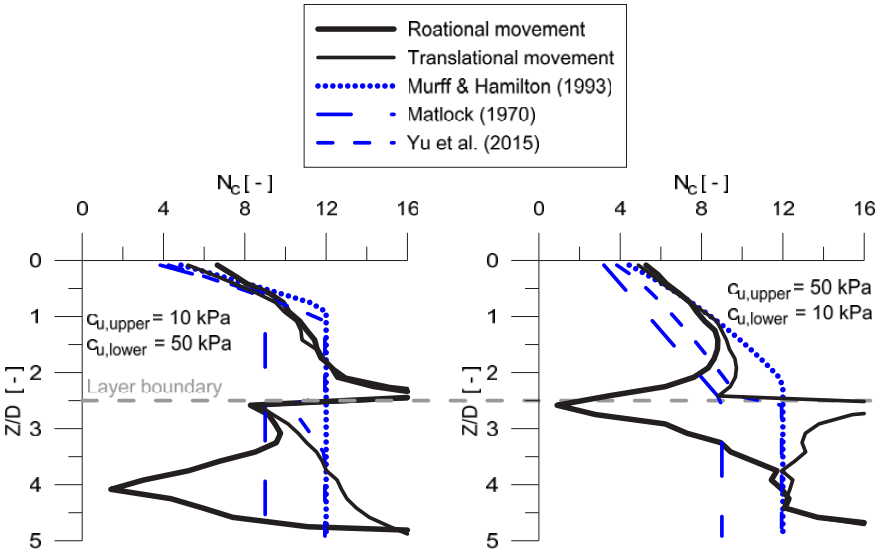

Figure 5-24. Comparison of N_c-value for layered soil.

Pile Diameter

Simulations are performed for three different pile diameters. The pile length is kept constant at L = 30 m. The bearing capacity factor N_c found from 3D-FE simulations is compared with the solutions from Yu et al. (2015) and Murff and Hamilton (1993) in Figure 5-25. For homogeneous shear strength, the size of the pile diameter does not appear to affect the predicted bearing capacity factor.

Undrained Ultimate Resistance at the Pile Toe

The bearing capacity factor at the pile toe is observed to be higher than the plane strain solution from Randolph and Houlsby (1984) for all the simulations presented above. The increase starts approximately 0.5D above the pile toe and increases almost linearly to a peak value at the pile toe. In Figure 5-26, the bearing capacity factor at the pile toe is plotted against the pile diameter (a) and against the undrained shear strength (b). The increase in N_c is larger for the rotational movement of the pile, compared to the translational movement. For the rotational pile movement, N_c varies from 17 to 36 for the performed simulations, while N_c for translational pile movement varies from 10 to 20. No exact relationship is found between the bearing capacity factor at pile toe and pile diameter/undrained shear strength.

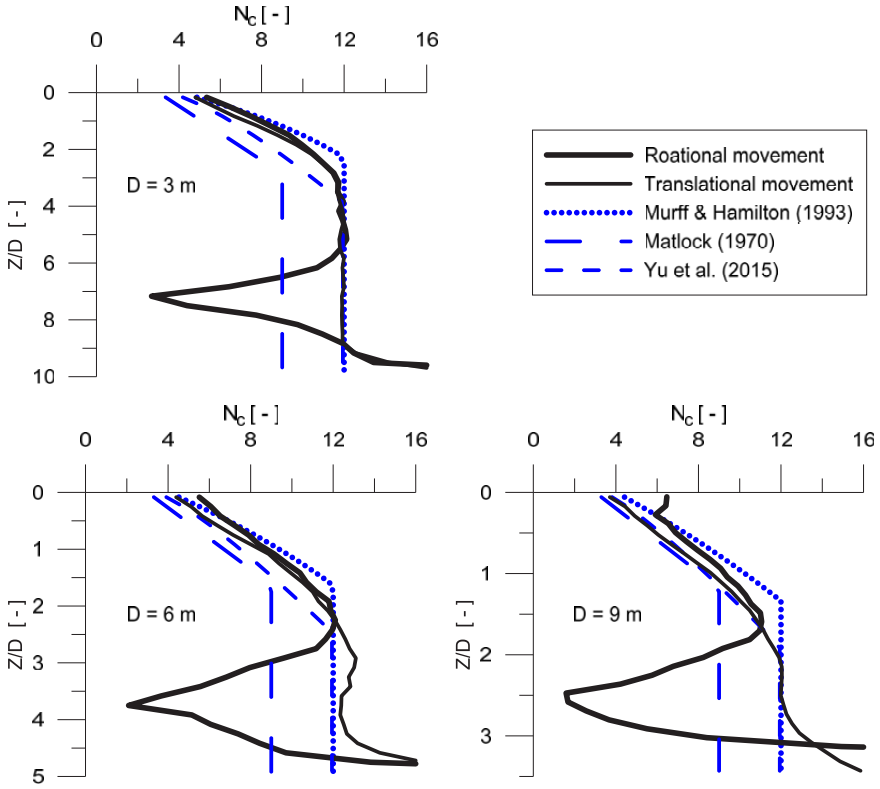

Figure 5-25. Comparison of bearing capacity factor N_c for different pile diameters. Homogeneous soil shear strength c_u = 30 kPa.

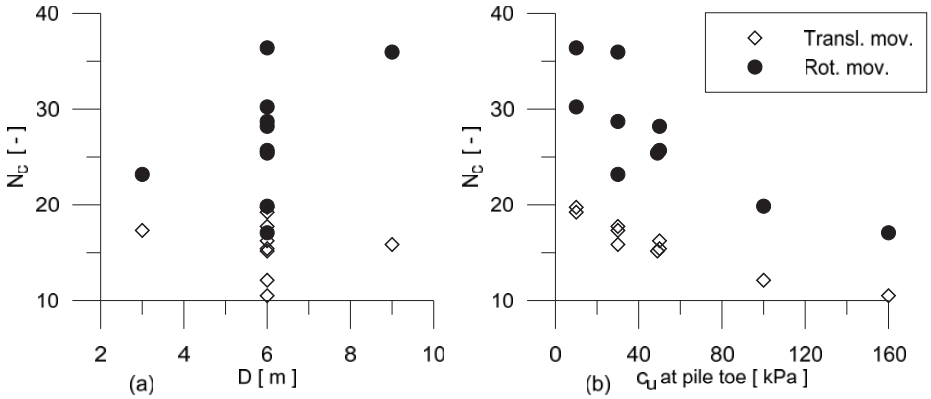

Figure 5-26. Bearing capacity factor N_c at the pile toe from simulations presented in Figure 5-22 to Figure 5-25. (a) Against pile diameter (b) Against undrained shear strength c_u at the pile toe

Ultimate Resistance for p-y Curves in Clay – Summary

Ultimate resistance for p-y curves for clay is extracted from 3D-FE simulations and compared to the analytical solutions from Matlock (1970), Murff and Hamilton (1993) and Yu et al. (2015). The 3D-FE simulations are performed for both rotational and translational pile movement. Both the solution from Murff and Hamilton (1993) and Yu et al. (2015) have adopted the plane strain solution from Randolph and Houlsby (1984) with depth.

The solution from Murff and Hamilton (1993) is considered to provide the overall best fit to the ultimate resistance found from the presented simulations. It is however predicting higher resistance than the 3D-FEM at several occasions. The solution from Yu et al. (2015) is considered to predict lower ultimate resistance than the ultimate resistance derived from the 3D-FEM, and to perform better than the Murff and Hamilton (1993) solution for linearly increasing shear strength. The solution from Matlock (1970) is seen to consequently underpredict the ultimate resistance for all the performed simulations.

Due to the limitations of the FE model, results from the FE simulations can be expected to be higher than the "real" ultimate resistance. Although the solution from Murff and Hamilton (1993) provided the overall better fit for the performed simulations, it did over-predict the ultimate resistance at several occasions. The solution from Yu et al. (2015) was consequently on the correct side of the ultimate resistance found from the 3D-FEM, and might therefore be better suited for pile design in practice. None of the solutions account for continuum effects from layer boundaries.

At the pile toe, the bearing capacity factor is observed to be higher than all the analytical solutions discussed previously, including the plane strain solution from Randolph and Houlsby (1984). The increased bearing capacity was observed from approximately half a diameter above the pile toe, and increasing almost linearly to a peak value at the pile toe.

5.5.2 Ultimate Resistance of p-y Curves for Sand

In contrast to the simulations performed for the ultimate resistance of piles in clay, the simulations for sand are limited to rotational pile movement. For soils with a Mohr-Coulomb failure criterion, the ultimate resistance is dependent on the effective stress level, and the effective stress level is increasing with depth due to the eigen weight of the soil. This gives an increasing ultimate resistance with depth, which implies that the weaker, near surface soil will reach failure first. For the typical load regime of offshore monopile foundations, the ultimate resistance at greater depths is believed to be of

Table 5-5. Parameter variations. Each cell defining one load case, giving a total of 8 load cases.

Parameter	Unit				BaseCase		
E_s	[kN/m^2]				**50 000**		
μ	[-]				**0.3**		
E_pI_p	[kNm^2]				**1.04e9**		
D	[m]			3	**6**	9	
L	[m]				**30**		
φ	[°]	20	25	30	**35**	40	45
c	[kPa]				**0.1**		

minor importance. In order to limit the computational effort[2], emphasis has been given to the shallow failure mode.

An overview of the simulations performed for the performed parameter study is given in Table 5-6. With the exception of the base case parameters in bold, each cell is defining one load case. The ultimate resistance for near-surface cohesionless soil is investigated for five different friction angles and three different pile diameters.

The drained ultimate shear strength is modeled with a Mohr-Coulomb failure criterion, where the governing soil parameter is the internal angle of friction (φ), the cohesion (c) and the post-peak dilatancy angle (ψ). The pile-soil interface roughness α is taken as 1. By not including cohesion and dilatancy into the simulations, the resulting ultimate resistance is considered to be on the conservative side, compared to actual soil behavior.

In Chapter 3, both analytical and empirical expressions were presented for the shallow failure mode. Reese et al. (1974) gave a semi-empirical solution, considering a wedge shaped geometry of soil moving up and away from the pile. An analytical solution was derived from the assumed failure geometry and compared to measurements from a full-scale pile test. An empirical factor was assigned to the analytical solution in order to describe the results from this pile test. Broms (1964) and Fleming et al. (1992) suggested empirical approaches, relating the ultimate resistance for shallow pile sections to the Rankine passive soil pressure. These solutions are repeated in Eq.(5-11) for convenience.

[2] The simulations are aborted before the ultimate capacity of the entire pile is reached. The simulations have been aborted when (at least) the upper five meters of the soil profile meets the criteria for ultimate resistance defined in Figure 5-20. Average calculation time of the aborted calculations is 19 hours.

Broms (1964):

$$p_u = 3K_p D\,\gamma' z \tag{5-11a}$$

Fleming et al. (1992):

$$p_u = K_p^2 D\,\gamma' z \tag{5-11b}$$

Reese et al. (1974)

$$p_u = A\gamma' z\left[\frac{K_0 z\tan\varphi\sin\beta}{\tan(\beta-\varphi)\cos\alpha}+\frac{\tan\beta}{\tan(\beta-\varphi)}(D+ z\tan\beta\,\tan\alpha)+K_0 z\tan\beta\,(\tan\varphi\sin\beta-\tan\alpha)-K_a D\right] \tag{5-11c}$$

For the deep failure mode, the ultimate resistance from Reese et al. (1974) is seen to correspond well with the frictional part of the ultimate resistance from Meyerhof (1951) when β =15°. The expressions for the deep failure mechanism from Reese et al. (1974) and the frictional part of the solution from Meyerhof (1951) can both be written on the form:

$$p_u = N_q\,\gamma' z\,D \tag{5-12}$$

where

p_u = ultimate resistance of p-y curve
N_q = dimensionless, bearing capacity factor (given in Chapter 3)
γ' = effective unit weight of soil
z = depth below ground surface
D = pile diameter

Pile Diameter and Soil Friction Angle

p-values normalized on the pile diameter and the vertical effective stress is shown in Figure 5-27 and Figure 5-28. Figure 5-27 shows results for different pile diameters, while Figure 5-28 presents results for different soil friction angles. Since the simulations are aborted before ultimate capacity for the entire pile is reached, the results from the 3D-FEM is only representing ultimate resistance at the very top of the soil profile. The simulations do however give a clear indication of the performance of the different expressions given in Eq.(5-11).

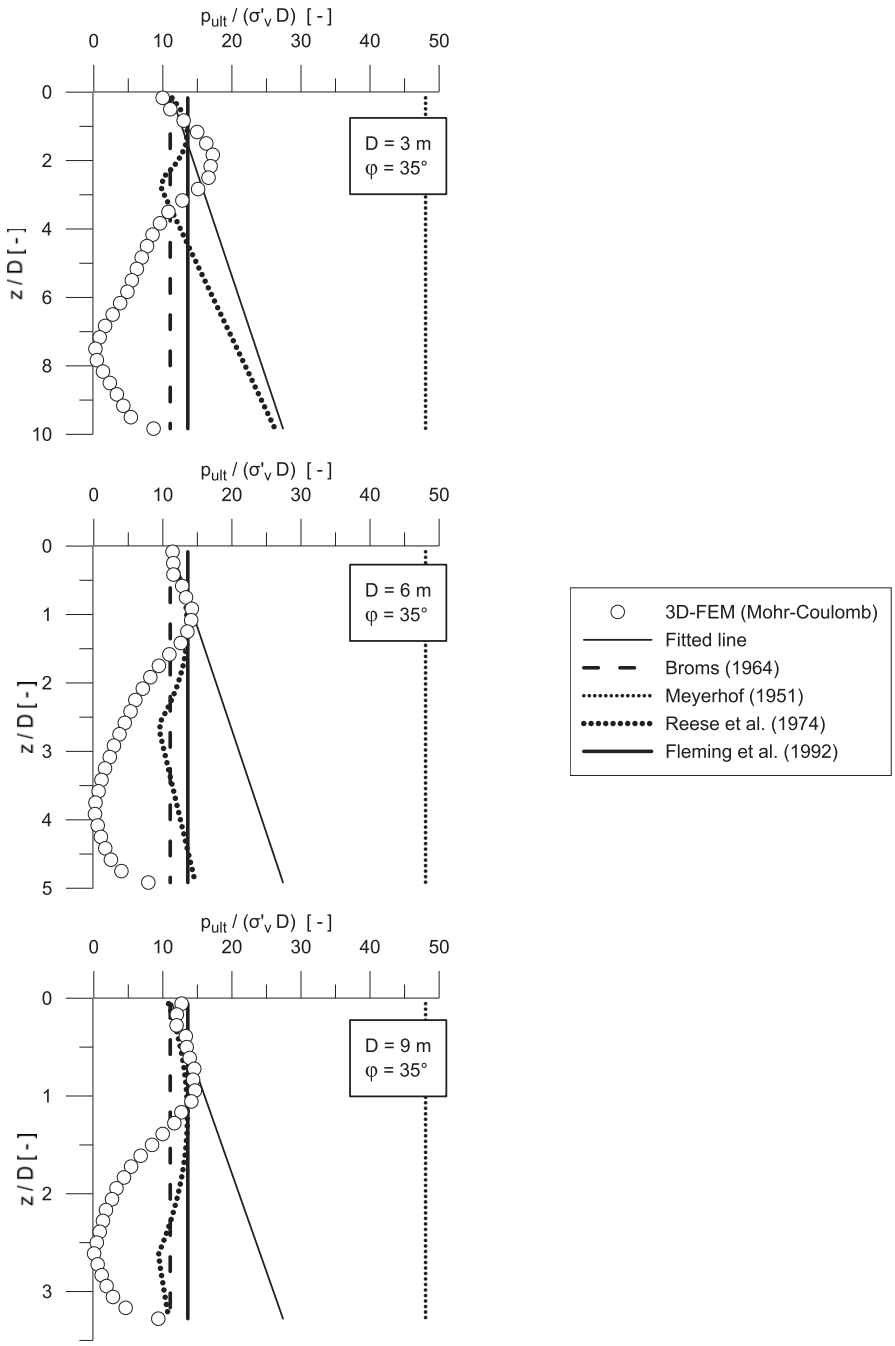

Figure 5-27. Variation of pile diameter. Normalized mobilized resistance from 3D-FE simulations compared to analytical and empirical solutions for ultimate resistance found in the literature. Equation for fitted line given in Eq.(5-13).

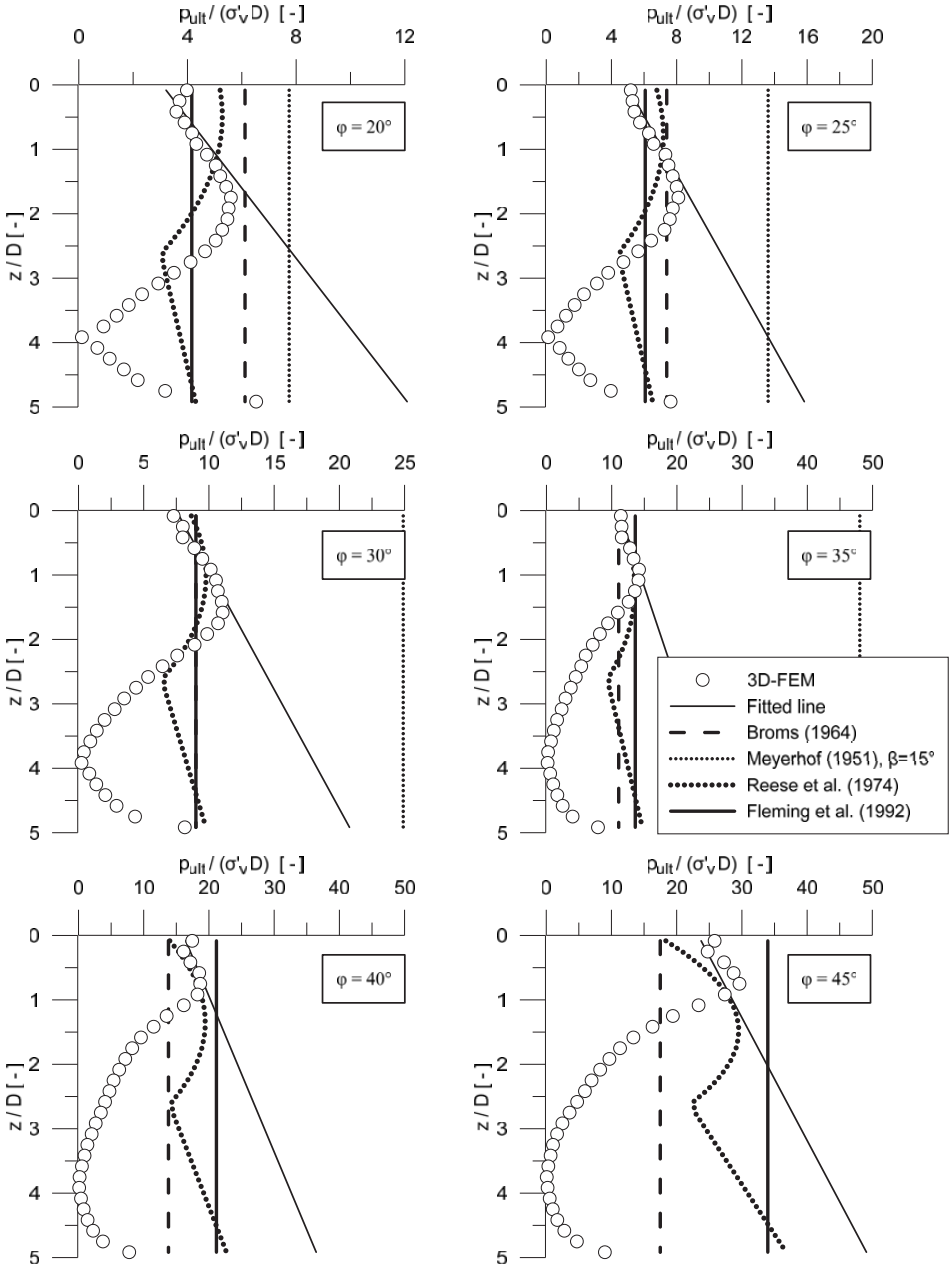

Figure 5-28. Variation of soil friction angle. Normalized mobilized resistance from 3D-FE simulations compared to analytical and empirical solutions for ultimate resistance found in the literature. Equation for fitted line given in Eq.(5-13).

The FE results in Figure 5-27 and Figure 5-28 indicate that the normalized ultimate resistance increases with depth, as suggested by Reese et al. (1974). The solution from Reese et al. provides a fair overall match to the FE results close to the soil surface. With depth, the solution predicts a decay in normalized resistance that is not reflected in the FE results. It is further noticed that the Reese et al. solution appears to perform better for soil friction angles close to the sand used for the original calibration of the method (Mustang Island sand, $\varphi = 39°$). The empirical expressions from Broms (1964) and Fleming et al. (1992) are both approximating the ultimate resistance found by the FEM at the top with varying accuracy, and fail to capture the rate of increase with depth.

Figure 5-27 and Figure 5-28 also display a curve denoted "fitted line". The expression for the fitted line is inspired by the Broms (1964) and Fleming et al. (1992) approach where the ultimate resistance is correlated with the Rankine passive soil pressure. To fit the simulation results, a dependency on the effective vertical stress is included. The fitted line is described by the equation:

$$p_u = \left(\frac{\varphi^\circ - 5^\circ}{10^\circ} + 1.5 \frac{\sigma'_v}{p_{atm}} \right) K_p \, \sigma'_v \, D \qquad \textbf{(5-13)}$$

where

p_u = ultimate resistance of p-y curve
φ = soil friction angle (in degrees)
σ'_v = effective vertical stress
p_{atm} = atmospheric pressure (100 kPa)
K_p = Rankine passive soil pressure ($K_p = [1+\sin \varphi]/[1-\sin \varphi]$)
D = pile diameter

Drained Ultimate Resistance – Summary

Ultimate resistance for p-y curves for sand is extracted from 3D-FE simulations and compared to the semi-empirical solution from Reese et al. (1974) and the empirical expressions from Broms (1964) and Fleming et al. (1992). The 3D-FE simulations are performed for a rotational pile movement.

The FE-results in Figure 5-27 and Figure 5-28 indicate that the normalized ultimate resistance increases with depth, as suggested by Reese et al. (1974). The Reese et al. (1974) solution is further seen to provide the best overall fit of the three solutions compared. None of the expressions found in the literature have proven able to capture the ultimate resistance seen from the top 1~2D in the 3D-FE results. An empirical expression is fitted to the 3D-FE results, given as Eq.(5-13)

5.6 Initial Stiffness of M-θ Curves

The theoretical solutions for initial stiffness of M-θ curves presented in Chapter 4 gave the initial stiffness as a function of the elastic soil stiffness (Young's modulus or shear modulus) and pile geometry (diameter and length). The three solutions presented are repeated in Eq.(5-14) for convenience.

Novak et al. (1978):
$$k_\theta = \pi G_s r^2 (1 + \mathrm{i}\, d_s)\left[a_0^* \frac{K_0(a_0^*)}{K_1(a_0^*)} + 1 \right] \quad \textbf{(5-14a)}$$

Davidson (1982a):
$$k_\theta = 0.55 E_{pr} D^2 \quad \textbf{(5-14b)}$$

Gerolymos and Gazetas (2006):
$$k_\theta = 0.85\left(\frac{L}{D}\right)^{-1.71} E_s L^2 \quad \textbf{(5-14c)}$$

The term initial stiffness here denotes the stiffness before yield occurs in any material-point in the soil. To ensure that material yielding close to the ground surface does not influence the initial stiffness of the extracted curves, a linear-elastic soil model is considered appropriate. The numerical investigation is performed as a parameter-study with emphasis on variation in soil stiffness and pile dimensions. An overview of the performed simulations is given in Table 5-6 and Table 5-7. Table 5-6 presents variation of soil Young's modulus, soil Poisson's ratio, pile bending stiffness and pile diameter. For these simulations, the pile length is kept constant at 30 m. Table 5-7 presents variations in pile length and the pile L/D ratio. In total, 28 simulations are performed. For all calculations, the horizontal distance from the pile center to the model boundary is six times the pile diameter (6D).

Table 5-6. Parameter variation. Each cell defining one load case, giving a total of 21 load cases.

Parameter	Unit			BaseCase		
E_s	[kN/m^2]	10 000	20 000	**30 000**	40 000	50 000
μ	[-]	0.2	0.25	**0.3**	0.4	0.49
E_pI_p	[kNm^2]	4.94e7	2.47e8	**1.04e9**	3.95e9	7.90e9
D	[m]	2 3	4 5	**6**	7 8	9 10

Table 5-7. Parameter variation. Each cell defining one load case, giving a total of 9 load cases.

Pile Length	Length/Diameter ratio		
	D = 3 m	D = 6 m	D = 9 m
10 m	3.33	1.67	1.11
20 m	6.67	3.33	2.22
30 m	10	5	3.33

5.6.1 Soil Stiffness

The M-θ stiffness has unit FL/L. The expressions given in Eq.(5-14) obtain this unit by multiplying soil stiffness (FL^{-2}) by pile diameter (alt. length) squared (L^2). The assumption of that M-θ stiffness can be normalized on soil stiffness times the pile diameter squared is made for the presented investigation.

To check this assumption with respect to soil stiffness, M-θ curves are extracted for five load cases where only the soil Young's modulus is varied. Geometry and soil are otherwise as described for the base case simulation with linear-elastic soil in Table 5-1 and Table 5-2. The results in Figure 5-29 show congruent curves for the middle part of the pile, with deviations close to the pile ends. Disregarding end effects, normalizing the M-θ stiffness on the soil stiffness is considered appropriate. Davidson (1982a) and Gerolymos and Gazetas (2006) correlated the M-θ stiffness with the soil Young's modulus, while Novak et al. (1978) correlated the M-θ stiffness with the soil shear modulus. For a constant Poisson's ratio, the ratio between the Young's modulus and the shear modulus is constant. As expected, Figure 5-29 shows no difference for whether the M-θ stiffness is normalized on E_s or G_s. If however the Young's modulus of the soil is kept constant, and the Poisson's ratio is varied, the ratio between E_s and G_s are no longer constant. Results from simulations with different Poisson's ratio are shown in Figure 5-30. When the soil Poisson's ratio is varied, a deviation of less than 20 % is observed when the stiffness at the middle part of the pile is normalized on the soil shear modulus. This variation increases to above 30 % when the M-θ stiffness is normalized on the Young's modulus of the soil.

The normalized M-θ stiffness shows considerable end effects at both the top- and bottom-end of the pile.

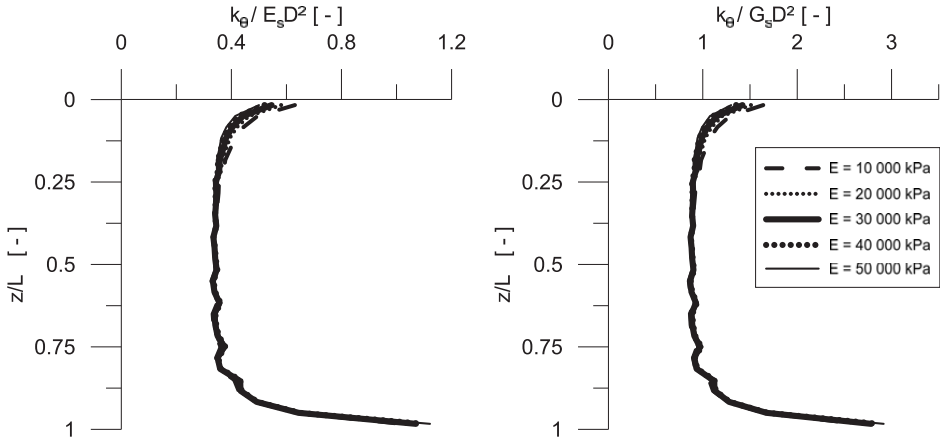

Figure 5-29. Normalized M-θ stiffness. Comparison of five variations with different soil Young's modulus.

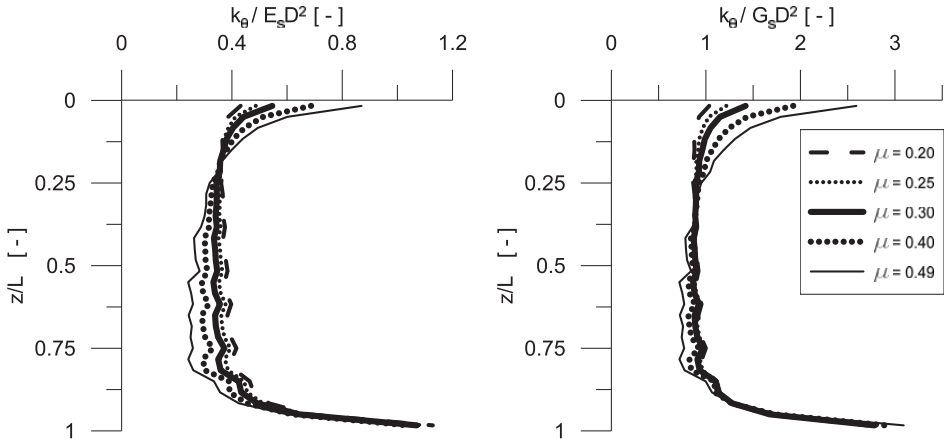

Figure 5-30. Normalized M-θ stiffness. Comparison of five variations with different soil Poisson's ratio.

5.6.2 Pile Diameter

In Figure 5-29 and Figure 5-30, the M-θ stiffness is normalized on the square of the pile diameter. In Figure 5-31, normalized M-θ stiffness is compared for nine different pile diameters, ranging from 2 to 10 m. From this figure, it is evident that the curves are not congruent, and that there is an apparent trend of increasing normalized stiffness with increasing pile diameter.

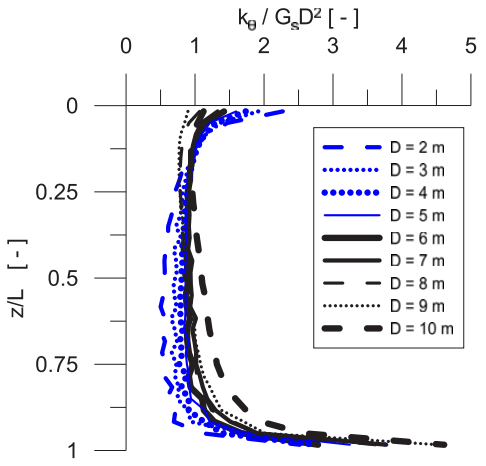

Figure 5-31. Normalized M-θ stiffness. Comparison of nine simulations with pile diameters ranging from 2 to 10 m.

5.6.3 Pile L/D ratio

Gerolymos and Gazetas (2006) gave M-θ stiffness as a function of the L/D ratio and the pile length (ref. Eq.(5-14c)). To investigate the effect of the pile L/D ratio, nine simulations are performed for different pile diameters and a constant pile length of 30 m. In addition, three variations of pile length are simulated for each of three different pile diameters. An overview of the performed simulations is given in Table 5-6 and Table 5-7.

In Figure 5-29 to Figure 5-31 the normalized rotational stiffness is plotted with depth, and distinct edge effects are visible at both the top- and bottom-end. If these end effects are disregarded, the normalized M-θ stiffness is close to constant. To ease the study of the influence from the pile L/D ratio, a single value for the stiffness of each simulation is selected as a representative stiffness. This representative stiffness is defined as the stiffness at half of the pile embedment depth (Z/L = 0.5). The point at half of the embedment depth is chosen as the point where edge effects are believed to be of least influence. In Figure 5-32, the representative normalized stiffness is plotted against the pile L/D ratio. A trend of decreasing normalized stiffness with increasing L/D ratio is visible, and can be approximated by:

$$k_\theta / G_s D^2 = 1.1 e^{-0.045 \frac{L}{D}} \qquad \textbf{(5-15)}$$

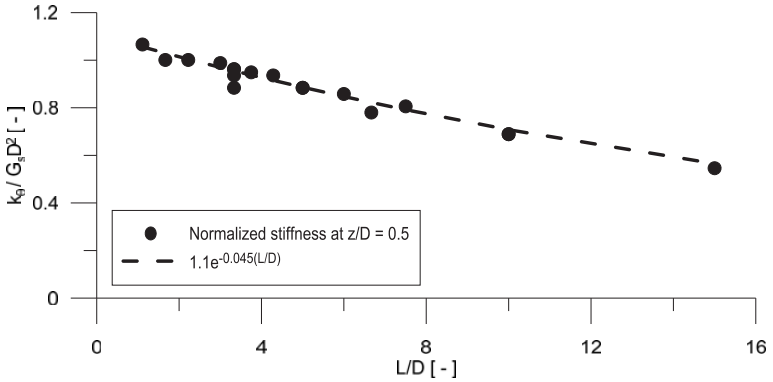

Figure 5-32. Normalized M-θ stiffness at half of the pile embedment depth, plotted against the pile L/D ratio.

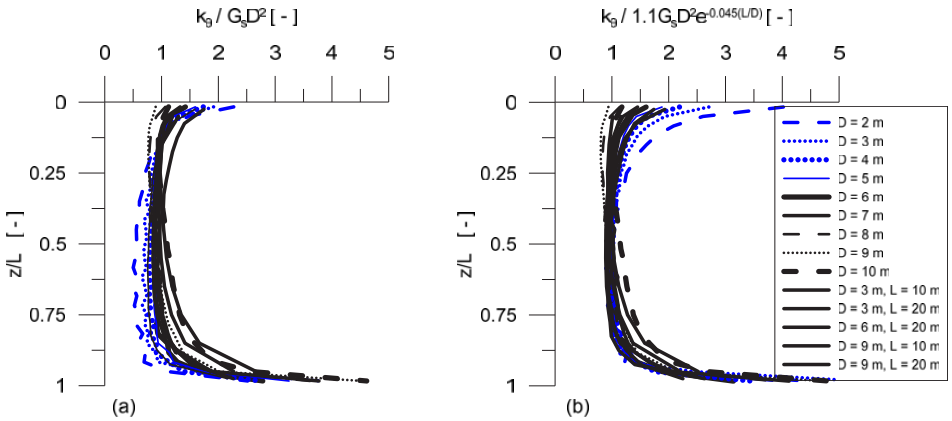

Figure 5-33. Normalized M-θ stiffness. (a) Comparison of varying pile diameters and pile length without correction for the L/D ratio. (b) Comparison of varying pile diameters and pile length with correction for the L/D ratio.

The scatter in normalized stiffness with varying pile diameters and pile lengths are shown in Figure 5-33a). Figure 5-33b) presents the reduced scatter when the pile L/D ratio is accounted for. As the curves are not perfectly congruent, Eq.(5-15) must be considered an approximation, and valid only for the range of pile diameters and pile lengths simulated.

5.6.4 Pile Bending Stiffness

The effect of pile bending stiffness to the M-θ stiffness is shown in Figure 5-34, where the normalized stiffness is plotted against depth. The pile bending stiffness is varied by changing the Young's modulus of the pile, while the pile geometry is kept constant. With the exception of the softest pile, little to no variation is seen in normalized M-θ stiffness due to pile bending stiffness.

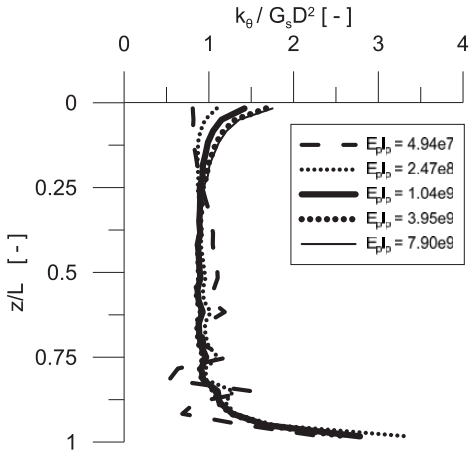

Figure 5-34. Normalized M-θ stiffness. Comparison of five simulations with different pile bending stiffness. Pile bending stiffness varied by changing the Young's modulus of the pile for a constant geometry.

5.6.5 End Effects at Pile Top

As for the p-y curves, all plots of normalized M-θ stiffness presented in Figure 5-29 to Figure 5-34 show an increased normalized stiffness at the pile top, compared to the normalized stiffness further down the pile. The increased stiffness is at its maximum at the very top of the pile, and reduces to the stiffness expressed in Eq.(5-15) approximately 0.5 pile diameters below the pile top.

The normalized rotational stiffness is seen to be dependent on soil Poisson's ratio, soil Young's modulus, pile diameter and the pile displacement shape. Due to this wide range of dependencies, the fit of a simplified expression to describe the top end effect for M-θ curves is considered inexpedient. If the top end increase in stiffness is to be accounted for, a detailed investigation is recommended for the specific pile geometry and soil parameters.

5.6.6 End Effects at Pile Toe

All plots of normalized M-θ stiffness presented in Figure 5-29 to Figure 5-34 show increased stiffness at the pile toe compared to the normalized stiffness elsewhere along the pile. The increased stiffness is at its maximum at the pile toe, and reduces to the stiffness expressed in Eq.(5-15) approximately 0.5 pile diameters above the pile toe. In Figure 5-35, the extracted rotational stiffness is normalized in Eq.(5-15) and plotted against the pile diameter and the pile L/D ratio. Based on Figure 5-35, the rotational stiffness of the bottom spring is approximated as:

$$k_{\theta,bottom} \approx 4\,k_{\theta} \qquad \textbf{(5-16)}$$

where k_θ is given by Eq.(5-15).

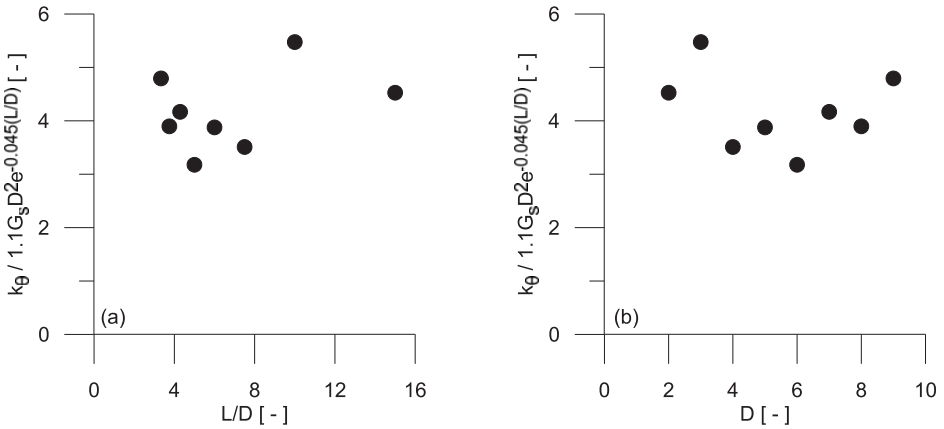

Figure 5-35. Normalized M-θ stiffness at pile toe from Figure 5-33.

5.6.7 Initial Stiffness of M-θ Curves – Summary

From the above investigations, it is found that the initial stiffness of M-θ curves can be approximated by the expression in Eq.(5-15). At the pile toe, Eq. (5-15) is suggested to be multiplied by 4, as given by Eq.(5-16).

Three solutions from the literature was given in Eq.(5-14). A comparison of the approximate expression in Eq.(5-15) to the solutions found in literature is given in Figure 5-36 for a pile length of 30 m. For the solution from Novak et al. (1978), a dimensionless frequency of $a_0 = 0.25$ is assumed representative for static loading. Only the real part of this solution is presented in Figure 5-36. The expression in Eq.(5-15) is seen to give a stiffness between the predictions from Davidson (1982a) and Novak et al. (1978). The expression from Gerolymos and Gazetas (2006) was originally developed for rigid piers. It overshoots the stiffness found from the FE simulations by more than 300 %.

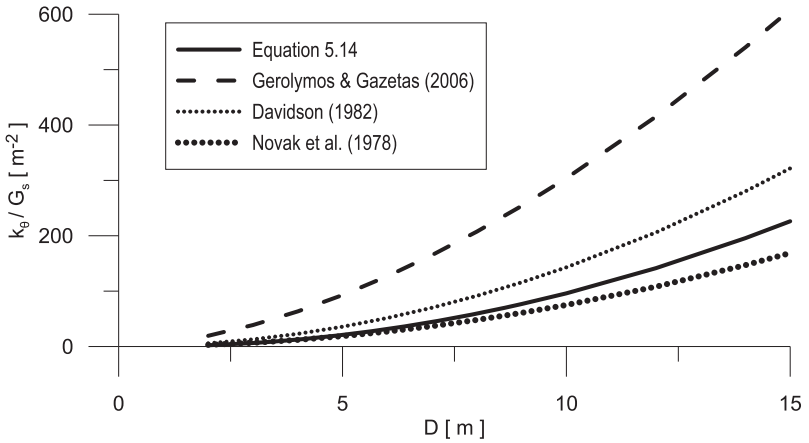

Figure 5-36. Comparison of M-θ stiffness with solutions from the literature. Comparison made for a pile length of 30 m and varying pile diameter.

5.7 Ultimate Resistance for M-θ Curves in Clay

A solution for ultimate resistance of M-θ curves from Davidson (1982b) was presented in Chapter 4. Davidson assumed that a crack would open on the back side of the pile, so that the vertical shear would only act at the front side of the pile. The expression for ultimate resistance of one side of the pile is repeated in Eq.(5-17a) for convenience.

$$M_{ult,1side} = \frac{\pi}{8} \alpha c_u D^2 \qquad \textbf{(5-17a)}$$

$$M_{ult,2sides} = \frac{\pi}{4} \alpha c_u D^2 \qquad \textbf{(5-17b)}$$

where

M_{ult} = ultimate moment resistance (unit kNm/m)
c_u = undrained shear strength
D = pile diameter
α = pile/soil interface roughness

Clay is able to take tensile forces in undrained loading, and in Chapter 4, a solution for rotational restraint from both sides of the pile was given by assuming symmetry. If symmetry is assumed, contribution from two sides is found by multiplying Eq.(5-17a) by two, and Eq.(5-17b) is obtained. The solution from Davidson (1982b) with contribution from one and two sides is compared to the results from the 3D-FE simulations in Figure 5-37. As seen from the figure, the ultimate resistance of the distributed moment springs is overshooting the solution with contribution for one side in Eq.(5-17a) with ~10-25 % at the upper part of the pile. Further down the pile, the moment capacity is close to zero or even negative.

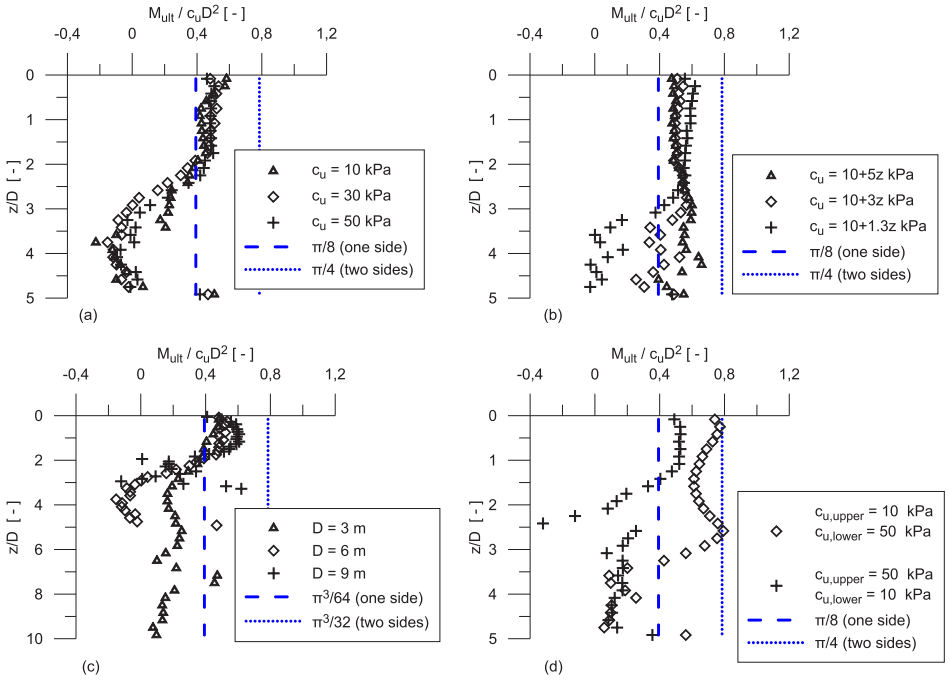

Figure 5-37. Ultimate resistance of distributed moment springs. Comparison of results from 3D-FE simulations to the proposed solution. (a) Uniform shear strength (b) Linearly increasing shear strength with depth (c) Different pile diameters (d) Soil layering.

Zero mobilized moment resistance a distance down the pile contradicts the results found with elastic soil for the evaluation of stiffness (Paragraph 5.6). A closer look at the FE results revealed however an explanation. Both the lack of moment resistance a distance down the pile and the reduced ultimate resistance at the upper part is seen to be caused by continuum effects. At the upper part of the pile, the soil is seen to fail in tension in the horizontal direction at the back, leaving no vertical capacity to the soil-pile interface. A distance down the pile, the soil appears to move along with the rotational pile movement, leaving no relative movement between the pile and the soil. An example of total displacements at failure is shown in Figure 5-38.

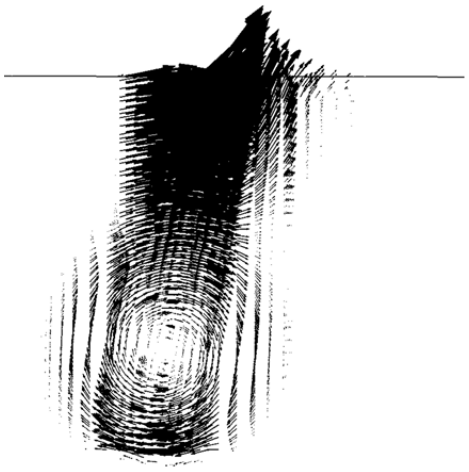

Figure 5-38. Total displacements at ultimate horizontal load. Cross section through the pile in the load direction (from left to right).

In Figure 5-39, the difference in development of rotational resistance is shown for two different depths along the pile. M-θ curves extracted from the simulation denoted c_u = 30 kPa in Figure 5-37a) is shown for the two normalized depths of z/L = 0.25 and z/L = 3.60. In Figure 5-37a), the ultimate moment resistance at z/L = 0.25 overshoots the solution with contribution from one side with ~20%, while the ultimate moment resistance at z/L = 3.60 is seen to be close to zero. The ultimate resistance presented in Figure 5-37 is taken when the ultimate horizontal load capacity of the entire pile is reached. Figure 5-39 however shows that the ultimate resistance of the M-θ curves is not mobilized simultaneously to the overall pile capacity.

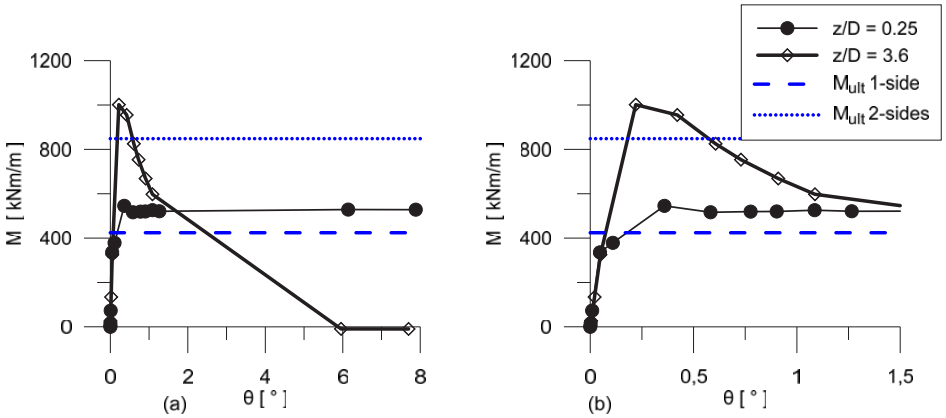

Figure 5-39. M-θ curves from the simulation denoted c_u = 30 kPa in Figure 5-37a). Curves from the normalized depths z/D = 0.25 and z/D = 3.6, plotted together with the ultimate resistance for one- and both sides of the pile. (a) x-axis from 0 - 8° rotation. (b) x-axis from 0 - 1.5° rotation.

The curve at z/D = 3.6 is seen to reduce the rotational restraint to zero in post-peak softening, after mobilizing a peak capacity approximately 20 % higher than the proposed solution with contribution from both sides of the pile. We recall that the material model used is linear-elastic, perfectly plastic, meaning that there is no material softening causing this effect.

Based on the results presented in Figure 5-37 to Figure 5-39, the proposed solution for ultimate moment resistance predicts a capacity close to 80 % of the capacity found with numerical simulations. The moment resistance is however seen to reduce at large rotations, after reaching the peak resistance. The reduction in moment resistance after the peak is due to a rotational failure of the soil. When pile and soil are rotating together, there is no relative displacement between pile and soil at the pile/soil interface, and shear is not mobilized on the interface. The post-peak softening is seen to be most pronounced at greater depths.

5.8 Ultimate Resistance of M-θ Curves in Sand

A solution for ultimate resistance of M-θ curves from Davidson (1982b) was presented in Chapter 4. Davidson assumed that a crack would open on the back side of the pile, so that the vertical shear would only act at the front side of the pile. The contribution was found to be a function of pile diameter, soil friction angle, cohesion and the limiting horizontal stress. The expression for ultimate resistance and the equation for the limiting horizontal stress is repeated in Eq.(5-18) for convenience.

$$M_{ult} = \alpha \frac{D^2}{2}\left(\frac{\pi}{4}c + \frac{2}{3}\sigma_r' \tan\varphi\right) \qquad \textbf{(5-18a)}$$

$$\sigma_r' = \max\left(k_0 \cdot \sigma_v' \quad , \quad \frac{p - \frac{\alpha D c \pi}{4}}{D\left(\frac{\pi}{4} + \frac{\alpha}{3}\tan\varphi\right)}\right) \qquad \textbf{(5-18b)}$$

The ultimate resistance of M-θ curves in sand are evaluated from the same FE simulations as the ultimate resistance for p-y curves in sand. An overview of these simulations is given in Table 5-5. The simulations for ultimate resistance of p-y curves were aborted before the ultimate capacity of the entire pile was achieved. The criterion used for abortion was that at least the 5 upper meters of the soil were brought to failure. As such, the M-θ curves cannot be expected to be mobilized to the ultimate resistance over the entire pile length.

In Figure 5-40, the mobilized, distributed moment from the FE-simulations is plotted together with the ultimate resistance envelope from Eq.(5-18a) for different soil friction angles. The limiting horizontal stress σ'_r is calculated from Eq.(5-18b), where the up

integrated p-values from the FE analysis is used to determine the limiting horizontal stress. The solution from Davidson (1982b) appears to capture the observed capacity from the FE simulations, indicating that it is only the upper part of the soil that is brought to failure. Figure 5-41 presents similar plots for variations in pile diameter. The solution from Davidson (1982b) appears to be consistent when the pile diameter is varied.

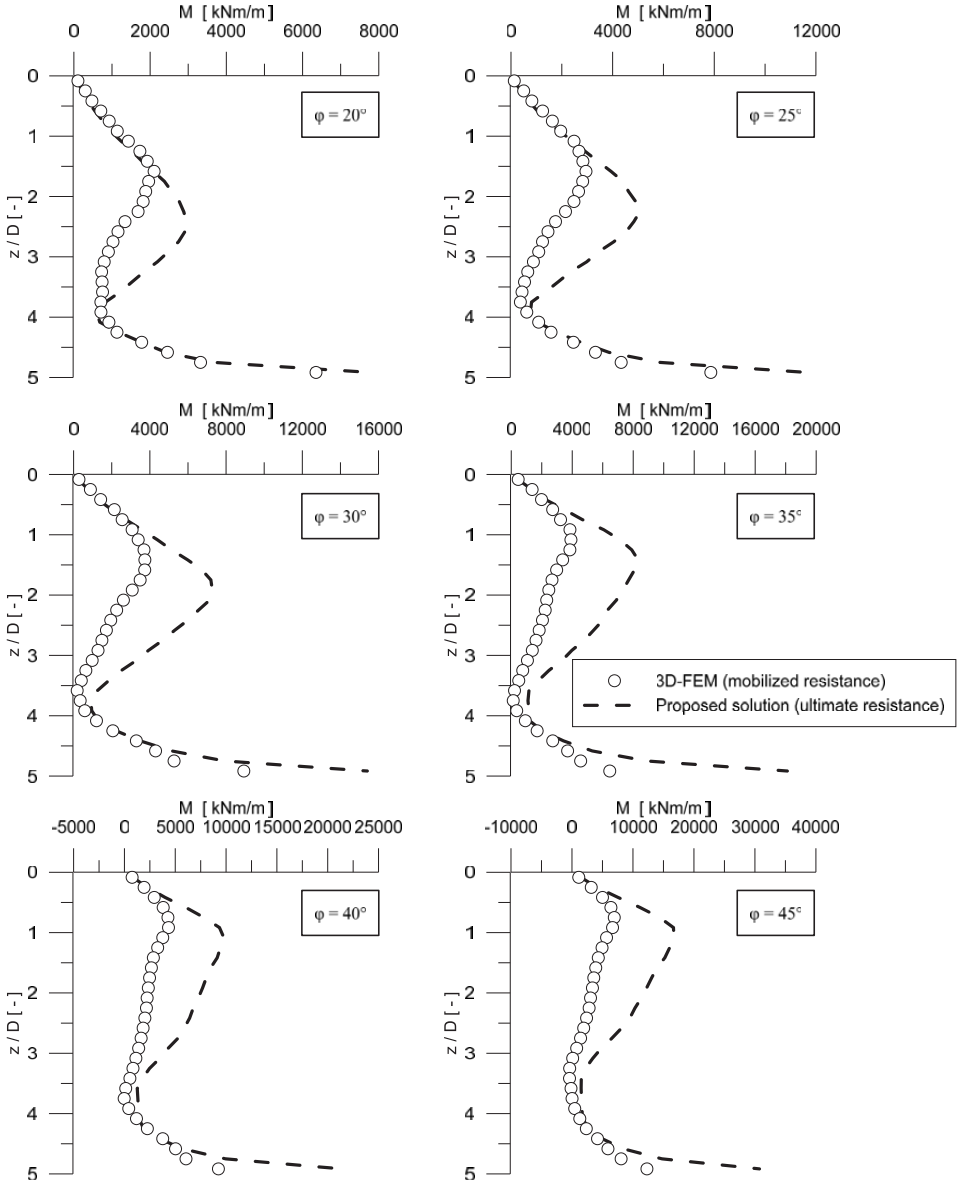

Figure 5-40. Variation of soil friction angle. Distributed, mobilized moment from 3D-FE simulations compared to the proposed solution for ultimate capacity in Eq.(5-18)

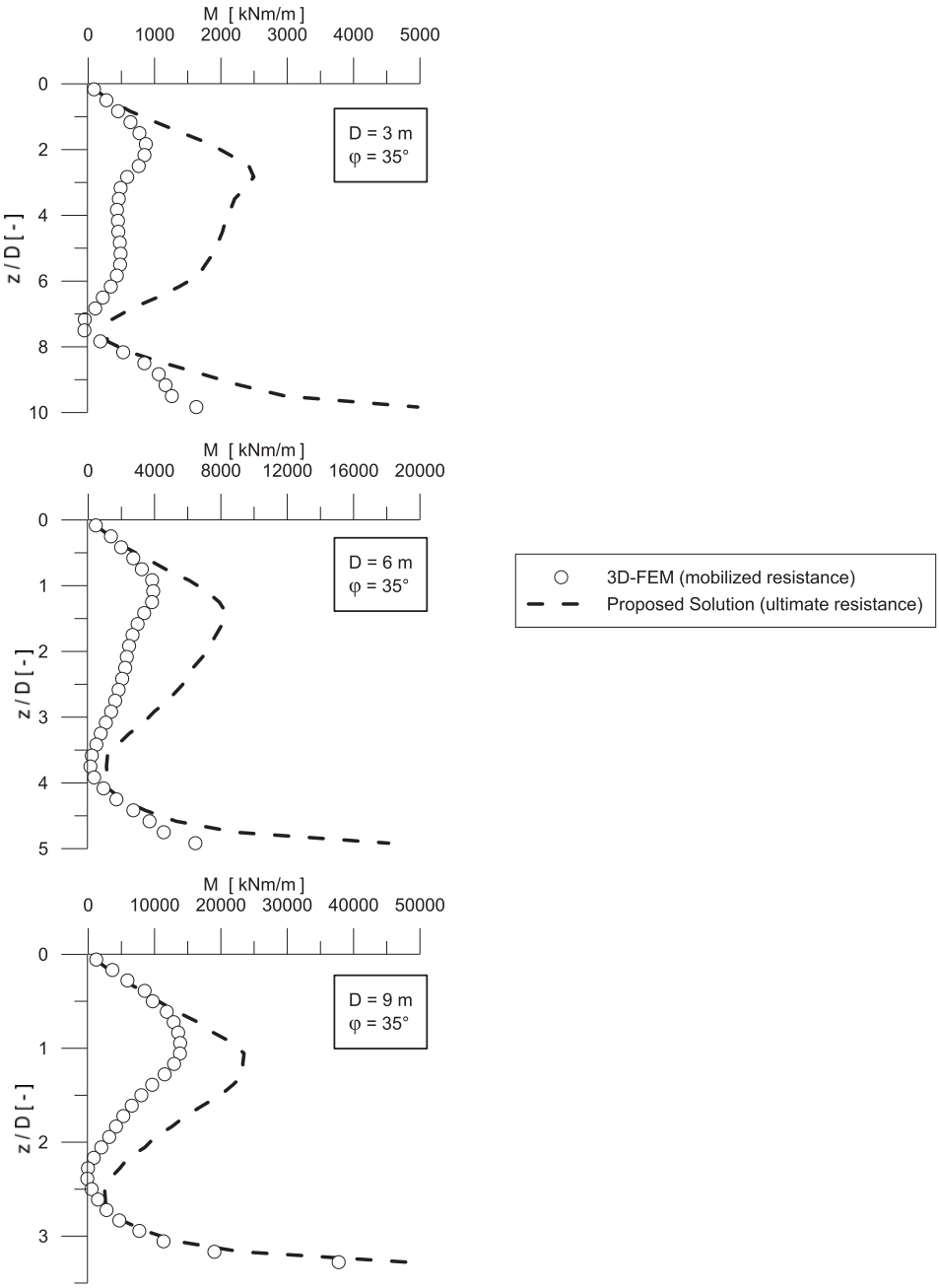

Figure 5-41. Variation of pile diameter. Distributed, mobilized moment from 3D-FE simulations compared to the proposed solution for ultimate capacity in Eq.(5-18)

5.9 Chapter Summary

In this chapter, a numerical study of soil springs has been presented. The numerical study is performed with a 3D-FE code, and the soil springs are extracted from the FE code as stresses and displacements of interface- and pile elements. An overview of the methodology that is used for creating the soil springs is given. Variation in stiffness for both lateral and rotational springs are compared with variation in soil and pile properties, and with analytical solutions from 2D theory. A correlation between soil stiffness and spring stiffness is observed and described. Continuum effects to the stiffness were observed at the pile ends, and described by empirical equations.

Ultimate resistance for lateral springs is compared to analytical and empirical solutions from the literature for piles in both clay and sand. For clay, solutions from the literature were found to fit the 3D-FE results well, both near the soil surface and at greater depths. For sand, none of the solutions from the literature were seen to provide an accurate solution. An empirical equation was therefore fitted to describe the ultimate resistance close to the soil surface. The ultimate resistance of the rotational springs is compared to a solution found in the literature. The ultimate resistance found from the 3D-FE simulations for sand was seen to correspond well with this solution. Influence from installation effects was not considered. For clay, the proposed solution only fitted the upper part of the pile. Observed post-peak softening caused by simultaneously rotation of pile and soil contributed to an inconsistency between the solution from the literature and the observed ultimate resistance at greater depths

Chapter References

Achmus, M, Abdel-Rahman, K & Kuo, Y (2007) Numerical modelling of large diameter steel piles under monotonic and cyclic horizontal loading. In *Tenth International Symposium on Numerical Models in Geomechanics*. Taylor & Francis London, pp. 453-459.

Ashour, M & Norris, G (2000) Modeling Lateral Soil-Pile Response Based on Soil-Pile Interaction. *Journal of Geotechnical and Geoenvironmental Engineering* **126(5)**:9.

Ashour, M, Norris, GM & Pilling, P (1998) Lateral Loading of a Pile in Layered Soil Using the Strain Wedge Model. *Journal of Geotechnical and Geoenvironmental Engineering* **124(4)**:303-315.

Augustesen, A, Sørensen, SPH, Ibsen, LB, Møller, M & Brødbæk, KT (2010) Comparison of calculation approaches for monopiles for offshore wind turbines. In *Numerical Methods in Geotechnical Engineering*. CRC Press, pp. 901-906.

Baguelin, F, Frank, R & Saïd, YH (1977) Theoretical study of lateral reaction mechanism of piles. *Geotechnique* **27**:405-434.

Benz, T (2007) Small-Strain Stiffness of Soils and its Numerical Consequences. In *Fakultät für Bau– und Umweltingenieurwissenschaften*. Universität Stuttgart, Stuttgart, vol. PhD, 150 p.

Broms, BB (1964) Lateral Resistance of Piles in Cohesionless Soils. *ASCE Journal of the Soil Mechanics and Foundations Division* **90(SM 3)**:123-156.

Brown, DA & Shie, C-F (1991) Some numerical experiments with a three dimensional finite element model of a laterally loaded pile. *Computers and Geotechnics* **12(2)**:149-162.

Byrne, BW, Mcadam, R, Burd, HJ, Houlsby, GT, Martin, CM, Zdravkovic, L, Taborda, DMG, Potts, DM, Jardine, RJ, Sideri, M, Schroeder, FC, Gavin, K, Doherty, J, Igoe, D, Muir-Wood, A, Kallehave, D & Gretlund, JS (2015) New design methods for large diameter piles under lateral loading for offshore wind applications. In *Frontiers in Offshore Geotechnics III*. CRC Press, pp. 705-710.

Davidson, HL (1982a) *Laterally loaded drilled pier research. Vol 1: Design Methodology*. Pennsylvania: Gai Consultants Inc., Report EPRI-EL-2197.

Davidson, HL (1982b) *Laterally loaded drilled pier research. Vol.2: Research Documentation*. Pennsylvania: Gai Consultants Inc., Report EPRI-EL-2197.

Fan, C-C & Long, JH (2005) Assessment of existing methods for predicting soil response of laterally loaded piles in sand. *Computers and Geotechnics* **32(4)**:274-289.

Fleming, K, Weltman, A, Randolph, M & Elson, K (1992) *Piling Engineering, Second Edition.* Taylor & Francis.

Gazetas, G (1983) Analysis of machine foundation vibrations: state of the art *Soil Dynamics and Earthquake Engineering* **2(1)**:2-42.

Gerolymos, N & Gazetas, G (2006) Winkler model for lateral response of rigid caisson foundations in linear soil. *Soil Dynamics and Earthquake Engineering* **26(5)**:347-361.

Gibson, RE (1967) Some Results Concerning Displacements and Stresses in a Non-Homogeneous Elastic Half-space. *Geotechnique* **17(1)**:58-67.

Hanssen, SB, Giese, S, Bye, A, Athanasiu, C & Tistel, J (2013) Modeling of Lateral Soil Restraint for Buckling Analysis of Suction Caissons in Clay In *Proceedings*

of The Twenty-third International Offshore and Polar Engineering Conference. International Society of Offshore and Polar Engineers, ISOPE.

Ibsen, LB, Roesen, HR, Wolf, TK & Rasmussen, KL (2013) Assesment of p-y Curves from Numerical Methods for a Non-Slender Monopile in Cohesionless Soil. In *23rd International Offshore and Polar Engineering Conference*. Anchorage, Alaska, USA, vol. 2, pp. 436-443.

Janbu, N (1963) Soil Compressibility as Determined by Oedometer and Triaxial Tests. In *3rd European Conference on Soil Mechanics and Foundation Engineering*. Wiesbaden, Germany, vol. 1, pp. 19-25.

Kim, Y & Jeong, S (2011) Analysis of soil resistance on laterally loaded piles based on 3D soil–pile interaction. *Computers and Geotechnics* **38(2)**:248-257.

Matlock, H (1970) Correlation for Design of Laterally Loaded Piles in Soft Clay. In *Offshore Technology Conference*. Houston Texas, pp. 577-607.

Mcgann, C, Arduino, P & Mackenzie-Helnwein, P (2011) Applicability of Conventional p-y Relations to the Analysis of Piles in Laterally Spreading Soil. *Journal of Geotechnical and Geoenvironmental Engineering* **137(6)**:557-567.

Mcgann, C, Arduino, P & Mackenzie-Helnwein, P (2012) Simplified Procedure to Account for a Weaker Soil Layer in Lateral Load Analysis of Single Piles. *Journal of Geotechnical and Geoenvironmental Engineering* **138(9)**:1129-1137.

Meyerhof, GG (1951) The Ultimate Bearing Capacity of Foundations. *Geotechnique* **2(December)**:301-322.

Murff, J & Hamilton, J (1993) P-Ultimate for Undrained Analysis of Laterally Loaded Piles. *Journal of Geotechnical Engineering* **119(1)**:91-107.

Novak, M, Nogami, T & Aboul-Ella, F (1978) Dynamic Soil Reactions for Plane Strain Case. *ASCE Journal of the Engineering Mechanics Division* **104(4)**:953-959.

Plaxis Bv (2011) Possible over-estimation of lateral circular pile bearing capacity. In *Plaxis Knowledgebase*. Bv, P. (ed).

Poulos, HG (1971) Behavior of Laterally Loaded Piles: I-Single Piles. *ASCE Journal of the Soil Mechanics and Foundations Division* **97(5)**:711-731.

Randolph, MF (2013) Analytical contributions to offshore geotechnical engineering. In *Proceedings of the 18th International Conference on Soil Mechanics and Geotechnical Engineering - 2nd McClelland Lecture*. Paris, France.

Randolph, MF & Houlsby, G (1984) Limiting pressure on a circular pile loaded laterally in cohesive soil. *Geotechnique* **34(4)**:613-623.

Reese, L, Cox, W & Koop, F (1974) Analysis of Laterally Loaded Piles in Sand. In *Offshore Technology Conference*. Houston, pp. 473–483.

Skempton, AW (1951) The bearing capacity of clays. In *Building Research Congress*. London, vol. 1, pp. 180-189.

Suryasentana, SK & Lehane, BM (2014) Numerical derivation of CPT-based p-y curves for piles in sand. In *Geotechnique*. vol. 64, pp. 186-194.

Sørensen, SPH, Møller, M, Brødbæk, KT, Augustesen, AH & Ibsen, LB (2009) *Numerical Evaluation of Load-Displacement Relationships for Non-Slender Monopiles in Sand*. University, A., Aalborg, Report 80, 28 p.

Terzaghi, K (1955) Evaluation of Coefficients of Subgrade Reaction. *Geotechnique* **5(4)**:297-326.

Yu, HS & Houlsby, GT (1991) Finite cavity expansion in dilatant soils: loading analysis. In *Geotechnique*. vol. 41, pp. 173-183.

Yu, J, Huang, M & Zhang, C (2015) Three-dimensional upper bound analysis for ultimate bearing capacity of a laterally loaded rigid pile in undrained clay. *Canadian Geotechnical Journal*.

Østergaard, MU, Knudsen, BS & Ibsen, LB (2015) P-y curves for bucket foundations in sand using finite element modeling. In *Frontiers in Offshore Geotechnics III*. Meyer, V. (ed) CRC Press, pp. 343-348.

6 New Framework for Soil Reaction Springs

In Chapter 2, the "traditional way" of constructing p-y curves was described as a 3-step procedure:

1) Define an ultimate resistance per unit length of pile
2) Define a reference stiffness for a pile unit length
3) Describe the decrease in stiffness with increasing displacements by a mathematical function fitted to measurements from pile loading tests at field or model scale.

The ultimate resistance and reference stiffness can be based on either theoretical or empirical considerations.

Keeping the thought of creating soil springs as a 3-step process, the new framework to be presented is similar to the "traditional way" in the two first points. At the third point however, the decrease in stiffness with increasing displacement is approached somewhat differently. Rather than assigning a mathematical function to test data from field tests, the degradation in stiffness with the increase in displacement is related directly to the stress-strain behavior of the soil. This is performed through the empirical Hardin-Drnevich equation for stiffness degradation.

From the numerical investigations performed in Chapter 5, it is recognized that simplified and general expressions never will be able to describe the exact continuum response from the soil towards the pile. Computed pile displacements and bending moments are however known not to be very sensitive to changes in the soil stiffness (Matlock and Reese, 1960), and approximately correct is therefore sufficient in most cases. With this in mind, the proposed framework for soil reaction springs does not aim for other than being approximately correct.

6.1 Relationship between Soil Spring Stiffness and Soil Stiffness

Chapter 5 described how the initial stiffness of both p-y curves and M-θ curves are controlled by the soil stiffness. The basis for the new framework is an assumed linear relation between soil stiffness and p-y stiffness. A linear relationship implies linearly scalable axes between the force-displacement space and the stress-strain space, as shown in Figure 6-1.

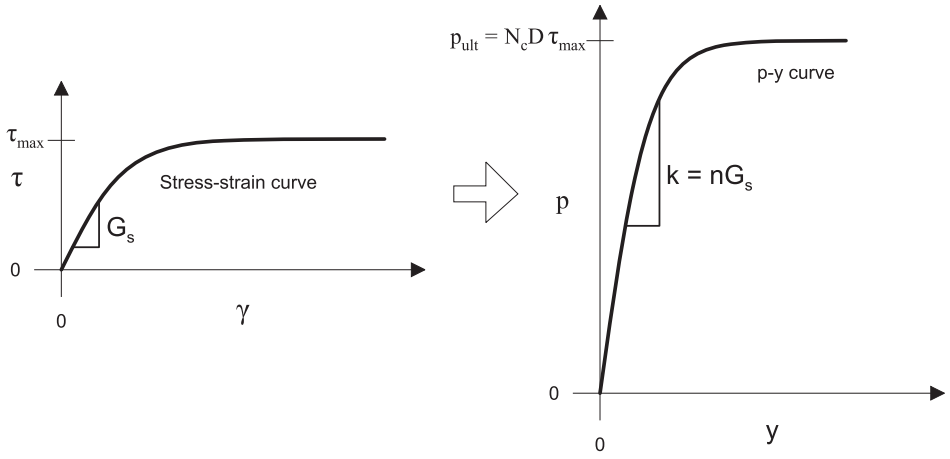

Figure 6-1. Axes in the stress-strain plot scaled linearly for the p-y plot. The same principle applies for the M-θ plot, however with different scaling factors.

In Chapter 3, it was shown how a stress distribution from elasticity is different from the failure pattern from plasticity which makes different soil elements reach failure at different times. It was observed there how this made the transition from linear elasticity to perfect plasticity curved, rather than being a sharp corner point. As such, linearly scalable axes do not represent the exact response, and must be considered an approximation.

By studying Figure 6-1, the scaling factor for the vertical axis is seen to be N_cD. The relation between τ and p is then $p = \tau N_c D$. The scaling factor for the horizontal axis is found from considering the curve tangent. It can be shown that if the p-axis is scaled by N_cD and the curve tangent is scaled by n, scaling of the y-axis is given by:

$$y = \frac{N_c D}{n} \gamma \tag{6.1}$$

6.2 Creating Soil Springs with the Hardin-Drnevich Equation

In Chapter 2, the importance of incorporating small strain stiffness for laterally loaded monopile foundations for offshore wind turbines was emphasized. At larger depths, the soil is experiencing very small strains and the soil response will be dominated by the small strain stiffness. Closer to the soil surface, the soil will experience larger strains. Dependent on both pile and soil properties, it is possible to have soil at failure strains at the top end, and strains representative for small-strain stiffness further down. To be able to cover the soil response over such a wide range of strain, the p-y curves need to contain information about both the stiffness at very small strains and the stiffness at larger strains.

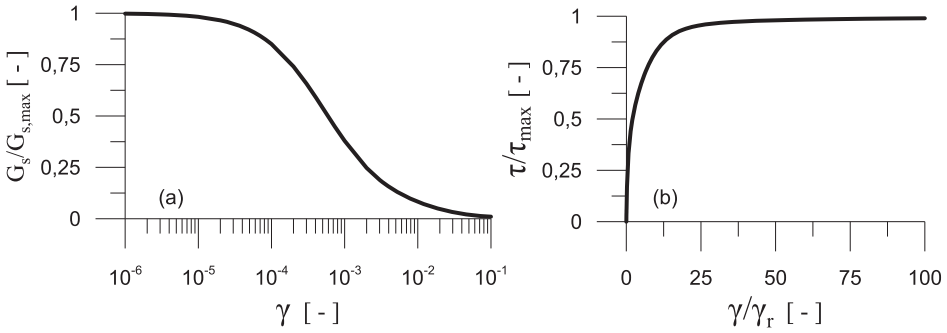

Figure 6-2. Example of decay in tangential shear modulus predicted by the Hardin-Drnevich equation. Parameters used for plotting: $\tau_{max}/G_{s,max}$ = 1000, a = 0.78, b = 1,

Hardin and Drnevich (1972) proposed a description of the decay in shear modulus as a function of shear strain by the hyperbolic equation:

$$G_s(\gamma) = \frac{1}{1+\frac{\gamma}{\gamma_r}\left[1+a\exp(-b\frac{\gamma}{\gamma_r})\right]} G_{s,max} \qquad \textbf{(6.2)}$$

where:

G_s = soil shear modulus
γ = shear strain
γ_r = reference shear strain, defined as $\gamma_r = \tau_{max}/G_{s,max}$
a = empirical constant
b = empirical constant
$G_{s,max}$ = soil shear modulus at very small strains

An example of how the shear stiffness degrades with strain according to the Hardin-Drnevich equation is shown in Figure 6-2. For a chosen set of parameters, the shear modulus is plotted against shear strain in Figure 6-2a) and the shear stress τ is plotted against shear strain in Figure 6-2b).

We note that the Hardin-Drnevich formulation contains information about the initial stiffness and the ultimate resistance. As such, the equation describes the entire strain range from zero to failure. When soil springs are created based on the Hardin-Drnevich equation, the same information is necessary as when p-y curves are created in the "traditional way", namely:

- Ultimate resistance
- Initial stiffness

The same principles is applied to both the p-y and the M-θ curves, but the notation p-y is used in the following as an example.

If the ultimate resistance is expressed as $p = \tau N_c D$ and the stiffness is expressed as $k = nG$, the soil spring takes the form of:

$$p = n G_s(y) \mathrm{y} \tag{6.3}$$

We note that the shear modulus G_s is expressed as a function of the displacement y rather than the shear strain γ, in contrast to the original formulation from Hardin and Drnevich (1972) in Eq.(6.2). Inserting Eq.(6.2) into Eq.(6.3), we obtain the full equation for the soil spring as:

$$p = \frac{n}{1 + \frac{y}{y_r}\left[1 + a\exp(-\mathrm{b}\frac{y}{y_r})\right]} G_{\mathrm{s,max}}\ \mathrm{y} \tag{6.4}$$

where the reference displacement y_r is defined as $y_r = p_{ult} / n G_{s,\max}$.

6.3 p-y Curves for Clay

6.3.1 Ultimate Resistance

In Chapter 3, it was shown that the ultimate resistance for p-y curves in clay can be written on the form:

$$p_{ult} = N_c D c_u \tag{6.5}$$

where N_c is a bearing capacity factor, D is the pile diameter and c_u is the undrained shear strength of the soil. Results from the numerical simulations in Chapter 5 indicates that the bearing capacity factor N_c can be well approximated by the expression from Yu et al. (2015), given in Eq.(6.6)

$$N_c = \min\left\{ N_{p0} + \frac{\gamma' z}{c_u},\ 9 + 3\alpha \right\} \tag{6.6}$$

with N_{p0} defined as:

$$N_{p0} = 11.94 - (1-\alpha) - 8.72\left[1 - \left(\frac{z}{14.5D}\right)^{0.6}\right]^{1.35} \quad \textbf{(6.7)}$$

The expression from Yu et al. (2015) is therefore adopted as the ultimate resistance of the proposed p-y curves in clay.

At the pile toe, the bearing capacity factor N_c is found to be larger than the values from the plane strain solution. No unambiguous correlations with pile or soil properties have been identified. It is therefore proposed that the bearing capacity factor at the pile toe only is increased if case specific studies of this effect are performed.

6.3.2 Stiffness

In Chapter 3, different analytical solutions for p-y stiffness were listed and compared. The compared solutions were all seen to be a function of the elastic soil stiffness, and could therefore be expressed as a function of the Young's modulus of the soil. In Chapter 5, 3D simulations of horizontally loaded piles were performed. The solution for the 2D case of a rigid disc in an elastic continuum (Baguelin et al., 1977) was used to determine the distance from pile center to the boundary of the soil volume. The boundaries were created such that the 2D stiffness from the rigid disc matched the solution for a cylinder moved laterally in an elastic half space (Gazetas, 1983). When continuum effects at the pile toe, pile top and at the pile rotation point are disregarded, the p-y stiffness from the 3D simulations were found to match the 2D theory well.

To be able to use the Hardin Drnevich equation directly, the p-y stiffness is expressed by the soil shear stiffness G_s rather than by the Young's modulus E_s. The shear modulus is related to the soil Young's modulus and the soil Poisson's ratio as:

$$G_s = \frac{E_s}{2(1+\mu)} \quad \textbf{(6.8)}$$

Assuming that the distance of 6D from pile center to the boundary represents the reality within a reasonable degree of approximation, the p-y stiffness can be approximated as Eq.(6.9) when the end effects are disregarded:

$$\frac{p}{y} = 4G_s \quad \textbf{(6.9)}$$

End effects

Both at the top and bottom end of the pile, continuum effects are seen to increase the stiffness for a length along the pile of approximately one diameter from the end. In Figure 6-3, the curved shape of the increase is shown in black, together with a linear approximation shown in red. The linear approximation is given over a distance of half a pile diameter from the pile ends. If end effects are to be included, the influenced length along the pile will need to be specified (as p-values are given as soil resistance per unit length of pile).

At pile top, the p-y stiffness can be approximated as

$$\left(\frac{p}{y}\right)_{top} = \left[4 + 0.17\left(\frac{D}{D_{ref}}\right)^{1.56}\right] G_s \qquad \textbf{(6.10)}$$

where D_{ref} = 1 m. The expression is based on the results from FE simulations presented in Chapter 5.

At pile toe, the p-y stiffness can be approximated as:

$$\left(\frac{p}{y}\right)_{bottom} = \left[4 + 208\left(\frac{L}{D}\right)^{-1.4}\right] G_s \qquad \textbf{(6.11)}$$

The expression is based on the results from FE-simulations presented in Chapter 5.

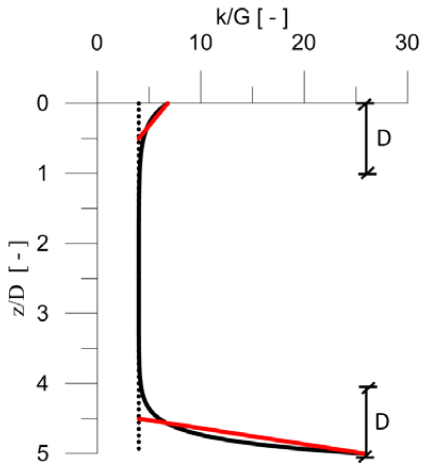

Figure 6-3. Increased p-y stiffness at pile ends due to continuum effects. Linear approximation in red over a distance of 0.5D from pile ends.

Pile Rotational Point

As discussed in Chapter 3, forces acting at and nearby the pile rotation point have a limited contribution to the moment equilibrium of the pile. Lateral pile displacements are also small at and nearby the rotational point, and small displacements mobilize small forces when the soil is modeled with p-y curves. Although the normalized p-y stiffness at the pile rotation point in Chapter 5 showed significant deviation from the rest of the pile, numerical p-values were still small. Effects of the pile rotation point are therefore neglected in the proposed p-y concept. The effect of neglecting the continuum effects around the pile rotation point has been investigated by Stene (2015). He concluded that for a 30 m long and 6 m diameter pile embedded in sand, the difference in pile head displacement was less than 0.5 % when continuum effects around the rotation point were neglected.

6.3.3 p-y Curves for Clay, Summary of Equations

Summarized, the equations that constitute the proposed p-y curves for clay are:

$$p = \frac{n}{1+\frac{y}{y_r}\left[1+a\exp(-\mathrm{b}\frac{y}{y_r})\right]} G_{\mathrm{s,max}}\,\mathrm{y} \tag{6.4}$$

The reference displacement y_r is defined as $y_r = p_{ult} / n G_{s,\max}$. Where continuum effects at the pile ends cannot be neglected (short and rigid piles), the parameter n is defined as:

$$z/D \geq 0.5 \;\&\; (L-z)/D \geq 0.5, \quad \mathrm{n} = 4$$

$$z/D \leq 0.5, \qquad \mathrm{n} = 4 + 0.17\left(\frac{D}{D_{ref}}\right)^{1.56}\left(1-\frac{z/D}{0.5}\right) \tag{6.12}$$

$$(L-z)/D \leq 0.5, \qquad \mathrm{n} = 4 + 208\left(\frac{L}{D}\right)^{-1.4}\left(1-\frac{(L-z)/D}{0.5}\right)$$

Where continuum effects at the pile ends can be neglected (long and slender piles), the parameter n can be taken as n = 4 over the entire pile depth. The parameter D_{ref} = 1 m. The parameters a, b and $G_{s,max}$ are determined based on laboratory and/or field tests.

The ultimate resistance is given by

$$p_{ult} = N_c D c_u \tag{6.5}$$

with N_c defined as:

$$N_c = \min\left\{ N_{p0} + \frac{\gamma' z}{c_u},\ 9 + 3\alpha \right\} \tag{6.6}$$

and N_{p0} defined as:

$$N_{p0} = 11.94 - (1-\alpha) - 8.72\left[1 - \left(\frac{z}{14.5D} \right)^{0.6} \right]^{1.35} \tag{6.7}$$

α is the interface roughness between the pile and the soil, and D is the pile diameter.

6.4 M-θ Curves for Clay

6.4.1 Ultimate Resistance

The theoretical ultimate resistance for M-θ curves in clay was presented in Chapter 4, with an option of including resistance from either both sides of the pile, or the front side only. In Chapter 5, these alternatives were compared to 3D-FE analysis. An exact match was not obtained, however the moment resistance from the upper part of the pile was close to the calculated contribution from one side of the pile. The resistance to lateral loading of a pile is believed to be controlled by the soil reactions near the top end of the pile. The ultimate distributed moment resistance per unit length of pile is therefore taken as the ultimate moment resistance at the front side of the pile:

$$M_{ult} = \alpha\ c_u \frac{\pi}{8} D^2 \tag{6.13}$$

where α is a factor varying from 0 to 1, describing the pile-soil interface roughness, D is the pile diameter and c_u is the undrained shear strength.

6.4.2 Stiffness

In Chapter 4, three different solutions for M-θ stiffness were listed and compared. As for the p-y stiffness, these three solutions were all a function of the elastic soil stiffness, and could therefore be expressed as a function of the Young's modulus of the soil.

Apart from the common feature of relating the M-θ stiffness to the soil stiffness, the three solutions from the literature showed poor correspondence with each other. They were also unable to capture the observed performance from the 3D simulations of horizontally loaded piles performed in Chapter 5.

If end effects at the pile toe are disregarded, the M-θ stiffness found in Chapter 5 can be approximated by Eq.(6.14a). Noting that the last part of Eq.(6.14a) will be in the range of 0.95~0.99 for typical monopile dimensions, the expression can be simplified as Eq.(6.14b). Considering the approximate nature of the 1D beam, the simplification is assumed not to influence the engineering accuracy.

$$k_\theta = 1.1\, G_s D^2\, e^{-0.045\frac{L}{D}} \tag{6.14a}$$

$$k_\theta \approx G_s D^2 \tag{6.14b}$$

Based on the findings in Chapter 5, the M-θ stiffness at the pile toe can be expressed as:

$$k_{\theta,bottom} \approx 4 G_s D^2 \tag{6.15}$$

As for the p-y curves, the increase in stiffness is "curved" over a distance along the pile. In Chapter 5, this distance was found to be noticeable to approximately half a pile diameter above the pile toe. For the sake of simplicity, the curved increase is approximated linearly over a distance of 0.25D.

It should be noticed that an end effect for rotational stiffness was observed also at the top end of the pile in Chapter 5. It was however not identified any simple equation that could represent this effect. Due to the approximate nature of the proposed framework, it is believed that neglecting this effect can be done without loss of engineering accuracy.

6.4.3 M-θ curves for Clay, Summary of Equations

Written in the form of Eq.(6.2), the M-θ curves for clay are expressed as:

$$M = \frac{n}{1+\frac{\theta}{\theta_r}\left[1+a\exp(-\mathrm{b}\frac{\theta}{\theta_r})\right]} G_{s,\max}\theta \tag{6.16}$$

where the reference rotation θ_r is given as $\theta_r = M_{ult}/nG_{s,\max}$. M_{ult} is given in Eq.(6.13) and the parameter *n* is defined as:

$$(L-z)/D \geq 0.25, \qquad \mathrm{n} = D^2$$
$$(L-z)/D < 0.25, \qquad \mathrm{n} = 4D^2\left(1-\frac{(L-z)/D}{0.25}\right) \tag{6.17}$$

6.5 p-y Curves for Sand

6.5.1 Ultimate Resistance

In Chapter 3, different theoretical and empirical solutions for the ultimate resistance of p-y curves in sand were presented. The solutions concerning the ultimate resistance close to the ground surface were investigated in a numerical study presented in Chapter 5. None of the solutions found in the literature were able to fit the results of all the parameter variations performed in the numerical study. An empirical equation that relates the ultimate resistance to the Rankine passive soil pressure was fitted to the numerical results, and is adopted as the ultimate resistance for the proposed p-y curves:

$$p_{u,shallow} = \left(\frac{\varphi^\circ - 5}{10} + 1.5\frac{\sigma'_v}{p_{atm}}\right) K_p\, \gamma' z\, D \tag{6.18}$$

where

$p_{u,shallow}$	=	ultimate resistance of p-y curves close to the soil surface
φ	=	soil friction angle (in degrees)
σ'_v	=	effective vertical stress
p_{atm}	=	atmospheric pressure (100 kPa)
K_p	=	Rankine passive soil pressure ($K_p = [1+\sin\varphi]/[1-\sin\varphi]$)
γ'	=	effective unit weight of soil
z	=	depth below ground surface
D	=	pile diameter

The lateral pile response in sand will for most cases be controlled by the near surface soil, and the ultimate lateral resistance at greater depths is believed to be more of academic interest. The ultimate resistance at greater depth is however needed for constructing the stiffness decay with increasing displacement for the proposed p-y curves. The analytical solution for the plane strain case by Reese et al. (1974) is adopted for the proposed p-y curves:

$$p_{u,deep} = D\,\gamma' z\left(K_a\,(\tan^8\beta_r - 1) + K_0 \tan\varphi \tan^4\beta_r\right) \tag{6.19}$$

where

p_u = ultimate lateral resistance from the sand
K_a = Rankine coefficient for active soil pressure
K_0 = coefficient of soil pressure at rest
γ' = effective unit weight of sand
z = depth below ground surface
φ = soil internal friction angle
β_r = $45° + \varphi/2$

The ultimate resistance at arbitrary depth is determined by:

$$p_u = \min\left(p_{u,shallow}, p_{u,deep} \right) \tag{6.20}$$

6.5.2 Stiffness

The stiffness of the p-y curves for sand is identical to the stiffness for clay, as the stiffness is derived from the theory of elasticity. The p-y stiffness was in Chapter 5 seen to be not very sensitive to the Poisson's ratio of the soil. The expressions for the parameter *n* presented in Eq.(6.12) for clay are therefore valid also for sand.

6.5.3 p-y Curves for Sand, Summary of Equations

Written in the form of Eq.(6.2), the p-y curves for sand are expressed as:

$$p = \frac{n}{1 + \frac{y}{y_r}\left[1 + a\exp(-b\frac{y}{y_r})\right]} G_{s,\max}\, y \tag{6.4}$$

The reference displacement y_r is defined as $y_r = p_{ult} / n G_{s,\max}$. Where continuum effects at the pile ends cannot be neglected (short and rigid piles) , the parameter *n* is defined as:

$z/D \geq 0.5$ & $(L-z)/D \geq 0.5$, $\quad n = 4$

$$z/D \leq 0.5, \qquad n = 4 + 0.17\left(\frac{D}{D_{ref}}\right)^{1.56}\left(1 - \frac{z/D}{0.5}\right) \tag{6.12}$$

$$(L-z)/D \leq 0.5, \qquad n = 4 + 208\left(\frac{L}{D}\right)^{-1.4}\left(1 - \frac{(L-z)/D}{0.5}\right)$$

Where continuum effects at the pile ends can be neglected (long and slender piles), the parameter n can be taken as n = 4 over the entire pile depth. The parameter D_{ref} = 1 m. The parameters a, b and $G_{s,max}$ are determined based on laboratory- and/or field tests.

The ultimate resistance at arbitrary depth is given by

$$p_u = \min\left(p_{u,shallow}, p_{u,deep}\right) \tag{6.20}$$

Where the shallow ultimate resistance is given by:

$$p_{u,shallow} = \left(\frac{\varphi^\circ - 5}{10} + 1.5\frac{\sigma'_v}{p_{atm}}\right) K_p\, \gamma' z\, D \tag{6.18}$$

and the deep ultimate resistance is given by:

$$p_{u,deep} = D\,\gamma' z\left(K_a\ (tan^8\beta_r - 1) + K_0 \tan\varphi \tan^4\beta_r\right) \tag{6.19}$$

where

p_u = ultimate lateral resistance
K_a = Rankine coefficient for active soil pressure
K_0 = coefficient of soil pressure at rest
γ' = effective unit weight of sand
z = depth below ground surface
φ = soil internal friction angle
β_r = 45°+ φ/2

6.6 M-θ Curves for Sand

6.6.1 Ultimate Resistance

The ultimate resistance of M-θ curves in sand were presented in Chapter 4. The ultimate resistance in sand can be shown to be dependent on the limiting normal stress, denoted σ'_r. The horizontal stress in the soil in front of the pile will increase with lateral pile movement. As such, the true limiting stress is dependent on the lateral pile movement. The expression for the limiting stress is given by Eq.(6.21), where p is the mobilized lateral soil resistance, determined by the horizontal pile displacement.

$$\sigma_r' = \max\left(k_0 \cdot \sigma_v' \quad , \quad \frac{p - \frac{\alpha D c \pi}{4}}{D\left(\frac{\pi}{4} + \frac{\alpha}{3}\tan\varphi\right)} \right) \tag{6.21}$$

The ultimate moment resistance in granular materials is given as Eq.(6.22) with the limiting pressure taken from Eq.(6.21).

$$M = \alpha \frac{D^2}{2}\left(\frac{\pi}{4}c + \frac{2}{3}\sigma_r' \tan\varphi\right) \tag{6.22}$$

where α is a factor varying from 0 to 1, dependent on the pile-soil interface roughness, c is cohesion, φ is the soil internal friction angle and D is the pile diameter.

6.6.2 Stiffness

As for p-y curves, the stiffness of the M-θ curves is based on elastic theory, and seen not to be very sensitive to variations in the Poisson's ratio of the soil. The expressions for the parameter *n* given in Eq.(6.17) are therefore valid for both sand and clay.

6.6.3 M-θ Curves for Sand, Summary of Equations

Written in the form of Eq.(6.2), the M-θ curves for sand are expressed as:

$$M = \frac{n}{1 + \frac{\theta}{\theta_r}\left[1 + a\exp(-b\frac{\theta}{\theta_r})\right]} G_{s,\max}\theta \tag{6.16}$$

where the reference rotation θ_r is given as $\theta_r = M_{ult} / nG_{s,\max}$. M_{ult} is given in Eq.(6.22) and the parameter n is defined as:

$$\begin{aligned} &(L-z)/D \geq 0.25, && n = D^2 \\ &(L-z)/D < 0.25, && n = 4D^2\left(1 - \frac{(L-z)/D}{0.25}\right) \end{aligned} \tag{6.17}$$

6.7 When to Include the Rotational Restraint from Vertical Shear Forces (M-θ Curves)

The contribution from vertical shear stresses between the pile and the soil was pointed out in Chapter 4 to be of increasing importance for decreasing pile L/D-ratios. As we recall, the vertical shear stresses influences the moment equilibrium around the horizontal axis normal to the load direction.

In order to quantify the contribution from M-θ curves to the overall pile performance, the soil springs that were extracted to investigate initial stiffness in Chapter 5 are used. The p-y and M-θ curves extracted for different pile diameters and pile lengths in Chapter 5 are used in a beam column model, with beam properties equivalent to the pile used in the 3D-FE simulations. One set of calculations is performed with the extracted p-y springs only, and one set of calculations is performed with both the extracted p-y and M-θ curves. The pile top-end displacement is compared to the pile top-end displacement from the 3D-FE simulation in Figure 6-4. From the figure, it is seen that when the soil is represented by both p-y and M-θ curves, the error in predicted top-end displacement varies from 0.2 - 1.4 %. When the soil is represented by p-y curves only, the error is below 5 % when the L/D ratio is larger than approximately L/D = 5. For L/D < 5, the error is increasing somewhat exponentially, to more than 60 % for a ratio of L/D = 1.11.

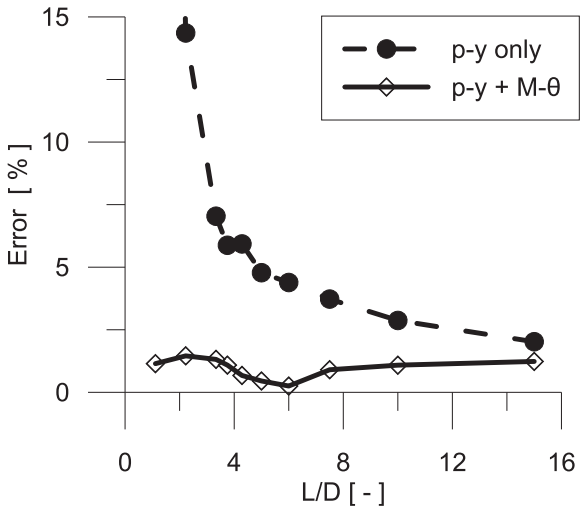

Figure 6-4. Error in calculated pile head displacement compared to full 3D-FE simulation when the soil is represented with p-y only and p-y and M-θ curves.

The curves in Figure 6-4 are based on linear springs extracted in the numerical study in Chapter 5. The trend of increasing importance of M-θ springs for decreasing L/D ratios is however not limited to linear springs only. Stene (2015) used the same methodology as described in Chapter 5, and extracted nonlinear springs from 3D-FE simulations. When the soil springs where used in a beam model, a trend similar to the one in Figure 6-4 was found.

An error of 5 % displacement is often considered sufficient accuracy for engineering purposes. An error of 5 % is observed for an L/D ratio of approximately $L/D \approx 5$, and the error is increasing rapidly when the L/D ratio decreases below 5. Based on the above findings, it is recommended that M-θ springs are included when the pile L/D ratio is below 5.

The demand for accuracy may however be different for different problems. It is observed that the displacement calculated with both p-y and M-θ springs is closer to the FE results for all L/D ratios, compared to when p-y springs are used alone. If high accuracy is required, M-θ springs are recommended to be used regardless of the pile L/D ratio.

6.8 Comparison with p-y Springs Given in Design Guidelines

The p-y springs given in design guidelines like API-RP2 (API, 2011) and DNV-CN30.4 (DNV, 1992) are used for a comparison of the proposed p-y curves. In the following, the springs from the design-guidelines will be referred to as the "API p-y curves", while the p-y curves proposed herein will be referred to as "proposed p-y curves".
The increased p-y stiffness near the pile ends is neglected for all calculation examples presented.

6.8.1 Calculation Examples, Clay

The equations for the API p-y curves for clay were derived by Matlock (1970) and is given in Appendix B. For the calculation examples below, the API-curves follows the multi-linear discretization given in API-RP-2A, while the proposed p-y curves follows a smooth function. The performance of the proposed p-y curves is compared to the performance of the API p-y curves for two full scale load tests:

1) The Sabine river pile test, wherefrom the p-y curves by Matlock (1970) was calibrated
2) The Albany pile test from Sa'don (2012)

The Sabine River pile test is performed in soft clay, while the Albany pile test is performed in stiff, over-consolidated clay.

Sabine River Pile Test

The Sabine River pile test is one of two pile tests that were used to calibrate the API p-y curves for clay. The test pile was a 12.8 m long, open ended steel pile of diameter 0.32 m. Limited information about the soil conditions for Sabine River is given in Matlock (1970), the clay is however described as soft with an average shear strength of 300 lb/ft^2 (14.3 kPa). For the proposed p-y curves, the correlation from Hardin and Black (1968) is used to estimate the small strain soil stiffness on the basis of an assumed void ratio of e = 1.0 and an assumed OCR = 1.0 (Eq.(6.23)). The soil stiffness degradation parameters a and b are taken as $a = 1$ and $b = 1.3$, based on the recommendations in Hardin and Drnevich (1972). The soil parameters used to create the p-y curves are shown in Table 6-1 and Table 6-2.

$$G_{s,\max} = 1230 \frac{(2.973 - e)^2}{(1+e)} (OCR)^K \sigma_m^{0.5} \tag{6.23}$$

Table 6-1. Soil parameters, API p-y curves for the Sabine River pile test

Parameter	Unit	Value
c_u	[kPa]	14.3 (uniform)
ε_{50}	[-]	0.007
γ'	[kN/m^3]	10
J	[-]	0.5

Table 6-2. Soil parameters, proposed p-y curves for the Sabine River pile test. Altered values for the best fit stiffness reduction curve in brackets.

Parameter	Unit	Value
c_u	[kPa]	14.3
γ'	[kN/m^3]	10
α	[-]	0.5 (0.0)
e	[-]	1.0
a	[-]	1.0 (1.9)
b	[-]	1.3 (0.1)
OCR	[-]	1.0

A comparison of pile head displacements is given in Figure 6-5a). Measured pile head displacements were not presented for the static load case in Matlock (1970), they are however presented in Reese (1996). Figure 6-5b) and c) compares the p-y curves at the depths of 1D and 10D, where D is the pile diameter.

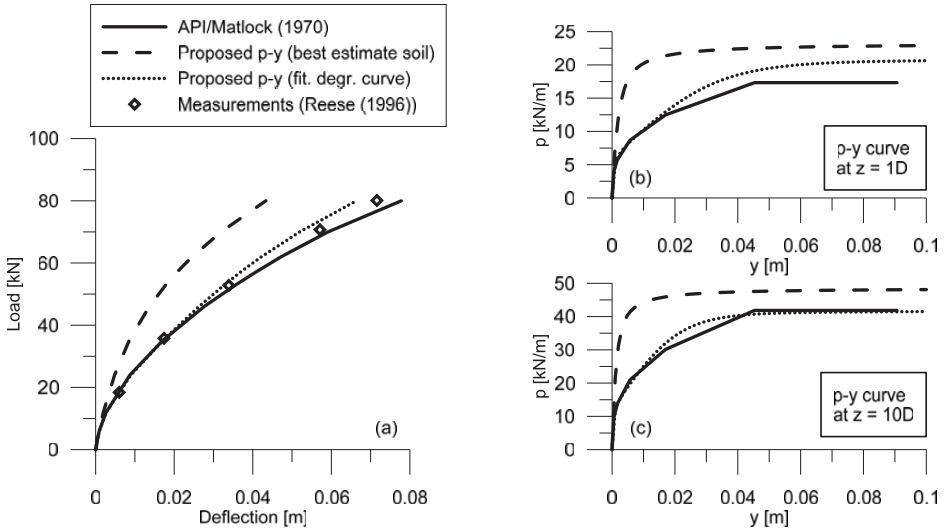

Figure 6-5. (a) Comparison of pile head displacements for the Sabine River pile test. (b) Comparison of p-y curves at z = 1D (0.32 m) (c) Comparison of p-y curves at z = 10D (3.24 m)

The pile head displacement is not captured when the curve fitting parameters *a* and *b* are based on the recommendations for clay in Hardin and Drnevich (1972). From Figure 6-5b) and -c), this is seen to be caused by p-y curves that are significantly stiffer than the API-curves. By altering the curve fitting parameters for the stiffness degradation curve (*a* and *b*) to best fit values for reproducing the API p-y curves, an excellent fit of the pile head displacements is obtained.

The excellent fit of the pile head displacements is of limited value itself. In fact it illustrates the main weakness of the proposed p-y curves: The dependency of the non-physical curve fitting parameters *a* and *b* in the Hardin-Drnevich equation. The recommendations given by Hardin and Drnevich (1972) were aimed at a good fit for the stiffness decay in the small-strain area, while the static load test just presented appeared to be controlled by the response at larger strains.

The Albany Pile Test

The Albany pile test is performed close to Auckland, New Zealand and is reported in Sa'don (2012). The pile is a close-ended, 6.5 m long steel pile of 0.273 m diameter, installed by driving. The soil at site is Auckland residual clay, an over-consolidated clay of medium to high plasticity with a constant undrained shear strength of ~100 kPa over the pile embedment depth. The soil conditions are documented through CPTs, vane shear tests and seismic methods for determination of the soil small-strain stiffness. The seismic investigation were performed with seismic CPT, spectral analysis of surface waves (SASW) and wave activated stiffness tests (WAK). The parameters *a* and *b* for

Table 6-3. Soil parameters for the Albany pile test

Parameter	Unit	Value	Ref.
c_u	[kPa]	100 (uniform)	Sa'don (2012)
ε_{50}	[-]	0.01	Assumed
γ	[kN/m^3]	17	Sa'don (2012)
J	[-]	0.5	Assumed
$G_{s,max}$	[MPa]	40 (uniform)	Sa'don (2012)
a	[-]	1.9	Assumed
b	[-]	0.1	Assumed
α	[-]	0.5	Assumed

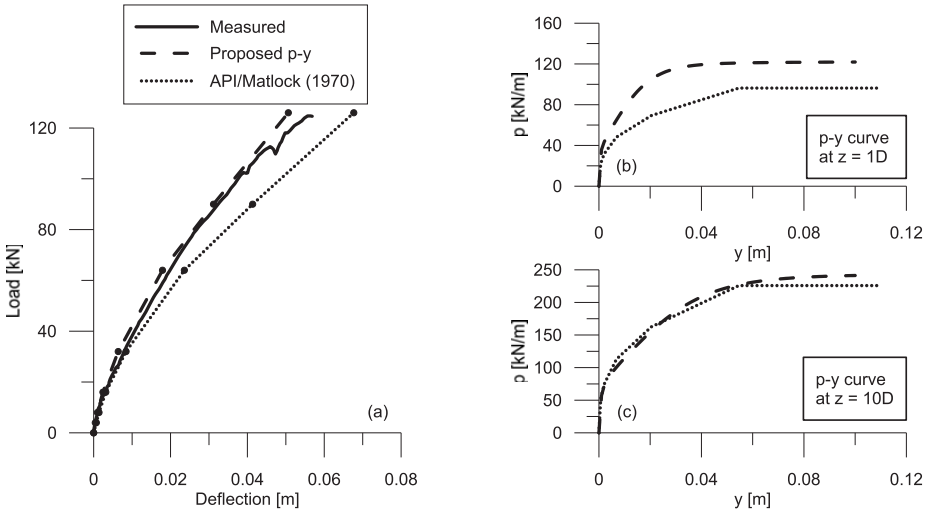

Figure 6-6. (a) Comparison of pile head displacements for the Albany pile test. (b) Comparison of p-y curves at z = 1D (0.27 m) (c) Comparison of p-y curves at z = 10D (2.73 m)

the soil stiffness degradation curve are based on the best fit parameters from the previous calculation example. An overview of soil parameters used for the calculation is given in Table 6-3.

The pile testing program at Albany consisted of both static cyclic and dynamic testing. A series of low-amplitude two-way cycles were performed at the test pile before the static test, causing a gap opening of approximately 0.3 m depth behind the pile. As such, an average pile-soil interface-roughness of 0.5 is assumed.

The calculation with the proposed p-y curves matches the measured pile head response closely in Figure 6-6a). The API p-y curves predicts a response softer than measured. Considering the comparison of the different p-y curves in Figure 6-6b) and c), the different curves are almost identical at greater depths. The difference in pile head predictions appear therefore to be caused by the different expression for ultimate

resistance close to the surface in the different p-y formulations. For the Albany pile load test, the near surface ultimate resistance expression from Yu et al. (2015) is indicated to be superior to the near-surface failure criteria from Matlock (1970).

6.8.2 Calculation Examples, Sand

The equations for the API p-y curves for sand are based on work by Reese et al. (1974) and O'Neill and Murchison (1983) and is given in Appendix B. The performance of the proposed p-y curves is compared to the performance of the API p-y curves for two pile load tests:

1) The Mustang Island pile test, reported by Reese et al. (1974) and Cox et al. (1974)
2) The Blessington pile test, reported by Doherty et al. (2012)

The Mustang Island Pile Test

The Mustang Island pile test is performed at Mustang Island in Texas, USA, and is reported in Reese et al. (1974) and Cox et al. (1974). The pile was driven open ended to an embedment depth of 21 m. The pile diameter was 0.61 m, and the wall thickness 9.5 mm. The sand at the test site varied from clean, fine sand to silty fine sand, both having high relative densities. The internal friction angle was reported to be 39°. Table 6-4 shows the soil parameters used for the calculation example. The small-strain shear modulus is estimated from Eq.(6.24), based on correlations from Wichtmann and Triantafyllidis (2014). The soil parameters are otherwise taken from Reese et al. (1974) and Cox et al. (1974).

$$G_{s,\max} = A\frac{\left(a_1 - e\right)^2}{\left(1+e\right)}\left(p_{atm}\right)^{1-n^*}\sigma_m'^{\,n^*} \tag{6.24}$$

Table 6-4. Soil parameters. Mustang Island test site (Reese et al., 1974, Cox et al., 1974)

Parameter	Symbol	Unit	Value
Submerged unit weight	γ'	[kN/m^3]	10
Friction angle	φ	[°]	39
Stiffness coefficient (API)	k_1	[MN/m^3]	34
Uniformity coefficient	Cu	[-]	2.08
Void ratio	e	[-]	0.72

Table 6-5. Empirical correlations from Wichtmann and Triantafyllidis (2014)

Coefficient	Unit	Correlation
a	[-]	a = 1.070 ln(Cu)
b	[-]	b =1
n^*	[-]	$n^* = 0.40\ (Cu)^{0.18}$
A	[-]	$A = 1563+3.13(Cu)^{2.98}$
a_1	[-]	$a_1 = 1.94\ \exp(-0.066\ Cu)$

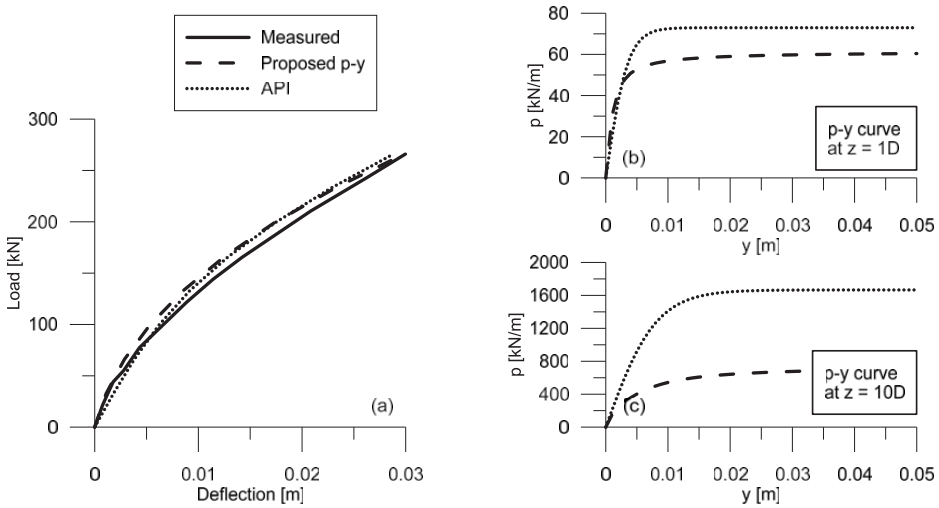

Figure 6-7. (a) Comparison of pile head displacements for the Mustang Island pile load test. (b) Comparison of p-y curves at z = 1D (0.61 m) (c) Comparison of p-y curves at z = 10D (6.10 m)

Both the proposed p-y curves and the API p-y curves predict pile head displacements close to the measured values from Reese et al. (1974). The comparison of the different p-y curves in Figure 6-7 b) and c) reveals however an increasing difference in ultimate resistance with depth. At a depth of 10D below the soil surface, the difference is more than 150 %. The difference in ultimate resistance at depth appears to be of limited influence on the pile head displacement in this case.

Blessington Pile Test

The Blessington pile test is conducted at Blessington, near Dublin, Ireland. The pile test is reported in Doherty et al. (2012). The test pile were driven open ended to an embedment depth of 2.2 m. The pile diameter is 0.34 m, and the wall thickness 14.0 mm. Blessington sand is by Doherty et al. (2012) described as an heavily over-consolidated dense sand with relative density Dr = 100 % and a peak friction angle of $\varphi = 43°$. The particle grading is described as ranging from silty sand to coarser sand, and the groundwater table is well below the pile tip. The small-strain stiffness is taken from Igoe et al. (2011) who gave values ranging from 17 to 30 MPa for Blessington sand in the upper two meters of the soil. An overview of the soil parameters used in the calculation is given in Table 6-6. The curve fitting parameters *a* and *b* for the decay in soil stiffness with increasing strain is based on the recommendations from Wichtmann and Triantafyllidis (2014) in Table 6-5.

Table 6-6. Soil parameters. Blessington test site (Doherty et al., 2012, Igoe et al., 2011)

Parameter	Symbol	Unit	Value
Submerged unit weight	γ	[kN/m^3]	20
Friction angle	φ	[°]	43
Stiffness coefficient (API)	k_1	[MN/m^3]	45
Uniformity coefficient	Cu	[-]	2.50

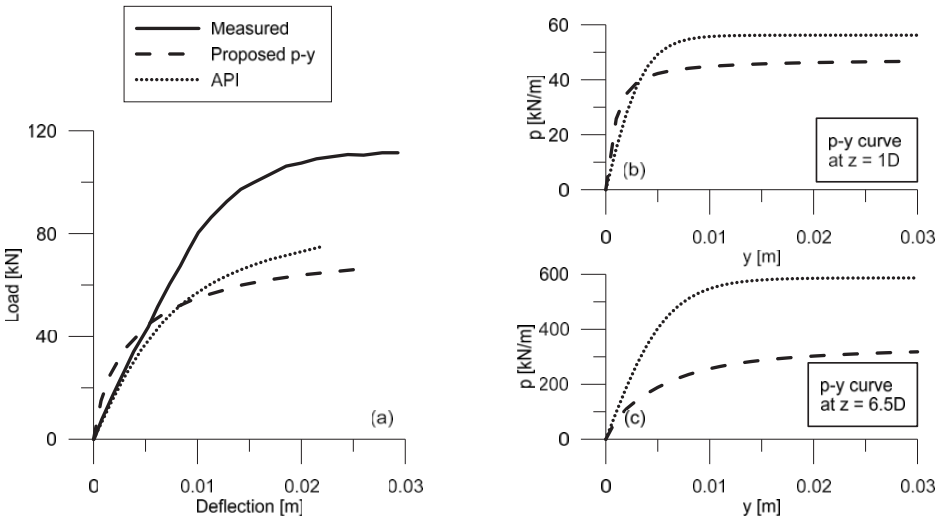

Figure 6-8. (a) Comparison of pile head displacements for the Blessington pile load test. (b) Comparison of p-y curves at z = 1D (0.34 m) (c) Comparison of p-y curves at z = 6.5D (2.20 m)

From Figure 6-8, it is seen that none of the two p-y curve simulations are able to capture the actual pile response. At 0.02 m pile head displacement, the measured load is more than 70 % higher than the predictions. The proposed p-y curves are over-predicting the initial stiffness, and under-predicting the ultimate resistance. The reason for the large deviation in observed and predicted behavior is not fully identified. It is however noted that the ultimate resistance for both methods is based on effective vertical stresses, while the dense, over-consolidated sand is likely to hold large horizontal stresses induced by previous overburden pressures. The ultimate resistance for the proposed p-y curves is based on FEM simulations of a "normally consolidated" Mohr-Coulomb material, while the semi-empirical ultimate resistance for the API p-y curves has the built-in assumption of a $k_0 = 0.4$.

6.8.3 Comparison of Initial Stiffness

The main difference between the initial stiffness for the proposed and the API p-y curves is that the proposed p-y curves relate the stiffness to parameters defined in

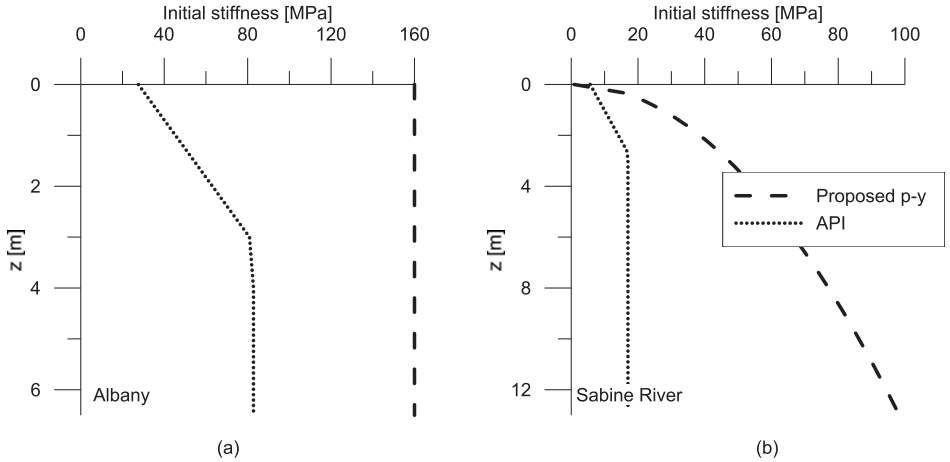

Figure 6-9. Comparison of initial stiffness for the proposed p-y curves and the API p-y curves for clay. (a) Albany test site, constant $G_{s,max}$ measured by Sa'don (2012). (b) Sabine River test site, $G_{s,max}$ estimated from correlations with void ratio and mean stress level after Hardin and Black (1968).

continuum mechanics (E- and G- modulus, Poisson's ratio), while the API curves make use of empirical stiffness correlations. In Figure 6-9a), a comparison of the initial stiffness for the Albany pile test is shown. A comparison of the initial stiffness for the Sabine River pile test is shown in Figure 6-9b).

When the initial stiffness of the proposed p-y curves is compared to the p-y curves given in API-RP-2A, the comparison is made to the linear discretization given in API-RP-2A. The original formulation by Matlock (1970) gives the soil resistance p as a 3rd root-function of the displacement y. As such, if the mathematical expression for these curves is used, the initial stiffness is infinite ($p/y = \infty$). The initial stiffness of the proposed p-y curves corresponds to four times the small-strain shear stiffness of the soil. For the Albany test site, a constant shear stiffness was given over the pile depth by Sa'don (2012). The initial stiffness of the proposed p-y curves is more than four times the API-stiffness at soil surface, the difference reduces to two times the API stiffness with depth. At Sabine River, the $G_{s,max}$ profile is estimated from correlations with void ratio and mean-stress level. The difference in initial stiffness is increasing with increasing depth, to more than 500 % at the pile toe.

When the initial stiffness of the proposed and the API p-y curves for clay are compared, the initial stiffness is seen to be significantly higher for the proposed p-y curves. For sand however, the situation is somewhat different. Figure 6-10 shows a comparison of the initial stiffness for the proposed and the API p-y curves for sand. At the Blessington test site, the initial stiffness of the proposed p-y curves is based on measurements from

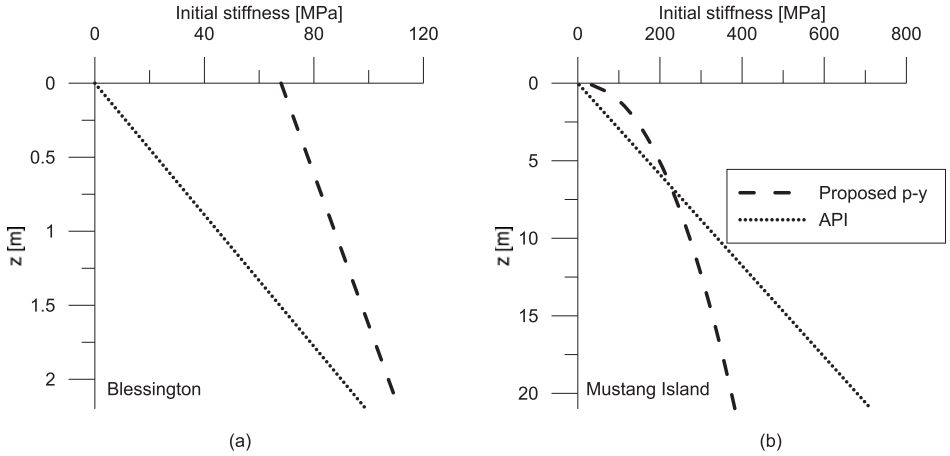

Figure 6-10. Comparison of initial stiffness for the proposed p-y curves and the API p-y curves for sand. (a) Blessington test site, $G_{s,max}$ measured by Igoe et al. (2011). (b) Sabine River test site, $G_{s,max}$ estimated from correlations with the uniformity coefficient and mean stress level from Wichtmann and Triantafyllidis (2014).

Igoe et al. (2011). At the Mustang Island test site, the initial stiffness is based on correlations with the coefficient of uniformity and mean-stress level, proposed by Wichtmann and Triantafyllidis (2014). For both cases, the same picture is drawn; the initial stiffness of the API p-y curves is smaller than for the proposed curves near the soil surface, and increases more rapidly with depth. The higher rate of increase gives the API p-y curves the highest initial stiffness with depth.

The initial stiffness of the proposed p-y curves is equivalent to 4 times the initial shear modulus ($4G_{s,max}$) of the soil. Randolph (2013) suggested $4G_{s,max}$ to be considered an upper limit for the stiffness of p-y curves in clay. It is therefore interesting to note that the initial stiffness of the API p-y curves for sand exceeds this suggested upper bound with depth.

6.8.4 Comparison of Ultimate Resistance

Figure 6-11 compares the ultimate resistance for the soil profiles at the Albany and the Sabine River test sites. For an assumed pile-soil interface roughness of $\alpha = 0$, the ultimate resistance at depth is identical. The proposed p-y curves are seen to provide a higher ultimate resistance close to the soil surface, at the Albany test site up to 30 % at the most.

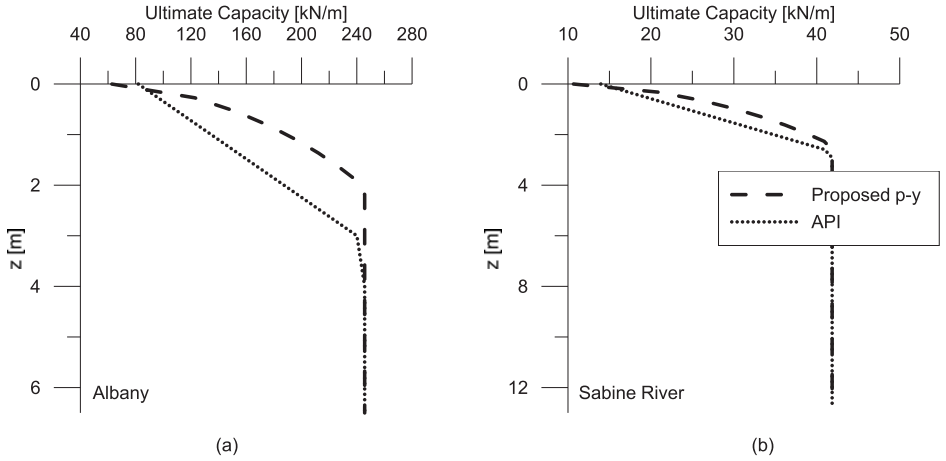

Figure 6-11. Comparison of ultimate resistance for the proposed p-y curves and the API p-y curves for clay. (a) Albany test site. (b) Sabine River test site.

The difference in ultimate resistance is larger between the proposed- and the API p-y curves for sand, with increasing difference with dept. For the Mustang Island sand, the difference is more than 300 % at the pile toe, while the maximum difference at Blessington is close to 200 %. It is important to note that the ultimate resistance of the proposed p-y curves for sand are calibrated by the near surface resistance only (a depth of 1 to 2 pile diameters) and might be prone to error at larger depths.

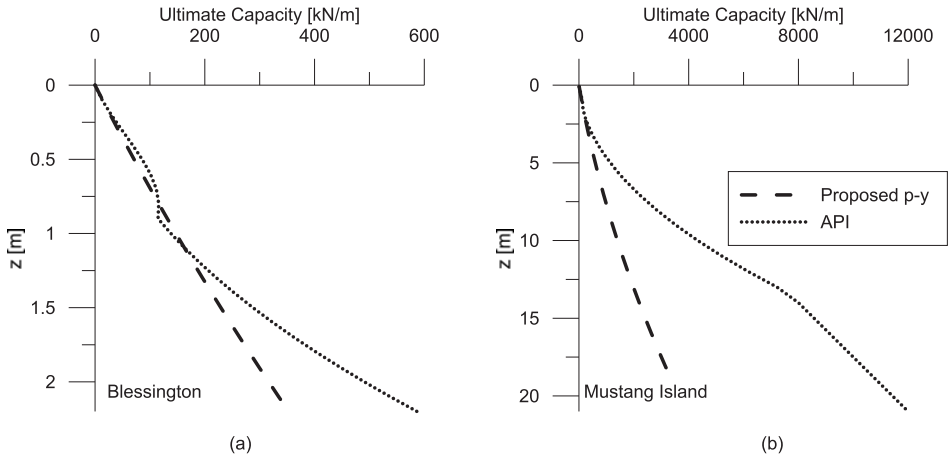

Figure 6-12. Comparison of ultimate resistance for the proposed p-y curves and the API p-y curves for sand. (a) Blessington test site. (b) Mustang Island test site.

6.9 Chapter Summary

A new framework for static soil reaction springs has been proposed where the soil reactions are divided into lateral and rotational springs. The initial stiffness and the ultimate resistance of the springs are based on the findings in Chapters 3, 4 and 5, relating both the stiffness and the ultimate resistance to soil parameters that can be measured in the laboratory or in situ. The transition from initial stiffness to ultimate resistance is proposed modeled by the soil stiffness degradation curve from Hardin and Drnevich (1972), implicitly assuming linearly scalable axis between the stress-strain behavior of the soil and the p-y response.

Due to the theoretical basis of the proposed spring curves, they can incorporate site specific expressions for either of the expressions for ultimate resistance, initial stiffness and stiffness degradation. These can be changed individually, e.g. a change in the expression for ultimate resistance will not influence the initial stiffness and vice versa.

Although the proposed spring curves have a theoretical basis, they represent an idealization of reality and are uncoupled, and not capable of capturing all the continuum effects that will be present in the soil around a laterally loaded pile.

Chapter References

Api, API (2011) API-RP-2GEO: Geotechnical and Foundation Design Considerations. Washington, USA, API Publishing Services.

Baguelin, F, Frank, R & Saïd, YH (1977) Theoretical study of lateral reaction mechanism of piles. *Geotechnique* **27**:405-434.

Cox, W, Reese, L & Grubbs, B (1974) Field testing of laterally loaded piles in sand. In *Offshore Technology Conference*. Houston, Texas, pp. 459-472.

Dnv (1992) DNV-CN-30.4: Classification Note No. 30.4, Det Norske Veritas.

Doherty, P, Li, W, Gavin, K & Casey, B (2012) Field Lateral Load Test on Monopile in Dense Sand. In *Offshore Site Investigation and Geotechnics Integrated Geotechnologies – Present and Future*. London, pp. 459-464.

Gazetas, G (1983) Analysis of machine foundation vibrations: state of the art *Soil Dynamics and Earthquake Engineering* **2(1)**:2-42.

Hardin, BO & Black, WL (1968) Vibration Modulus of Normally Consolidated Clay. *Journal of the Soil Mechanics and Foundations Division* **94(SM2)**:353-369.

Hardin, BO & Drnevich, VP (1972) Shear modulus and damping in soils: Design equations and curves. *Journal of the Soil Mechanics and Foundations Division* **98(7)**:667-692.

Igoe, D, Gavin, K & O'kelly, B (2011) Shaft Capacity of Open-Ended Piles in Sand. *Journal of Geotechnical and Geoenvironmental Engineering* **137(10)**:903-913.

Matlock, H (1970) Correlation for Design of Laterally Loaded Piles in Soft Clay. In *Offshore Technology Conference*. Houston Texas, pp. 577-607.

Matlock, H & Reese, LC (1960) Generalized Solutions for Laterally Loaded Piles. *ASCE Journal of the Soil Mechanics and Foundations Division* **86(5)**:63-91.

O'neill, MW & Murchison, JM (1983) *Evaluation of p-y Relationships in Sands*. Houston, Texas, USA, Report Research Report No. GT-DF02-83.

Randolph, MF (2013) Analytical contributions to offshore geotechnical engineering. In *Proceedings of the 18th International Conference on Soil Mechanics and Geotechnical Engineering - 2nd McClelland Lecture*. Paris, France.

Reese, L, Cox, W & Koop, F (1974) Analysis of Laterally Loaded Piles in Sand. In *Offshore Technology Conference*. Houston, pp. 473–483.

Reese, LC (1996) *Compilation of benchmark lateral load tests on piles in sand and clay*. Port Huneme, CA, USA, Report CR 96.009.

Sa'don, NM (2012) Full scale static and dynamic lateral loading of a single pile. In *Department of Civil and Environmental Engineering*. The University of Auckland, Auckland, New Zealand, vol. PhD.

Stene, VK (2015) Tilbakeregning av fjærkurver for monopelfundament med stor diameter i kohesjonsløst materiale. In *Institutt for Bygg, Anlegg og Transport*. NTNU, Trondheim, vol. MSc.

Wichtmann, T & Triantafyllidis, T (2014) Stiffness and Damping of Clean Quartz Sand with Various Grain-Size Distribution Curves. *Journal of Geotechnical and Geoenvironmental Engineering* **140(3)**:06013003.

Yu, J, Huang, M & Zhang, C (2015) Three-dimensional upper bound analysis for ultimate bearing capacity of a laterally loaded rigid pile in undrained clay. *Canadian Geotechnical Journal*.

7 Impact Vibration Test of Monopile Foundation Model in Dry Sand

7.1 Chapter Preface

The content of this chapter is identical to the paper *Impact Vibration Test of Monopile Foundation Model in Dry Sand* by Hanssen et al. (2015). The motivation behind the performed model test is:

a) To study the physical response of a laterally loaded monopile, and see if it is possible to learn something from the observations
b) To investigate whether the observed under prediction of soil-pile interaction stiffness (Hald et al., 2009, Kallehave et al., 2012, Kallehave et al., 2015) can be related to small-strain soil stiffness.
c) To provide a benchmark test for comparison and validation of different calculation methods

The test has been performed in the NTNU foundation laboratory. The laboratory consists of a 4x4x3 m sand tank, equipped with an automatic sand handling system, documented by Lieng et al. (1984). The sand tank has been modified as a part of this project, in order to make it possible to apply surface loads by a vacuum system. A brief description of this modification is given as a part of the following chapter.

The co-writers, T.E. Helle and two unknown peer reviewers are acknowledged for valuable feedback in reviewing the manuscript for this chapter. The writer is grateful for all the help with both the physical modeling and modification of the sand tank from the technicians Einar Husby, Gunnar Winther, Frank Stæhlie, Per Østensen, Jan Jønland and Tage Westrum. Project student Jørn Hetland is acknowledged for valuable assistance with model set-up and testing.

7.2 Introduction

7.2.1 Motivation

Offshore wind turbines are providing an increasing portion of world-wide energy generation capacity, and are in Europe alone targeted to increase from 5 GW (2012) to 150 GW by 2030 (EWEA, 2009, EWEA, 2013). Harsh environmental conditions, considerable structural dimensions and strict performance criteria bring challenges to engineering design of the support structures, including the foundations. This paper focuses on the monopile foundation concept, and in particular on the horizontal soil-structure interaction stiffness of monopiles in the Fatigue- and Serviceability Limit State (FLS and SLS) conditions.

Measurements on full-scale, operating offshore wind turbines have shown that the lateral soil response to monopiles is under-predicted by current design methods (Kallehave et al., 2012, Hald et al., 2009). Offshore wind turbines experience large lateral loads from wind and waves, and the lateral foundation stiffness is of particular interest due to both the dynamic nature of the excitation forces and strict deformation criteria. Environmental loads such as wind and waves, repeated loads from the rotor and blade passing drag-effects all underline the importance of controlling the structural and soil dynamics present in the system. The different aforementioned loads may all be categorized inside limited frequency bands as shown in Figure 7-1 (Lombardi et al., 2013). The first eigenfrequency of offshore wind structures is commonly targeted to fall within the narrow frequency band denoted soft-stiff in the same figure. The term soft-stiff refers to an eigenfrequency lower than the blade passing frequency (3P) and higher than the rotor frequency (1P). Precise prediction of the horizontal foundation stiffness is required in design to keep the system eigenfrequency outside the excitation frequency bands in order to avoid system resonance.

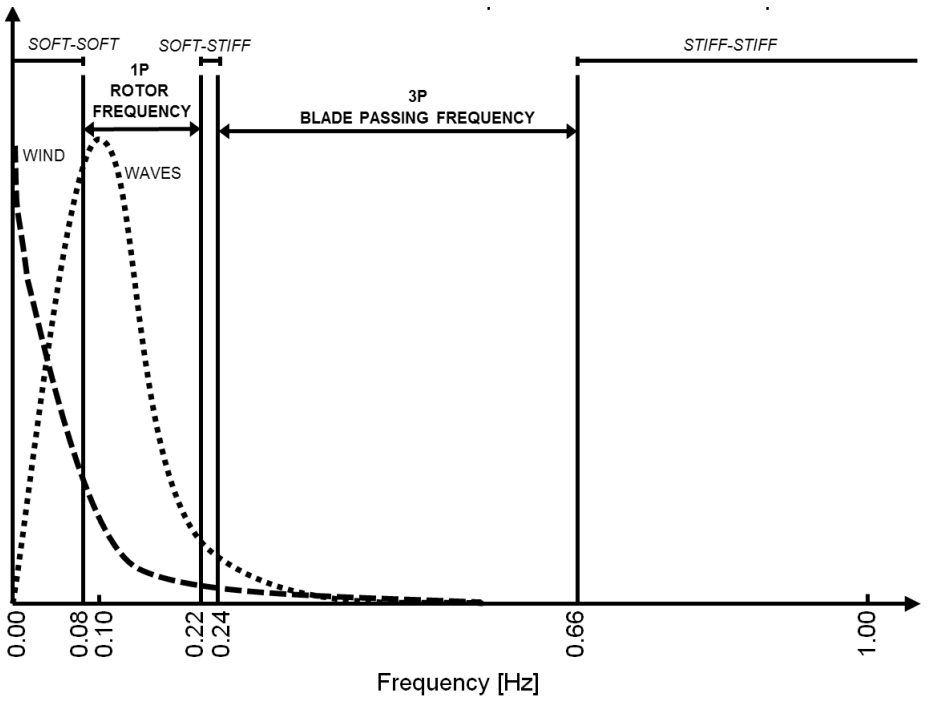

Figure 7-1. Simplified power spectral density of the force frequencies applied to typical three bladed 3·6 MW offshore wind turbine with an operational interval in the range of 0.08–0.22 Hz. (Lombardi et al., 2013)

7.2.2 Soil Stiffness

One of the key components in the horizontal pile-soil interaction stiffness is the soil shear stiffness. Soil shear stiffness is known to vary among soil types and to be dependent on both stress and strain magnitude. Figure 7-2, based on Atkinson and Sallfors (1991), shows the characteristic trend for the variation of the shear stiffness G based on variation in shear strain γ. The reduction in soil shear stiffness is typically more than a factor of 10 for shear-strains increasing from 0 to 1 %, and is highly nonlinear.

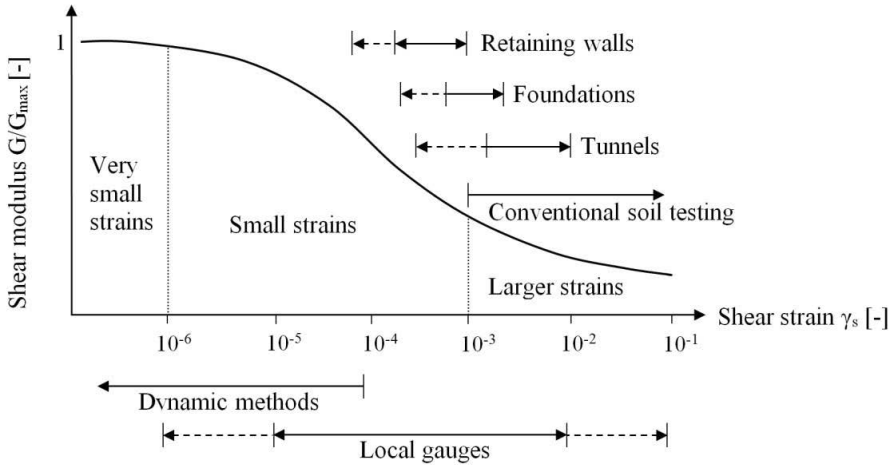

Figure 7-2. Characteristic stiffness-strain behavior of soil with typical strain ranges for laboratory tests and structures. After Atkinson and Sallfors (1991), Mair (1993) and Benz (2007).

Figure 7-3a) shows the pile displacement profile from Augustesen et al. (2010) calculated for a static ultimate limit state (ULS)-load of a 2.0 MW wind turbine at Horns Rev, offshore Denmark. The outer diameter of the monopile considered is 4.0 m. No exact relationship between average representative strain and lateral pile displacements exist; however, simple linear relations have been suggested (e.g. Kagawa and Kraft (1980), Klar (2008), Osman and Bolton (2005)). The expression from Kagawa and Kraft (1980) in Eq.(7.1) is based on the theory of elasticity and may be written as:

$$\gamma_{avg} = \frac{1+\mu}{2.5D} y \qquad \textbf{(7.1)}$$

where μ = Poisson's ratio of the soil, D = pile diameter, and y = lateral pile displacement. Eq.(7.1) is an approximate relationship, but serves well for illustrative purposes and is used for Figure 7-3b) which shows the estimated average representative shear strain with depth for the corresponding displacement profile in Figure 7-3a). By comparing the soil

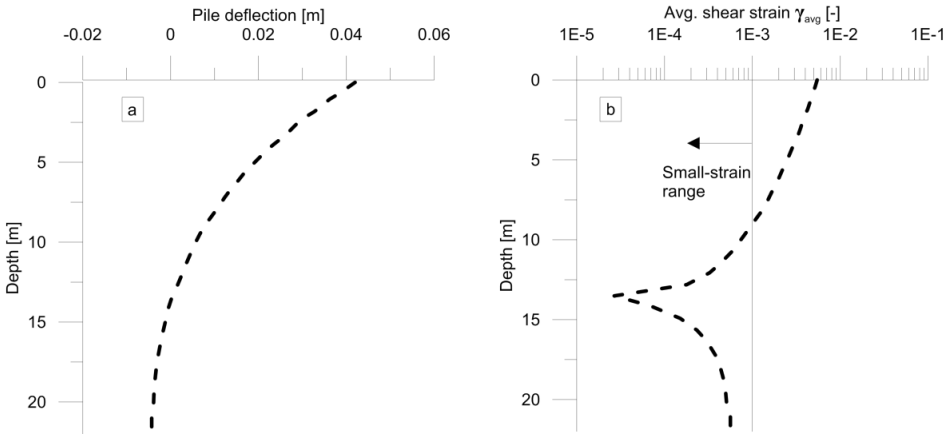

Figure 7-3. (a) Pile deflection from ULS loads (Augustesen et al., 2010) and b) estimated average soil shear strain based on Eq.(7.1).

strain profile in Figure 7-3b) with Figure 7-2 from Atkinson and Sallfors (1991), it becomes evident that a significant part of the soil along the pile is experiencing representative strains below the small strain limit defined in Figure 7-2 even in ULS-condition. As SLS-and FLS loads are considerably smaller than ULS loads, an even larger portion of the soil is expected to be in the small-strain area for these limit states. Following the above reasoning, small-strain stiffness is expected to contribute significantly to the lateral soil response experienced by monopiles of the size used for offshore wind turbines. For the model test presented in this paper, emphasis is placed on the relation between lateral soil response and the small-strain stiffness of the soil.

7.2.3 Model Test Performed in This Study

This paper presents a 1:20 model scale test of a monopile foundation for offshore wind turbines, installed in dry laboratory sand. The test is performed at 1g, under fully controlled laboratory conditions. Near surface soil effects are eliminated by overburden pressures applied with a vacuum system. Soil-pile interaction stiffness is measured from a free vibration test, with vibration initiated by a horizontal impact load to the top of the pile. Overburden pressures and corresponding stress-dependent soil stiffness are controlled by adjusting a vent on the underpressure system. Eigenfrequencies of the pile-soil system are derived from pile accelerations and bending moments, measured with accelerometers and strain gauges mounted on the pile. Small strain soil stiffness is derived from shear wave velocity measurements in the sand. In this context, the system-eigenfrequency is an indirect measure of the pile-soil interaction stiffness. The pile displacement profile for different oscillation amplitudes is up-integrated from accelerometer- and strain gauge measurements. The underlying idea for the presented model test is to provide benchmark results for comparison of different calculation methods of laterally loaded monopile foundations. The model test presented gives

important insight into the physics of the problem of laterally loaded piles with small length to diameter ratios. As a tool for benchmarking of calculation methods, the scale model and the presented results can be used directly. If the presented results are to be used at prototype scale, scaling laws as suggested by Iai (1989), Iai et al. (2005) and Bhattacharya et al. (2011) should be used.

7.3 Test Setup

The test setup is sketched in Figure 7-4a). A horizontal impact load generates an initial velocity at the pile top and excites it over a wide range of frequencies. The horizontal impact load is modeled by a 15.9 kg, soft-tipped hammer. The hammer acceleration and duration of the impact are measured by one accelerometer of model 353B03, manufactured by PCB Piezontronics Inc, USA, mounted at the rear end of the hammer. The hammer is suspended in two vertical strings of 2.7 m length. The impact load is obtained by dragging the hammer 0.13 m sideways and releasing it into a pendulum swing aligned in direction with the strain gauges mounted on the pile.

7.3.1 Sand Tank and Overburden Pressure System

The sand tank is box shaped with sides of 4.0 m and a maximum depth of 3.0 m. For the current test-setup it is filled with 2 m of Hokksund sand, and sealed with an airtight tarpaulin at the soil surface. The concrete floor and walls of the sand tank are made airtight by paint to prevent any air leakage through the concrete, and by silicone rubber seals along any perforations. A liquid ring vacuum pump of type ME X250/GX manufactured by Finder Pompe S.p.a., Italy, is connected to two lines of perforations in the tank floor, creating an underpressure chamber. The perforations in the tank floor are

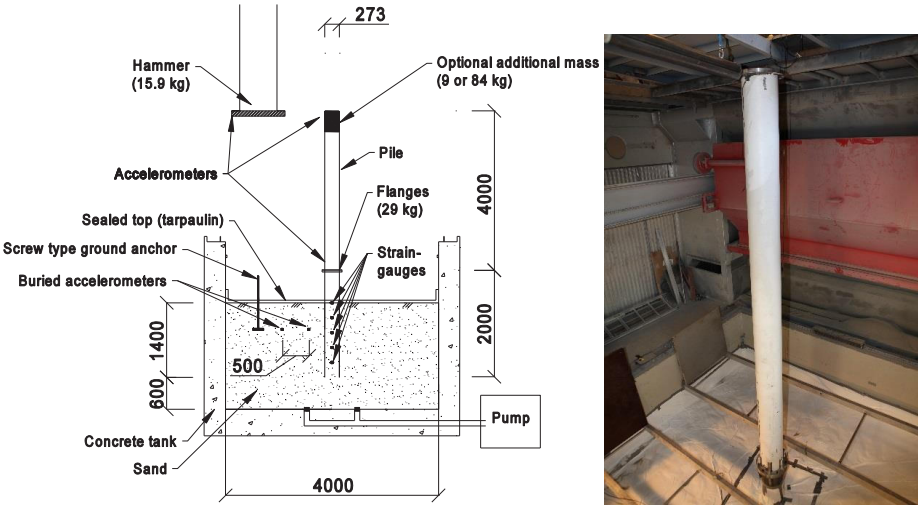

(a) (b)

Figure 7-4. Model test setup.

covered by geotextiles to prevent sand from getting into the pump. Applying overburden pressures through an underpressure chamber makes it possible to overcome near surface scale effects by increasing soil effective stresses. For the current test setup, a maximum underpressure of -56 kPa has been achieved. The underpressure can be adjusted to any value between 0 and -56 kPa by regulating air leakage of the system through a vent installed on the pipeline between the vacuum pump and the sand tank. The tank itself is equipped with an automatic sand handling system, making it possible to manage the considerable amount of sand necessary for filling the tank.

7.3.2 Model Pile

The model pile is replicating a monopile foundation of 5.6 m diameter and 28 m embedded length at approximately 1:20 scale. The pile is extended above the soil surface, replicating a total length of 95 m of in-water length and turbine tower height. The model pile is made from regular construction steel (steel grade P235TR1), with an outer diameter of 0.273 m and wall thickness of 4.0 mm. Total length of the open ended steel pipe is 6.0 m, whereof 1.4 m is embedded. The steel pipe is divided into a 2.0 m long lower part and a 4.0 m long upper part that after installation into the sand tank are mounted together by flanges (welded onto the outer surface of both parts of pile). A division of the pipe pile into two parts is mainly done for practical reasons; however, it is noted that the extra mass from flanges, bolts and nuts of 29 kg is favorable with respect to replicating the connection piece between foundation and structure found on full-scale offshore wind turbines.

The embedded part of the pile is instrumented with 5 sets of strain gauges, type 6/120ALY11, manufactured by Hottinger Baldwin Messtechnick GmbH, Germany. The strain gauges have a gauge factor of 2.07 and are arranged in line at 280 mm center-to-center spacing and attached to the outer surface of the pile using a fast curing acrylic polymer based adhesive. The lowermost set of strain gauges is located at a distance of 280 mm above the pile tip, while the upper one is located in level with the sand surface. The strain gauges are mounted at front and back of the pile with respect to load direction, utilizing full Wheatstone bridge circuit configuration. A thin cover layer of solvent based polyurethane lacquer is applied over the attached gauges and also locally on their lead connections, in order to prevent mechanical damage during handling, installation and testing. The lower pile section with strain gauges mounted is shown in Figure 7-5a).

The upper part of the pile is instrumented by two accelerometers of model 353B03, manufactured by PCB Piezontronics Inc, USA. These are located at the top end and just above the connection flange. A close-up of the accelerometer mounted just above the connection flange is shown in Figure 7-5b). Pile and flange properties are listed in Table 7-1 and visualized in Figure 7-4.

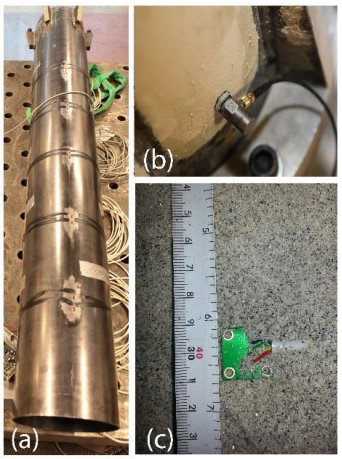

Figure 7-5. Instrumentation: (a) strain gauges mounted on the lower part of the pile; (b) accelerometer mounted just above the connection flange; and (c) accelerometer to be buried in the sand

Table 7-1. Pile Parameters

Parameter	Unit	Model Scale
Diameter	[m]	0.273
Total height	[m]	6.00
Wall thickness	[m]	0.004
Pipe bending stiffness	[kNm^2]	6422
Steel unit weight	[kN/m^3]	7850
Flange mass	[kg]	29
Optional top mass	[kg]	84/9
Embedded pile depth	[m]	1.40

7.3.3 Sand Characterization

The model pile is partially embedded in a uniform, medium grained, medium dense, quartz sand from a natural glacifluvial deposit in Hokksund (Norway). The grain shape varies from cubical to somewhat elongated and angular.

The sand is air-pluviated into the tank by a spreader wagon to a porosity of n = 39.9 %. During filling, the vertical distance between the sand surface and the spreader wagon is gradually decreasing. The effect of this with respect to sand density has been investigated by Lieng et al. (1984) by isotopic sounding, Cone Penetration Testing and ordinary unit

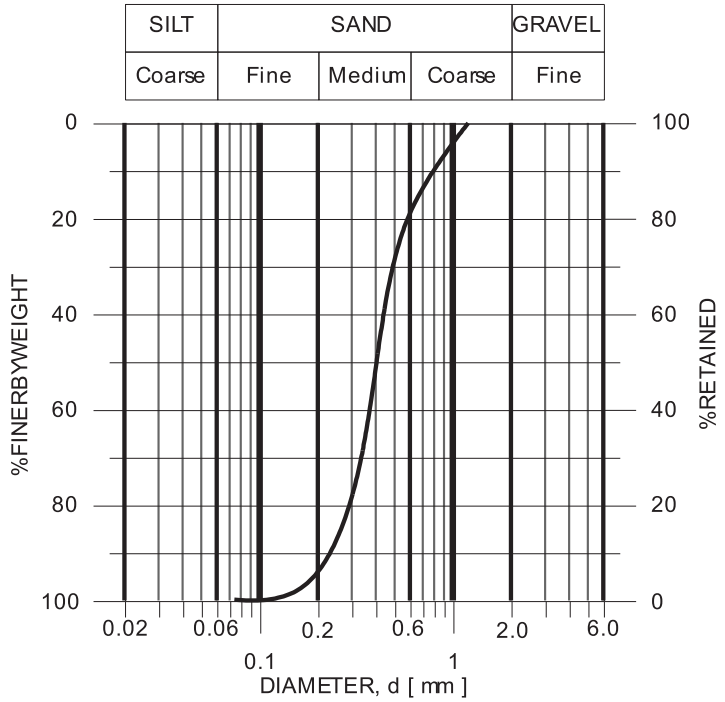

Figure 7-6. Grain size distribution of Hokksund sand

Table 7-2. Key parameters Hokksund sand

Parameter	Unit	Value
Internal angle of friction (ϕ)	[°]	38
Porosity (n)	[%]	39.9
Min. porosity (n_{min})	[%]	36.4
Max. Porosity n_{max})	[%]	48.8
Relative density (Dr)	[%]	76
Density (γ)	[kN/m^3]	16.0
Specific density (γ_s)	[kN/m^3]	27.1
Coefficient of uniformity ($C_u = d_{60} / d_{10}$)	[-]	2.04
Mean grain size (d_{50})	[mm]	0.38

Table 7-3. Mineral content Hokksund Sand (Moen, 1978)

Mineral	%
Quarts	35
Na-Feldspar	25
K-Feldspar	20
Mica	10
Amphibole	5
Other	5

weight measurements and only small and very limited variation in sand unit weight (± 0.7 %) where found.

Hokksund Sand has been employed as model sand for the Norwegian University of Science and Technology for more than three decades and is well documented (Moen, 1978, Lieng, 1988, Leahy, 1984, Tadesse, 2000). A list of key parameters for Hokksund Sand at a porosity of n = 39.9 % is given in Table 7-2. The grain size distribution and mineral composition is presented in Figure 7-6 and Table 7-3 respectively.

7.3.4 Sand and Pile Installation Procedure

After depositing the first 0.6 m of sand, the lower part of the model pile is lowered into the tank by crane and aligned vertically at the tank center. During filling, temporary support to the connection flange is provided by horizontal steel wires tensioned to the tank corners. A few cm penetration of the pile tip ensures horizontal support at the lower end. Sand is rained in inside and around the pile to a pile embedment depth of 1.4 m, resulting in 2.0 m depth of the sand bed. The connection flange is removed from the lower part of the pile during sand deposition to limit turbulence effects around the pile. The open-ended top and bottom of the pile and the described installation procedure represents a “wished in place” installation. An airtight, custom-made tarpaulin is put on top of the sand and sealed against the tank walls and the perforation for the pile with standard duct-tape. The upper part of the pile is mounted using connection flanges and 6 bolts/nuts equally spaced around the circumference of the pile. A system of temporary walking bridges attached to the steel top frame of the sand tank have been used consistently throughout the installation and testing process to avoid disturbing the soil surface by walking on it. The walking bridges have adjustable height and may be used for all levels of filling. They are removed during sand deposition.

7.3.5 Buried Accelerometers for Shear Wave Velocity Measures

The small-strain soil stiffness is derived from measured shear wave velocities in the sand. The small-strain shear modulus is related to the shear wave velocity and the density of the sand as described by Eq.(7.2) (e.g. Kramer (1996)). Two three-way

accelerometers of type ADXL335, manufactured by Analog Devices Inc., USA, are installed 0.5 m below the sand surface for recording shear wave velocities at different overburden pressures. A close-up photo of one of the buried accelerometers is shown in Figure 7-5c). A screw type ground anchor is installed to the same depth of 0.5 m, and used as an excitation source. Shear waves are induced by hitting the ground anchor vertically, resulting in shear waves spreading radially out from the ground anchor. Differences in shear wave arrival time and a known distance of 0.50 m (ref. Figure 7-4) between the two accelerometers are used to calculate shear wave velocities. Setup and testing for wave speed measurements are performed separate from the lateral pile testing to avoid interfering waves.

$$G = v_s^2 \rho \tag{7.2}$$

Accelerometer Installation Procedure

After depositing the first 1.5 m of sand, the accelerometers were placed and leveled on the sand surface at a radial distance of 0.45 m and 0.95 m from center of the ground anchor. Travel time for p- and s-wave reflections from the tank floor and walls were calculated based on typical wave speeds for dry sand (Bartake and Singh, 2007, Bauer et al., 2007), and the specified radial distances were chosen with ~20 % allowance with respect to reflected signals from the tank boundaries. The two accelerometers and their local lead connections were covered by a thin layer of solvent based polyurethane lacquer for protection against mechanical wear, and buried locally by an approximately 0.05 m thick layer of sand, laid out by hand to protect leveling of the accelerometers before depositing the last 0.5 m of sand. The ground anchor was screwed down to 0.5 m below the sand surface after the entire sand volume had been deposited.

7.3.6 Data Acquisition and Instrumentation

The overburden pressure applied by the vacuum pump is measured by a digital pressure sensor, type Panasonic DP101A-E-P (manufactured by Panasonic Electric Works SUNX Co. Ltd), located just underneath the tarpaulin. An analog vacuum manometer of type Wika 111.10, manufactured by Wika GmbH&Co, Germany is located on the pipe system in front of the vacuum pump to check the uniformity of the applied pressure through the soil. The strain gauge signal is sent to a laptop through amplifiers of type Clip AE301, manufactured by Hottinger Baldwin Messtechnick GmbH, Germany, and a DAQ of type NI-USB6210 manufactured by National Instruments Co., USA. One amplifier was used for each full bridge circuit. The amplifiers had an accuracy of ±0.03 % and the DAQ an accuracy of ±50 ppm of the sample frequency (recorded eigenfrequency of the pile). Output from the buried accelerometers were sent to the laptop through a DAQ, type NI-USB6210, while the signal from the accelerometers at

the rear end of the hammer and the upper part of the pile went through a signal conditioner of type 482A22 from PCB Piezotronics Inc., USA, and a DAQ, type NI-USB6210.

A series of recording scripts were programmed on the laptop in the Windows-based programming language LabView, and set up to sample the strain gauge signal and the pile mounted accelerometers with a sampling rate of 15 kHz. The signal from the buried accelerometers was sampled at a rate of 30 kHz, while the signal from the accelerometer mounted at the rear end of the hammer was sampled at 1 kHz.

7.4 Test Program

A test program of 60 impact vibration tests and 60 measurements of shear wave arrival time has been performed. To verify the repeatability of the test-setup, five tests were run for each load case. 12 load cases were run for the impact vibration test of the model pile, 6 load cases were run for the shear wave arrival time measurements for the buried accelerometers.

Table 7-4. Test program

Overburden pressure	**Top mass 84 kg**	**Top mass 9 kg**	**Shear wave velocity measurements**
[kPa]	No. of tests:	No. of tests:	No. of tests:
0	5	5	10
10	5	5	10
20	5	5	10
30	5	5	10
40	5	5	10
55	5	5	10

7.4.1 Impact vibration testing of model pile

The pile is hit horizontally at the pile top, exciting it at a broad spectra of frequencies. The first eigenfrequency and damping of the pile-soil system and its dependency of overburden pressure and structural mass are investigated. Six different overburden pressures and two different top-masses are combined into a total of 12 load cases. The impact vibration tests are performed with small deflection amplitudes to obtain a strain magnitude in the soil assumed representative for the soil in fatigue and serviceability limit state conditions around full-scale monopiles.

7.4.2 Shear Wave Velocity Measurements

Shear wave arrival times are measured for the 6 different overburden pressures, thus defining 6 different load cases. The particle motion induced by a travelling shear wave

corresponds to strains of several magnitudes less than strains for traditional engineering problems (cf. Figure 7-2). The corresponding shear stiffness found from the shear wave velocity is assumed to represent the small-strain stiffness of the sand (G_{max}).

7.5 Results

7.5.1 Impact vibration tests

Almost identical results were obtained for all tests at each overburden pressure for the impact vibration testing, implying excellent repeatability of the tests. Figure 7-7 and Figure 7-8 presents the experimental results in terms of the recorded time series from the uppermost strain gage (the strain gauge in line with the soil surface). Bending moment amplitudes for the different strain gauge locations are shown in Figure 7-9. The synchronized oscillations for the different strain gauge locations imply that the first eigenmode is the dominating one, and that bending moments from higher modes are negligible. The axial strain in the pile is recorded over a time interval of 8 s. The high sampling frequency (15 000 Hz) and the short time series (8 s) provides a resolution in the time domain ($6.67*10^{-5}$ s) superior to the resolution in the frequency domain (~0.12 Hz). Both the first eigenfrequency and damping of the pile-soil system are therefore analyzed in the time domain. The first eigenfrequency is the inverse of the first eigenperiod. The system damping is evaluated from the logarithmic decrement formula e.g. Kramer (1996).

Eigenfrequency

One of the main findings from the tests presented is that the first eigenfrequency of the pile-soil system is non-constant over the measurement. Figure 7-10 and Figure 7-11 show the variation in eigenfrequency plotted against time for all load cases. The eigenfrequency increases with time for all tests, being less pronounced for the tests where more overburden pressure is applied. The system mass, the structural stiffness and the applied overburden pressure are kept constant throughout each test. The only known variable in the system is then the strain dependency of the soil stiffness and the strain-dependent material damping in the soil, implying that the eigenfrequency of the pile-soil system is dependent on the representative strain level in the sand. If the first eigenmode of this system is approximated by a 1DOF system, the influence from damping on the eigenfrequency may be estimated by Eq.(7.3):

$$f_{n,d} = f_n\sqrt{1-\xi^2} \tag{7.3}$$

where $f_{n,d}$ is the damped eigenfrequency, f_n is the undamped eigenfrequency and ξ is the damping. As will be described later in this section, the system damping is found to be in the range from 0.2 % - 3 %. According to Eq.(7.3), a change in system damping from 3 % - 0.2 % will reduce the damped eigenfrequency with $\sim 3\cdot 10^{-3}$ Hz for the range of

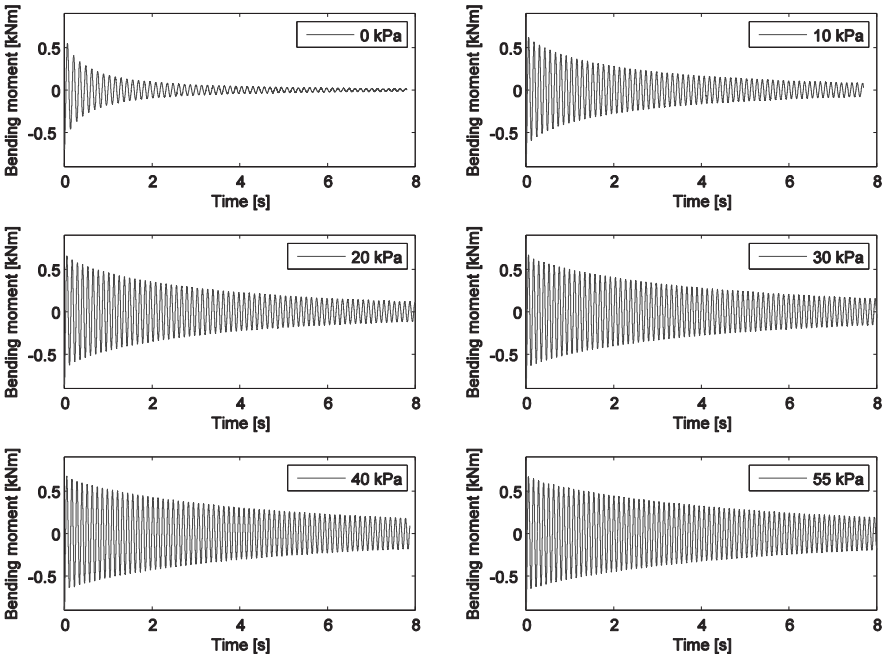

Figure 7-7. Recorded time series for six different overburden pressures, 9 kg top mass

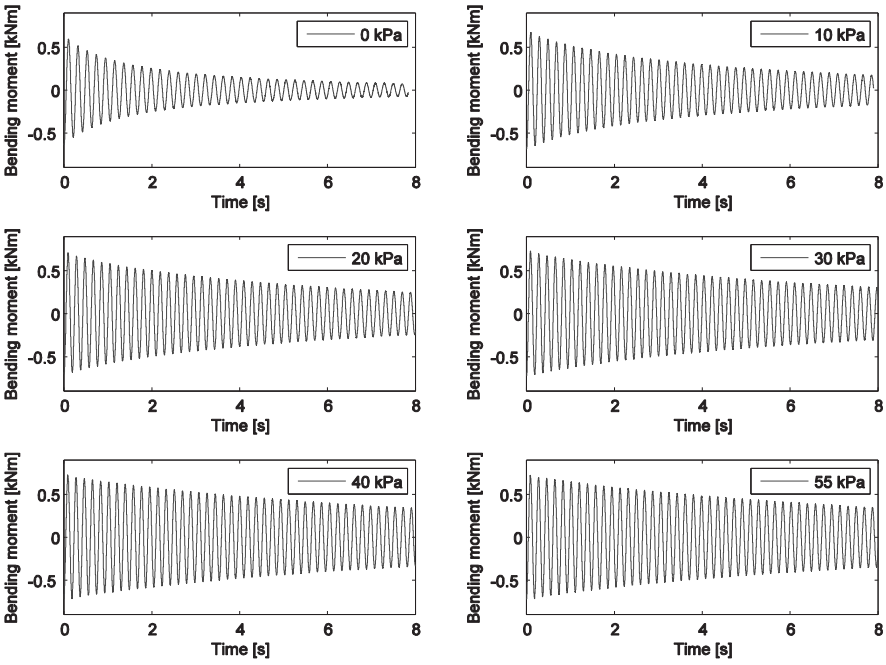

Figure 7-8. Recorded time series for six different overburden pressures, 84 kg top mass.

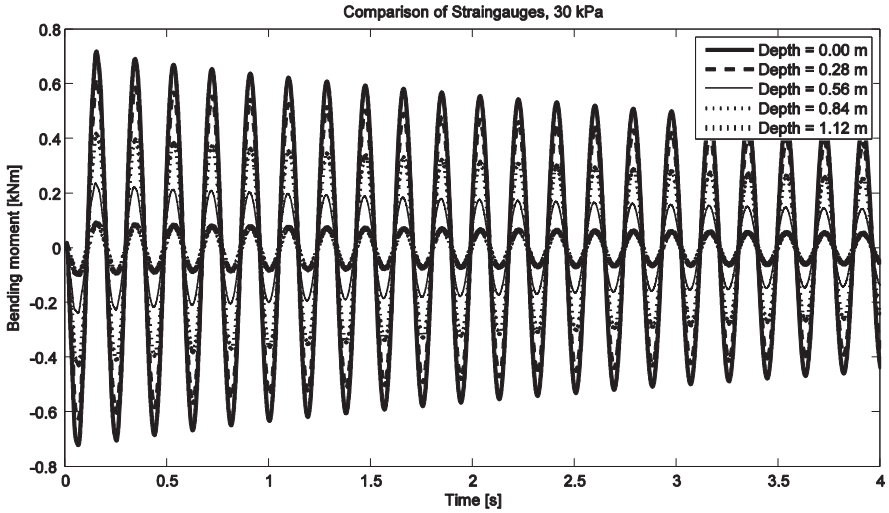

Figure 7-9. Comparison of time series with different strain gauge levels; applied overburden pressure of 30 kPa.

frequencies measured. Considering the 1DOF analog, the influence from damping to the change in first eigenfrequency is likely to be negligible. Excluding the variation in damping as a probable cause for the change in eigenfrequency leaves the influence of the strain dependent soil stiffness as the main explanation of the observed change.

Figure 7-10 and Figure 7-11 reveal a distinct relationship between applied overburden pressure and system eigenfrequency. This relationship fits well with classical theory of

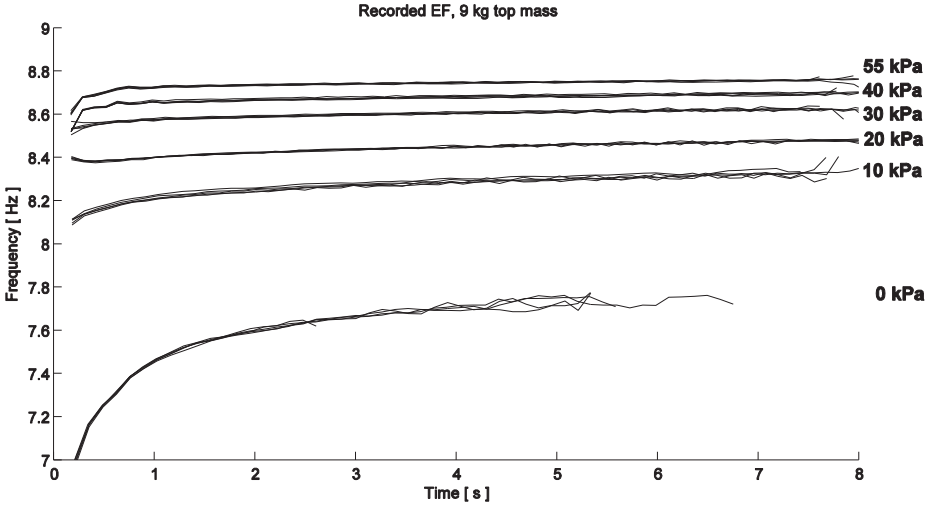

Figure 7-10. Recorded eigenfrequency, 9 kg top mass. EF, eigenfrequency.

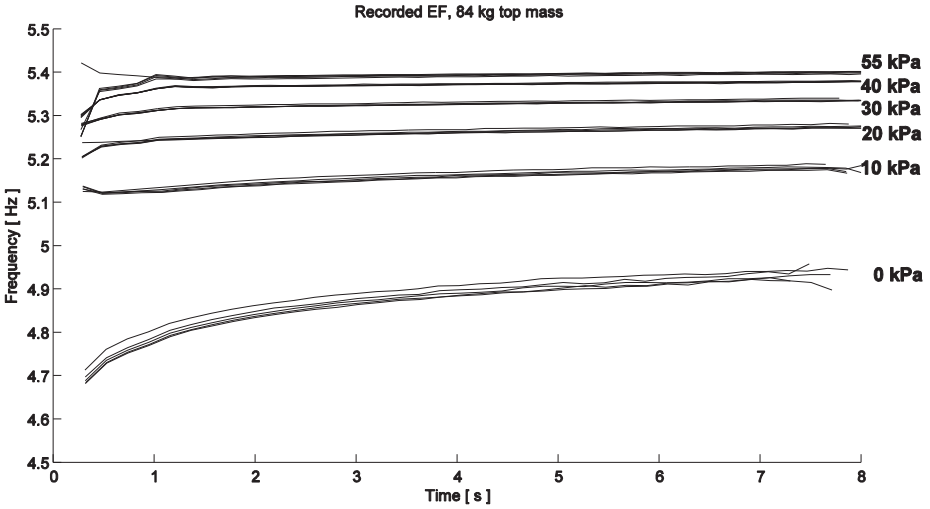

Figure 7-11. Recorded eigenfrequency, 84 kg top mass. EF, eigenfrequency

Table 7-5. Recorded eigenfrequencies

Applied overburden pressure	1st eigen frequency 9 kg Top Mass	1st Eigen frequency, 84 kg Top Mass
[kPa]	[Hz]	[Hz]
0	6.98 - 7.72	4.68 - 4.93
10	8.10 - 8.32	5.11 - 5.18
20	8.34 - 8.47	5.21 - 5.27
30	8.51 - 8.62	5.28 - 5.34
40	8.52 - 8.69	5.30 - 5.38
55	8.60 - 8.76	5.26 - 5.40

stress dependent stiffness of sands, e.g. as described by Ohde (1939), Janbu (1963), Seed and Idriss (1970) and Hardin and Richart (1963). Numerical values for the recorded eigenfrequencies are given in Table 7-5.

System Damping

As for the first system eigenfrequency, the system damping at the first eigenfrequency is found to be non-constant over the free vibration time. The variation of system damping with time shown in Figure 7-12 and Figure 7-13 is calculated based on the ratio between neighboring amplitudes in the time domain. The damping shown in Figure 7-12 and Figure 7-13 thereby expresses the damping over one deformation cycle, displaying how more energy is dissipated during the first cycles of deformation compared to the later ones. As no changes are expected for the structural damping during the tests, all variation in system damping during testing is assumed to be caused

by damping in the soil. Soil damping can be divided into radiation damping and material damping (hysteresis). The hysteresis material damping is known to be highly dependent on the strength mobilization

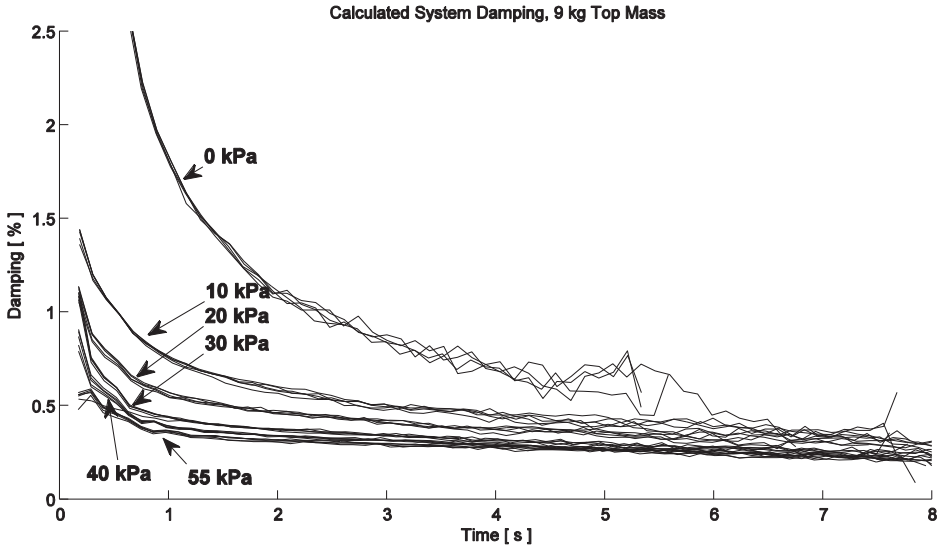

Figure 7-12. Calculated system damping, 9 kg top mass.

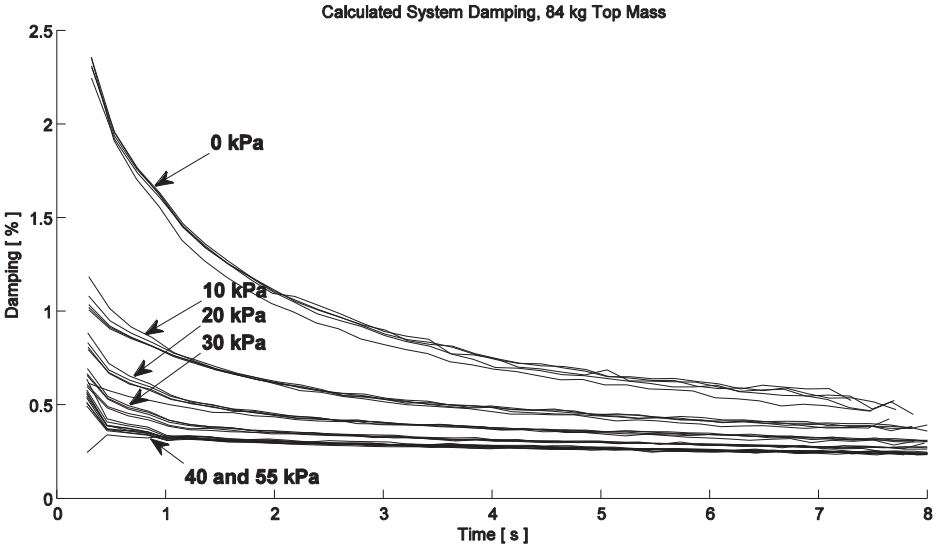

Figure 7-13. Calculated system damping, 84 kg top mass.

in the soil, and is believed to be the main source of variation in damping for the different overburden pressures. For a given geometry, only small and negligible variation in radiation damping is expected. The damping presented in Figure 7-12 and Figure 7-13 reduces rapidly over the first few seconds of the recording, and displays a strong dependency on the applied overburden pressures. The observed trends indicate that damping at all pressure levels approaches the same asymptotic value of $\xi = 0.2$ % with time. Although the damping values presented are for the entire pile-soil system, the observed dependency of soil stress level and pile bending moment amplitude are in line with existing knowledge of soil damping from e.g. Seed et al. (1986) and Wichtmann and Triantafyllidis (2013) who have described soil damping as a function of confining stresses and soil shear strain level. Back calculation of the presented tests with respect to estimating the soil damping as a function of the observed system damping is considered to be outside the scope of this work.

Pile Displacements

By combining the equations of motion and beam theory, the pile displacement u may be described as a function of time and location on the pile:

$$u = f(x,t) \tag{7.4}$$

The second derivative of the beam displacement with respect to time is acceleration, and the second derivative of beam displacement with depth is curvature:

$$\frac{\partial^2 u}{\partial t^2} = a \tag{7.5a}$$

$$\frac{\partial^2 u}{\partial x^2} = \frac{M}{EI} \tag{7.5b}$$

where u = displacement, x = distance along the pile, t = time, a = acceleration, M = pile bending moment and EI = pile bending stiffness.

The test pile is instrumented with two accelerometers (cf. Section 7.3), and the peak displacement at the accelerometer locations is found by integrating the peak acceleration twice with respect to time. The recorded acceleration time histories show a damped sinusoidal motion around the initial equilibrium position. A sinusoidal motion oscillating around zero gives integration constants of zero, and no further boundary conditions are needed when integrating from accelerations to displacements at the accelerometer locations.

The curvature amplitudes found from strain gauge measurements on the embedded part of the pileare used to create a displacement profile for the embedded portion. A fifth-order polynomial equation is fitted to the curvature profile with the least squares method, and is integrated twice to obtain the displacement profile for the embedded part

of the pile. In order to integrate from curvature to displacements, boundary conditions are required to determine the integration constants. A dynamic 2D-analysis of the model pile is performed with the FEM-program Robot Structural Analysis (Autodesk, 2015), where

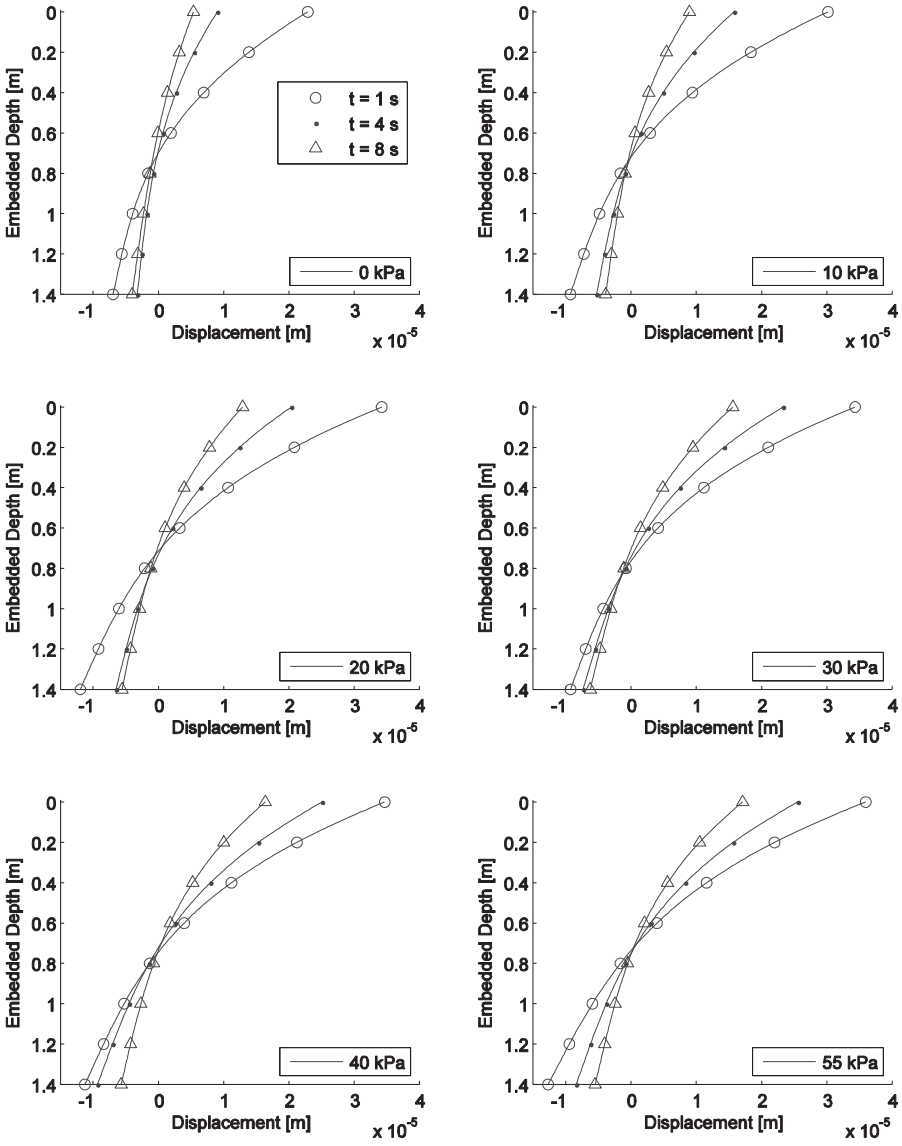

Figure 7-14. Peak-displacement profiles for the embedded part of the pile; peak displacement after 1, 4 and 8 s

the pile is idealized as a beam. The structural data given in Table 7-1 is used to model the beam. The sand is represented by linear elastic springs, with spring stiffness calibrated to match the first eigenfrequency of the pile-soil system. The first modal shape of the structure found from the 2D-simulation is used to extrapolate the displacements found from the top accelerometer down to the soil surface. The extrapolated displacement and the first modal shape are used as boundary conditions for rotation and displacement at the soil surface. Known boundary conditions at the soil surface are then sufficient information to integrate the curvature twice and find the pile displacement profile. The obtained displacement profiles for the load cases with 84 kg top mass are presented in Figure 7-14.

Figure 7-14 shows peak displacements at 1, 4 and 8 seconds after the impact load for different applied overburden pressures and a top-mass of 84 kg. By studying Figure 7-14 it is observed that the peak displacements are increasing with increasing applied overpressure. For an undamped system, the opposite trend would be expected, namely that the softer system would have the larger displacements. This is also the expected initial response in a damped system. However, for the system in question, the displacement some time after the impact is influenced by the energy dissipated due to damping. The system damping is found to decrease with applied overburden pressure (cf. Figure 7-12 and Figure 7-13), and thereby is the displacements with time larger for the larger applied overpressures. In Figure 7-14, the effect of dissipated energy due to damping is visible already after 1 s of vibration.

Hammer Impact

The variation in peak acceleration found from the rear end of the hammer was limited to the range 62.3 m/s^2 - 68.1 m/s^2, giving an average peak force of ~ 1 kN. Impact time was

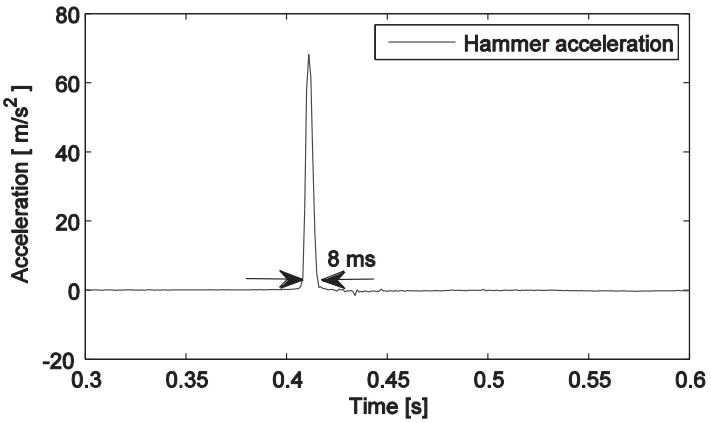

Figure 7-15. Average recorded hammer acceleration.

averaged to 0.008 s, with variation <0.001 s. The acceleration curve might well be approximated by the shape of an isosceles triangle, as seen from the example impact acceleration shown in Figure 7-15

7.5.2 Shear Wave Velocity Measurements

Figure 7-16 gives the arrival times at the accelerometer locations for the 6 load cases tested. One test is presented for each load case. Figure 7-17 shows the interpreted shear wave velocity and the calculated shear stiffness plotted against vertical effective stress, and Table 7-6 shows the shear wave velocities along with their standard deviations. The difference in shear wave arrival time has been interpreted both manually by visual control and automatically by cross-correlation, with consistency in results from both methods. The shear stiffness is calculated based on the theory of linear, isotropic elasticity, as described in Eq.(7.2). The small-strain shear modulus G_{max} can be treated as a function of porosity (void ratio) and effective mean stress (Hardin and Drnevich, 1972).

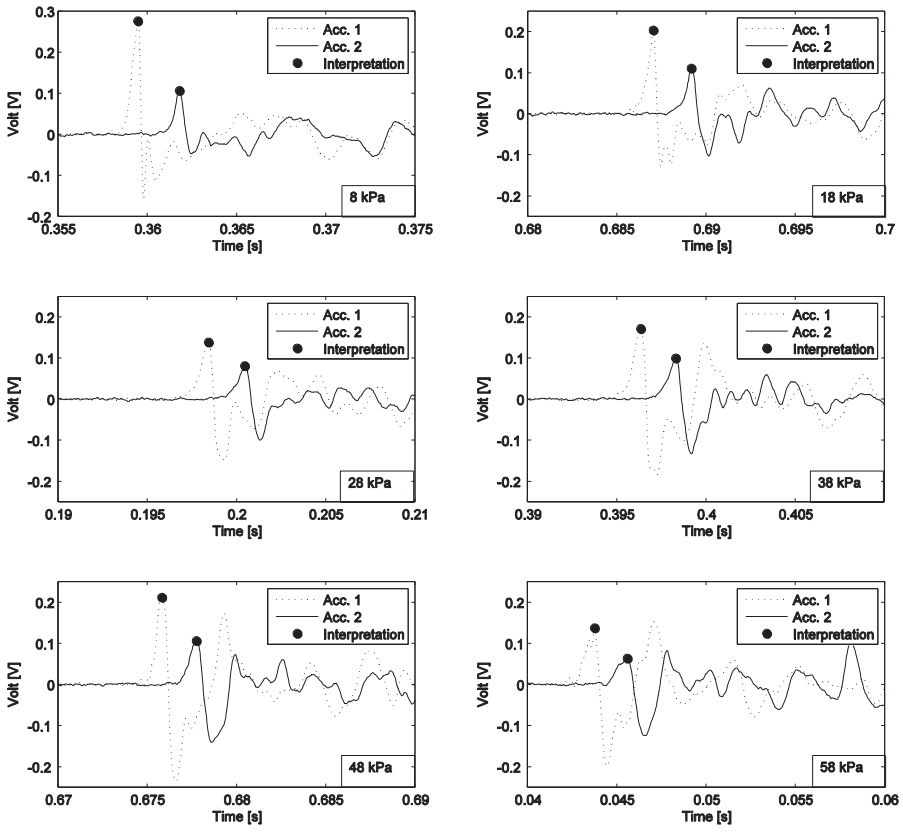

Figure 7-16. Time series, shear wave measurements.

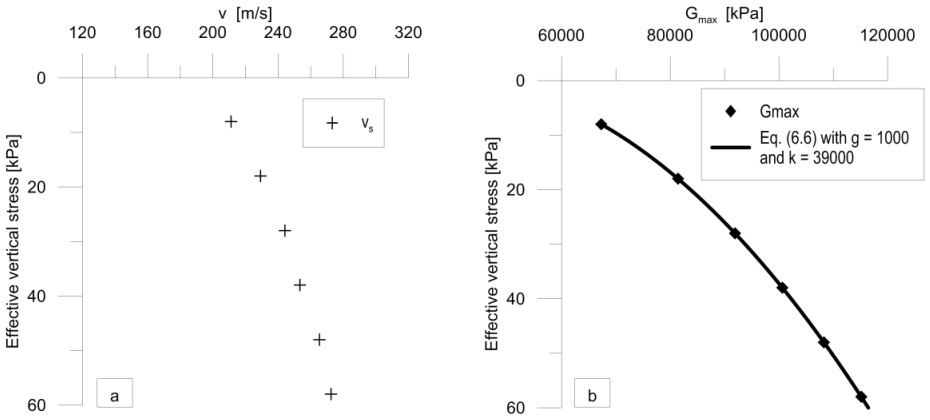

Figure 7-17. (a) Shear wave velocity (v_s) and p-wave velocity (v_p) against effective vertical stress and (b) small-strain shear modulus (G_{max}) against effective vertical stress.

For the soil conditions present in the sand tank (constant porosity), a simple function of the form of Eq.(7.6) has been fitted to the test data. As horizontal soil stresses are not measured in the current test setup, Eq.(7.6) has been fitted based on vertical stress, rather than the more common expression based on mean stress. A mean-stress based equation may be obtained by assuming an appropriate K_0-value. Using Eq.(7.6) with p_{ref} = 100 kPa, g = 1000 and a constant k = 39 000 kPa gives an R^2 = 0.993 in the range of vertical stresses applied. The recorded wave speeds are inside the range of previous experience for quartz sands with comparable void ratios at comparable stress-levels (e.g. Hardin and Richart (1963), Bartake and Singh (2007), Bauer et al. (2007)).

$$G_s = g\left(p_{ref}\,\sigma_v'\right)^{0.5} + k \tag{7.6}$$

Table 7-6. Interpreted shear wave velocities

Vertical stress [kPa]	v_s [m/s]	Standard deviation [m/s]
8	204.1	2.0
18	225.9	1.8
28	238.1	1.8
38	250.9	3.9
48	258.3	6.6
58	270.6	9.7

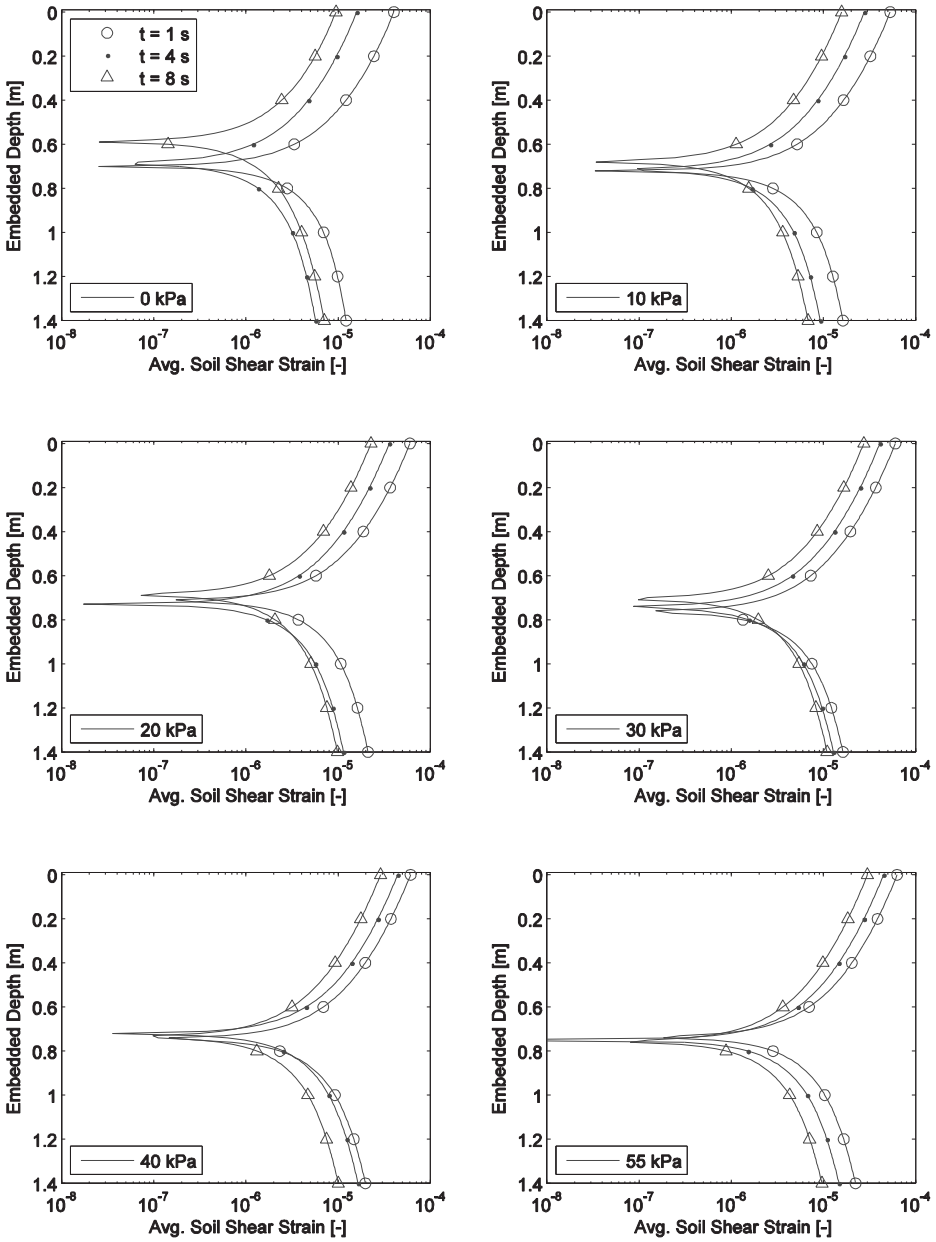

Figure 7-18. Representative soil shear strain around the model pile with a top mass of 84 kg, based on peak displacement profiles after 1, 4 and 8 s.

7.6 Evaluation of Representative Soil Shear Strain Level During Testing

The model test presented is performed in the context of monopiles for offshore monopile foundations. Following the reasoning in Section 7.2, small-strain effects on the soil stiffness are believed to contribute to the soil-structure interaction stiffness. In Figure 7-3b), the representative shear strain level around a full scale monopile foundation at Horns Rev was estimated. The resulting shear strain profile was then based on a deformation profile presented by Augustesen et al. (2010) and an approximate relationship from Kagawa and Kraft (1980), given as Eq.(7.1). The same exercise is repeated for the peak displacement profiles presented in Figure 7-14, and the representative shear strain level around the model pile found by the use of Eq(7.1) is presented in Figure 7-18. The results presented in Figure 7-18 give strains in the order of 10^{-5}. Shear strains below 10^{-4} are well inside the small-strain range defined in the conceptual sketch in Figure 7-2, and it is therefore assumed that small-strain effects on the soil stiffness are significant for the performed model test.

7.7 Chapter Summary and Conclusions

Measurements on full scale, operating offshore wind turbines reported in the literature have shown that the horizontal foundation stiffness appears to be under-predicted by current design methods. The current paper presents data and results for a 1:20 model scale test of a monopile foundation for offshore wind turbines, under fully controlled conditions. The test is performed as a free vibration test, with overburden pressure and stress dependent soil stiffness successfully controlled by a vacuum system. Repeatability of the impact vibration testing is proven to be excellent. The pile-soil system stiffness is measured indirectly by the first system eigenfrequency, and small-strain soil stiffness is measured indirectly by wave travelling times in sand. The presented data and results constitute high-quality information for back calculation and evaluation of calculation methods for horizontal stiffness of monopile foundations. The system eigenfrequencies and system damping are shown to be dependent on both confining stresses and the pile displacement amplitude. This effect is attributed to strain-dependent stiffness and damping of the soil.

Chapter References

Atkinson, JH & Sallfors, G (1991) Experimental determination of stress-strain-time characteristic in laboratory and in situ tests. In *X ECSMFE*. A.A. Balkema, Firenze, vol. III, pp. 915-956.

Augustesen, A, Sørensen, SPH, Ibsen, LB, Møller, M & Brødbæk, KT (2010) Comparison of calculation approaches for monopiles for offshore wind turbines. In *Numerical Methods in Geotechnical Engineering*. CRC Press, pp. 901-906.

Autodesk (2015) Robot Structural Analysis.

Bartake, PP & Singh, DN (2007) Studies on the determination of shear wave velocity in sands. *Geomechanics and Geoengineering* **2(1)**:41-49.

Bauer, RA, Su, W-J, Counts, RC & Karaffa, MD (2007) *Shear Wave Velocity, Geology and Geotechnical Data of Earth Materials in the Central U.S. Urban Hazard Mapping Areas* Champaign, Illinois, USA, 40 p.

Benz, T (2007) Small-Strain Stiffness of Soils and its Numerical Consequences. In *Fakultät für Bau– und Umweltingenieurwissenschaften*. Universität Stuttgart, Stuttgart, vol. PhD, 150 p.

Bhattacharya, S, Lombardi, D & Wood, DM (2011) Similitude relationships for physical modelling of monopile-supported offshore wind turbines. *International Journal of Physical Modelling in Geotechnics* **11(2)**:58-68.

Ewea (2009) *Pure Power - Wind energy targets for 2020 and 2030*. Brussels, Belgium.

Ewea (2013) *The European offshore wind industry - key trends and statistics 2012*.

Hald, T, Mørch, C, Jensen, L, Bakmar, CL & Ahle, K (2009) Revisiting monopile design using p-y curves –Results from full scale measurements on Horns Rev. In *European Offshore Wind Conference & Exhibition 2009*. Curran Associates, Inc, Stockholm, Sweden, vol. 3, pp. 1926-1935.

Hanssen, SB, Eiksund, G & Nordal, S (2015) Impact Vibration Test of Monopile Foundation Model in Dry Sand. *International Journal of Physical Modelling in Geotechnics*.

Hardin, BO & Drnevich, VP (1972) Shear modulus and damping in soils: Design equations and curves. *Journal of the Soil Mechanics and Foundations Division* **98(7)**:667-692.

Hardin, BO & Richart, FE (1963) Elastic wave velocities in granular soils. *ASCE Journal of the Soil Mechanics and Foundations Division* **89(SM1)**:33-65.

Iai, S (1989) Similitude for shaking table tests on soil-structure-fluid model in 1g gravitational field. *Soils and Foundations* **29(1)**:105-118.

Iai, S, Tobita, T & Nakahara, T (2005) Generalised scaling relations for dynamic centrifuge tests. *Geotechnique* **55(5)**:355-362.

Janbu, N (1963) Soil Compressibility as Determined by Oedometer and Triaxial Tests. In *3rd European Conference on Soil Mechanics and Foundation Engineering*. Wiesbaden, Germany, vol. 1, pp. 19-25.

Kagawa, T & Kraft, LM (1980) Seismic p-y responses of flexible piles. *ASCE Journal of the Geotechnical Engineering Division* **106(GT8)**:899-918.

Kallehave, D, Leblanc, C & Liingaard, MA (2012) Modification of the API P-y Formulation of Initial Stiffness of Sand In *Proceedings of Offshore Site*

Investigation and Geotechnics: Integrated Technologies - Present and Future. Society for Underwater Technology, pp. 465-472.

Kallehave, D, Thilsted, CL & Troya, A (2015) Observed variations of monopile foundation stiffness. In *Frontiers in Offshore Geotechnics III*. CRC Press, pp. 717-722.

Klar, A (2008) Upper Bound for Cylinder Movement Using "Elastic" Fields and Its Possible Application to Pile Deformation Analysis. *International Journal of Geomechanics* **8(2)**:162-167.

Kramer, SL (1996) *Geotechnical earthquake engineering.* Upper Saddle River, N.J., Prentice Hall.

Leahy, D (1984) *Deformation of dense sand: triaxial testing and modelling.* Trondheim, NTH.

Lieng, JT (1988) *Behavior of laterally loaded piles in sand: large scale model tests.* Trondheim, NTH.

Lieng, JT, Moen, TI & Senneset, K (1984) Large Scale Model Tests - Test Facilities and Test Examples. In *NGM 1984*. Linköping, Sweden, vol. 3, pp. 177-185.

Lombardi, D, Bhattacharya, S & Muir Wood, D (2013) Dynamic soil–structure interaction of monopile supported wind turbines in cohesive soil. *Soil Dynamics and Earthquake Engineering* **49(0)**:165-180.

Mair, RJ (1993) Unwin Memorial Lecture 1992- Developments in Geotechnical Engineering Research: Application to Tunnels and Deep Excavations. Delivered at the ICE on 17 March 1992. In *Proceedings of the ICE - Civil Engineering*. vol. 97, pp. 27-41.

Moen, TI (1978) *Hokksund Sand. Determination of the Sand's Routine Data, Deformation and Strength Characteristics.*, Report F.78.04.

Ohde, J (1939) Zur Theorie der Druckverteilung im Baugrund. *Der Bauingenieur* **20(33/34)**:451-459.

Osman, AS & Bolton, MD (2005) Simple plasticity-based prediction of the undrained settlement of shallow circular foundations on clay. *Geotechnique* **55(6)**:435-447.

Seed, H & Idriss, I (1970) *Soil moduli and damping factors for dynamic response analyses*. Report EERC 70-10.

Seed, H, Wong, R, Idriss, I & Tokimatsu, K (1986) Moduli and Damping Factors for Dynamic Analyses of Cohesionless Soils. *Journal of Geotechnical Engineering* **112(11)**:1016-1032.

Tadesse, S (2000) Behaviour of saturated sand under different triaxial loading and liquefaction. In *Department of Civil and Transport Engineering*. Norwegian University of Science and Technology, Trondheim, vol. PhD, 144 p.

Wichtmann, T & Triantafyllidis, T (2013) Effect of Uniformity Coefficient on G/Gmax and Damping Ratio of Uniform to Well-Graded Quartz Sands. *Journal of Geotechnical and Geoenvironmental Engineering* **139(1)**:59-72.

8 Back Analysis of the Impact Vibration Test

One reason to conduct the impact vibration test presented in Chapter 7 was to validate the hypothesis of contributions from small-strain soil stiffness to the eigenfrequency of monopile foundations. Further, the model test provide an opportunity to benchmark the performance of the soil springs proposed in Chapter 6. The model test is back-calculated with the 3D-FE software Plaxis3D (Plaxis BV, 2014), and with a 1D-beam model in the FE-software Autodesk Robot Structural Analysis (Autodesk, 2015). For the 1D-beam model, soil support is provided as uncoupled springs. This chapter presents the performed calculations and the corresponding results.

8.1 Back Analysis with 3D-FEM

The 3D-FE modeling is performed in the time domain, with three different approaches to the soil stiffness:

- A linear elastic soil model with stiffness obtained from oedometer tests
- A linear elastic soil model with stiffness obtained from shear wave measurements
- An isotropic hardening soil model that models the entire stiffness range of the soil from small-strain stiffness to stiffness at engineering strains (Hardening Soil Small model).

For each of the three different approaches to the soil stiffness, simulations with six different applied overpressures and two different top masses are performed. Summarized, this gives a total of 36 simulations.

The geometry of the 3D-FE model is shown in Figure 8-1. To reduce the calculation time, only half of the geometry is modeled, using symmetry boundary conditions along the symmetry line. The model geometry is limited at the walls of the concrete tank. The concrete tank is assumed to act like a rigid boundary in the physical model test, and fixed boundaries are therefore chosen in the FE-model. The pile is located in the center of the pile tank, with a horizontal distance from the tank wall to pile center of 2 m in both x- and y-directions. The calculations are run in the time domain, and the eigenfrequency is evaluated based on the time history of horizontal displacements at the pile top. The impact load from the hammer is given as a nodal, dynamic load at the center of the pile top.

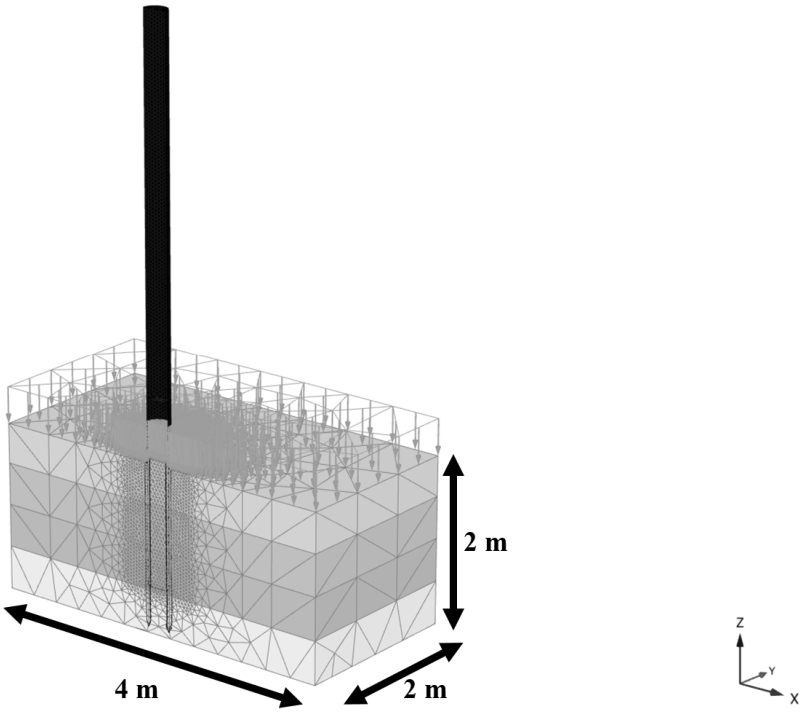

Figure 8-1. Geometry of the 3D-FEM model. Only half of the geometry is modeled, due to symmetry. The overburden pressure applied through the vacuum-system is modeled as a surface load.

8.1.1 Pile Properties

The pile is modeled by 6-noded triangular plate elements, with unit weight, bending stiffness and virtual thickness corresponding to the properties of the physical pile. The additional weights at the pile head and the connection flange are modeled as horizontal plates. The connection flange is assumed not to influence the bending stiffness of the pile. Material damping in the steel is assigned through Rayleigh damping. 6-noded triangular interface elements of zero thickness are assigned between the pile and the soil, and a soil-pile interface roughness of $\alpha = 1$ is assigned. The pile elements are modeled with a linear-elastic material law. An overview of the pile parameters is provided in Table 8-1.

Table 8-1. Pile parameters

	Unit	Value
Pile diameter (D)	[m]	0.273
Embedded length (L)	[m]	1.40
Total length	[m]	6.00
Wall thickness (t)	[mm]	4.0
Unit weight	[kg/m^3]	7850
Young's modulus (E_{steel})	[GPa]	210
Poisson's ratio (μ)	[-]	0.3
Additional top-mass	[kg]	9 and 84
Mass at connection flange	[kg]	29
Interface roughness (α)	[-]	1

8.1.2 Soil Properties

Soil parameters for Hokksund Sand are obtained from Moen (1978), in addition to the shear wave velocities measured in Chapter 7. The soil is modeled by 83457 10-noded tetrahedral volume elements.

Linear Elastic Soil with Stiffness from Oedometer Testing

The soil stiffness measured in the oedometer by Moen (1978) can be described by the Janbu equation for stress dependent stiffness (Janbu, 1963) as:

$$M_s = m(p_{atm}\sigma'_v)^{0.5} \tag{8.1}$$

with M_s being the constraint modulus of the soil, the modulus number m = 500 and the atmospheric pressure p_{atm} = 100 kPa. Young's modulus of the sand is calculated from elastic theory (Eq.(8.2)) and an assumed Poisson's ratio of μ = 0.2.

$$E_s = M_s \frac{(1+\mu)(1-2\mu)}{(1-\mu)} \tag{8.2}$$

The nonlinear increase in stiffness with vertical stress is modeled by dividing the soil into four layers of 0.5 m thickness, approximating the square root function with a piecewise linear curve. An example of stiffness profiles for applied overburden of 0 and 30 kPa is shown in Figure 8-2. The accuracy of the piecewise linear fit is seen to increase with applied overburden pressure, and at an applied overburden of 30 kPa the curves are congruent.

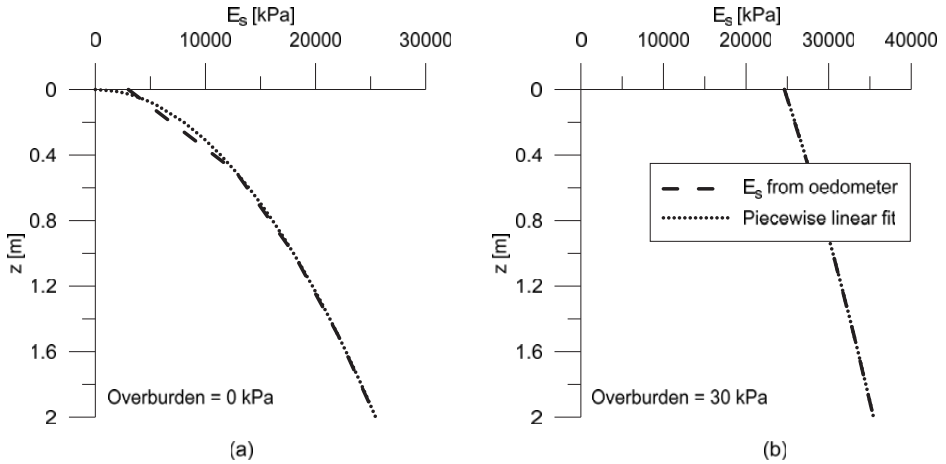

Figure 8-2. Stress-dependent stiffness from the oedometer (Eq.(8.1)) together with a piecewise linear approximation. (a) Applied overburden pressure of 0 kPa. (b) Applied overburden pressure of 30 kPa.

Linear Elastic Soil with Stiffness from Shear Wave Velocity Measurements

The soil stiffness found from the shear wave velocity measurements in Chapter 7 was fitted by the equation:

$$G_{s,\max} = 1000\left(p_{ref}\,\sigma_v'\right)^{0.5} + 39\,000 \tag{8.3}$$

Young's modulus of the soil is calculated from elastic theory and an assumed Poisson's ratio of $\mu = 0.2$:

$$E_s = G_s\, 2(1+\mu) \tag{8.4}$$

The nonlinear increase in stiffness with vertical stress is modeled by dividing the soil into four layers of 0.5 m thickness, approximating the square root function by a piecewise linear curve. An example of stiffness profiles for applied overburden of 0 and 30 kPa is shown in Figure 8-3. The accuracy of the piecewise linear fit is seen to increase with applied overburden pressure.

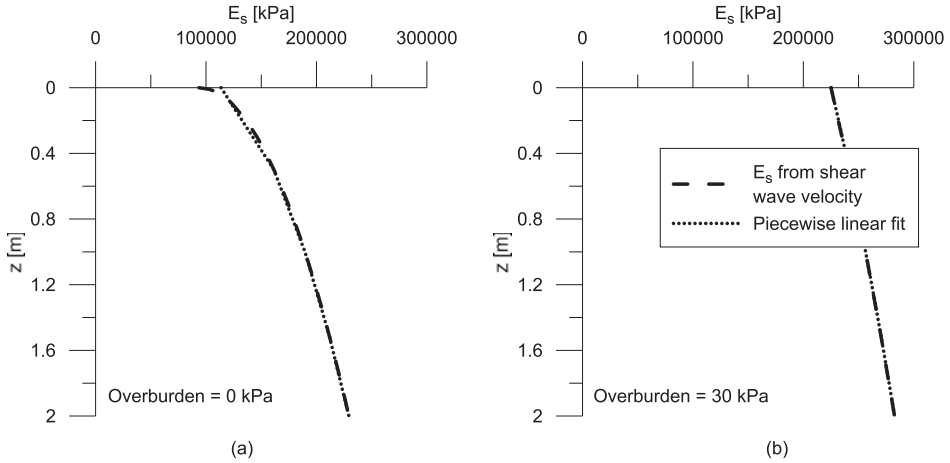

Figure 8-3. Stress-dependent stiffness from shear wave velocity measurements (Eq.(8.3)) together with a piecewise linear approximation. (a) Applied overburden pressure of 0 kPa. (b) Applied overburden pressure of 30 kPa, and at an applied overburden of 30 kPa the curves are congruent.

Isotropic Hardening Soil with Stiffness from Shear Wave Velocity Measurements for the Small Strain Stiffness Range and Stiffness from the Oedometer for Larger Strains

The Hardening Soil Small model (HSS-model) is one of the default soil models in Plaxis3D. The main features of the model is:

- Stress dependent stiffness according to a power law
- Plastic straining due to primary deviatoric loading
- Plastic straining due to primary compression
- Failure according to the Mohr-Coulomb failure criterion
- Small-strain stiffness and a nonlinear dependency on strain amplitude and strain history.
- A threshold strain between the small-stiffness range and the range for larger strains

A detailed description of the soil model can be found in the Plaxis User's Manual (Plaxis BV, 2014) and in Benz (2007).

Soil parameters for the HSS model is based on the shear wave velocity measurements in Chapter 7 and the oedometer stiffness given by Eq.(8.1). The stress dependent soil stiffness in the HSS-model is given by Eq.(8.5) to Eq.(8.7) (Note that compression is negative).

$$E_s = E_{s,50}^{ref}\left(\frac{c\cos\varphi - \sigma_3'\sin\varphi}{c\cos\varphi + p_{ref}\sin\varphi}\right)^m \qquad \textbf{(8.5)}$$

$$G_{s,\max} = G_{s,\max}^{ref} \left(\frac{c\cos\varphi - \sigma_3' \sin\varphi}{c\cos\varphi + p_{ref} \sin\varphi} \right)^m \quad \textbf{(8.6)}$$

$$M_s = M_{s,50}^{ref} \left(\frac{c\cos\varphi - \frac{\sigma_3'}{K_0^{nc}} \sin\varphi}{c\cos\varphi + p_{ref} \sin\varphi} \right)^m \quad \textbf{(8.7)}$$

The reference stiffnesses $M_{s,50}^{ref}$ and $E_{s,50}^{ref}$, together with the stiffness exponent *m,* are selected to give a stiffness equal to the constraint modulus and the Young's modulus in Eq.(8.1) and Eq.(8.2). For a cohesionless soil, the influence of the soil friction angle and cohesion in Eq.(8.5) and Eq.(8.7) disappears, and the soil stiffness depends entirely on the vertical and horizontal stress, the stress exponent *m* and the reference stiffnesss. The input parameters given in Table 8-2 were kept for all the simulations with the HSS model. The reference shear modulus $G_{s,\max}^{ref}$ and the corresponding threshold shear strain $\gamma_{0.7}$ is calculated separately for each layer and each applied overburden pressure. Due to the last term in Eq.(8.3), the shape of the $G_{s,max}$ profiles described by Eq.(8.3) and Eq.(8.6) do not match. The soil volume is therefore divided into four layers of 0.5 m thickness, with the reference shear modulus $G_{s,\max}^{ref}$ adjusted to fit the profile described in Eq.(8.3). The exponent *m* in Eq.(8.5) to Eq.(8.7) is given by a single input parameter. As a consequence, the small-strain shear stiffness is fitted by a piecewise square-root function. An example of the shear stiffness profile for 0 and 30 kPa surcharge pressure is shown in Figure 8-4. The accuracy of the piecewise square root function is increasing with increasing overburden pressure, and a close match is obtained already at 30 kPa applied overburden pressure. The expression for the threshold shear strain recommended in Benz (2007) is given in Eq.(8.8).

$$\gamma_{0.7} = \frac{1}{9G_{s,\max}} \left[2c(1+\cos(2\varphi)) + \sigma_1'(1+K_0)\sin(2\varphi) \right] \quad \textbf{(8.8)}$$

where K_0 is the earth pressure coefficient at rest and σ'_1 is the effective vertical stress (compression positive).

Table 8-2. Soil Parameters Hardening Soil Small model

Symbol	Unit	Value
φ	[°]	38
c'_{ref}	[kPa]	0.1
$E^{ref}_{s,50}$	[MPa]	82.036
$M^{ref}_{s,50}$	[MPa]	50
$E^{ref}_{s,ur}$	[MPa]	190
γ	[kN/m^3]	16
m	[-]	0.5
$\mu'_{s,ur}$	[-]	0.2
ψ	[°]	0

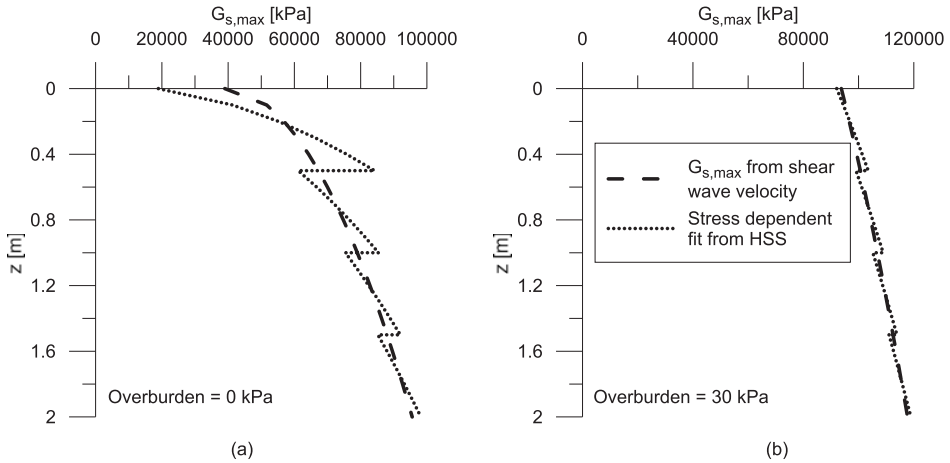

Figure 8-4. Stress-dependent stiffness from shear wave velocity measurements (Eq.(8.3)) together with an approximation of the form of Eq.(8.6). (a) Applied overburden pressure of 0 kPa. (b) Applied overburden pressure of 30 kPa.

8.1.3 Time Integration

The 3D-FEM is performed in the time domain, with a Newmark integration procedure (implicit integration). A time history of 0.5 s is modeled, and 500 time steps are stored. The default option in Plaxis3D for deciding on the number of dynamic sub-steps is chosen in order to ensure that waves do not move a distance larger than the minimum dimension of an element. Reference is made to Plaxis BV (2014) for details.

8.1.4 Results

The eigenfrequency of the pile-soil system is evaluated based on the time history of horizontal displacements at the pile top. Eq.(8.9) describes a damped 1DOF-system, and is fitted to the resulting time series by the nonlinear least squares method. The eigenfrequency is found by dividing the angular frequency ω by 2π to get the frequency

in Hz. A visual inspection of each fit is performed in addition to the accuracy indicated by the R^2-value from the nonlinear least squares method. An example of how a result compares to the expression for a 1DOF-system from Eq.(8.9) is shown in Figure 8-5.

$$u(t) = Ae^{-\omega_n D t}\cos(\omega_d t - \phi) \tag{8.9}$$

where A represents the amplitude, D the damping and ϕ the phase angle. ω_n is the undamped angular eigenfrequency and ω_d is the damped angular eigenfrequency.

Figure 8-6 compares the eigenfrequency for the case of 9 kg top mass calculated with the 3D-FEM to the eigenfrequency measured in the model test from Chapter 7. The same comparison is made in Figure 8-7 for a top mass of 84 kg.

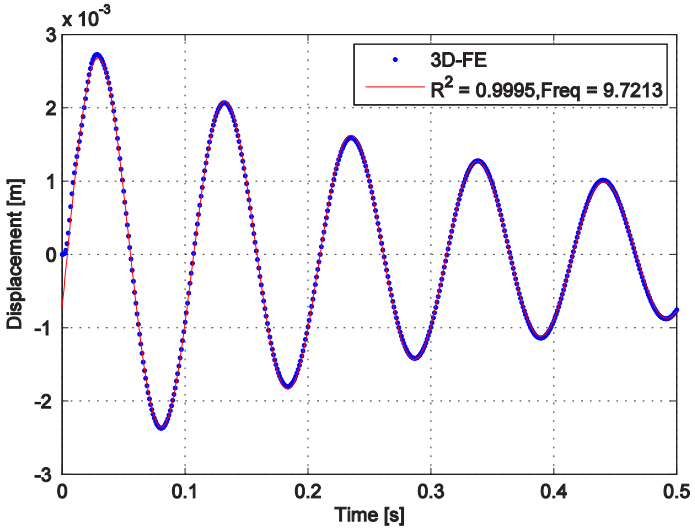

Figure 8-5. Comparison of displacements at the pile top from 3D-FE and Eq.(8.9), fitted with the least squares method. Comparison shown for the case of linear elastic soil with stiffness from $G_{s,max}$, applied overburden pressure of 55 kPa and 9 kg top mass.

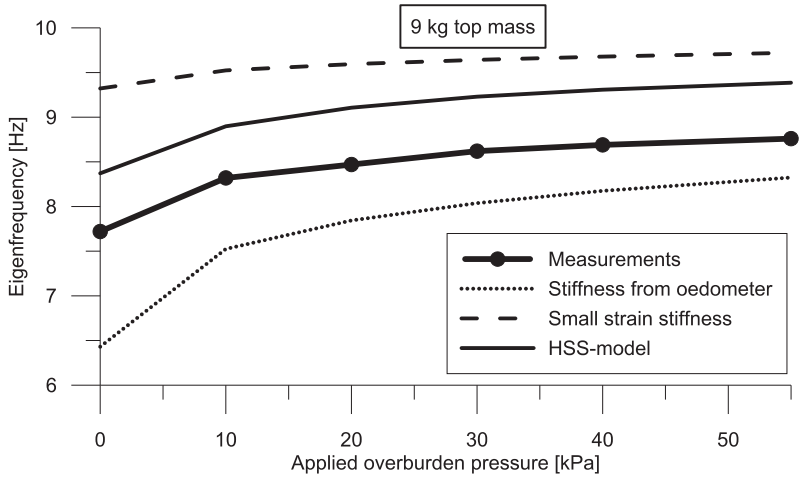

Figure 8-6. Comparison of calculated and measured eigenfrequencies for a top mass of 9 kg. Eigenfrequencies calculated with 3D-FEM. The physical measurements of eigenfrequencies are presented in Chapter 7.

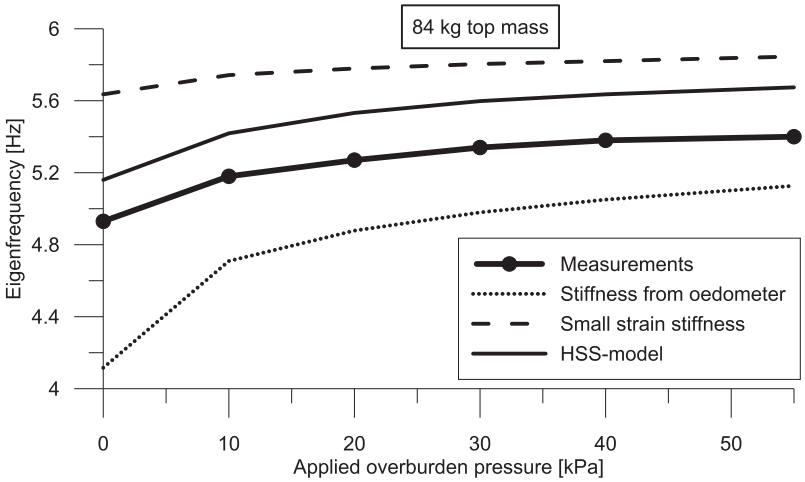

Figure 8-7. Comparison of calculated and measured eigenfrequencies for a top mass of 84 kg. Eigenfrequencies calculated with 3D-FEM. The physical measurements of eigenfrequencies are presented in Chapter 7.

The calculated eigenfrequencies presented in Figure 8-6 and Figure 8-7 indicate a representative soil stiffness somewhere in between the oedometer stiffness and the small-strain stiffness. This is seen for both top masses. The rate of increase in eigenfrequency with applied overburden pressure appears to be captured by the simulations. The simulations performed with the HSS model predicts a too stiff

response, indicating that the strain-dependent stiffness of the material is not captured correctly in the calculation model.

Figure 8-8 and Figure 8-9 compare the calculated eigenfrequencies, normalized on the measured eigenfrequency. The predictions with the HSS model are seen to be ~8 % too stiff for the simulations where the top mass is 9 kg. For the 84 kg top mass, the simulations with the HSS model are seen to predict an eigenfrequency ~5 % too stiff. The deviation between measured and calculated eigenfrequency is seen to be constant, regardless of the applied overburden pressure. When the measured eigenfrequency is compared to the linear elastic soil based on the oedometer stiffness, the calculated frequency is 5-17 % too low. Soil springs based on the small-strain stiffness of the soil gives a calculated eigenfrequency 8-21 % too high. For both of the simulation series with linear elastic soil, the largest deviation from measured eigenfrequencies is seen for low overburden pressures. This deviation reduces with increased overburden pressures.

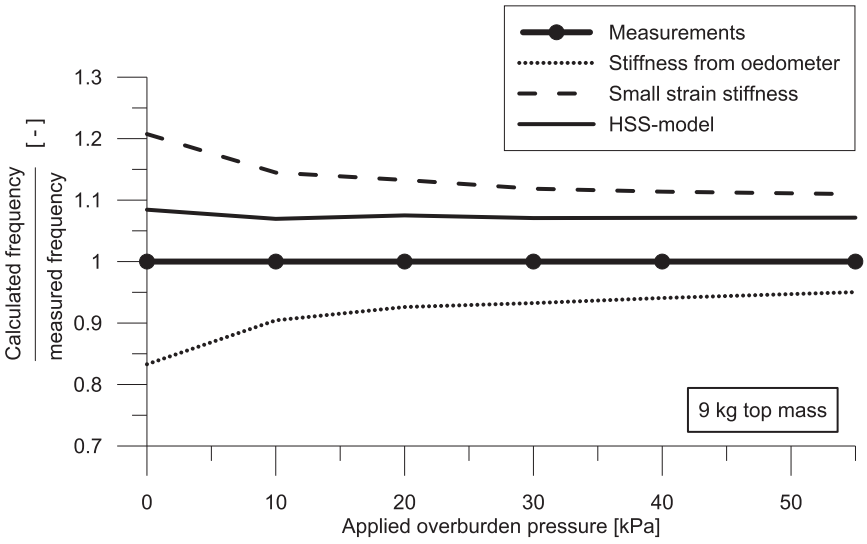

Figure 8-8. Comparison of the performance for the different soil springs and a top mass of 9 kg. Eigenfrequencies calculated 3D-FEM. The physical measurements of eigenfrequencies are presented in Chapter 7.

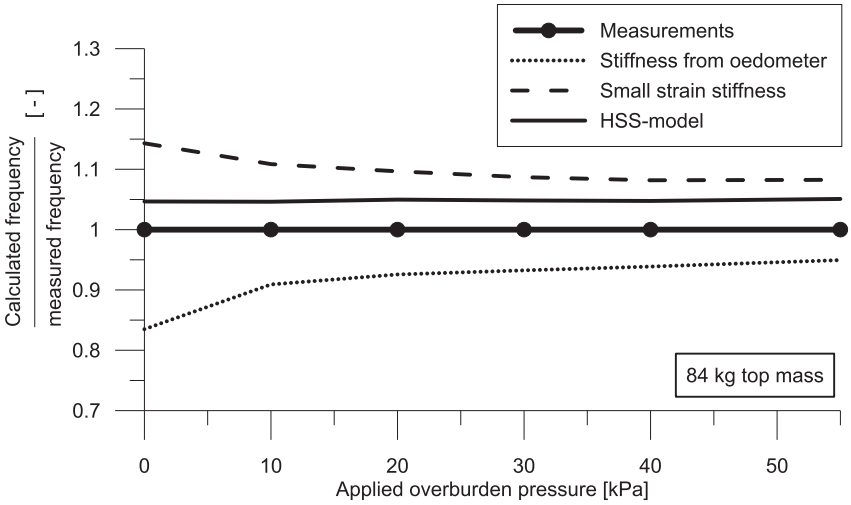

Figure 8-9. Comparison of the performance for the different soil springs and a top mass of 84 kg. Eigenfrequencies calculated with 3D-FEM. The physical measurements of eigenfrequencies are presented in Chapter 7.

8.2 Back Analysis with Winkler Beam (1D-FE)

The 1D-FE modeling is performed both in the frequency domain and in the time domain, dependent on the type of soil springs applied. The beam model consisted of 60 beam elements, 15 lateral springs and 15 rotational springs. Four different approaches to the spring stiffness is made:

- Linear elastic soil springs, based on the relationship between soil stiffness and spring stiffness presented in Chapter 6. Soil stiffness from the oedometer (Eq.(8.1)).
- Linear elastic soil springs, based on the relationship between soil stiffness and spring stiffness presented in Chapter 6. Soil stiffness from the shear wave velocity measurements presented in Chapter 7 (Eq.(8.3)).
- The nonlinear soil springs for sand proposed in Chapter 6. $G_{s,max}$ values from Eq.(8.3) and stiffness degradation according to Hardin and Drnevich (1972).
- The API p-y curves for sand (linear initial stiffness).

The simulations with linear elastic soil springs are performed as modal analysis, for the sake of computational efficiency. The simulations with nonlinear soil springs are performed in the time domain. For each of the four different approaches to spring stiffness, simulations with stiffness corresponding to six different applied overburden pressures and two different top-masses are ran. Combined, this gives a total of 48 simulations.

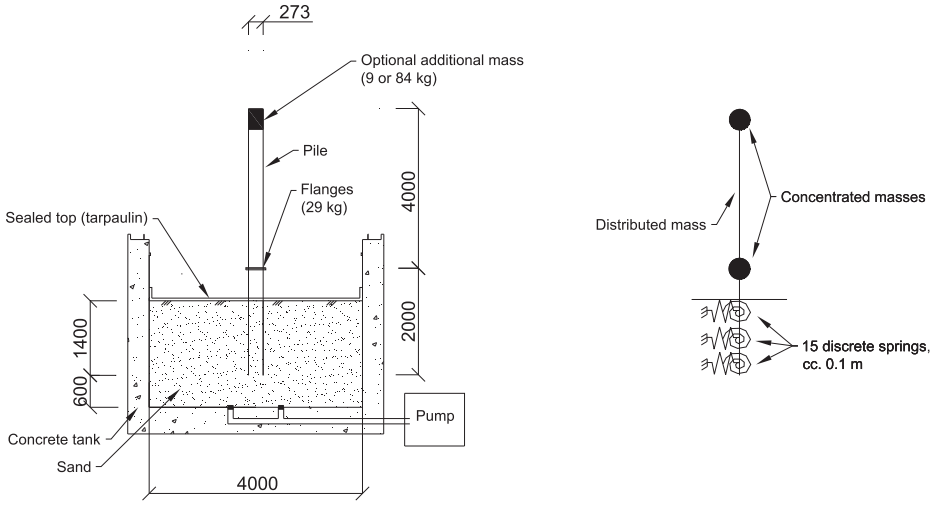

Figure 8-10. Sketch of Winkler-beam model for the back analysis of the model pile. The beam is assigned a distributed mass, lumped masses are assigned at the location of the connection flange and the pile top. Soil springs are assigned with cc. 0.1 m over the 1.4 m embedment depth. Measures on the left sketch given in mm.

The geometry of the 1D-FE model is shown in Figure 8-10. The 6 m long beam is given a distributed mass, a bending stiffness and concentrated masses at the top end and location of the connection flange. An overview of the pile properties is given in Table 8-1. The initial velocity for the time domain is given as an impact load at the node at pile top. The soil springs are given with 0.1 m spacing over the pile embedment depth. For the calculations ran in the time domain, the eigenfrequency is evaluated based on the time history of horizontal displacements at pile top.

8.2.1 Spring Properties

The soil is modeled by 15 rotational and 15 translational springs. The calculation with API p-y curves for sand is performed without rotational springs.

Linear Elastic Soil Springs Based on Oedometer Stiffness

In Chapter 6, the stiffness of both rotational and translational springs were given as a function of the soil shear stiffness G_s. With k denoting the translational stiffness and k_θ denoting the rotational stiffness, the linear elastic stiffness (when end effects are disregarded) is given as:

$$k = 4G_s \tag{8.10}$$

$$k_\theta = G_s D^2 \tag{8.11}$$

The pile length and diameter is given in Table 8-1, while the soil shear stiffness G_s is calculated from its elastic relation to the constraint modulus as:

$$G_s = \frac{M_s(1-2\mu)}{2(1-\mu)} \tag{8.12}$$

The constraint modulus (M_s) was fitted by Moen (1978) with Eq.(8.1) and a modulus number $m = 500$. The stress-dependent shear stiffness is adjusted for the actual overburden pressure and embedment depth for each spring.

Linear Elastic Soil Springs Based on Shear Wave Velocity Measurements
The relation between soil shear stiffness and spring stiffness described by Eq.(8.10) and Eq.(8.11) is applied. The soil shear stiffness is taken as the small-strain shear stiffness described by Eq.(8.3). The stress-dependent shear stiffness is adjusted for the actual overburden pressure and embedment depth for each spring.

Nonlinear Soil Springs for Sand Proposed in Chapter 6
The full equations for both the translational and the rotational springs are given in Chapter 6, with the exception of ultimate capacity of the rotational springs. The software used for back-calculation is not able to update the ultimate capacity of the spring iteratively, and a fixed ultimate capacity is obtained by replacing p with p_{ult} in Eq.6.21.

In addition to the input parameters listed in Table 8-3, the small-strain soil stiffness described by Eq.(8.3) is given as input. The stress-dependent shear stiffness is adjusted for the actual overburden pressure and embedment depth for each spring. The curve fitting parameters *a* and *b* for the Hardin-Drnevich degradation curve are based on correlations with the coefficient of uniformity (C_u), recommended by Wichtmann and Triantafyllidis (2014).

Table 8-3. Soil and Pile Parameters for the Nonlinear Curves Proposed in Chapter 6

Symbol	Unit	Value
φ	[°]	38
C_u	[-]	2.04
a	[-]	1.070 ln(C_u)
b	[-]	1
γ	[kN/m^3]	16
D	[m]	0.273
L	[m]	1.40

API p-y Curves for Sand

The API p-y curves for sand are given by API (2011) as:

$$p = Ap_u \tanh\left(\frac{k_1 z}{Ap_u} y\right) \tag{8.13}$$

where

p	=	lateral resistance
p_u	=	ultimate lateral resistance
A	=	empirical coefficient
k_1	=	stiffness coefficient dependent on the soils internal angle of friction
y	=	displacement
z	=	depth below ground surface

The term Ap_u describes the ultimate resistance, and the term $k_1 z$ describes the initial stiffness. The tanh-function returns tanh(x) = x for small values of x, and tanh(x) = 1 for large values of x. In the context of Eq.(8.13), $p = Ap_u$ for large deformations (large values of y) and $p \approx k_1 z\, y$ for small deformations. The vibrating pile in the model test was in Chapter 7 found to have displacements less than 10^{-4} m. For the model pile, this is well inside the range where the API p-y curves return $p \approx k_1 z\, y$, and linear springs can be assumed over the expected deformation range.

Linear interpolation between tabulated values of k_1 in the API guidelines (API, 2011) gives a value of $k_1 = 35.8$ MN/m^3 for a soil friction angle of $\varphi = 38°$. The expression in Eq.(8.13) accounts implicitly for a stress dependent stiffness, by relating the stiffness to the spring embedment depth. As described in Appendix B, this can be traced back to an assumption made in Terzaghi (1955), namely that the submerged unit weight of most sands can be taken as $\gamma' = 10$ kN/m^3. The model test setup increases the effective vertical stresses in the sand by a vacuum system. An equivalent depth z_{eqv} is therefore defined to keep the original intention of stress dependency for the initial stiffness of the API-curves. The equivalent depth is then:

$$z_{eqv} = \frac{\sigma'_v}{\gamma'} \tag{8.14}$$

where γ' is the effective unit weight of the dry sand (17 kN/m^3). The stiffness of the linear springs representing the API p-y curves becomes:

$$k = 35800\, z_{eqv}\ kPa \tag{8.15}$$

8.2.2 Calculation

The time domain 1D-FEM calculation is performed with a Newmark integration procedure. A time history of 4.0 seconds is modeled, and 4000 time steps are stored. Damping is assigned as Rayleigh damping, and Autodesk Robot Structural Analysis applies the Rayleigh coefficients to the stiffness and mass matrices of the entire system by default. The Rayleigh coefficients are chosen as $\alpha = 1.269$ and $\beta = 0.0016$, giving a damping $\xi \approx 0.05$ in the range 5-10 Hz. Both the modal- and the time-history analysis are run with a consistent mass matrix.

8.2.3 Results

For the simulations performed as modal analysis, the frequency for the first eigenmode is taken as the result. For the simulations run in the time domain, the eigenfrequency is evaluated from the time history of horizontal displacements at the pile top. As for the interpretation of results from the 3D-simulations, the equation for a damped 1DOF-system in Eq.(8.9) is fitted to the results by the nonlinear least squares method. The eigenfrequency is found by dividing the angular frequency ω by 2π to get the frequency in Hz. A visual inspection of each fit is performed in addition to the accuracy indicated by the R^2-value from the nonlinear least squares method. An example of how a result compares to the expression for a 1DOF-system from Eq.(8.9) is shown in Figure 8-11.

Figure 8-12 compares the eigenfrequency for the case of 9 kg top mass calculated with the 3D-FEM to the eigenfrequency measured in the model test from Chapter 7. The same comparison is made in Figure 8-13 for a top mass of 84 kg.

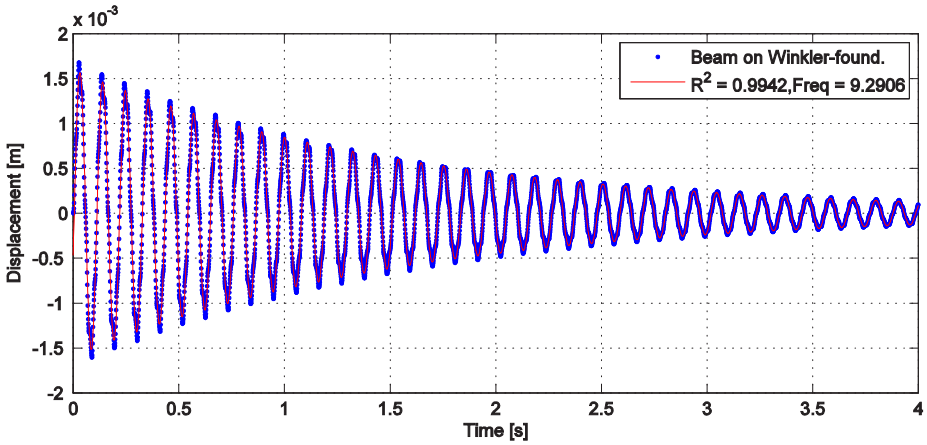

Figure 8-11. Comparison of displacements at pile top from 1D-FE and Eq.(8.9) fitted with the least squares method. Comparison shown for the case of nonlinear, proposed soil springs, applied overburden pressure of 55 kPa and 9 kg top mass.

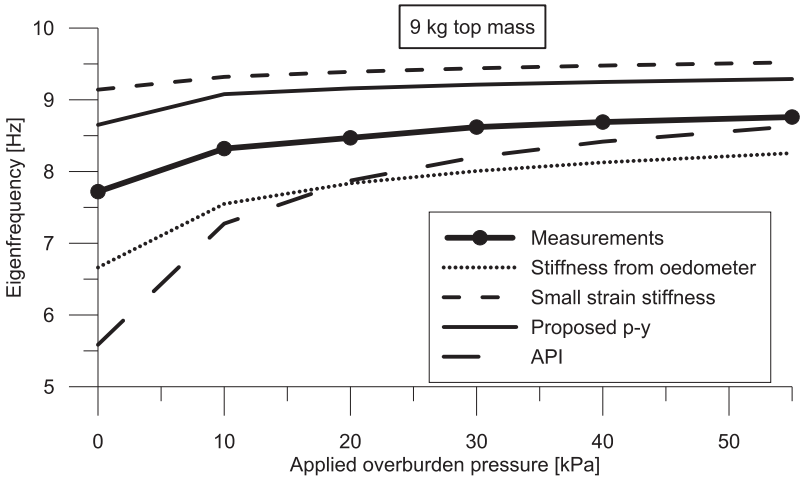

Figure 8-12. Comparison of calculated and measured eigenfrequencies for a top mass of 9 kg. Eigenfrequencies calculated with a beam on Winkler foundation model. The physical measurements of eigenfrequencies are presented in Chapter 7.

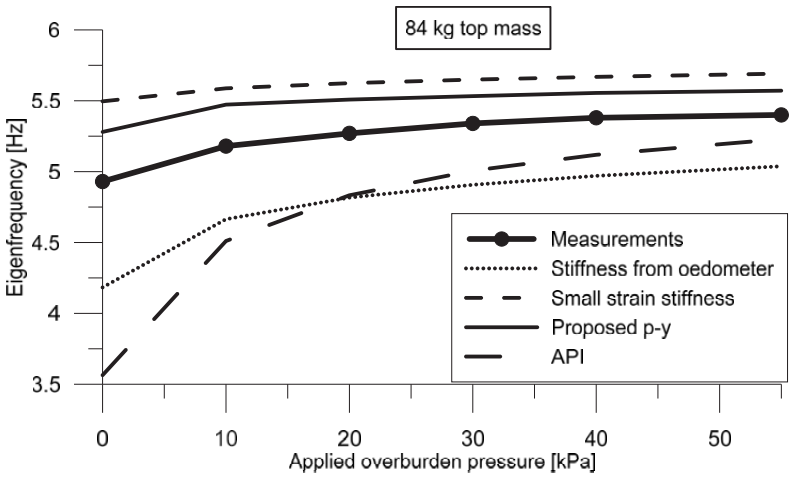

Figure 8-13. Comparison of calculated and measured eigenfrequencies for a top mass of 84 kg. Eigenfrequencies calculated with a beam on Winkler foundation model. The physical measurements of eigenfrequencies are presented in Chapter 7.

In conformity with the results from the 3D-FE simulations, the results from the 1D-FE indicate a representative soil stiffness somewhere in between the oedometer stiffness and the small-strain stiffness. This is seen for both top masses. The rate of increase in eigenfrequency with applied overburden pressure appears to be captured by the three spring sets based on the measured soil stiffness. This indicates that the rate of increase

in spring stiffness follows the rate of increase in soil stiffness. The API p-y curves predict a too soft response at low effective stresses in the soil, and are approaching the measured eigenfrequencies at higher levels of effective stress. This indicates that the linear increase in stiffness with depth captures the actual stiffness increase poorly. The proposed soil springs from Chapter 6 predict a too stiff response, and close to the response predicted from small-strain soil stiffness. The closeness to the result from small-strain stiffness suggests that the stiffness degradation curve adopted might not be representative for the current problem.

Figure 8-14 and Figure 8-15 compare results from the different simulations, normalized on the measured eigenfrequency. The eigenfrequency found with the API p-y curves are seen to underpredict the measured eigenfrequency with more than 25 % for the cases with no overburden pressure. The deviation between predicted and measured frequencies reduces with increasing overburden pressures, to a deviation of 1 % at 55 kPa overburden pressure. The predictions with the proposed soil springs are 3-12 % too stiff. As for the predictions with the API curves, the predictions perform better for increasing effective stress level in the soil. When the measured eigenfrequency is compared to the calculations with linear soil springs based on the oedometer stiffness, the calculated frequency is 6-15 % too low. The linear soil springs based on the small strain stiffness of the soil gives a calculated eigenfrequency that is 5-18 % too high.

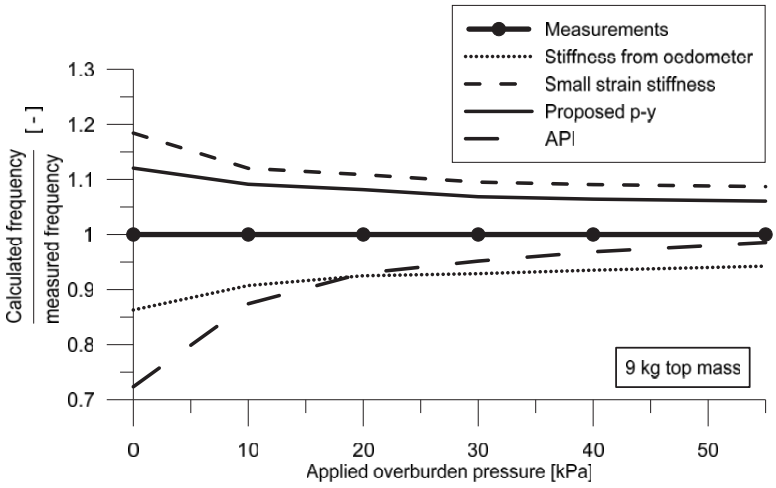

Figure 8-14. Comparison of the performance for the different soil springs and a top mass of 9 kg. Eigenfrequencies calculated with a beam on Winkler foundation model. The physical measurements of eigenfrequencies are presented in Chapter 7.

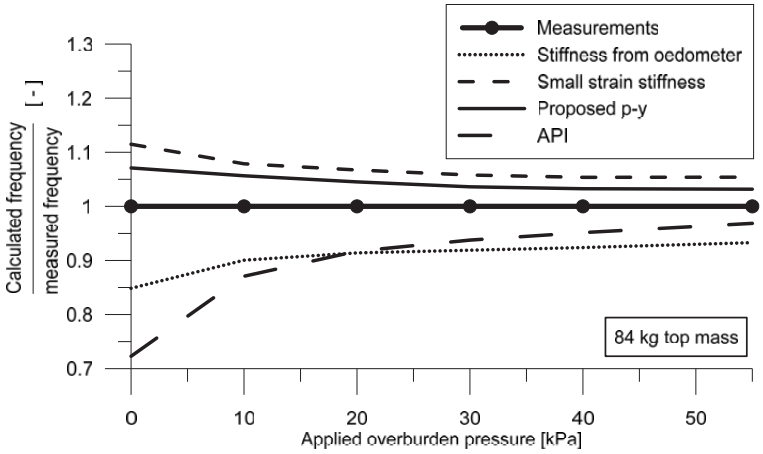

Figure 8-15. Comparison of the performance for the different soil springs and a top mass of 84 kg. Eigenfrequencies calculated with a beam on Winkler foundation model. The physical measurements of eigenfrequencies are presented in Chapter 7.

8.3 Discussion

The work presented in previous chapters of this thesis has been concerned with springs for static loading. To be able to model the exact soil response in the model test, an unloading-reloading extension would be required for all springs, and all calculations would need to be performed in the time domain. The 3D-FEM simulations with the Hardening Soil Small strain model (HSS model) incorporates unloading-reloading loops obeying Masing's rule. A detailed study of these effects and how they compare with the actual response in the model test are considered outside the scope of this thesis and left for further work. However, for the aim of exploring the strain dependency of the resultant soil stiffness, the linear- and nonlinear elastic springs applied are found sufficient.

The results from the back calculation with both 3D and 1D FEM suggests that the soil stiffness experienced by the pile corresponds to a representative soil stiffness somewhere in between the stiffness from shear wave velocities and the stiffness measured in the oedometer. It underlines the importance of a calculation tool capable of capturing the soil stiffness over a wide range of strain ranges. Further, the above results imply that calculations based on only oedometer- or small strain-stiffness will fail to capture the actual soil-pile interaction stiffness.

Both the Hardening Soil Small model and the proposed soil springs have been found to predict a stiffer response than observed in the model test. The predicted response being too stiff indicates either:

- that the strain dependent stiffness is not captured correctly in the models, or
- that the input small-strain stiffness is too high.

With respect to the last point, it should be noted that the small-strain stiffness is found from measurements of shear wave velocity with a cross-hole method. Both the proposed soil springs and the Hardening Soil Small model have adopted the shear stiffness degradation curve from Hardin and Drnevich (1972). Hardin and Drnevich based their stiffness degradation curves on laboratory resonant column tests, which might correspond to a higher strain level than the strain level during wave propagation. The difference between the two might in some cases be significant, e.g. as described by Lambson et al. (1993) where measurements of shear stiffness with cross-hole seismic gave 10 times the shear stiffness found with resonant column tests in the laboratory.

Another interesting observation from the presented results is the performance of the API p-y curves. Both the 3D-FE simulations and the proposed spring curves showed a rather steady deviation from the measured eigenfrequencies for changing levels of effective stress. In contrast, the API p-y curves had both the worst (28 % off at 0 kPa overburden and 9 kg top mass) and the best predictions (1 % off at 55 kPa overburden and 84 kg top mass), indicating that the linear increase in stiffness with depth fail to capture the actual stiffness increase.

8.3.1 Comparison of Predictions with 1D- and 3D-FEM

The predictions from 3D- and 1D-FEM are compared in Figure 8-16 and Figure 8-17. The input stiffness for the linear elastic soil and the linear-elastic springs are equal, and allows for a direct comparison. When the soil stiffness is based on the results from the oedometer, the difference in predicted eigenfrequency from 3D- and 1D-FEM is seen to be less than 2 %, regardless of overburden pressures. For the small strain stiffness, the predictions with 3D-FEM are 2-3 % higher than with 1D-FEM.

A deviation of 3 % or less between the 1D- and 3D-FEM is considered satisfactory with respect to the simplifications involved for 1D-approach, and it is concluded that the simplification from a 3D to a 1D geometry is successful for the linear elastic case.

When the predictions from the proposed, nonlinear soil springs are compared to the predictions from the HSS-model, the difference in predicted eigenfrequency is seen to be 3 % or less. Both models have incorporated the Hardin-Drnevich curve for stiffness degradation; however, it is incorporated differently. The HSS model controls the shape of the degradation curve through a reference strain after Santos and Correia (2001) and Benz (2007), while the proposed soil springs use the two curve fitting parameters *a* and *b* recommended by Wichtmann and Triantafyllidis (2014). For the model test in question, this appears to be of minor importance.

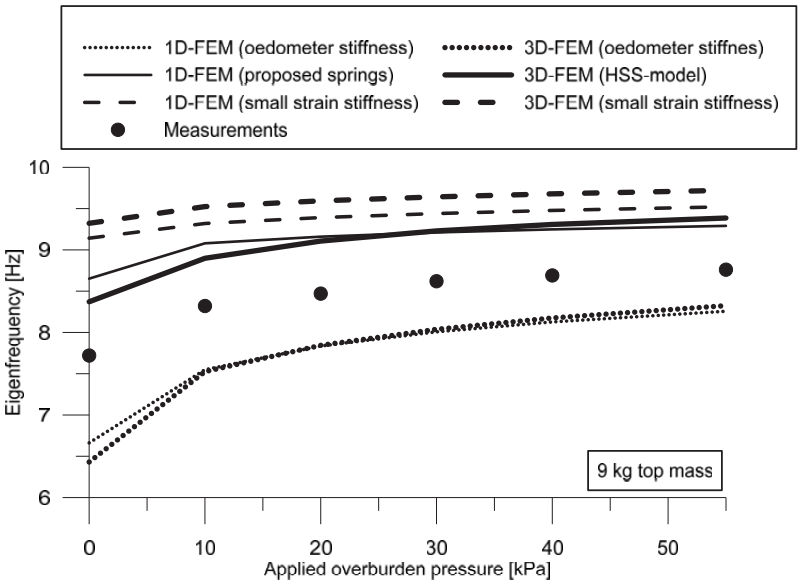

Figure 8-16. Comparison of predictions with 3D- and 1D-FEM for the top mass of 9 kg.

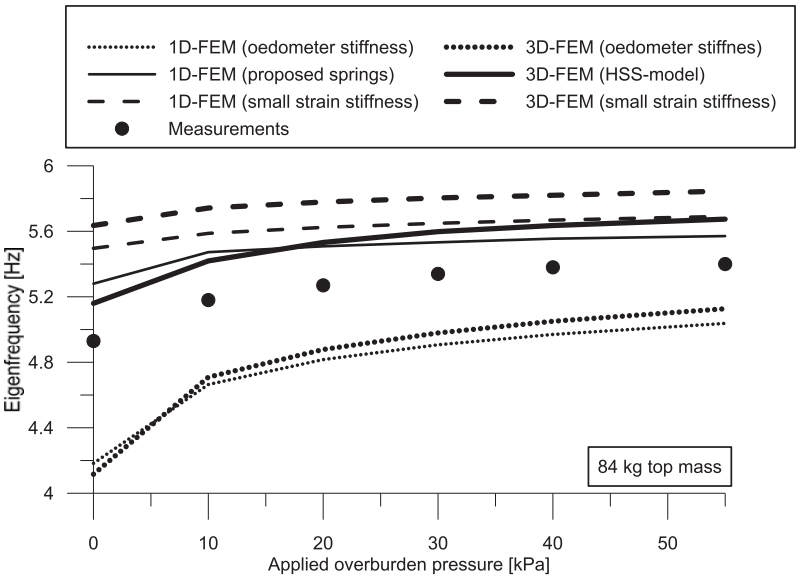

Figure 8-17. Comparison of predictions with 3D- and 1D-FEM for the top mass of 84 kg.

8.4 Chapter Summary and Conclusions

This chapter presents a back analysis of the model test in Chapter 7, performed with 3D- and 1D-FEM. The representative soil stiffness experienced by the model pile is found to correspond to a soil stiffness somewhere in between the stiffness measured in the oedometer test and the small-strain stiffness. The proposed soil springs from Chapter 6 are found to reproduce the predictions from the 3D-FEM with 3 % deviation (or less) for the linear elastic case. The same difference was seen between the predictions from the nonlinear proposed soil springs and the HSS model with 3D-FEM. Both the nonlinear springs and the HSS model were found to give a too stiff response compared the physical test.

Chapter References

Api, API (2011) API-RP-2GEO: Geotechnical and Foundation Design Considerations. Washington, USA, API Publishing Services.

Autodesk (2015) Robot Structural Analysis.

Benz, T (2007) Small-Strain Stiffness of Soils and its Numerical Consequences. In *Fakultät für Bau– und Umweltingenieurwissenschaften*. Universität Stuttgart, Stuttgart, vol. PhD, 150 p.

Hardin, BO & Drnevich, VP (1972) Shear modulus and damping in soils: Design equations and curves. *Journal of the Soil Mechanics and Foundations Division* **98(7)**:667-692.

Janbu, N (1963) Soil Compressibility as Determined by Oedometer and Triaxial Tests. In *3rd European Conference on Soil Mechanics and Foundation Engineering*. Wiesbaden, Germany, vol. 1, pp. 19-25.

Lambson, MD, Clare, DG, Senner, DWF & Semple, RM (1993) Investigation and interpretation of Pentre and Tilbrook Grange soil conditons. In *Large-scale pile tests in clay*. Clarke, J. (ed) Thomas Telford, London, vol. 1, pp. 134-196.

Moen, TI (1978) *Hokksund Sand. Determination of the Sand's Routine Data, Deformation and Strength Characteristics.*, Report F.78.04.

Plaxis Bv (2014) Plaxis3D - User's Manual.

Santos, JA & Correia, AG (2001) Reference threshold shear strain of soil. Its application to obtain an unique strain-dependent shear modulus curve for soil. In *Proceedings of Fifteenth International Conference on Soil Mechanics and Geotechnical Engineering*. A. A. Balkema vol. 1, pp. 267-270.

Terzaghi, K (1955) Evaluation of Coefficients of Subgrade Reaction. *Geotechnique* **5(4)**:297-326.

Wichtmann, T & Triantafyllidis, T (2014) Stiffness and Damping of Clean Quartz Sand with Various Grain-Size Distribution Curves. *Journal of Geotechnical and Geoenvironmental Engineering* **140(3)**:06013003.

9 Summary and Conclusions

This thesis presents the results from analytical, numerical and experimental work on spring stiffness for simplified calculations of laterally loaded piles. Analytical solutions for initial stiffness and ultimate resistance collected from the literature are compared to results from a numerical study. The numerical study is performed with the 3D-FEM, and a procedure is developed for post-processing the results so they can be used as lateral and rotational springs in a 1D-FE program. The results from the numerical and analytical work are combined, and coupled with the Hardin-Drenevich equation for stiffness degradation. This constitutes a framework of proposed soil springs.

The proposed soil springs are compared to pile load tests from the literature and to a series of model tests performed at a "large" model scale. The model tests are impact vibration tests at a 1:20 scale of a simplified offshore wind turbine geometry, and are performed and reported as a part of the work. The test series is performed at different levels of vertical effective stress in the soil, controlled by a surcharge load induced by a vacuum system. The NTNU Foundation Lab has been modified to accommodate the vacuum system as a part of the work.

Finally, the model test is back analyzed with 3D- and 1D-FEM, in order to investigate the influence of strain dependent soil stiffness to the overall stiffness of the pile-soil system.

The main contributions from this work are:

- It is demonstrated that the lateral spring stiffness is closely related to the soil stiffness. The relation between soil stiffness and spring stiffness is confirmed analytically, numerically and experimentally.
- A procedure for extraction of lateral and rotational springs from 3D-FEM is developed and described. An important feature of the developed procedure is that the accuracy of the extracted lateral springs can be checked by means of horizontal equilibrium.
- It is demonstrated that there is a need for rotational springs when the pile length to diameter ratio (L/D) is lower than $L/D \approx 5$.
- The ultimate capacity of both lateral and rotational springs are investigated. Analytical solutions from the literature has been compared to 3D-FE analyses for both a Mohr-Coulomb and a Tresca failure criterion.
- Initial stiffness of both lateral- and rotational springs has been investigated with 3D-FEM. Empirical expressions describing the spring stiffness in terms of soil stiffness and pile geometry is developed and presented. The influence of end-effects is included.

- Shortcomings in the formulation of p-y curves provided by offshore design guidelines (e.g. API-RP-2A, DNV-CN-30.4) are identified and described. The p-y curves for clay are found to underpredict the ultimate resistance close to the ground surface, and to give an initial stiffness purely dependent on the linear discretization of a curve with infinite initial stiffness. The p-y curves for sand are found to underpredict the spring stiffness close to the ground surface and over predict the stiffness at greater depths.
- High quality measurements of eigenfrequencies and shear wave velocities from a model test are provided. The model test is thoroughly described and documented, and well suited as a benchmark test.
- The eigenfrequency of the model pile was observed to be non-constant, and increasing with decreasing displacement amplitude. It is suggested that the change in eigenfrequency is related to the strain dependent stiffness of the sand.
- A new set of springs for laterally loaded piles is proposed. Initial testing of these springs show promising results; however, they tend to provide a too stiff response and further work and calibration is needed.

9.1 Objectives Set Out in Chapter 1

Four objectives where stated in Chapter 1. The answer to these objectives can be summarized as follows:

- The hypothesis of an unknown scaling effect related to lateral stiffness of large diameter piles has been investigated. No such scaling effect is identified or indicated.
- A contribution to the understanding of the soil response to lateral pile movement is provided. This thesis links the stiffness of p-y curves to the shear modulus of the soil (alternatively the Young's modulus of the soil). Further, this thesis describes the need for rotational springs at low pile L/D ratios for the beam model to be a valid representation of reality.
- The contribution from small-strain soil stiffness to the lateral foundation stiffness is investigated through a back-calculation of a model test. The lateral foundation stiffness is found to correspond to a stiffness in-between the small strain- and the oedometer stiffness of the soil. This means that the entire soil stiffness degradation curve must be accounted for in order to capture the exact lateral foundation response.

9.2 Recommendations for Choice of Soil Springs in Design of Laterally Loaded Piles

Although a general recommendation for the choice of soil springs for design of laterally loaded piles would be wishful, such an outcome is not obtained from the current work. However, for design situations requiring soil springs for the soil representation, along with high accuracy of the stiffness prediction, it is recommended to derive site specific

soil springs. A typical example of where site specific soil springs would be beneficial is monopile foundations for offshore wind turbines.

The methodology for extraction of soil springs from 3D-FEM described in Chapter 5 is used in the present work as a tool to study specific properties of soil springs. It is however recognized that this methodology has a potential also in routine design of piles. If used in routine design, features previously reserved for 3D-FEM can be accounted for, such as:

- pile kinematics
- continuum effects close to the pile ends
- internal shear effects in the soil
- effects of layering

When soil reactions from the 3D-FEM are extracted and given as nonlinear springs in a 1-D beam program, the beam program is shown to recreate the behavior in the 3D-FEM with high accuracy. After the extraction process is programmed once, a complete set of soil springs is obtained automatically from the results of the 3D-FEM. In the present work, the extraction is performed from the commercially available code Plaxis3D. The principles of the methodology are however universal, and can be applied regardless of the code used, as long as it allows for interface elements between the pile and the soil.

An important aspect to remember when applying this methodology in routine design is that the extracted soil springs will never be better than the 3D-FE simulation they are extracted from. If soil springs are created from 3D-FEM, the engineer should be certain that the 3D-FE simulation is a close approximation to reality.

9.3 Recommendations for Further Work

- The model test presented in Chapter 7 contains valuable information about damping of the pile-soil system. Analyzing these data has been outside the scope of this thesis, however this is highly recommended for further work.
- The proposed soil springs show promising results; however, further work is needed in order to improve their performance. In particular, the shape and the mathematical description of the stiffness degradation curve requires further work.
- The proposed soil springs are presented in a static context. A cyclic extension of the proposed soil springs would be required for use in the context of cyclically loaded piles.

Annex A - Derivation of the 4th order beam equation.

The derivation presented here is based on the derivation described in Chapter 2.2 of Reese and Van Impe (2001). For an Euler-Bernoulli beam, the following assumptions are made:

1. The beam is straight and has a uniform cross-section
2. The beam has a longitudinal plane of symmetry; loads and reactions lie in that plane
3. The beam material is homogeneous and isotropic over the length considered
4. The proportional limit of the material is not exceeded
5. The modulus of elasticity of the beam material is the same in tension and compression
6. Transverse deflection of the beam is small
7. The beam is subjected to static loading
8. Deflections due to shear stresses are small.

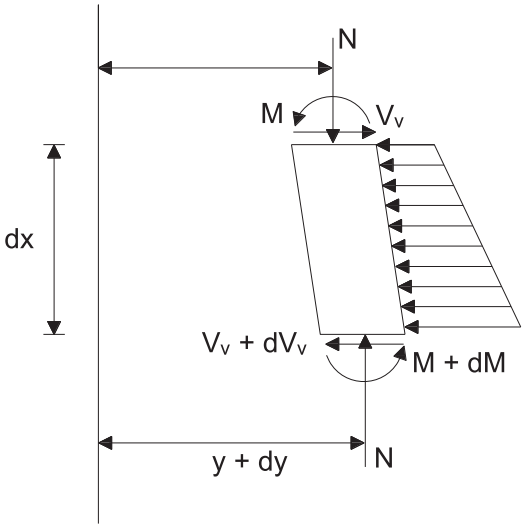

Figure A-1. Infinitely small element from beam column. After Reese and Van Impe (2001).

A bar on an elastic foundation is assumed to be subjected to horizontal loading and a pair of compressive forces N, acting in the center of gravity of the end cross-sections of the bar. Figure A1 shows an infinitely small element that is cut out of this bar, bounded by two horizontals a distance dx apart. By ignoring second-order terms, the moment equilibrium for the element in Figure A-1 becomes:

$$(M + dM) - M + Ndy - V_v\, dx = 0 \qquad \textbf{(A.1)}$$

Rewritten, we obtain Eq.(A.2):

$$\frac{dM}{dx} + N\frac{dy}{dx} - V_v = 0 \qquad \textbf{(A.2)}$$

By differentiating Eq.(A.2) with respect to x, the following equation is obtained:

$$\frac{d^2M}{dx^2} + N\frac{d^2y}{dx^2} - \frac{dV_v}{dx} = 0 \qquad \textbf{(A.3)}$$

The following identities are noted for the bending moment M, the curvature κ and the distributed load p:

$$M = E_p I_p \kappa \qquad \textbf{(A.4)}$$

$$\kappa = \frac{d^2y}{dx^2} \qquad \textbf{(A.5)}$$

$$\frac{dV_v}{dx} = p = k \cdot y \qquad \textbf{(A.6)}$$

By making the indicated substitutions, Eq.(A.3) becomes

$$E_p I_p \frac{d^4y}{dx^4} + N\frac{d^2y}{dx^2} - ky = 0 \qquad \textbf{(A.7)}$$

where

E_pI_p = beam bending stiffness
y = beam displacement normal to the 1D-beam
N = axial force
k = reaction stiffness from the elastic foundation
x = direction along the beam

The relation between the deflection y and its four first derivatives is shown in Figure A-2.

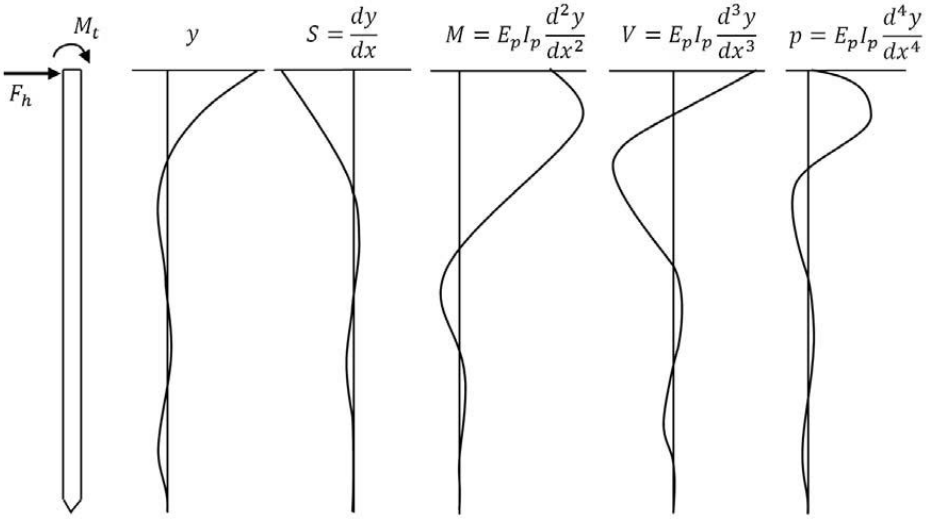

Figure A-2 Derivatives of the 4th order beam equation. After Reese and Van Impe (2001).

Timoshenko beam theory

If the beam becomes short and non-slender, assumption number 8 might not hold true. In the case where deflections due to shear stresses in the beam no longer are small the shear force V_v is expressed by:

$$V_v = G_p \kappa_T A_e \gamma_p \tag{A.8}$$

where

G_p = beam shear stiffness
γ_p = shear strain in the beam
A_e = effective shear area
κ_T = Timoshenko shear coefficient

For the case where shear deflections in the beam cannot be ignored, plane cross-sections are no longer plane and the rotation S is no longer equal to the 1st-order derivative of the displacement y. The rotation S is in this case expressed by:

$$\frac{dy}{dx} = S - \frac{E_p I_p}{\kappa_T A_e G_p} \frac{d^3y}{dx^3} \tag{A.9}$$

and consequently the bending moment M and the shear force V_v is expressed by:

$$M = E_p I_p \frac{dS}{dx} \tag{A.10}$$

$$V_v = \kappa_T A_e G(-S + \frac{dy}{dx}) \tag{A.11}$$

The 4th-order differential equation earlier expressed as Eq.(A.7) becomes then:

$$E_p I_p \frac{d^4 y}{dx^4} + N \frac{d^2 y}{dx^2} - p + \frac{E_p I_p}{\kappa_T A_e G_p} \frac{d^2 p}{dx^2} = 0 \tag{A.12}$$

The extension of the Euler-Bernoulli beam theory to account for shear deformations is referred to as Timoshenko beam theory.

Annex B – Review of the API p-y Curves

Soil springs for laterally loaded piles are often referred to as p-y curves. “p” denotes the lateral reaction force from the soil to the pile, while “y” denotes the local pile displacement. The p-y curves describing clay soils in relevant offshore design guidelines like API-RP2-GEO (API, 2011), DNV-CN-30.4 (DNV, 1992) and ISO-19902:1997 (ISO, 2007) are based on the work from Matlock (1970). p-y curves for sand adopted for the same design-guidelines are based on the work from Reese et al. (1974) and O'Neill and Murchison (1983). The p-y curves adopted in the above design guidelines are in this thesis referred to as “the API p-y curves for clay” and “the API p-y curves for sand”.

Figure B-1 shows an example set of API p-y curves for a static loaded pile in sand. The p-y curves in Figure B-1 are generated for every 5 meters of a 30 m long monopile with 5 m diameter. From the figure it is seen how both the ultimate resistance and the initial stiffness increases with depth (soil confining pressure) and how the stiffness is reduced with increasing deformation (soil strain level). It should be noted that a real design case will require less spacing between the springs along the pile.

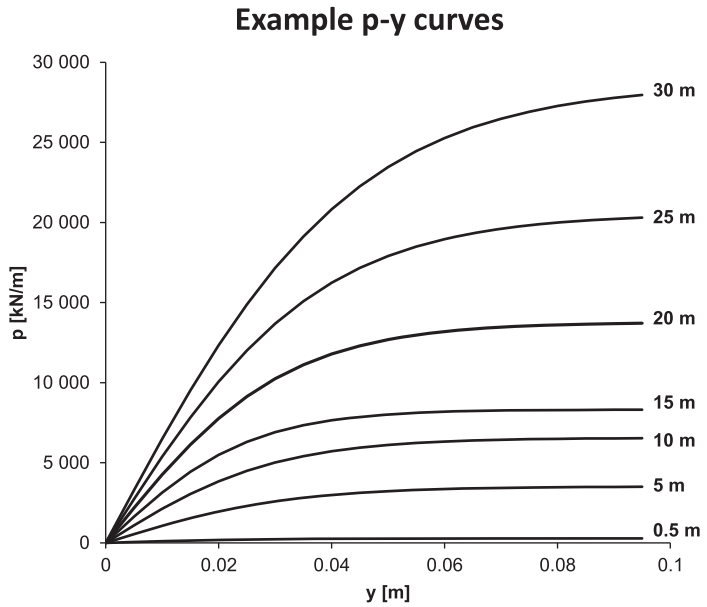

Figure B-1. Example of p-y curves for sand (φ=35°, γ’=10 kN/m^3) for a 30 m long, 5 m diameter pile.

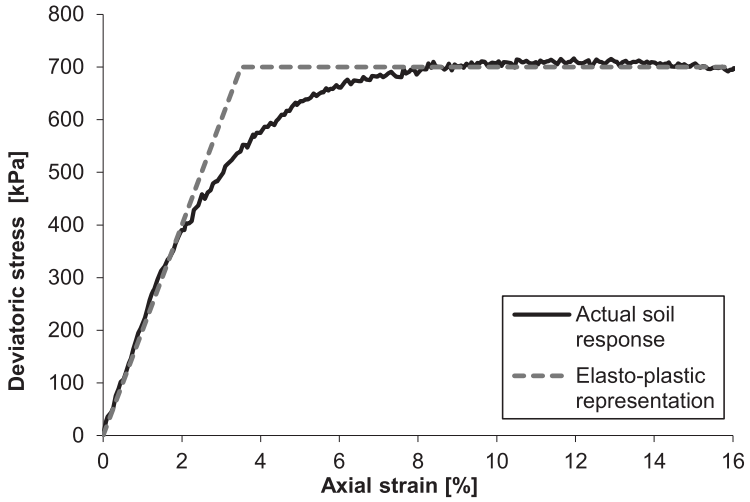

Figure B-2. Example on stress-strain curve from triaxial test on saturated Hokksund Sand

Different p-y formulations have been suggested by a variety of authors (e.g. Grande (1976), Svanø et al. (1992), McVay and Niraula (2004), Jeanjean (2009), Suryasentana and Lehane (2014), Choi et al. (2015) and also others); however, this Appendix is limited to a review of the API p-y curves.

The API p-y curves for sand and clay are both constructed in a similar manner. First, an ultimate resitance and a reference stiffness are defined; second, the reference stiffness part and the ultimate resistance are joined together by a mathematical function, describing the transition between them. Figure B-2 shows a stress-strain curve for a triaxial test on saturated Hokksund Sand, along with a linear-elastic, perfectly plastic idealization. P-y curves show a resemblance in shape with soil stress-strain curves from triaxial tests, meaning that this idealization can be used also for explaining the behavior of p-y curves.

In the context of p-y curves the linear elastic part of the idealization represents the initial stiffness of the curve, and the perfect plasticity the ultimate resistance of the curve. The mathematical function used to join the initial stiffness and the ultimate resistance together should provide a reasonable amount of nonlinearity in the transition between elasticity and plasticity.

In the following, the theoretical basis for the p-y formulations from Matlock (1970) and Reese et al. (1974) will be presented in detail.

B.1 API p-y curves for clay

For design of laterally loaded piles in clay, the procedure for obtaining load-displacement curves recommended by API originates from a publication by Matlock (1970). In short the procedure can be summarized as:

1. Predict the ultimate lateral resistance (p_u)
2. Predict a reference displacement (y_c). The reference displacement is taken as the displacement at half of the ultimate lateral resistance.
3. Construct the curve from the equation shown in Figure B-3 by using the ultimate lateral resistance and the reference displacement a as input.

A detailed description on how to construct the curves can be found in API-RP2-GEO (API, 2011)

The shape of this curve is shown together with the curve equation and the equation for the reference displacement in Figure B-3. p_u denotes the ultimate resistance, y_c the reference displacement, D the pile diameter and ε_c the strain at one-half the maximum deviator stress in laboratory undrained unconsolidated triaxial tests of undisturbed soil samples. The stiffness k of the p-y curves is defined as $k = p/y$. This stiffness is dependent on the curve shape (given from the curve equation), the reference displacement (based on correlations with soil deformation parameters and pile diameter) and ultimate resistance (based on correlations with soil shear strength and pile diameter). The stiffness dependency on the reference displacement and ultimate resistance is shown by red arrows in Figure B-3.

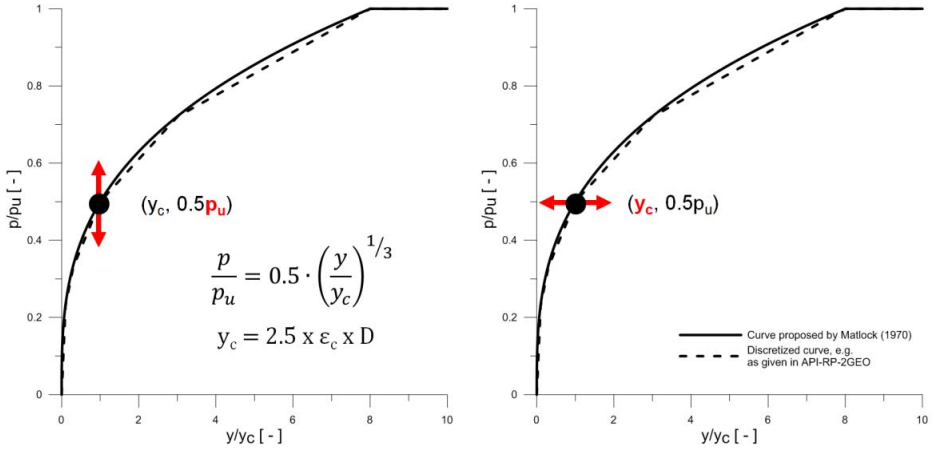

Figure B-3. Influence of ultimate lateral resistance (left) and reference displacement (right) on stiffness.

B.1.1 Initial Stiffness

The initial stiffness in the Matlock (1970) p-y curves for clay is defined through a reference displacement. The p-y curves are forced through a point defined by the reference displacement and half the ultimate resistance. The reference displacement is given as:

$$y_c = 2.5\,\varepsilon_c\,D \qquad \textbf{(B.1)}$$

where

y_c = reference displacement
ε_c = the strain at one-half the maximum deviator stress in laboratory undrained compression tests of undisturbed soil samples
D = pile diameter

The equation for the reference displacement is based on a concept from Skempton (1951), originally developed for estimating short time settlement characteristics of buried strip footings in clay. Skempton's concept is again based on the classic equation for settlements of a rectangular foundation on a linear elastic, isotropic half space:

$$\Delta = q \times B \times I_\rho \times \frac{1-\mu^2}{E_s} \qquad \textbf{(B.2)}$$

where

Δ = displacement
q = foundation pressure
I_ρ = influence value depending upon the shape and rigidity of the foundation
μ = Poisson's ratio of the solid
B = foundation width
E = Young's modulus of the solid

Following Skempton (1951), Eq.(B.2) is multiplied with $\frac{q_f}{q_f}$ and $\frac{c_u}{c_u}$ to establish a connection to bearing capacity theory:

$$\Delta = \frac{q}{q_f} \times \frac{q_f}{c_u} \times B \times I_\rho \times \frac{1-\mu^2}{E_s/c_u} \qquad \textbf{(B.3)}$$

where

c_u = undrained shear strength
q_f = ultimate bearing capacity

The term $\frac{q}{q_f}$ is thought to represent the mobilization level in the soil, while the term $\frac{q_f}{c_u}$ is recognized from bearing capacity theory, defined by Prandtl (1920) for strip-footings on clay without additional surface load as:

$$q_f = N_C \times c_u \tag{B.4}$$

where N_c is the bearing capacity factor. In the undrained compression test, the axial strain is given by:

$$\varepsilon = \frac{\sigma_1 - \sigma_3}{E_s} \tag{B.5}$$

where $(\sigma_1 - \sigma_3)$ is the deviatoric stress. Multiplying Eq.(B.5) with $\frac{(\sigma_1-\sigma_3)_f}{(\sigma_1-\sigma_3)_f}$ and $\frac{c_u}{c_u}$, Eq.(B.5) can be written as:

$$\frac{(\sigma_1 - \sigma_3)}{(\sigma_1 - \sigma_3)_f} = \varepsilon \times \frac{c_u}{(\sigma_1 - \sigma_3)_f} \times {E_s}/{c_u} \tag{B.6}$$

Skempton (1951) assumed that the stress ratio in the undrained compression test could be set equal to the stress ratio in the loaded foundation case, expressed by Eq.(B.7). Inserting Eq.(B.7), Eq.(B.6) and Eq. (B.4) into Eq.(B.3), the strain in the undrained compression test relates to the displacement of the loaded foundation by Eq.(B.8):

$$\frac{(\sigma_1 - \sigma_3)}{(\sigma_1 - \sigma_3)_f} = \frac{q}{q_f} \tag{B.7}$$

$$\Delta = \varepsilon \times \frac{c_u}{(\sigma_1 - \sigma_3)_f} \times {E_s}/{c_u} \times N_c \times B \times I_\rho \times \frac{1-\mu^2}{E_s/c_u} \tag{B.8}$$

Rewriting Eq.(B.8) and inserting the definition of undrained shear strength from the undrained triaxial compression test $c_u = \frac{(\sigma_1-\sigma_3)_f}{2}$ and the typical Poisson's ratio for undrained clay $\mu = 0.5$ gives:

$$\Delta = 0.375 \times \varepsilon \times N_c \times B \times I_\rho \tag{B.9}$$

When Matlock (1970) adopted Skempton's (1951) concept, Matlock chose a bearing capacity factor $N_c = 5.3$ and an influence value $I_\rho = 1.26$. Both the bearing capacity factor and the elastic influence value are corresponding to a rectangle on the ground

surface, with length to width ratio D/B = 10. Finally, by inserting numerical values for the bearing capacity factor and elastic influence factor, Eq.(B.10) is obtained:

$$\Delta = 2.5 \times \varepsilon \times B \qquad \textbf{(B.10)}$$

which in Matlock's (1970) notation reads (D being the pile diameter):

$$y_c = 2.5 \times \varepsilon_c \times D \qquad \textbf{(B.11)}$$

B.1.2 Ultimate Lateral Resistance – Deep Failure Mode

In general, the ultimate lateral resistance for a pile section in cohesive soil can be written as:

$$p_u = N_c \times c_u \times D \qquad \textbf{(B.12)}$$

where

p_u = ultimate lateral resistance
N_c = non-dimensional coefficient dependent on failure geometry
c_u = undrained shear strength
D = pile diameter

At greater depths, the lateral translation of a pile section is essentially unaffected by the soil surface, and plain strain conditions can be assumed. For this deeper regions Matlock (1970) chose a value of $N_c = 9$ based on empirical observations from earlier writers (Broms, 1964, McClelland and Focht, 1956, Meyerhof, 1951, Reese, 1957).

B.1.3 Ultimate Lateral Resistance – Shallow Failure Mode

At the upper portion of the pile, the assumption of plane strain conditions is no longer valid, due to simultaneous movement of the soil in both vertical and the two horizontal dimensions. Matlock (1970) states that:

"*very near the surface the soil in front of the pile will fail by shearing forward and upward and the corresponding value of N_c reduces to the range of 2 to 4, depending on whether the pile segment is considered as a plate with only frontal resistance or whether it is a square cross section with soil shear acting along the sides.*"

Matlock (1970) adopted a concept first presented by Reese (1957), who considered the ultimate soil resistance at the top-end of the pile. The top-end ultimate resistance was based on equilibrium considerations of a wedge-shaped failure geometry developing in front of a square-shaped pile. The wedge geometry considered by Reese (1957) is shown in Figure B-4, the horizontal equilibrium of the wedge geometry is described by Eq.(B.13) to Eq.(B.21) .

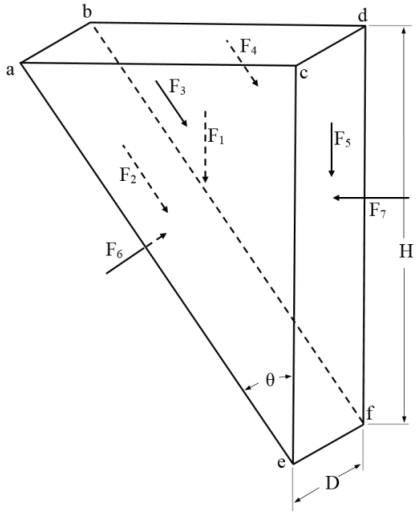

Figure B-4. The wedge failure geometry considered by Reese (1957) and Matlock (1970)

$$F_1 = \tfrac{1}{2}\gamma DH^2 \tan\theta \quad \textbf{(B.13)}$$

$$F_2 = \frac{c_u DH}{\cos\theta} \quad \textbf{(B.14)}$$

$$F_{3,H} = F_{4,H} = \tfrac{1}{2} c_u H^2 \tan\theta \quad \textbf{(B.15)}$$

$$F_5 = c_u DH \quad \textbf{(B.16)}$$

Equilibrium in the vertical direction gives the vertical component of F_6:

$$F_6 \sin\theta = F_1 + F_2 \cos\theta + 2F_3 \cos\theta + F_5 \quad \textbf{(B.17)}$$

Equilibrium in the horizontal direction gives the total soil resistance F_7:

$$F_7 = F_2 \sin\theta + 2F_3 \sin\theta + F_6 \cos\theta \quad \textbf{(B.18)}$$

Written out and simplified by trigonometric identities, Eq.(B.18) takes the form:

$$F_7 = \tfrac{1}{2}\gamma DH^2 + \frac{\alpha \mathrm{c_u}\, DH}{\tan\theta} + \frac{\mathrm{c_u}\, DH}{\sin\theta\cos\theta} + \frac{\mathrm{c_u}\, H^2}{\cos\theta} \quad \textbf{(B.19)}$$

By including side shear resistance of the square shaped pile along with shear resistance on the back of the pile, the total horizontal soil resistance becomes:

$$p_u = \tfrac{1}{2}\gamma DH^2 + \frac{\alpha \mathrm{c_u}\, DH}{\tan\theta} + \frac{\mathrm{c_u}\, DH}{\sin\theta\cos\theta} + \frac{\mathrm{c_u}\, H^2}{\cos\theta} + 2\,\mathrm{c_u}\, DH + \frac{\alpha \mathrm{c_u}\, DH}{\tan\theta} \qquad \textbf{(B.20)}$$

The derivative of Eq.(B.19) with respect to depth (H) and a Tresca failure criterion ($\theta = 45°$) gives a horizontal soil resistance with depth as expressed by Eq.(B.21).

$$p_u(h) = \gamma DH + 2\alpha_{fb} c_u D + 2\alpha_s c_u D + 2\,\mathrm{c_u}\, D + 2c_u H \qquad \textbf{(B.21)}$$

In Eq.(B.21), the first term is representing the weight of the soil wedge, the second term the vertical shear resistance along the front- and backside of the pile and the third term the shear resistance on the sides of the square cross section. The fourth term represents the shear resistance on the plane *abfe* in Figure B-4, and the last term represents the shear resistance along the planes *ace* and *bdf*.

When adopting this concept, Matlock (1970) made the following additional assumptions:

- No adhesion on the front and back-side of the pile (α_{fb}=0)
- Side shear of a cylindrical cross section can be approximated as half of the side shear for a square shaped cross-section (α_s=0.5)
- The shear resistance on the planes *ace* and *bdf* are only partly mobilized. The degree of mobilization could be described by an empirical constant J.

With Matlock's assumptions included, Eq.(B.21) reduces to

$$p_u = 3c_u D + \gamma HD + JHc_u \qquad \textbf{(B.22)}$$

When written on the form of Eq.(B.4), the bearing capacity factor N_c for the upper part of the pile becomes:

$$N_c = 3 + \frac{\gamma H}{c_u} + \frac{JH}{D} \qquad \textbf{(B.23)}$$

The transition between N_c close to the soil surface and N_c at greater depth is controlled by $N_c = \min(N_{c\_Shallow}; N_{c\_Deep})$.

B.1.4 Empirical Fitted Curve Equation

The empirically fitted curve-shape is based on field test of two instrumented, open ended, full scale piles, both having a diameter of 0.32 m (12.75 in) and an embedded length of 12.8 m (42 ft). Following the methodology from McClelland and Focht (1956) (briefly described in Chapter 1), Matlock constructed a *p*-profile and a *y*-profile for several load-steps based on integration and derivation of bending moments from the pile

loading tests. The curves at each depth were found to fall roughly along straight lines at slopes yielding an exponent of 1/3 on a semi-logarithmic plot. Eq.(B.24) was found to describe the experimental curves with a reasonably accuracy.

$$p = 0.5\left(\frac{y}{y_c}\right)^{1/3} p_u \qquad \textbf{(B.24)}$$

A problematic feature with this equation is that, due to its exponent of 1/3, it assigns an initial stiffness (k=p/y) that approaches infinity as the displacement y approaches zero. This is not only unphysical; it also introduces a computational obstacle when used in computer programs. The common solution is to give a linear discretization of the curve, thus leading to an initial stiffness of the curve purely dependent on the choice of where to assign the first discretization point.

B.1.5 Discrepancies in Matlock's Concept

The problematic feature of an infinite initial stiffness due to the equation describing the curve shape is discussed above. There are however several features with the Matlock p-y curves that are unfortunate:

- The numerical value of the bearing capacity factor N_c used in the derivation of the reference displacement is not consistent with the bearing capacity factor N_c used for ultimate resistance.
- The elastic shape factor used in the derivation of the reference displacement represents a rectangular surface foundation with L/B ratio of 10. The shape factor is a function of Poisson's ratio, embedment depth, foundation stiffness and foundation shape, and will have a different value for a pile section.
- The bearing capacity factor for the deep failure mode is assumed based on earlier empirical observations. Randolph and Houlsby (1984) and Martin and Randolph (2006) have later shown analytically that N_c varies between 9.14 – 11.94 dependent on pile-soil interface adhesion.
- In the derivation of a bearing capacity factor for the shallow failure mode, no adhesion was assumed at the front and back of the pile, while partly adhesion was assumed for side shear. Although adhesion might be lost close to the surface on the back side of the pile due to gap formation, an equal adhesion would be expected around the circumference of a circular pile.
- In the derivation of a bearing capacity factor for the shallow failure mode, the wedge is a thin slice with the width of one pile diameter. The width of the wedge would be expected to increase with distance away from the pile.
- In the derivation of a bearing capacity factor for the shallow failure mode, the empirical factor J is included simply because the theoretical solution did not fit the measured data.

The errors in the reference displacement y_c introduced by choosing numerical values for the bearing capacity factor and the elastic shape factor not consistent with pile geometry is however of minor importance. This is due to an empirical constant of 0.5 in Eq.(B.24). The effect is shown in Eq.(B.25).

$$p = \frac{0.5}{2.5^{1/3}} \left(\frac{y}{\varepsilon_c D} \right)^{1/3} p_u \qquad \textbf{(B.25)}$$

B.2 API p-y Curves for Sand

For the design of laterally loaded piles in sand, the procedure for obtaining load-displacement curves recommended in the API guidelines are originating from Reese et al. (1974). The version found in the design guidelines at present is a version refined by O'Neill and Murchison (1983), who simplified the mathematical formulation from Reese et al. (1974) describing the shape of the curves. The procedure for determining initial stiffness and ultimate resistance is as first suggested by Reese et al. (1974). In short, the procedure can be summarized as:

1. Predict the ultimate lateral resistance (p_u)
2. Choose an initial stiffness from tabulated relations with the soil friction angle.
3. Construct the curve from the Eq.(B.31) by using the ultimate lateral resistance and the initial stiffness as input.

A detailed description on how to construct the curves can be found in API-RP2-GEO (API, 2011).

B.2.1 Initial Stiffness

As for clay, the load displacement relationships defining the initial stiffness are based on the theory of elasticity. Terzaghi (1955) postulated that displacements beyond a distance of 3 diameters away from the pile have practically no influence on the local bending moments in the pile. Hence, he assumed, the displacement y can be computed in the assumption that the load p acts on an elastic layer with thickness 3D. Terzaghi (1955) assumed that the elastic influence factor for a uniformly loaded rectangle on the surface of a finite half space provided by Steinbrenner (1934) ($I_\rho = 1.484$) to be appropriate, and that a Poisson's ratio of 0.3 was representative for most sands. Inserting into Eq.(B.2), Eq.(B.26) is obtained:

$$q = y \frac{E_s}{1.35D} \qquad \textbf{(B.26)}$$

where

q = foundation pressure
y = local pile displacement
E_s = Young's modulus of the soil
D = pile diameter

The soil modulus for sand was assumed to increase linearly with overburden pressure, implying a linearly increase with depth for homogeneous soils, by the relation:

$$E_s = A_1 \gamma' z \tag{B.27}$$

where

A_1 = coefficient dependent on relative density of the sand
γ' = effective unit weight of sand. (Taken as 10 kN/m^3 by Terzaghi)
z = depth below ground surface

Inserting Eq.(B.27) into Eq.(B.26) and assuming a submerged density of sand $\gamma' = 10$ kN/m^3, defines the initial stiffness as:

$$\frac{p}{y} = \frac{A_1 \gamma' z}{1.35} = k_1 z \tag{B.28}$$

Terzaghi (1955) termed the coefficient k_1 the "coefficient of subgrade reaction" and gave values for k_1 based on experience-values for A_1 and typical densities for wet sand. For the p-y concept of Reese et al. (1974), the Terzaghi k_1-values were found to give a too soft response compared to full-scale tests. Based on test data, Reese et al. (1974) recommended k_1-values 2.5 times larger than the values reported by Terzaghi (1955). The idea of a linearly increasing soil modulus with depth was however kept.

B.2.2 Ultimate Lateral Resistance – Deep Failure Mode

At greater depths, the lateral translation of a pile section is essentially unaffected by the soil surface, and plain strain conditions can be assumed. Reese et al. (1974) assumed that a cylindrical pile section could be approximated by a square shaped rigid block of material, as shown in Figure B-5.

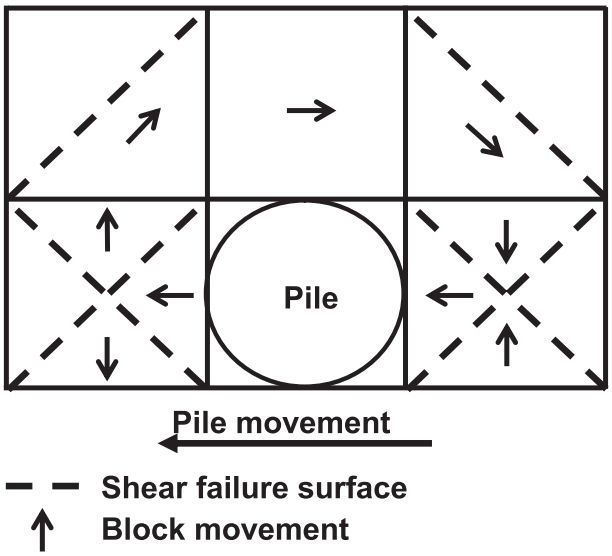

Figure B-5. Simplified geometry assumed by Reese et al. (1974). Figure after Reese et al. (1974) and Sørensen et al. (2012)

Ultimate resistance for the plane strain failure mode is calculated from Mohr-Coulomb theory, under the assumption that σ_1 cannot be less than the active earth pressure. Stresses acting in the horizontal direction are calculated from vertical overburden pressure and the coefficient of lateral soil pressure at rest. Following the failure pattern sketched in Figure B-5, the ultimate soil resistance can be determined from:

$$p_u = K_a D \gamma' z \,(\sin^8 \beta - 1) + K_0 D \gamma' z \tan\varphi \tan^4 \beta \qquad \textbf{(B.29)}$$

where

p_u = ultimate lateral resistance from the sand
K_a = Rankine coefficient for active soil pressure
K_0 = coefficient of soil pressure at rest
γ' = effective unit weight of sand
z = depth below ground surface
φ = soil internal friction angle
β = 45°+ φ/2

B.2.3 Ultimate Lateral Resistance – Shallow Failure Mode

Closer to the ground surface, the assumption of plane strain conditions is no longer valid due to simultaneous movement of the soil in both vertical and the two horizontal dimensions. In contrast to the assumptions made for clay, the geometry of the wedge is assumed to spread in the horizontal plane with an angle α. The angle α is by Reese et al. assumed to be related to the soil internal friction angle as $\alpha = \phi/2$.

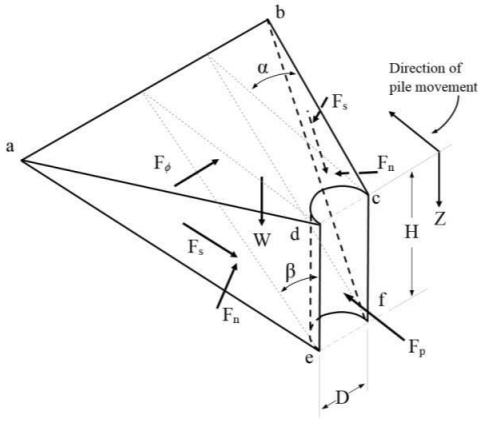

Figure B-6. Assumed failure mode close to ground surface in sand.

The shear resistance against the sides of the wedge is calculated from Mohr-Coulomb theory, where the acting horizontal stress is estimated from vertical overburden pressure and the coefficient for horizontal earth pressure at rest. Soil resistance at the front of the wedge are assumed to be equal to the passive earth pressure on the wedge, subtracted the active earth pressure on the back of the pile.

The soil resistance is found by considering horizontal equilibrium of the forces shown in Figure B-6, where the soil resistance is equal to the force denoted F_p. The soil resistance per unit length of pile is found by differentiating F_p with respect to the depth H. The result of this differentiation is given in Eq. (B.30)

$$p_u = \gamma' \mathrm{H}\left[\frac{K_0 H \tan\varphi \sin\beta}{\tan(\beta-\varphi)\cos\alpha} + \frac{\tan\beta}{\tan(\beta-\varphi)}(b + H\tan\beta\tan\alpha) + \ldots \right.$$
$$\left. K_0 H \tan\beta\,(\tan\varphi\sin\beta - \tan\alpha) - K_a b\right] \qquad \textbf{(B.30)}$$

where

K_a = Rankin coefficient for minimum active soil pressure
K_0 = coefficient of soil pressure at rest
H = depth below ground surface
b = pile diameter
γ' = submerged unit weight of soil
z = depth below ground surface
ϕ = soil internal friction angle
β = 45 + ϕ/2
α = a function of void ratio, approximately ϕ/2

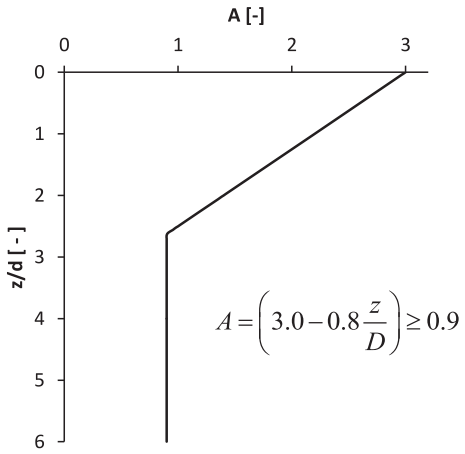

Figure B-7. Non-dimensional, empirical strength parameter A.

The theoretical framework for ultimate resistance as described above was by Reese et al. (1974) found to correspond poorly with the ultimate resistance measured from instrumented, full-scale, pile loading tests. The theoretically described resistance p_u was therefore multiplied by an empirical parameter A to match the empirical results. The empirical parameter A is shown in Figure B-7, and given to vary with depth normalized on the pile diameter.

B.2.4 Empirical Fitted Curve Equation

Reese et al. (1974) fitted a curve consisting of four individual curve segments to describe the p-y response measured from lateral load tests of two instrumented, full scale, open ended piles. The two test piles were both of diameter D = 0.6 m (24 in) and with an embedded depth of L = 21 m (69 ft). Following the methodology from McClelland and Focht (1956) (briefly described in Chapter 1), Reese et al. constructed a *p*-profile and a *y*-profile for several load steps based on integration and derivation of bending moments from the pile loading tests. The four curve segments described by Reese et al. (1974) consists of one parabola and three linear line segments. O'Neill and Murchison (1983) found that the empirical curve from Reese et al. (1974) could be replaced by a curve described by one single equation utilizing the features of the tanh-function, without significant loss of accuracy. The curve formulation from O'Neill and Murchison (1983) is the version currently found in design guidelines, and shown in Eq.(B.31). The tanh-function has the characteristic that tanh(x) = x for small values of x, and tanh(x) = 1 for larger values of x. In the context of Eq.(B.31), $p = (k_1 z)y$ at small values of y (≈ linear elastic) and $p = Ap_u$ (perfectly plastic) for large values of y.

$$p = Ap_u \tanh\left(\frac{k_1 z}{Ap_u} y\right) \quad \textbf{(B.31)}$$

A comparison between the curve shape from Reese et al. (1974) and O'Neill and Murchison (1983) is made in Figure B-8 for two different depths of a 5 m diameter pile embedded in saturated sand (friction angle φ =39°, soil unit weight γ' = 10 kN/m^3)

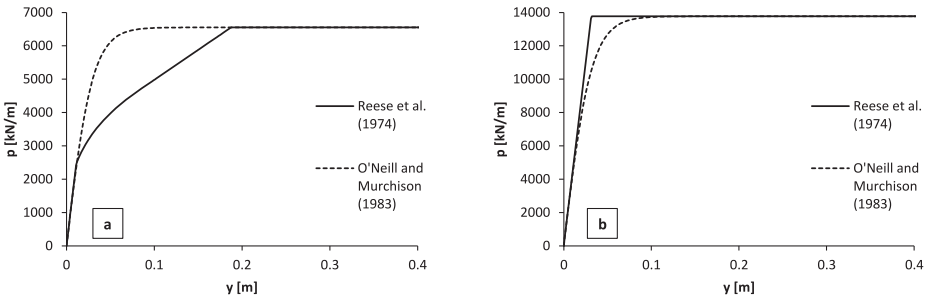

Figure B-8. Comparison of curve shapes for 5 m diameter pile.(a) 10 m depth (b) 20 m depth

B.2.5 Discrepancies in the API p-y Concept for Sand

Although more consistent in the theoretical assumptions than the API p-y curves for clay, some important discrepancies must be mentioned:

- *The assumption of linearly increasing soil stiffness with depth*. It is widely acknowledged that soil stiffness has a parabolic increase with confining pressure, e.g. as described by Ohde (1939), Janbu (1963), Hardin and Richart (1963) and Seed and Idriss (1970). The assumption of linear increase in soil stiffness with depth is likely to underestimate the soil stiffness at shallow depths, and overestimate the soil stiffness at greater depths. For piles loaded horizontally at the top, like the full scale field tests of Reese et al. (1974), the soil strain amplitudes close to the soil surface are larger, compared to the very small soil strain amplitudes with depth. Strain dependent stiffness might have partly compensated for the effect of a linear approximation to a parabolic phenomenon.
- *Geometry of the shallow failure mode.* Experimental evidence from Morita et al. (2007), Hajialilue-Bonab et al. (2011) and Lin et al. (2014) suggests that the zone with soil deformations in sand has a circular/log-spiral shape, and not a planar wedge type. A comparison of the bounding geometry for the wedge failure from Reese et al. (1974) and the observed localized strains from Morita et al. (2007) is shown in Figure B-9. The bounding geometry for the Reese-wedge in yellow dotted lines.

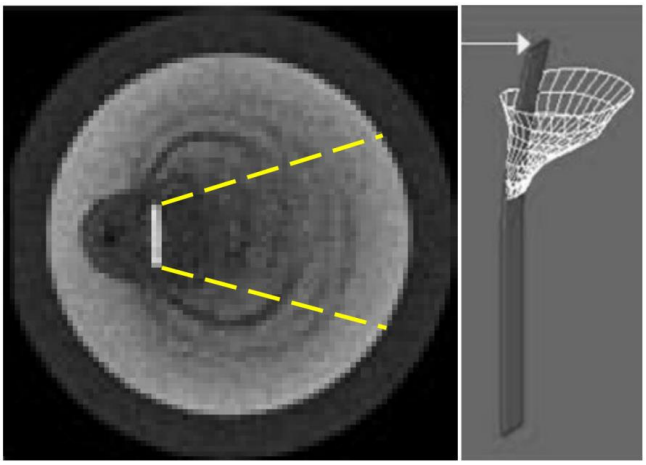

Figure B-9. Soil deformation at surface from Morita et al. (2007) together with bounding failure geometry from Reese et al. (1974) in yellow dotted lines. (D = 0.02 m, Toyoura sand, φ ≈ 32°)

- *Mismatch between measured- and theoretical ultimate resistance*. The most obvious discrepancy in the API p-y concept for sand is the mismatch between the analytical solution for ultimate resistance presented by Reese et al. (1974) and the ultimate resistance measured from pile loading tests by the same authors. This was identified already by Reese et al. (1974) and compensated by an empirical strength parameter "A."

B.3 API p-y Curves in the Context of Laterally Loaded, Large Diameter Monopiles

Laterally loaded piles used in the offshore oil and gas industry are often designed with criteria for cyclic and static ultimate limit state loads as design drivers. For this purpose, the Winkler beam approach with API p-y curves representing the soil has been considered "best practice" by the industry since the early 1970s. Piles supporting jacket structures are typically 40 – 100 m long and 1.2 - 1.8 m diameter, with several piles per jacket. In the context of offshore wind-turbines, monopile foundations are of a considerably larger diameter (typically 4 - 8 m) and considerably shorter embedded length (typically 20 – 40 m). In the context of offshore wind turbines, the serviceability- and fatigue limit states are potential design drivers at equal and/or higher importance than the ultimate limit state criteria. Accurate prediction of the load-deformation characteristics of the soil-pile system draws attention to the initial stiffness of the p-y curves. The initial stiffness of the p-y curves is a feature that has been less important in the context of designing jacket piles.

Hald et al. (2009) and Kallehave et al. (2012) documented the soil-pile interaction stiffness measured for installed, operating offshore wind turbines supported by monopile foundations in sand. The measured soil-pile interaction stiffness was significantly higher than predicted with the use of the API p-y curves and the Winkler beam approach. The amount of published data regarding measured soil-pile interaction stiffness for full-scale monopile foundations is limited; however, the conclusions from Hald et al. (2009) and Kallehave et al. (2012) were clear: The *API p-y curves and the Winkler beam approach are unconditionally under-predicting the lateral stiffness at working loads for large diameter monopiles when employed as foundations for offshore wind turbines.*

B.3.1 Criticism of the API p-y Curves in the Context of Offshore Wind Turbine Foundations

A paper by Stevens and Audibert (1979) claimed that the API p-y curves for clay under-predicted the horizontal stiffness of piles in clay, and that the deviation in observed and predicted stiffness were increasing for increasing pile diameters. Although not directly aimed at offshore wind turbine foundations, the statement of increasing deviation in measured and predicted displacements for increasing pile diameters are highly relevant for large diameter monopiles.

Wiemann et al. (2004), Lesny and Wiemann (2006), Augustesen et al. (2010), Sørensen et al. (2010), Roesen et al. (2010) and Achmus and Abdel-Rahman (2012) have all criticized the API p-y curves for sand for being too stiff at greater depths, based on finite element simulations of offshore wind turbine foundations. This is in contrast to the above mentioned physical observations from Kallehave et al. (2012) and Hald et al. (2009).

References Annex B

Achmus, M & Abdel-Rahman, K (2012) Design of Piles for Offshore Wind Energy Foundations with Respect to Horizontal Loading. In *International Offshore and Polar Engineering Conference*. pp. 143-150.

Api, API (2011) API-RP-2GEO: Geotechnical and Foundation Design Considerations. Washington, USA, API Publishing Services.

Augustesen, A, Sørensen, SPH, Ibsen, LB, Møller, M & Brødbæk, KT (2010) Comparison of calculation approaches for monopiles for offshore wind turbines. In *Numerical Methods in Geotechnical Engineering*. CRC Press, pp. 901-906.

Broms, BB (1964) Lateral Resistance of Piles in Cohesive Soils. *Journal of the Soil Mechanics and Foundations Division* **90(SM2)**:27-63.

Choi, J, Kim, M & Brandenberg, S (2015) Cyclic p-y Plasticity Model Applied to Pile Foundations in Sand. *Journal of Geotechnical and Geoenvironmental Engineering* **141(5)**:04015013.

Dnv (1992) DNV-CN-30.4: Classification Note No. 30.4, Det Norske Veritas.

Grande, LO (1976) Samvirke mellom pel og jord. In *Institutt for geoteknikk og fundamenteringslære*. Norges Tekniske Høgskole, Trondheim, vol. Dr.Ing.

Hajialilue-Bonab, M, Azarnya-Shahgoli, H & Sojoudi, Y (2011) Soil deformation pattern around laterally loaded piles. In *International Journal of Physical Modelling in Geotechnics*. vol. 11, pp. 116-125.

Hald, T, Mørch, C, Jensen, L, Bakmar, CL & Ahle, K (2009) Revisiting monopile design using p-y curves –Results from full scale measurements on Horns Rev. In *European Offshore Wind Conference & Exhibition 2009*. Curran Associates, Inc, Stockholm, Sweden, vol. 3, pp. 1926-1935.

Hardin, BO & Richart, FE (1963) Elastic wave velocities in granular soils. *ASCE Journal of the Soil Mechanics and Foundations Division* **89(SM1)**:33-65.

Iso (2007) ISO 19902:2007: Petroleum and natural gas industries -Fixed Steel Offshore Structures, ISO, International Organization for Standardization.

Janbu, N (1963) Soil Compressibility as Determined by Oedometer and Triaxial Tests. In *3rd European Conference on Soil Mechanics and Foundation Engineering*. Wiesbaden, Germany, vol. 1, pp. 19-25.

Jeanjean, P (2009) Re-assessment of P-Y curves for soft clays from centrifuge testing and finite element modeling. In *Offshore Technology Conference*. Houston,TX, vol. OTC-20158.

Kallehave, D, Leblanc, C & Liingaard, MA (2012) Modification of the API P-y Formulation of Initial Stiffness of Sand In *Proceedings of Offshore Site Investigation and Geotechnics: Integrated Technologies - Present and Future*. Society for Underwater Technology, pp. 465-472.

Lesny, K & Wiemann, J (2006) Finite-Element-Modelling of Large Diameter Monopiles for Offshore Wind Energy Converters. In *GeoCongress 2006*. pp. 1-6.

Lin, H, Ni, L, Suleiman, M & Raich, A (2014) Interaction between Laterally Loaded Pile and Surrounding Soil. *Journal of Geotechnical and Geoenvironmental Engineering* **141(4)**:04014119.

Martin, CM & Randolph, MF (2006) Upper-bound analysis of lateral pile capacity in cohesive soil. *Geotechnique* **56(2)**:141-145.

Matlock, H (1970) Correlation for Design of Laterally Loaded Piles in Soft Clay. In *Offshore Technology Conference*. Houston Texas, pp. 577-607.

Mcclelland, B & Focht, JA (1956) Soil Modulus for Laterally Loaded Piles. *ASCE Journal of the Soil Mechanics and Foundations Division* **82(4)**:22.

Mcvay, MC & Niraula, L (2004) *Development of P-Y curves for Large Diameter Piles/Drilled Shafts in Limestone for FBPIER*.

Meyerhof, GG (1951) The Ultimate Bearing Capacity of Foundations. *Geotechnique* **2(December)**:301-322.

Morita, K, Otani, J, Mukunoki, T, Hironaka, J & Pham, KD (2007) Evaluation of vertical and lateral bearing capacity mechanisms of pile foundations using X-ray CT. In *Advances in Deep Foundations*. Taylor & Francis, pp. 217-223.

O'neill, MW & Murchison, JM (1983) *Evaluation of p-y Relationships in Sands*. Houston, Texas, USA, Report Research Report No. GT-DF02-83.

Ohde, J (1939) Zur Theorie der Druckverteilung im Baugrund. *Der Bauingenieur* **20(33/34)**:451-459.

Prandtl, L (1920) Über die Härte plastischer Körper. *Nachrichten von der Gesellschaft der Wissenschaften zu Göttingen, Mathematisch-Physikalische Klasse* **1920**:74-85.

Randolph, MF & Houlsby, G (1984) Limiting pressure on a circular pile loaded laterally in cohesive soil. *Geotechnique* **34(4)**:613-623.

Reese, L, Cox, W & Koop, F (1974) Analysis of Laterally Loaded Piles in Sand. In *Offshore Technology Conference*. Houston, pp. 473–483.

Reese, LC (1957) Discussion of "Soil Modulus of Laterally Loaded Piles" by Bramlette McClelland and John A. Focht. *Journal of the Soil Mechanics and Foundations Division* **83(2)**:1228-21 -1228-34.

Roesen, HR, Thomassen, K, Sørensen, SPH & Ibsen, LB (2010) *Evaluation of Small-Scale Laterally Loaded Non-Slender Monopiles in Sand*. University, A., Aalborg, Report 91, 24 p.

Seed, H & Idriss, I (1970) *Soil moduli and damping factors for dynamic response analyses*. Report EERC 70-10.

Skempton, AW (1951) The bearing capacity of clays. In *Building Research Congress*. London, vol. 1, pp. 180-189.

Steinbrenner, W (1934) Tafeln zur Setzungsberechnung. *Die Strasse* **1**:121-124.

Stevens, J & Audibert, JME (1979) Re-examination of p-y curve formulations. In *Offshore Technology Conference*. Houston, Texas, pp. 397-404.

Suryasentana, SK & Lehane, BM (2014) Numerical derivation of CPT-based p-y curves for piles in sand. In *Geotechnique*. vol. 64, pp. 186-194.

Svanø, G, Tjelta, TI & Eide, A (1992) LDPT as calibration for new models. In *Recent large-scale fully instrumented pile tests in clay*. Clarke, J. (ed) Thomas Telford, London, pp. 463-484.

Sørensen, SPH, Brødbæk, KT, Møller, M & Augustesen, AH (2012) *Review of laterally loaded monopiles employed as the foundation for offshore wind turbines*. Aalborg, 54 p.

Sørensen, SPH, Ibsen, L & Augustesen, A (2010) Effects of diameter on initial stiffness of p-y curves for large-diameter piles in sand. In *Numerical Methods in Geotechnical Engineering*. CRC Press, pp. 907-912.

Terzaghi, K (1955) Evaluation of Coefficients of Subgrade Reaction. *Geotechnique* **5(4)**:297-326.

Wiemann, J, Lesny, K & Richwien, W (2004) Evaluation of Pile Diameter Effects on Soil-Pile Stiffness In *Proceedings of DEWEK 2004: 7. Deutsche Windenergie-Konferenz, .*

Annex C: Extraction of Soil Reaction Springs from Plaxis3D

This Annex presents a procedure for extracting load-displacement curves (p-y) and moment-rotation curves (M-θ) from the FE code Plaxis3D.

When the p-y curves are extracted, the displacements (y) along the pile are given as a default output from the FE code. The line load (p) is found from integration of horizontal stresses at the interface between pile and soil. For the distributed M-θ curves, rotations are found from the difference in displacement between neighboring nodes. The moment response is found from integration of vertical shear at the pile/soil surface, which is multiplied with the distance to the pile centerline. For both curve sets, the load at the pile top is increased step-vise, with each step defining one point on the p-y and M-θ curves. The described procedure gives one point on the p-y and M-θ curves, and is repeated for different loads to obtain more points on the curve.

C.1 Limitations

To be applied on an arbitrary pile placed at arbitrary coordinates in the soil volume, the presented procedure will need some modifications. To highlight the main principle of the procedure, it is presented for a pile with a circular cross section that meets the following requirements:

- The coordinate system is using z as the vertical axis, and center of the pile is in the x-y origin.
- The pile is loaded/displaced in the x-direction
- The pile is meshed with a structured mesh. In particular, it is important that element borders are at the same z-level around the pile circumference.

C.2 Extracting y-values

Pile displacements are given as default output of node values for plate elements in the Plaxis3D output program. By double clicking on the plate elements of interest, the selected plate elements will display in a new window. From the menu in this window, the option *Deformations→Total displacements→Table* presents node location and displacements in Cartesian coordinates for each node, along with the vector product of the displacements. The default header for this table is given in Table C-1.

Table C-1. Column headings for table of total displacements of plate elements in Plaxis3D.

Structural element	Node	Local number	X [m]	Y [m]	Z [m]	u_x [m]	u_y [m]	u_z [m]	|u| [m]

A top loaded pile free to rotate can have different horizontal displacements at front and back of the pile. Two different methods for getting the displacement at the pile centerline are found. Both methods give equally good results:

1) Sort all the pile nodes after z-value (vertical location). A structured mesh will give nodes at a discrete number of vertical levels, and with a uniform spacing between the nodes. Assuming that the pile cross section is not deformed during loading, the mean value of the displacements at one z-level will be equal to the pile centerline displacement.
2) If care is taken when the geometry is made, the automatic mesh generator in Plaxis3D can be forced to assign nodes at x = 0 (centerline of the pile). Displacements at the pile centerline are then found as a direct output by sorting the selected nodes after their x-coordinate.

C.3 Extracting p-values

Interface elements in Plaxis3D are triangular 2D-area elements of zero thickness. For the hollow, circular shaped pile in question, they are located between plate elements and soil elements. For a hollow pile, interface elements should be assigned on both sides of the pile (inside and outside). The Plaxis3D output program gives stresses in the interface nodes as a default output. For interface elements, shear- and normal stresses at the interface surface are given in the local element coordinate system. The local element coordinate system is oriented with one axis normal to the interface surface and two axes tangential to the interface surface. An example is shown in Figure C-1 for an outside interface on a circular cross section. As seen from the figure, every element around the cross section has its own coordinate system, all with different orientation relative to a global coordinate system. For the inside interface, the direction of the local horizontal axes are opposite of the outside interface.

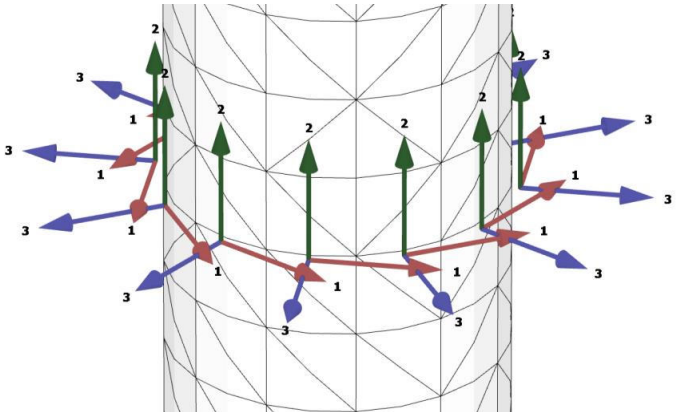

Figure C-1. Local coordinate systems for interface elements. Note that the mesh is structured.

P-values are extracted from the interface stresses acting in the horizontal plane (x-y plane of the global coordinate system for a vertical pile). This corresponds to stresses acting in direction of axis 1 and 3 in Figure C-1.

By double clicking on the interface elements of interest in the Plaxis3D Output program, the selected interface elements will display in a new window. From the menu in this window, the option *Interface stresses→Table of node values* presents node location in cartesian coordinates (global coordinate system) for each node, along with stresses and pore pressures. In total, the table contains 20 columns, whereof 8 columns are of particular interest for extraction of soil springs. Column headings for the 8 columns of interest are shown in Table C-2.

For finding the horizontal load component from an element, knowledge of the element orientation is necessary. For a vertical pile, the element orientation is found from the node coordinates in the x-y plane. Figure C-2 shows a pile with center in x-y origin. The orientation ψ of the element projection in the x-y plane can be found from trigonometry or vector mathematics.

Table C-2. Column headings for the columns of interest for extraction of p-values and M-values.

Structural element	Local number	X [m]	Y [m]	Z [m]	σ_N [kN/m^2]	τ_1 [kN/m^2]	τ_2 [kN/m^2]

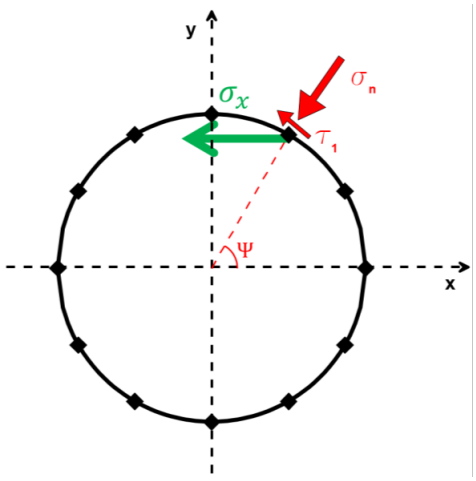

Figure C-2. Pile cross section and stress components in x-y plane

We recall the premise of that the pile is loaded in the x-direction and finds the component of stress in the x-direction for each node as:

$$\sigma_x = \sigma_N \cos\psi + \tau_1 \sin\psi \tag{C.1}$$

Knowing the x-component of stress in every node, the next step is to find the force component from each element. This is done by integrating stresses in the x-direction over the element area. In the presented procedure, this is done by Gaussian integration. Figure C-3 shows the local numbering of nodes and Gaussian integration points for the local coordinate system of the 6-noded area element used for interface elements in Plaxis3D. Local coordinates for the Gaussian integration points are given in Table C-3, and an auxiliary coordinate ζ is defined as ζ = 1-ξ-η. Expressed by the local coordinates (ξ and η) and the auxiliary coordinate, the shape functions for the 6-noded area element is given by Eq.(C.2). With help from the shape functions, the stress component in the x-direction is calculated for each Gaussian integration point, as shown in Eq.(C.3)

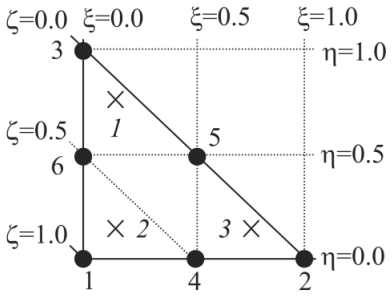

Figure C-3. Local numbering and positioning of nodes (●) and Gaussian integration points (x) for 6-noded area elements in Plaxis3D. Figure from Plaxis BV (2014).

Table C-3. Local positioning and weighting factors for Gaussian integration points for 6-noded area elements in Plaxis3D.

Point	ξ_i	η_i	w_i
1	1/6	2/3	1/3
2	1/6	1/6	1/3
3	2/3	1/6	1/3

$$\begin{aligned} N_1 &= \zeta_i\left(2\zeta_i - 1\right) \\ N_2 &= \xi_i\left(2\xi_i - 1\right) \\ N_3 &= \eta_i\left(2\eta_i - 1\right) \\ N_4 &= 4\zeta_i\xi_i \\ N_5 &= 4\xi_i\eta_i \\ N_6 &= 4\eta_i\zeta_i \end{aligned} \tag{C.2}$$

$$\sigma_{x,i} = \sum_{j=1}^{6} N_{i,j}\sigma_{x,\mathrm{j}} \tag{C.3}$$

In Eq.(C.3), the x-component of stress in Gaussian integration point *i* is calculated from the x-component in the nodes, with *j* being the node number. The Gaussian integration gives the representative stress component σ_x in the element from Eq.(C.4).

$$\sigma_x = \sum_{i=1}^{3} \sigma_{x,i} w_i \tag{C.4}$$

To find the force contribution from the element, the representative stress is multiplied by the element area. The area of a triangular shaped element can be calculated from the formula for a general triangle in 3-dimensional space given in Eq.(C.5).

$$A = \frac{1}{2}\sqrt{\begin{vmatrix} x_1 & x_2 & x_3 \\ y_1 & y_2 & y_3 \\ 1 & 1 & 1 \end{vmatrix}^2 + \begin{vmatrix} y_1 & y_2 & y_3 \\ z_1 & z_2 & z_3 \\ 1 & 1 & 1 \end{vmatrix}^2 + \begin{vmatrix} z_1 & z_2 & z_3 \\ x_1 & x_2 & x_3 \\ 1 & 1 & 1 \end{vmatrix}^2} \tag{C.5}$$

The numbering 1-3 corresponds to node-number 1-3 in Figure C-3.

The force contribution for one element is summarized for each “element row”. An example of an element row is shown in blue in Figure C-4. If one row of elements consists of *k* elements, the force contribution from one row is the integral of force in x-direction from element 1 to *k*. The force contribution from the element row is divided by the height of the element row to get the force per unit length of pile, also known as p:

$$p = \frac{\sum_{1}^{k} \sigma_{x,l} A_l}{dz} \tag{C.6}$$

where *dz* is the height of one “element row”, as defined in Figure C-4. With the definition from (C.6), p has the unit of FL^{-1}.

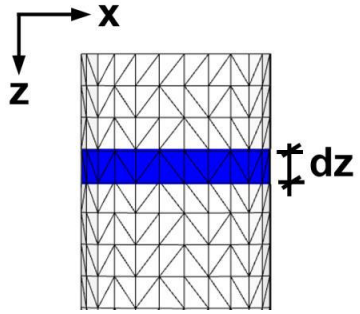

Figure C-4. Circular pile section meshed with a structured mesh. Note that the element boundaries are on the same z-level. Minimum spacing of the p-y curves are determined by the element size, e.g. each "row of elements" corresponds to one p-y curve. The elements in blue is an example of one "row of elements".

C.3.1 Extraction of p-values from Inside vs. Outside Interface

The same methodology is applied for extraction of p-values for interface elements both inside and outside the pile. The total p-value at one depth is the sum of the p-contribution from both sides at that depth. For the parametric study presented in this thesis, the global contribution from the inside interface was typically in the order of 5 - 10% of the applied load at pile top.

C.3.2 Control of Extracted p-values

If the extraction of p-values is done correctly, integration of p-values over the pile length will give the applied horizontal load at the pile top. The accuracy will be similar to the tolerated error in the 3D finite element calculation the p-values are extracted from, or less.

C.4 Extraction of θ-values

Rotations are not a default output in Plaxis3D, and is therefore calculated from the displacements. The angle between the displaced plate element and the original orientation is calculated from the difference in pile displacement for two neighboring nodes.

By double clicking on the plate elements of interest in the Plaxis3D Output program, the selected plate elements will display in a new window. From the menu in this window, the option *Deformations→Total displacements→Table* presents node location and displacements in cartesian coordinates for each node, along with the vector product of the different displacements. The default header for this table is given as Table C-1.
A top loaded pile free to rotate can have different horizontal displacement at the front and back of the pile. Displacements at the pile centerline are therefore used, with reference to Section C.2 for a description on how to find displacements of the pile centerline. When rotations are calculated, it is assumed that the plate element does not deform in axial direction. The plate elements are further assumed small enough that a uniform rotation can be approximated over the element without loss of accuracy.

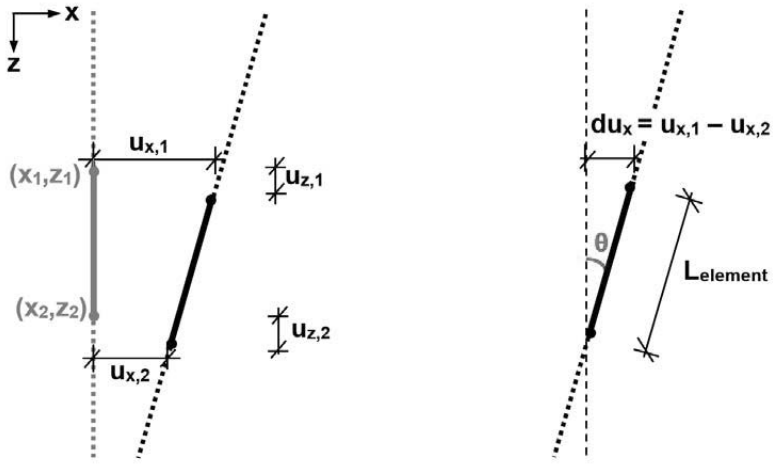

Figure C-5. Rotation of plate element. Definition of terms for Eq.(C.7)

A sketch of a rotating plate element is shown in Figure C-5. This figure also gives the definitions needed for Eq.(C.7a) and Eq.(C.7b), where the rotation θ is calculated from. Eq.(C.7a) gives the rotation around the y-axis for a plate element with an arbitrary start position in the x-z plane. For the common case of a vertical pile, the plate elements will initially be oriented along the z-axis, and the simpler Eq.(C.7b) that calculates the angle between the rotated plate element and the vertical axis can be used.

$$\theta = 2\arcsin\left(\frac{\sqrt{\left(u_{x,1}-u_{x,2}\right)^2+\left(u_{z,1}-u_{z,2}\right)^2}}{2L_{element}}\right) \qquad \textbf{(C.7a)}$$

$$\theta = \arcsin\left(\frac{du_x}{L_{element}}\right) \qquad \textbf{(C.7b)}$$

C.5 Extraction of M-values

As for the p-values, the M-values are extracted from the interface elements. Table C-2 gives the column headings of interest for both p-values and M-values. Where the p-values were concerned with the horizontal interface stresses, the M-values are concerned with the vertical interface stresses. Figure C-1 shows the local axis-system for outside interface elements of a vertical pile in Plaxis3D. For both inside- and outside interface elements for a vertical pile, the local axis number two is the vertical axis with positive direction upwards. The shear stresses acting in the axial direction of the pile are denoted τ_2 in the default output.

The first part of the procedure for extracting M-values follows the procedure for extracting p-values closely. Vertical shear stresses at the interface elements are given as default output at node locations. With help from the element shape functions in Eq.(C.2), the vertical shear at the location of the Gaussian integration points are given as:

$$\tau_{z,i} = \sum_{j=1}^{6} N_{i,j} \tau_{z,\mathrm{j}} \qquad \textbf{(C.8)}$$

where the subscript *i* denotes the stress point number and subscript *j* denotes the node number. Numbering of nodes and Gaussian integration points are given in Figure C-3. The Gaussian integration gives the representative stress component τ_z in the element from Eq.(C.9).

$$\tau_z = \sum_{i=1}^{3} \tau_{z,i} w_i \qquad \textbf{(C.9)}$$

The representative stress component τ_z are multiplied by the element area, given by Eq.(C.5) to get the vertical force contribution from the element:

$$F_z = \tau_z A \qquad \textbf{(C.10)}$$

The moment contribution from each element is then calculated as the vertical force from the element, multiplied with the moment arm. The moment arm is defined as the distance from center of the x-y projection of the element to the pile centerline in load direction (x-direction). The moment contribution from each element is integrated numerically over each “element row”, with “element row” defined as in Figure C-4. By dividing the moment contribution by the height of on “element row”, the moment contribution is expressed as moment contribution per unit length of pile. This is shown in Eq.(C.11).
If one row of elements consists of *k* elements, and the height of an element row is defined as *dz* in Figure C-4, the moment contribution per unit length of pile is:

$$\frac{M}{dz} = \frac{\sum_{1}^{k} F_{z,i} r \cos\psi_i}{dz} \qquad \textbf{(C.11)}$$

where r is the pile radius and ψ is defined in Figure C-2. With the definition from Eq.(C.11), M has the unit of [FL/L].

C.5.1 Extraction of M-values from Inside vs. Outside Interface

The same methodology is applied for extraction of M-values for interface elements both inside and outside the pile. The total M-value at one depth is the sum of the M-contribution from both sides at that depth.

C.6 Hints

The described methodology relies on a structured mesh for the plate elements to be working. The automatic mesh generator in Plaxis3D makes unstructured meshes, and needs to be forced by geometry lines, soil layering etc. to create a structured mesh.

- For the purpose of soil spring extraction, definition of layers in the borehole tool is found to be an efficient way of controlling the "element row height" dz.
- When creating the pile cross section with the polycurve tool, the cross section will be piecewise linear and not perfectly circular. This is shown in Figure C-6. The polycurve-tool lets the user control the angle χ in Figure C-6, which again to a large extent controls the location of element borders in the x-y plane. This will however also depend on the mesh density.
- As shown in the main text, properties of the extracted soil-springs will be dependent on the soil properties, pile kinematics and the model boundaries. When creating the 3D-FEM model, knowledge of how the model boundaries will influence the p-y stiffness for elastic and elasto-plastic soil models is of particular importance when deciding on model boundaries. Reference is made to Baguelin et al. (1977) and main text of this thesis for further reading.
- When load is applied to the top of the pile, it is in many cases convenient to assign a stiff top-plate at top of the pile and give the load as a point load. The stiff lid will distribute the load over the pile circumference, avoiding problems of local distortion at the load attachment point. The top-lid must be located some distance above ground surface to avoid that the top-lid take soil reactions that otherwise would be taken by the pile walls. In order to have the top-lid above the ground surface, the pile needs to be elongated above the ground surface.
- Plaxis3D Output offers "Table of stress point values". These stress points are of different location than the Gaussian Integration points and the two should not be mistaken.
- When p- and M-values are extracted from the inside interface, attention should be paid to that the orientation of the local axes 1 and 3 are opposite to the outside interface.
- The described methodology for soil-spring extraction can be implemented into a spreadsheet or a programming tool like MatLab or similar. The scriptable output

program released with the 2015-version of Plaxis3D makes it possible to fully automate the procedure.

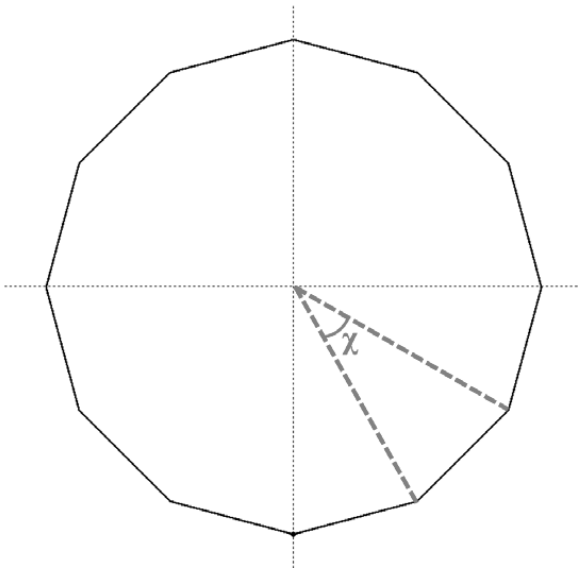

Figure C-6. Piecewise linear approximation to circular shape in the Plaxis3D polycurve tool. Discretization angle χ shown in red.

References Annex C

Baguelin, F, Frank, R & Saïd, YH (1977) Theoretical study of lateral reaction mechanism of piles. *Geotechnique* **27**:405-434.

Plaxis Bv (2014) Plaxis3D - User's Manual.